



**DEPARTAMENT DE FÍSICA APLICADA i ÒPTICA**

**Av. Diagonal 647, 08028 Barcelona**

**THIN FILM NANOCRYSTALLINE SILICON  
SOLAR CELLS OBTAINED BY HOT-WIRE CVD**

**Cristóbal Voz Sánchez**

**Programa de doctorat:** Física i Tecnologia de Materials

**Bienni:** 1995-1997

**Tutor:** Manuel Varela Fernández

**Director:** Jordi Andreu Batallé i José Miguel Asensi López

Memòria presentada per optar al grau de Doctor

Barcelona, Gener 2001

*a la família  
i els amics*

This work has been carried out in the Department of Applied Physics and Optics of the University of Barcelona, directed by Dr. Jordi Andreu and Dr. José Miguel Asensi, in the framework of the project *Crystalline silicon solar cells on low temperature substrates* (JOR3-CT97-0126) in the JOULE programme of the European Commission, and also with the aid of the projects MAT94-262, MAT97-1714-CE and MAT98-1305-CE of the CICYT of the Spanish Government.

## Thin film nanocrystalline silicon solar cells obtained by Hot-Wire CVD

|   |    |
|---|----|
| Acknowledgments.....  | 3  |
| Outline of this thesis.....   | 5  |
| 1. Introduction.....  | 7  |
| 1.1. The need for renewable energy sources.....                             | 7  |
| 1.2. The option for Solar Energy.....                                       | 8  |
| 1.3. Thin film technologies for reducing costs.....                         | 10 |
| 1.4. Thin film crystalline silicon solar cells.....                         | 13 |
| 1.5. The brief history of Hot-Wire CVD.....                                 | 17 |
| 2. The HWCVD set-up. Electrical and optical characterisations.....          | 21 |
| 2.1. The HWCVD set-up.....  | 21 |
| 2.2. Characterisation of samples.....                                       | 26 |
| 2.2.1. Dark conductivity.....   | 26 |
| 2.2.2. Steady state photoconductivity.....                                  | 28 |
| 2.2.3. Photothermal deflection spectrometry.....                            | 31 |
| 2.3. Characterisation of devices.....                                       | 36 |
| 2.3.1. Current density-voltage characteristic.....                          | 36 |
| 2.3.2. Spectral response and quantum efficiencies.....                      | 38 |
| 2.3.3. Depletion capacitance of rectifying contacts.....                    | 42 |
| 3. Nanocrystalline silicon by HWCVD. Optical and electrical properties..... | 47 |
| 3.1. Optical properties.....  | 47 |
| 3.1.1. Optical absorption coefficient.....                                  | 47 |
| 3.1.2. Enhanced optical absorption.....                                     | 50 |
| 3.1.3. Benefits from enhanced optical absorption.....                       | 54 |
| 3.1.4. Light scattering.....  | 58 |
| 3.1.5. Surface roughness.....   | 59 |
| 3.2. Electrical properties.....   | 65 |
| 3.2.1. Dark conductivity of undoped nanocrystalline silicon.....            | 65 |
| 3.2.2. Evidences of contaminants incorporation.....                         | 70 |
| 3.2.3. Dependence on the deposition rate.....                               | 72 |
| 3.2.4. Effective density of localised states.....                           | 73 |
| 3.2.5. Anticorrelation between photoconductivity and layer quality.....     | 76 |
| 3.2.6. Chemical stability.....  | 82 |
| 4. Physical aspects in thin film p-i-n solar cells.....                     | 85 |
| 4.1. Motivation of p-i-n structures.....                                    | 85 |
| 4.2. Equivalent circuit of low mobility thin film solar cells.....          | 86 |
| 4.2.1. The recombination term.....  | 86 |
| 4.2.2. Analytical model.....  | 87 |
| 4.2.3. The VIM method.....  | 88 |
| 4.2.4. The VIM method applied to nc-Si:H p-i-n structures.....              | 92 |

---

|   |     |
|---|-----|
| 4.3. Collection in p-i-n solar cells.....                                   | 94  |
| 4.3.1. The complexity of the problem.....                                   | 94  |
| 4.3.2. Non uniform internal electric field.....                             | 95  |
| 4.3.3. Short circuit recombination losses.....                              | 98  |
| 4.3.4. Predictions of the model.....  | 102 |
| 4.3.5. The link with the voltage collection.....                            | 104 |
| 4.3.6. Contaminated devices.....  | 106 |
| 5. Nanocrystalline silicon solar cells by HWCVD. Technological aspects..... | 111 |
| 5.1. Previous technological aspects.....                                    | 111 |
| 5.1.1. Selection of the TCO.....  | 111 |
| 5.1.2. Leakage currents.....  | 116 |
| 5.1.3. Doped layers.....  | 118 |
| 5.2. The role of the active layer in the device performance.....            | 120 |
| 5.2.1. The microdoping approach.....  | 120 |
| 5.2.2. Influence of the filament temperature.....                           | 125 |
| 5.2.3. Cleaner deposition conditions.....                                   | 127 |
| 5.2.4. Influence of the substrate temperature.....                          | 130 |
| 5.3. Stability of devices.....  | 132 |
| Conclusions.....  | 135 |
| References.....   | 139 |
| Acronym list.....   | 147 |
| Figure list.....  | 149 |
| Table list.....   | 155 |
| Resumen en castellano.....  | 157 |

## Acknowledgements

This Ph. D. Thesis is the result of more than four years of research. Though cooperation is always necessary to carry out so much work, now I feel that I had not succeeded without the help of many people:

First of all, I am grateful to Dr. J.L. Morenza, Head of the Department of Applied Physics and Optics at the University of Barcelona, for accepting me as a Ph. D. student to participate in this interesting work and for his kindness.

I thoroughly acknowledge Dr. J. Andreu and Dr. J.M. Asensi, codirectors of this thesis, and also Dr. J. Bertomeu, Dr. J. Puigdollers and Dr. J. Merten, for their wise hints and sincere friendship.

I am specially grateful to Dr. D. Peiró, who designed the deposition set-up and carried out all the structural characterisations of the samples. His previous studies have been essential to the development of this work.

I also acknowledge A. Muñoz, who shared many sometimes boring measurement tasks. I am also grateful to D. Soler and M. Fonrodona. Though latterly incorporated into the group, they have greatly cooperated in this thesis with a lot of technological work and additional points of view.

I am specially grateful to C. Guerrero, F. Benítez and J. Roldán, for their encouraging support and honest friendship, for the nice time we spent together.

I thank all the other fellows at the laboratory for their help and friendship.

I acknowledge the members of the Thesis Jury, for accepting our invitation and reading this manuscript.



## OUTLINE OF THIS THESIS

The Hot-Wire Chemical Vapor Deposition (HWCVD) allows both low substrate temperatures and fast deposition rates for obtaining small-grain crystalline silicon films. These features, along with the low implementation and upkeep costs, make the HWCVD technique a very attractive technology for a future industrial application. Hence, the development of this technique was included as one of the main tasks involved in the project *Crystalline silicon solar cells on low temperature substrates CRYSTAL* (JOR3-CT97-0126) in the JOULE programme of the European Commission. This project, led by BP Solar, was focused on the research of a suitable technology for the mass production of thin film crystalline silicon solar cells on inexpensive substrates. This thesis started in 1996 and has been developed in the framework of this project. An excellent collateral work [Peiró, 1999] deals with the design of the new HWCVD set-up in the laboratory and studies the influence of the deposition parameters on the microstructural properties of the samples. The present work concerns the optical and electrical properties of these nanocrystalline silicon layers obtained by HWCVD. Special attention is paid to those properties which would influence the photovoltaic performance of devices. Besides, technological and physical aspects about this thin film solar cell technology are considered. Finally, a comprehensive study of the solar cells obtained by HWCVD during the period of research within the *CRYSTAL* project is presented. A brief description of the contents of each chapter is presented below:

### **Chapter 1. Introduction**

In this chapter we evidence the need for renewable energy sources and we justify our option for photovoltaics. The thin film option as an alternative for lowering costs is presented and we review the state of the art in thin film crystalline silicon solar cells. Finally, we introduce the Hot-Wire Chemical Vapour Deposition as a promising technique to obtain nanocrystalline silicon inexpensively at high deposition rates.

**Chapter 2. The HWCVD set-up. Optical and electrical characterisations**

This chapter briefly describes the HWCVD set-up at University of Barcelona and the experimental characterisation techniques used to study the optical and electrical properties of our layers. An extensive description of the deposition set-up and the structural characterisation of the samples are part of a previous work[Peiró, 1999]. The specific characterisations carried out to the obtained devices will also be indicated in this chapter.

**Chapter 3. Nanocrystalline silicon by HWCVD. Optical and electrical properties**

In this chapter we will study the optical and electrical properties of nanocrystalline silicon obtained by HWCVD. Special attention will be paid to those properties which clearly influence the photovoltaic performance of devices. The influence of the deposition conditions on the photovoltaic suitability of the material is also discussed.

**Chapter 4. Physical aspects in thin film p-i-n solar cells**

The fundamental understanding of the device performance will be discussed in this chapter. An extended equivalent circuit and analytical model used in the literature to study thin film p-i-n structures is briefly described. An improved model which treats analytically the more general case including a non constant electric field is presented.

**Chapter 5. Nanocrystalline silicon solar cells by HWCVD. Technological aspects**

In this chapter we will consider some subjects which must be taken into account to fabricate thin film solar cells. Technological aspects such as the selection of a suitable front electrode or a method to reduce lateral leakage currents are considered. Besides, a comprehensive study of the p-i-n devices obtained by HWCVD during the period of research within the *CRYSTAL* project (JOR3-CT97-0126) is presented.

# Chapter 1

## Introduction

In this chapter we evidence the need for renewable energy sources and we justify our option for photovoltaics. The thin film option as an alternative for lowering costs is presented and we review the state of the art in thin film crystalline silicon solar cells. Finally, we introduce the Hot-Wire Chemical Vapour Deposition as a promising technique to obtain nanocrystalline silicon inexpensively at high deposition rates.

### 1.1. The need for renewable energy sources

The apparently unlimited growth of the Humankind has been ever based on an steadily increasing energy consumption. However, on the verge of the 21<sup>st</sup> century, we realise that our energy demand becomes unsustainable. This not only includes fossil fuels derived from oil, but also fissionable minerals used for nuclear power production. Moreover, the international community begins to be aware of the environmental impact of these traditional energy resources. Levels of carbon dioxide in the atmosphere have increased a 28% in the last centuries mainly because of fossil fuels combustion. As a result, the climate is becoming warmer due to the so-called Greenhouse effect[Fig. 1.1].

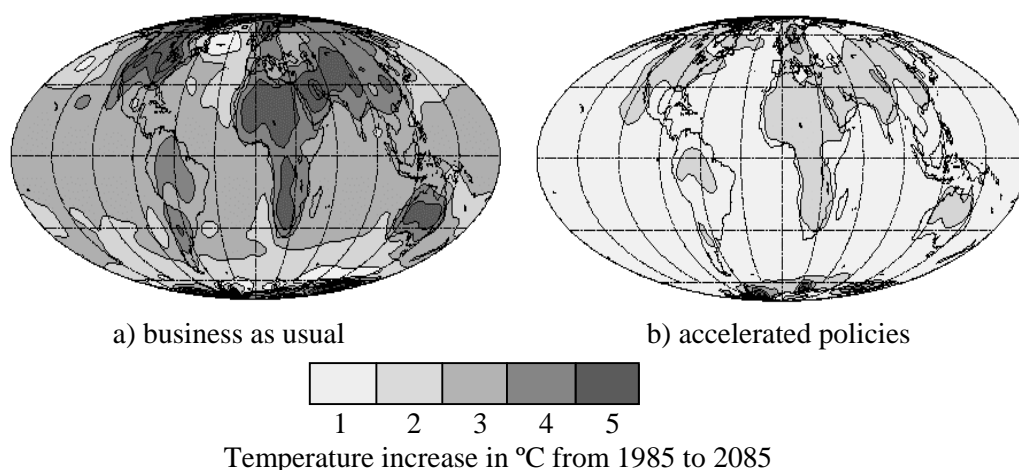


**Figure 1.1:** Expected global warming due to the Greenhouse effect during the next century computed at the Max Planck Institute for Meteorology a) for an unabated increase in carbon dioxide emissions and b) with accelerated policies promoting renewable energy sources in order to reduce carbon dioxide emissions[www.dkrz.de].

This problem could be even exacerbated in the near future by the accompanied deforestation. On the other hand, the production of nuclear power involves unaffordable harmful radioactive wastes. By contrast, renewable energy sources will never run out. It is energy for our children's children... and it is clean! The most outstanding of these never-ending energy sources are wind and solar photovoltaic (PV) energies[Table 1.1].

**Table 1.1:** Global trends in energy use by source, 1991-1997. Data provided by the Worldwatch Institute[Milford, 1999].

| Energy Source   | Annual rate of growth (%) |            |            |             |             |             |             |
|-----------------|---------------------------|------------|------------|-------------|-------------|-------------|-------------|
|                 | 1991                      | 1992       | 1993       | 1994        | 1995        | 1996        | 1997        |
| Wind            | 12.4                      | 15.7       | 19.1       | 23.1        | 31.0        | 26.9        | 24.8        |
| <b>Solar PV</b> | <b>19.1</b>               | <b>4.5</b> | <b>3.8</b> | <b>15.5</b> | <b>13.3</b> | <b>12.7</b> | <b>43.0</b> |
| Geothermal      | 2.9                       | 4.6        | -6         | 4.6         | 10.2        | 5.5         | *           |
| Hydro power     | 2.2                       | 2.2        | 2.2        | 1.7         | 1.6         | 0.8         | *           |
| Natural gas     | 1.9                       | 0.7        | 3.1        | 0           | 2.7         | 4.7         | 0.5         |
| Coal            | -4.4                      | 1.4        | -2         | 6.4         | 4.1         | 2.3         | 1           |
| Nuclear Power   | -0.9                      | 0.6        | 2.8        | 0.6         | 0.6         | 0.9         | 0           |

\* data unavailable

## 1.2. The option for Solar Energy

Wind energy presents some problems for its direct implementation in human environments. The current giant turbines for wind energy production can be hardly integrated in our cities. Besides, metallic parts of rotating blades interfere in TV and FM signals. It is easy, but not necessarily cheap, to install repeater stations to provide another direction to these signals for receivers. Therefore, wind energy must be produced in centralised wind farms far away from the cities, in the countryside or on hills where wind usually blows strongly. However, the visual impact in these natural sceneries is debatable. Besides, turbines must be separated by at least five to ten tower heights to allow the wind strength to reform and the air turbulence created by one rotor not to harm another turbine. Consequently, only about 1% of land area is used.

On the contrary, PV systems are easily integrated in the human environment, either on the roofs or the façades of our buildings, and hence directly connected to the electricity network. Besides, though beauty is in the eye of the beholder, there are not esthetic problems in this case. However, the high production cost of thick high efficiency crystalline silicon solar cells has inhibited extensive application of solar energy[Shi et al., 1997]. As a result, for a long time solar cells were only used for remote applications such

as telecommunications and marine navigation systems, where low maintenance and high reliability are required. Hence, much solar cell research has concentrated on reducing costs, thus making solar cells commercially viable to generate the energy that we actually need every day for industry, transportation or space heating.

Nowadays, the market for PV is growing over 30% per year and the cost of panels is declining continuously[Fig. 1.2] due to both new technologies and mass production. There are confident predictions from leading PV manufacturers all over the World that the price of solar energy will be competitive with mains electricity within 10 years. As costs continue to fall over the coming decade, we are likely to see solar cells become more commonplace in everyday applications. Those who placed solar cells on their roofs would be able to provide electricity to their local utility during the day when the sun is shining and take it back at night when it is not. If the PV system was large and efficient enough, the customer would receive every month a cheque instead of a bill.

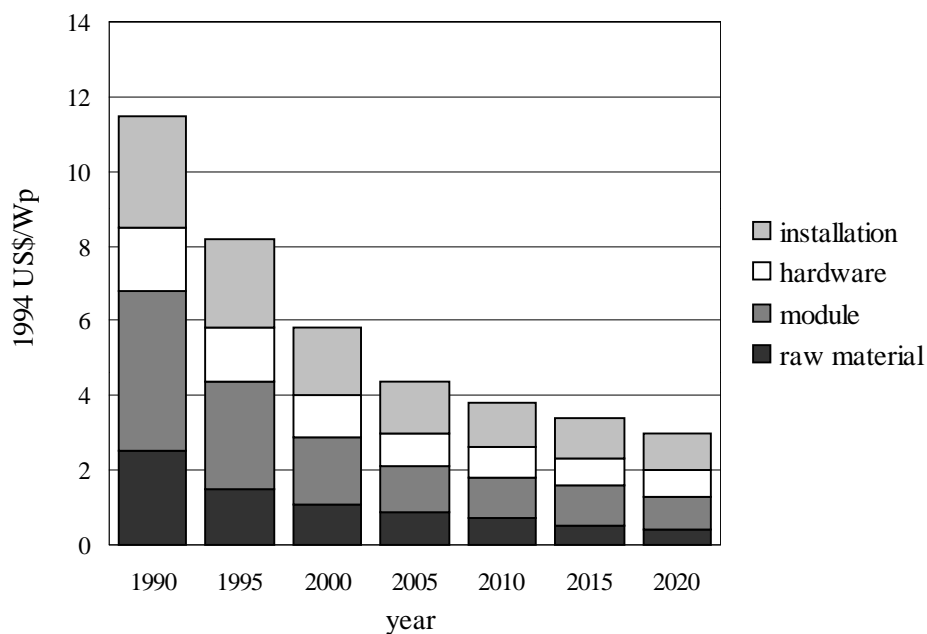


**Figure 1.2:** Prediction of averaged component costs in PV systems and price reduction over time[acre.murdoch.edu.au]. Thin film technologies must allow to reduce significantly the costs of module manufacturing.

Actually, building-integrated PV is now driving the development of the market throughout the World. Japan currently has a program that aims to build 70000 solar homes, installing 4600 MWp of PV by 2010. The Government of the USA also aims to install solar panels on one million roofs by 2010. In Europe several countries are supporting the construction of solar homes with the European parliament proposing a 1000 MWp

scheme[Palz, 2000]. In these projects solar cells are incorporated into roofing materials, cladding and windows. In this way, system costs are reduced by considering the price that standard building materials would suppose. The *Pompeu Fabra* public library in the city center of Mataro (53 kWp) or the PV roof in the City Hall of Barcelona (100 kWp) are our nearest examples. The PV industry has steadily grown during the last decade[Fig. 1.3] and now it is expected to grow even faster as demand has greatly increased. Unromantic studies predict a ten-fold increase in the PV market by 2010[Varadi, 1998].

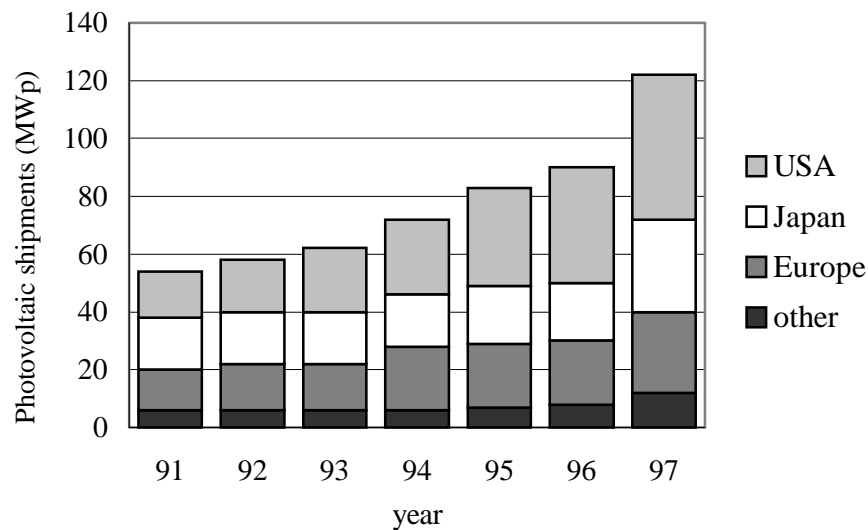


**Figure 1.3:** Worldwide PV shipments production[Curry, 1998]. The major manufacturers of solar panels are Solarex and USSC in the USA, Sanyo, Canon and Kyocera in Japan and BP Solar and Siemens Solar in Europe. There are many other smaller manufacturers.

### 1.3. Thin film technologies for reducing costs

Most commercially available solar cells are made from wafers of very pure monocrystalline or polycrystalline silicon. Such solar cells can attain efficiencies of up to 18% in commercial manufacture and over 20% in the laboratory. However, the silicon wafers used to make them are relatively expensive. Although silicon is highly abundant, comprising around one quarter of the Earth's crust, making a very pure wafer suitable for solar cell manufacture requires much energy and is therefore relatively costly. Moreover, a solar cell made using a 450  $\mu\text{m}$  thick wafer generates 90% of its energy from the top 15-20  $\mu\text{m}$  while the rest of the wafer is required simply to hold the device. Figure 1.4 shows the estimated percentage of costs for crystalline silicon solar modules based on wafer technology[Strese, 1988]. The production of clean silicon single crystal rods and wafers

represent the 38% of the total cost, which is certainly a very high percentage for the raw material only. Besides, in this study pure silicon was assumed to be available as waste from the semiconductor industry with a very low price[Strese, 1988]. When scaling up the production, this point could change drastically when such waste feedstock became insufficient.

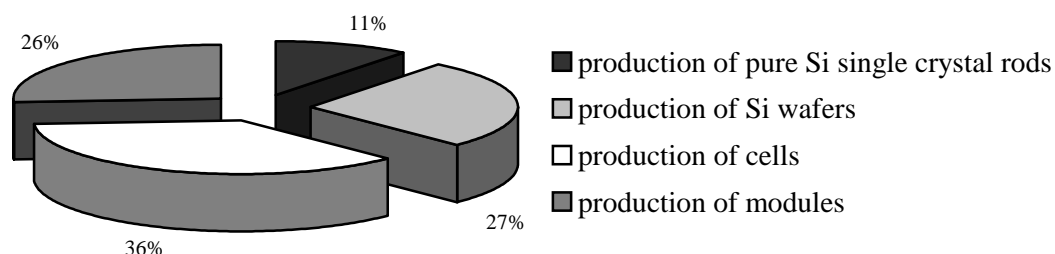


**Figure 1.4:** Percentage of costs for the production of crystalline-Si photovoltaic modules based on wafer technology (450  $\mu\text{m}$ ).

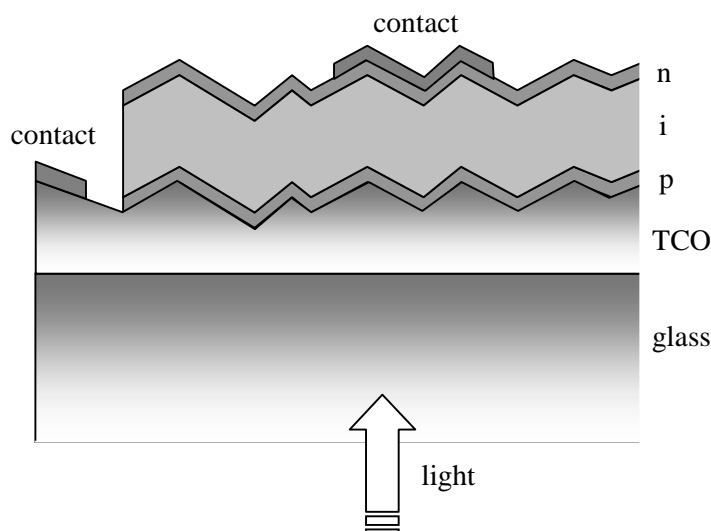


**Figure 1.5:** Typical thin film solar cell structure. Glass is used as a carrier for the front electrode and the active device, in this case a p-i-n structure. Contacts are usually thin metallic films thermally evaporated in high vacuum.

Undoubtedly, one possibility for significantly reducing costs is the development of thin film solar cell technologies. There are many advantages in thin film solar cells, such as the ability to be deposited over large areas on inexpensive substrates or building materials, the ease of mass production and the high suitability to large applications. In the long term, thin film silicon technology should indeed replace bulk crystalline silicon devices for most applications which demand inexpensive large area solar panels[Green, 1994]. These photovoltaic devices usually consists in semiconductor p-i-n structures deposited at

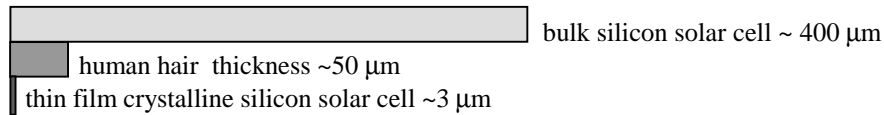


**Figure 1.6:** Relative thicknesses of conventional bulk silicon and thin film crystalline silicon solar cells compared to the thickness of a human hair.

relatively low substrate temperatures on inexpensive foreign substrates such as glass or plastic[Fig. 1.5], in contrast to traditional bulk crystalline silicon solar cells where the carrier is the own wafer. The front electrode is usually a transparent conductive oxide (TCO) which can be textured for light trapping. The most common ones are aluminium-doped zinc oxide (AZO), tin-doped indium oxide (ITO) and fluorine-doped tin oxide (FTO). Concerning the photovoltaic device itself, several thin film semiconductors can be used, such as cadmium telluride, copper indium selenide or gallium arsenide. Solar cells made from these compounds have yet to be fully commercialised but offer some promise of achieving low costs with reasonably good performance. However, the use of highly toxic elements or the availability of some of their components constitute clear limitations for their global application.

On the other hand, amorphous silicon solar cells have been commercially available for many years and are the most common devices employed in solar powered calculators and watches. In this case, there are not virtually feedstock limitations and the amount of silicon required to produce the same energy than with the traditional wafer technology is reduced in more than a factor 100[Goetz et al., 1994]. However, efficiencies of amorphous silicon solar cells are significantly lower than those of bulk silicon cells, less than 8% for the best commercial modules. In addition, amorphous silicon technology has still unsolved problems as the so called Staebler-Wronski effect[Staebler et al., 1977] causing further efficiency losses during operation. Even more unsatisfactory are the rather low deposition rates ( $<1\text{\AA}/\text{s}$ ) in current production plants, which produce amorphous silicon by the conventional glow discharge process at 13.56 MHz. Manufacturers would certainly welcome higher deposition rates with open arms in order to increase their throughputs.

## 1.4. Thin film crystalline silicon solar cells

The thin film crystalline silicon option has long been discarded due to the relatively poor optical absorption of crystalline silicon compared to amorphous silicon films. Despite this drawback, it is now well recognised that this is no longer an issue provided that light trapping is incorporated in cell designs. In this case, even more important than the saving of silicon[Fig. 1.7], is that materials of lower quality can be used, as the ratio of the collection length to the thickness becomes the factor which determines the collection of photogenerated carriers[Shah et al., 1995]. Therefore, polycrystalline (grain size  $>1 \mu\text{m}$ ), microcrystalline ( $\sim 1 \mu\text{m}$ ) and nanocrystalline ( $\sim 10 \text{ nm}$ ) silicon arise as very promising candidates for the foreseeable future. These kinds of small-grain silicon films can be grown at moderate temperatures allowing the use of low cost foreign substrates such as glass[Bergmann, 1999] or, in a more challenging approach, transparent polymer foils[Pernet et al., 1998]. Hence, thin film crystalline solar cells emerge as an exciting new field of research with potentially higher improvement perspectives than other traditional technologies. It is undoubtedly attractive the idea of combining the low temperature deposition techniques known from the amorphous silicon technology with the expected long term stability of crystalline silicon. Actually, there is a great interest in stack both amorphous and crystalline thin film solar cells in a tandem device. This combination leads to a true silicon-based tandem, with two distinct band gaps but without alloys involved, which has been called the micromorph concept. It has already allowed stabilised efficiencies higher than 10% [Meier et al., 1997; Saito et al., 1998], though in view of mass production there is a problem of low deposition rate for the crystalline cell that has still to be solved.

The classification attending to the grain size could be ambiguous and the terms polycrystalline and microcrystalline are often found in the literature referring actually to nanocrystalline films. As in the case of amorphous silicon, a considerable amount of hydrogen incorporates to these small-grain crystalline silicon materials obtained at low substrate temperatures. This hydrogen, in a few per cent atomic concentration [Peiró et al., 2000], has the beneficial effect of passivating grain-boundaries thus reducing the density of dangling bonds. Hence, the terms hydrogenated microcrystalline silicon ( $\mu\text{c-Si:H}$ ) and

hydrogenated nanocrystalline silicon (nc-Si:H) are used by analogy to the well established hydrogenated amorphous silicon (a-Si:H) nomenclature. The term polycrystalline silicon (p-Si) usually refers to materials which do not incorporate hydrogen due to the relatively high temperature processes required to obtain them. Throughout this work we will try to use the proper denomination in each case.

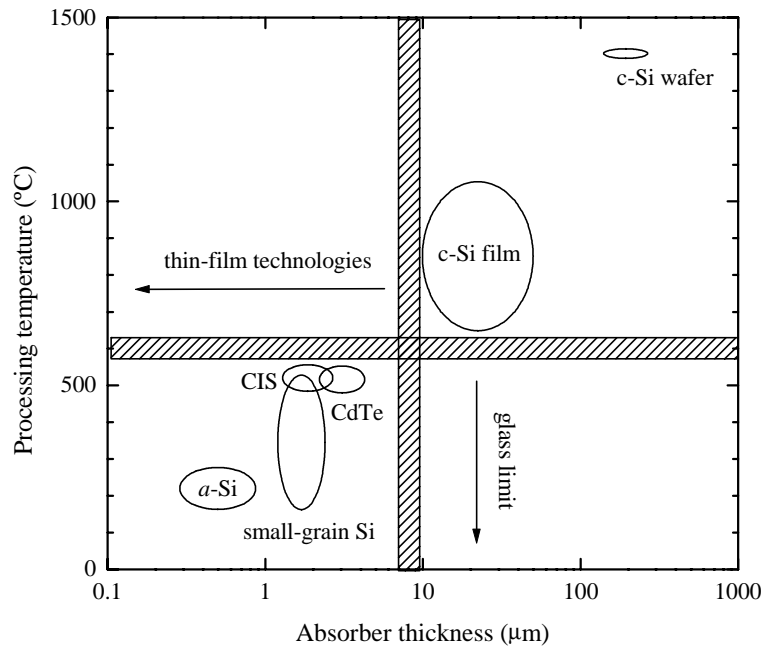


**Figure 1.7:** Processing temperatures and thicknesses of absorber materials for several photovoltaic technologies[Beneking et al., 1999].

Though thin film silicon solar cell approaches for high-temperature substrates already allow conversion efficiencies in the range of 15%[Bai et al., 1997], they do not fulfil the low-cost production requirements. If any of the deposition techniques compatible with foreign substrates succeeded, manufacturers would undoubtedly bet for it. And this success seems not to be so far. Recently, small-grain silicon has been successfully incorporated as the active layer of p-i-n structures by different deposition techniques.

Sanyo Corporation used solid-phase crystallisation to fabricate  $\mu\text{-Si:H}$  films for thin film solar cells. An undoped amorphous silicon film, on top of a highly phosphorous-doped a-Si:H layer deposited on a metal substrate, is crystallised at a temperature around 550-600°C for more than 10 hours. The cell with a heteroemitter consisting of p-doped a-Si:H achieves a conversion efficiency of 9.2%[Matsuyama et al., 1996]. This approach is not actively investigated any more by Sanyo due to the unaffordable long crystallisation times involved in the process.

A further successful approach was achieved at Kaneka Corporation by Plasma-Enhanced Chemical Vapour Deposition (PECVD) at substrate temperatures of 600°C[Yamamoto et al., 1998]. This group has reported a  $\mu\text{c-Si:H}$  device with a conversion efficiency of 10.1%. This so-called STAR structure fulfils efficient light trapping in a 2  $\mu\text{m}$  thick active layer by using a textured multilayer back side reflector. The active area of the n-i-p structure is 1.2  $\text{cm}^2$ . The deposition rate was in the range of 6-10  $\text{\AA/s}$ . Though the description of the process is very rudimentary, it could involve a previous laser crystallisation step of a highly doped contact layer which would increase the costs for potential industrial applications.

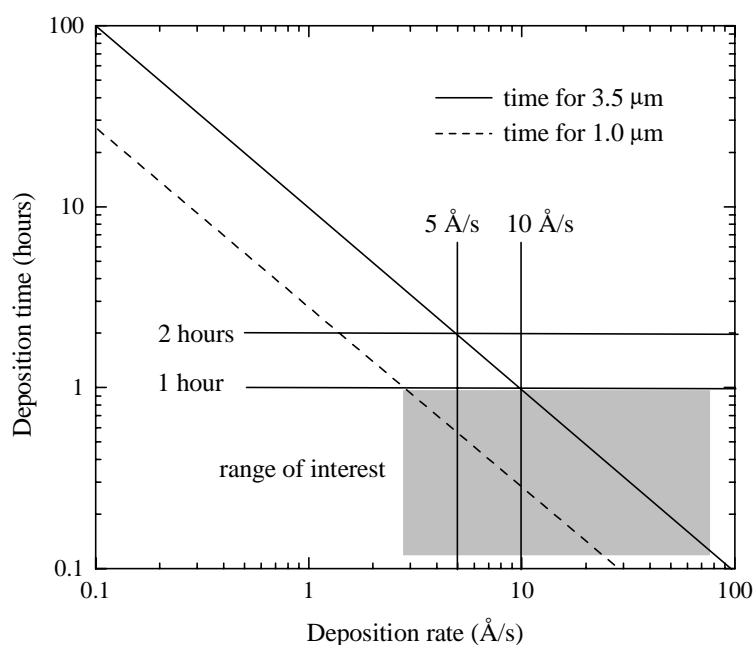


**Figure 1.8:** Deposition time as a function of the deposition rate. The filled region represents the field of interest for photovoltaic applications[Keppner et al., 1999].

At the Institut de Microtechnique at the University of Neuchâtel, the Very High-Frequency Plasma-Enhanced Chemical Vapour Deposition (VHF-PECVD) serves to deposit nc-Si:H on glass at substrate temperatures as low as 200°C. An increase in the plasma excitation frequency from the standard 13.56 MHz up to 130 MHz results in a higher flow of low energy atomic hydrogen ions promoting the crystalline growth[Kroll et al., 1997]. A solar cell with p-i-n structure based on this material achieved a maximum efficiency of 8.5% over an area of 0.33  $\text{cm}^2$  [Meier et al., 1998]. This device was entirely

grown by VHF-PECVD on FTO(Asahi-U™) without any previous solid-phase or laser-crystallisation step. Neither sophisticated light-trapping strategies were used apart from a relatively simple back reflector consisting of an AZO/Ag bilayer. The main problem with this device was the indeed low deposition rate only around 2 Å/s[Fig. 1.8]. Hence, almost 5 hours were required to grow the 3.5 µm thick undoped nc-Si:H active layer. Nevertheless, the enhancement of the deposition rate up to 10 Å/s (<1 hour) still resulted in a 5.2 % efficiency solar cell[Torres, 1998]. Though these results are extremely encouraging, set-ups and components designed to operate at these very high frequencies are at very early commercialisation stage. This would suppose a drawback for an easy industrialisation of the VHF-PECVD technique. Similar results were recently obtained by this technique at the Research Center Jülich in Germany which has reported a 7.5% p-i-n nc-Si:H solar cell with an active area of 0.7 cm<sup>2</sup>[Vetterl et al., 1999].

The different approach that we have chosen at University of Barcelona is the Hot-Wire Chemical Vapour Deposition (HWCVD) technique. To date, HWCVD has allowed the highest deposition rates of thin film nanocrystalline silicon layers ever reported. Several tens of Å/s can be easily achieved maintaining reasonably good microstructural properties[Cifre et al., 1994]. Furthermore, a HWCVD set-up is easier to handle and the implementation and upkeep costs are much lower than in a PECVD one. Very hopeful results have been obtained by this technique at the Debye Institute of University of Utrecht which has reported a 4.4% efficiency nc-Si:H solar cell on stainless steel obtained at a substrate temperature lower than 500 °C[Schropp et al., 1999]. The area of the device was 0.16 cm<sup>2</sup> and its thickness only 1.2 µm. Both doped layers of the n-i-p structure were obtained by PECVD in separate chambers whereas the active layer of the device was grown by HWCVD in less than 40 minutes. Considering that this device is grown on plain stainless steel and that the n-layer is rather thick to avoid metal diffusion into the active layer, it does not benefit much from back reflection. Hence, it would compare favourably with other a priori more efficient devices.

In the framework of the project which has allowed this work (JOR3-CT97-0126), our research focused on obtaining thin film crystalline silicon solar cells suitable for low cost applications. Therefore, high temperature processes must be avoided to allow the use of inexpensive substrates as glass. Besides, high deposition rates should be achieved in order to increase the productivity. These requirements discard the use of polycrystalline silicon

with a large grain size which either requires expensive substrates compatible with high temperature processes or is very time consuming in crystallisation techniques. Our choice was HWCVD on account of its suitability to obtain nc-Si:H inexpensively over large areas at low substrate temperatures with indeed high deposition rates.

## 1.5. The brief history of Hot-Wire CVD

In 1979, Wiesmann reported that a-Si:H thin films could be formed by cracking molecules of silane gas with a carbon or tungsten foil heated to 1400-1600°C[Wiesmann et al., 1979]. One year later, he patented this method as thermal CVD[Wiesmann, 1980]. However, his attempt was not successful because the electronic quality of their films was much worse than the obtained by PECVD at that time. Contrary to Wiesmann's results, Matsumura at the Japan Advance Institute of Science at Technology (JAIST) succeeded some years later in obtaining high quality a-Si:H by decomposing a silane-hydrogen gas mixture with a tungsten wire[Matsumura, 1986]. He called the method Catalytic CVD (Cat-CVD) and has always sustained the catalytic character of the reactions that take place on the surface of the hot wire[Matsumura, 1988]. In 1988, Doyle at University of Colorado also obtained high quality a-Si:H films by the same method which he called Evaporative Surface Decomposition (ESD). Mahan and coworkers at the National Renewable Energy Laboratory (NREL) continued Doyle's work. They extensively studied the properties of a-Si:H obtained by this technique and contributed to increase the research in this field. They first called the method Hot-Wire Chemical Vapour Deposition[Mahan et al., 1991] which seems to be the denomination most commonly found in the literature. Hence, this is the name that we have used in this work. Matsumura, who had continued developing this technique in parallel, demonstrated in 1991 the possibility of obtaining nc-Si:H films by this method at substrate temperatures only around 300°C[Matsumura, 1991]. Other groups achieved later similar results[Dusane et al., 1993] until our group at University of Barcelona reported the first nc-Si:H films obtained by this method in Europe[Cifre et al., 1994] with deposition rates over 30 Å/s. Besides, our group showed that doped nc-Si:H films could be easily obtained by adding controlled amounts of doping gases to the base silane-hydrogen gas mixture[Puigdollers et al., 1995]. By that time, a-Si:H by HWCVD had already been incorporated in thin film solar cells with promising results[Papadopoulos et al., 1993; Nelson et al., 1994]. By contrast, nc-Si:H obtained by this technique was not incorporated as the active layer of thin film solar cells until recently[Rath et al., 1996].

Research on HWCVD has gone on and a-Si:H solar cells with initial efficiencies of 9.8% have been obtained by this technique at deposition rates of  $16 \text{ \AA/s}$ [Mahan et al., 1998], more than one order of magnitude higher than by the conventional PECVD. To our knowledge, the best nc-Si:H cell ever obtained by HWCVD is the previously depicted 4.4% efficiency n-i-p structure obtained by the group at the Debye Institute[Schropp et al., 1999]. Very recently, the group at LPICM in the Ecole Polytechnique of Paris has reported a 3.6% efficiency n-i-p structure on FTO (Asahi-U<sup>TM</sup>) coated glass[Niikura et al., 2000]. However, the thickness and deposition rate of the active layer is not indicated. Similarly to the group at the Debye Institute, they only grew the active layer by HWCVD while both doped layers were obtained by PECVD. Furthermore, both groups profiled the active layer by varying the deposition conditions (hydrogen dilution) during its growth. These results seem to indicate that the doped/active layer interface plays an important role in the device performance and amorphous incubation layers there should be avoided. Apart from PV applications, a-Si:H[Meiling et al., 1997] and nc-Si:H[Rath et al., 1998; Puigdollers et al., 2000] by HWCVD have also been successfully incorporated as the active channel of thin film transistors (TFT).

As far as our laboratory is concerned, the development of the HWCVD technique started in July 1993 with a very elementary set-up. It was only a monochamber made of glass which shared the pumping system and gas lines of an existing PECVD installation. The vacuum specifications and the performance of the pumping system were honestly quite poor. In spite of that, it allowed us to gain invaluable knowledge about the method. Moreover, preliminary p-i-n structures which obviously showed very low efficiencies (<1%) could be obtained in this set-up[Peiró et al., 1997]. It was not until January 1998 that the currently operative new ultra-high vacuum multichamber set-up was available. This system, extensively described in a previous work[Peiró, 1999], was built at University of Barcelona during the first two years of research within the CRYSTAL project (JOR3-CT97-0126) in the JOULE programme of the European Commission. The first device was obtained in May 1998 after a lot of work to optimise not only the deposition conditions but also the HWCVD set-up itself. To date, our best solar cell showed a 2.5% conversion efficiency. It was a p-i-n structure entirely obtained by HWCVD on AZO-coated glass at an indeed low substrate temperature of  $150^\circ\text{C}$ . The undoped active layer  $2.4 \mu\text{m}$  thick was obtained at a high deposition rate of  $15 \text{ \AA/s}$ , thus the process time was less than 30 minutes. Neither textured TCO nor back reflector were used and the p-layer was certainly

too thick ( $\sim 500 \text{ \AA}$ ). Hence, just optical losses severely limited the maximum expected efficiency. Moreover, an n-i-p inverted structure illuminated from the top side would undoubtedly benefit from the enhanced quality of the material with respect to the initial stages of growth. This is the case for the 4.4% efficiency device obtained at the Debye Institute [Schropp et al., 1999]. However, we could not test this structure because the required low temperature top TCO has still to be optimised. We must say that even now we are at an early stage of our research and we honestly think that our results are very encouraging.



## Chapter 2

# The HWCVD set-up. Electrical and optical characterisations

This chapter briefly describes the HWCVD set-up at University of Barcelona and the experimental characterisation techniques used to study the optical and electrical properties of our layers. An extensive description of the deposition set-up and the structural characterisation of the samples are part of a previous work[Peiró, 1999]. The specific characterisations carried out to the obtained devices will also be indicated in this chapter.

### 2.1. The HWCVD set-up

A new HWCVD set-up[Fig. 2.1] was built at University of Barcelona during the first two years of research within the CRYSTAL project (JOR3-CT97-0126) in the JOULE programme of the European Commission. This set-up consists of three different ultra-high vacuum (UHV) chambers isolated between them by gate valves. Only two of the deposition chambers are intended for HWCVD processes whereas the other one is a load-lock. A magnetic transfer system is used to locate the substrate in the desired chamber.

Separate chambers are used to grow the doped and intrinsic nc-Si:H layers of devices in order to avoid undesired cross contamination in the active layer[Voz et al., 2000]. Processes involving doping gases are performed in the HWCVD chamber-2 whereas chamber-1 is preserved to obtain the undoped active layers of p-i-n solar cells. Figure 2.2 compares the boron profile by Secondary Ion Mass Spectroscopy (SIMS) in the intrinsic layer of a monochamber p-i-n solar cell to the case of a p-i-n structure whose active layer was grown in a different chamber. Such contaminated active layer turned out to be unsuitable for photovoltaic devices due to the screening of the internal electric field within the active layer. Hence, the multichamber requirement results justified.



**Figure 2.1:** Picture of the multichamber HWCVD set-up at University of Barcelona. The three inline UHV chambers were fabricated at the Vacuum Unit of the Scientific-Technical Service of University of Barcelona.

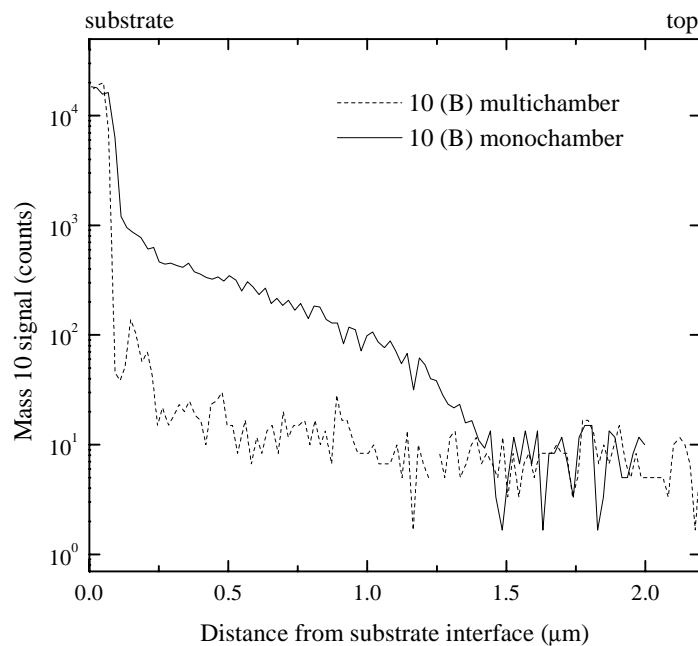


**Figure 2.2:** Boron profile by SIMS in the active layer of a p-i-n structure obtained in a sole chamber compared to the case of a p-i-n solar cell where the intrinsic layer was grown in a different chamber.

A commercial radio frequency (RF) magnetron sputtering unit was installed in the load-lock in order to deposit there the transparent front electrode required for thin film solar cells on glass. For that purpose, a ceramic target of  $\text{ZnO}:\text{Al}_2\text{O}_3$  (98:2 wt%, 99.99% purity

and 2'' diameter) was mounted in the sputtering unit to grow aluminium-doped zinc oxide layers. Therefore, a whole TCO/p-i-n structure can be grown on glass without exposing any interface to the atmosphere.

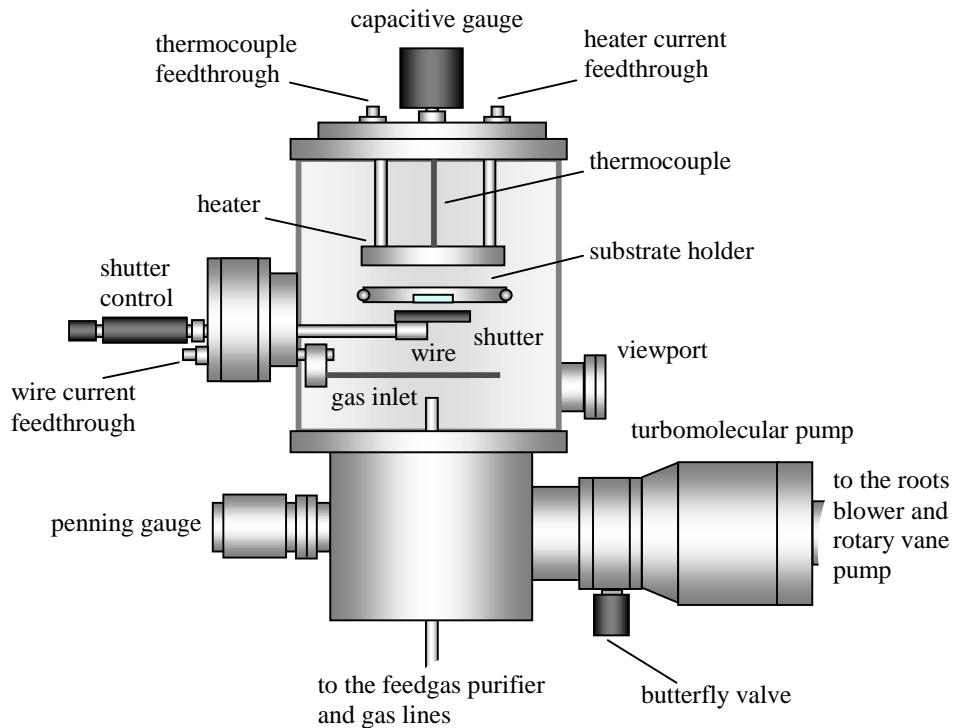


**Figure 2.3:** Schematic of one of the HWCVD chambers showing the inner arrangement of its accessories.

Figure 2.3 shows the inner arrangement of the accessories in each one of the HWCVD deposition chambers. The wire, heated to above 1600°C by the Joule effect, catalytically decomposes the gas mixture during the process resulting in atoms, radicals and electrons acting as deposition precursors. The commercial resistive heater of 10 cm diameter allows to obtain a good temperature uniformity over the whole substrate. The technological values of substrate temperature referenced in this work are those measured with the thermocouple touching the heater. A previous calibration with an additional thermocouple attached to the glass substrate showed that the actual substrate temperature is around 50°C higher. Therefore, the technological substrate temperature is only an estimation of the actual substrate temperature. Nevertheless, it is enough when comparing technological series where it was only changed the set-point in the PID electronics which controls the heater.

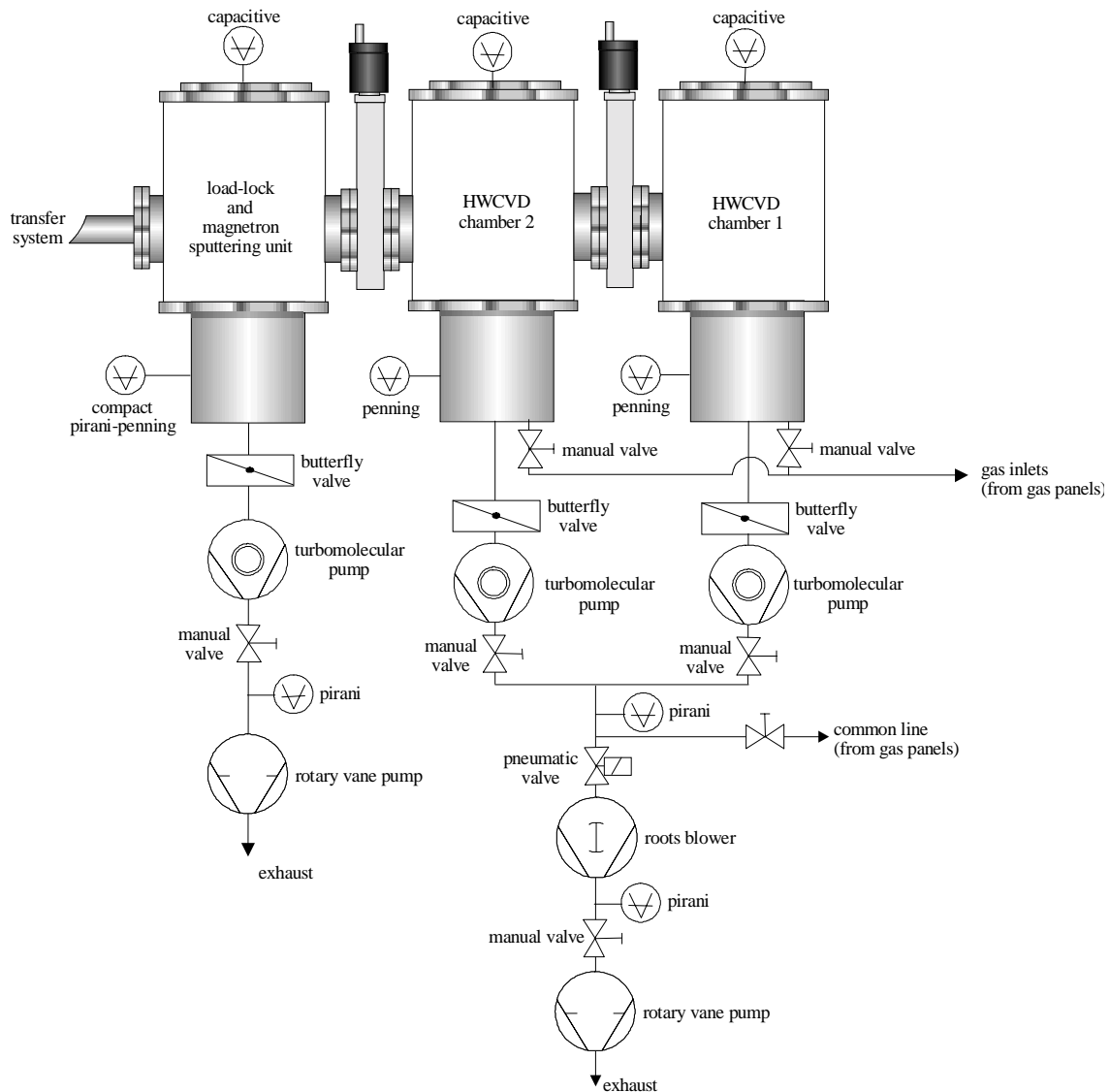


**Figure 2.4:** Detailed schematics of the multichamber HWCVD set-up and the pumping system [Peiró, 1999].

A detailed schematic of the pumping system is shown in figure 2.4. For the load-lock it consists of a turbomolecular pump and a conventional rotary vane pump. In the case of the HWCVD chambers, a roots blower was installed between the turbomolecular pumps (360 l/s) and the rotary vane pump (144 l/s) to allow a wider range of deposition conditions avoiding the eventual backstreaming of contaminants in the pumping lines. Figure 2.5 shows the panels with the required five gas lines. The base gas mixture of silane and hydrogen is fixed with mass flow controllers (MFC). Much lower flows of diborane

(diluted at 1% into hydrogen) and phosphine (diluted at 5% into silane) are added to obtain doped layers. Ultrapure gas bottles are used with the following specifications: 4.7 (99.997%) for silane and 6.0 (99.9999%) for hydrogen. Nitrogen is the purging gas. Note the zeolite feedgas purifier (SAES Getters MonoTorr®) to reduce contaminants (oxygen, carbon...) in the feedgas lines under ppb levels.

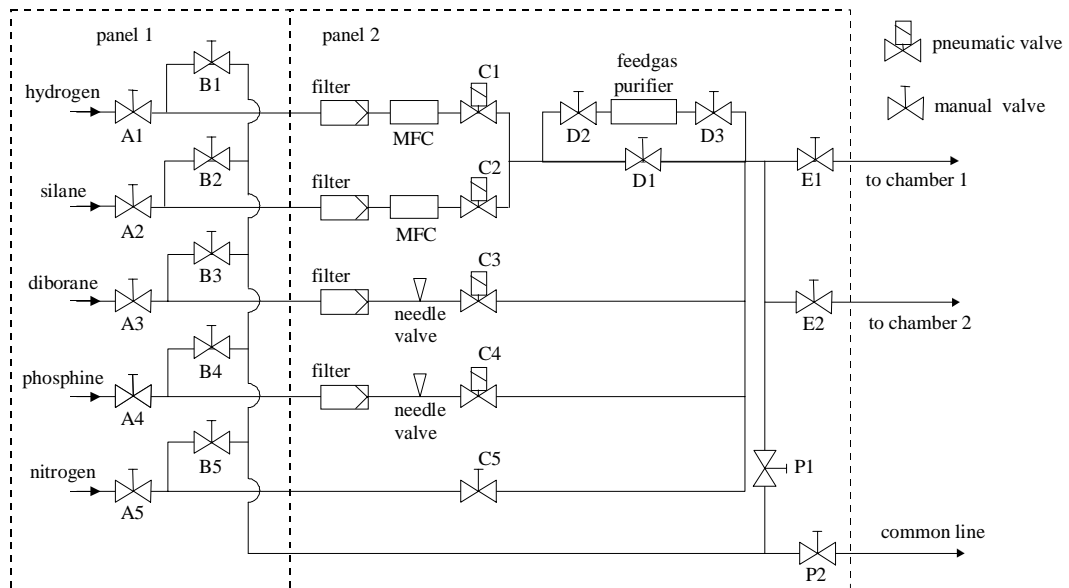


**Figure 2.5:** Diagram of the gas panels [Peiró, 1999]. Microflows of diborane and phosphine are added to the base silane-hydrogen gas mixture in the feedgas to p- and n-type dope respectively. Nitrogen is the purging gas.

## 2.2. Characterisation of samples

In the following sections we describe the different electrical and optical characterisations performed to the obtained nc-Si:H samples. Here we just briefly describe the experimental set-ups while specific details on the interpretation of these measurements are included in the next chapter.

### 2.2.1. Dark conductivity

The dark conductivity as a function of the temperature was measured for each nc-Si:H sample with the set-up shown in figure 2.6. The studied sample, with coplanar evaporated aluminium contacts, is located into an hermetic stainless steel chamber on a copper block. A primary vacuum is achieved by means of a rotary vane pump to eliminate moisture on the surface of the sample. Temperature is measured with a thermocouple and regulated by a PID electronics which controls the power supplied to power resistances inside the copper

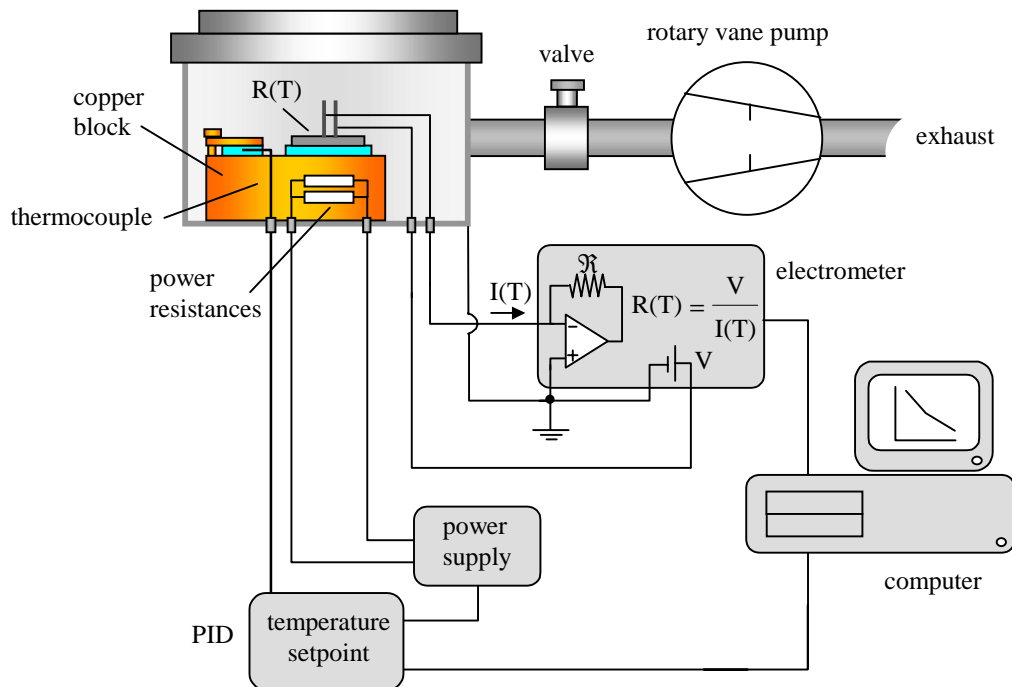
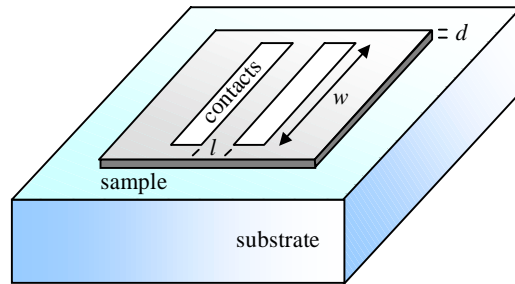


**Figure 2.6:** Experimental set-up used to perform the high-impedance dark conductivity measurements in vacuum.

block. Though it could seem an straight measurement, special care must be taken in the electrical connections to avoid parasitic leakages. Since the coplanar resistance of the thin film sample could be similar or even higher than the output resistance of the electrometer current source, the ohmmeter configuration is not suitable for this measurement. Hence, the electrometer is configured as a nanoamperimeter and a relatively high voltage ( $\sim 100$  V) is applied with its internal source. Once the PID stabilises the set-point temperature, the resistance  $R(T)$  is obtained as the ratio of the fix applied voltage  $V$  to the thermal dependent current  $I(T)$  flowing across the sample. Then, the dark conductivity  $\sigma(T)$  of the sample is calculated considering its thickness and the geometry of the evaporated coplanar aluminium contacts[Fig. 2.7].



$$R(T) = \rho(T) \frac{l}{wd}$$

$$\sigma(T) = \frac{1}{\rho(T)} = \frac{l}{wd R(T)}$$

**Figure 2.7:** Geometry of the coplanar electrodes on the samples. They are obtained by thermal evaporation of aluminium in high vacuum. The distance  $l$  between them is 1mm while their width  $w$  is 10mm. Since  $l \sim 10^3 d$  for typical film thicknesses, we neglect edge effects in the current lines to calculate the conductivity.

As expected for a semiconductor, a thermal activated behaviour[Eq. 2.1] is experimentally observed within a wide temperature range[Fig. 2.8]

$$\sigma = \sigma_o \exp\left(-\frac{E_a}{k_B T}\right) \quad (2.1)$$

where  $k_B$  is the Boltzmann's constant and we have introduced the thermal activation energy  $E_a$  and prefactor  $\sigma_o$  of the dark conductivity. The activation energy is related to the distance between the Fermi-level and the band which mainly contributes to the electronic transport, i.e., the conduction band for n-type or the valence band for p-type layers. In fully intrinsic samples it should be around a half of the band gap.

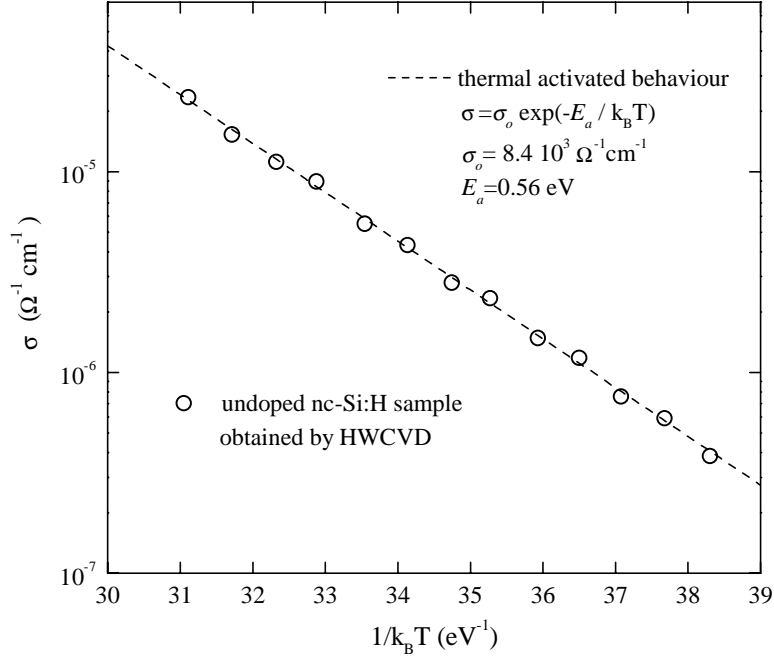


**Figure 2.8:** Thermal dependence of the dark conductivity for an undoped nc-Si:H sample obtained by HWCVD. Its high activation energy indicates the intrinsic character of the sample.

### 2.2.2. Steady State Photoconductivity

The photoconductivity of a sample is the relative change in its electrical conductivity when it is under illumination [Eq. 2.2]. It appears because the densities of free carriers in the bands increase compared with their values at thermal equilibrium

$$\sigma_{ph} = e(\mu_n \Delta n + \mu_p \Delta p) \quad (2.2)$$

The steady state excess of carrier densities relates to the generation rate by

$$G = \frac{\Delta n}{\tau_n} = \frac{\Delta p}{\tau_p} \quad (2.3)$$

where  $G$  is the generation rate and  $\tau_n$  and  $\tau_p$  the lifetimes of electrons and holes respectively.

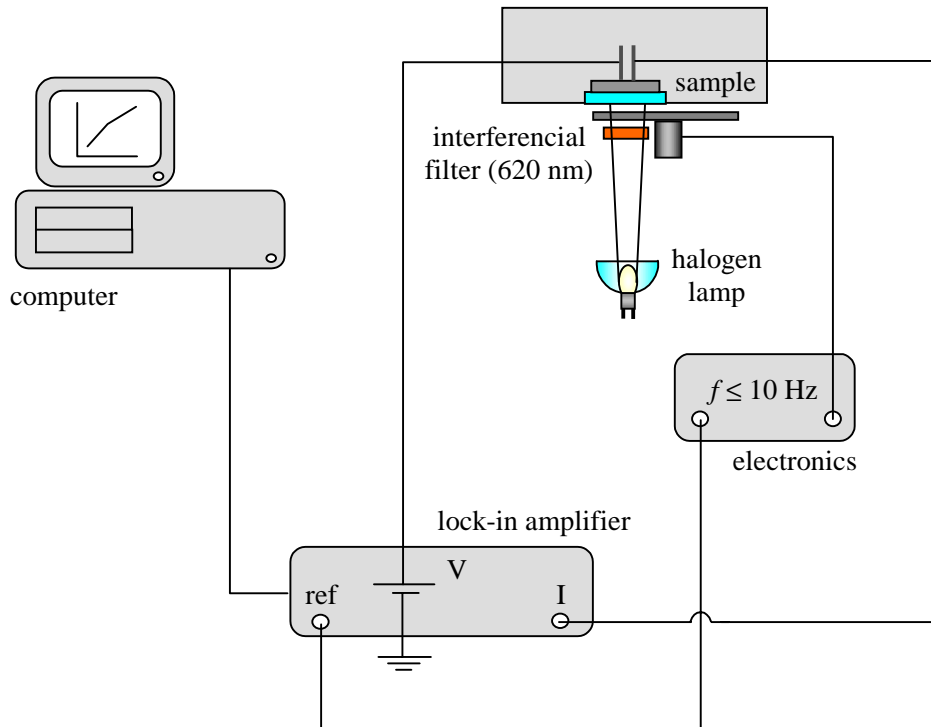


**Figure 2.9:** Experimental set-up for the steady state photoconductivity measurement. The monochromatic incident photon flux  $\Phi$  is determined with a calibrated photodetector. The absorption of these photons with energies higher than the band gap mainly result in the generation of electron-hole pairs.

Therefore, by introducing equation 2.3 in 2.2 we define the steady state photoconductivity  $\mu\tau$ -product as

$$\mu\tau_{ph} = \frac{\sigma_{ph}}{eG} = \mu_n\tau_n + \mu_p\tau_p \quad (2.4)$$

Though the  $\mu\tau$ -products of both carriers seem to contribute to  $\mu\tau_{ph}$ , it is actually determined by the majority carrier with a much longer lifetime[Rose, 1963]. Figure 2.9 shows the experimental set-up in our laboratory where steady state photoconductivity (SSPC) measurements were done. The current measured by the lock-in amplifier divided by the applied voltage is directly the increment in the conductance of the sample. The main problem to interpret the results is that the generation profile is not uniform. As a first approximation, we will consider that  $\mu\tau_{ph}$  does not strongly depend on the generation rate.

Then, if the sample is divided into infinitesimal slides  $dz$  and for the same geometry shown in figure 2.7, we obtain

$$\begin{aligned} \frac{I}{V} &= \int_0^d \sigma_{ph}(z) \frac{w}{l} dz = \int_0^d e\mu\tau_{ph} G(z) \frac{w}{l} dz = \\ &= \int_0^d e\mu\tau_{ph} \Phi \alpha \exp(-\alpha z) \frac{w}{l} dz = e\mu\tau_{ph} \Phi [1 - \exp(-\alpha d)] \frac{w}{l} \end{aligned} \quad (2.5)$$

where  $\alpha$  is the optical absorption coefficient at the given wavelength. If we define the mean generation rate according to

$$\langle G \rangle = \frac{\Phi [1 - \exp(-\alpha d)]}{d} \quad (2.6)$$

and the mean photoconductivity as

$$\frac{I}{V} = \langle \sigma_{ph} \rangle \frac{wd}{l} \quad (2.7)$$

from equations 2.5-2.7 we arrive at

$$\langle \sigma_{ph} \rangle = e\mu\tau_{ph} \langle G \rangle \quad (2.8)$$

In practice, it is observed a power-law behaviour  $\langle \sigma_{ph} \rangle \sim \langle G \rangle^\gamma$  in most nc-Si:H samples with  $\gamma < 1$  [Goerlitzer et al., 1996] because  $\mu\tau_{ph}$  actually depends on the generation rate [Fig. 2.10]. Thus, reported SSPC  $\mu\tau$ -products of different samples can not be compared as long as the experimental conditions for the measurement are not indicated. Furthermore, active layers with higher values of  $\mu\tau_{ph}$  do not necessary imply an enhanced photovoltaic performance but an undesired Fermi-level shift due to the incorporation contaminants [Section 3.2.5]. Nevertheless, it is a useful and easy technique to compare samples measured under similar generation profiles.

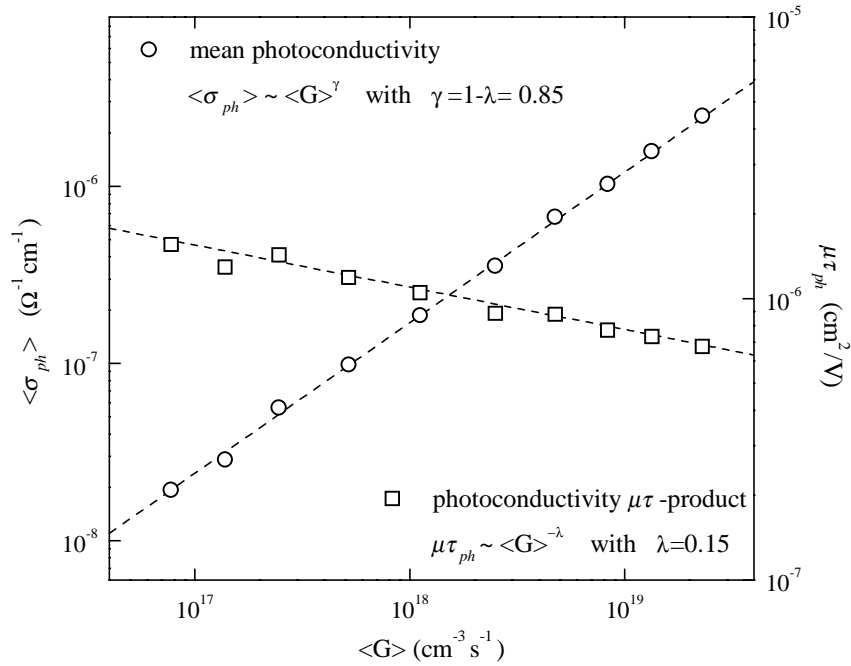


**Figure 2.10:** Mean steady state photoconductivity and SSPC  $\mu\tau$ -product as a function of the mean generation rate for a typical undoped nc-Si:H sample obtained by HWCVD. A sublinear behaviour  $\langle \sigma_{ph} \rangle \sim \langle G \rangle^\gamma$  with  $\gamma = 0.85$  is observed because  $\mu\tau_{ph}$  significantly depends on the generation rate.

### 2.2.3. Photothermal Deflection Spectrometry

The Photothermal Deflection Spectrometry (PDS) technique allows confident measurements of very low optical absorptions in the range of  $\alpha d < 10^{-5}$ . For comparison, conventional absorption measurements with combined transmittance-reflectance spectra present a detection limit only around  $10^{-2}$ . By PDS, the energy fraction absorbed within the sample is directly measured instead of analysing very slight variations (comparable to the experimental error) in high transmittance-reflectance data. Figure 2.11 shows an schematic of the PDS set-up in our laboratory. The sample under study, on a non absorbing substrate, is sinked into Fluorinert FC72™ by 3M Company. This transparent liquid presents an strong thermal dependence in its refractive index. The fraction of incident power optically absorbed within the sample is converted into heat by non radiative recombination. Then,

by thermal contact, a temperature gradient appears in the surrounding FC72™ enhanced by the low thermal conductivity and specific heat of this liquid[Table 2.1]. The thermal dependence of the refractive index of FC72™ leads to a gradient in the refractive index which causes the deflection of the probe beam by the mirage effect[Fig. 2.12].

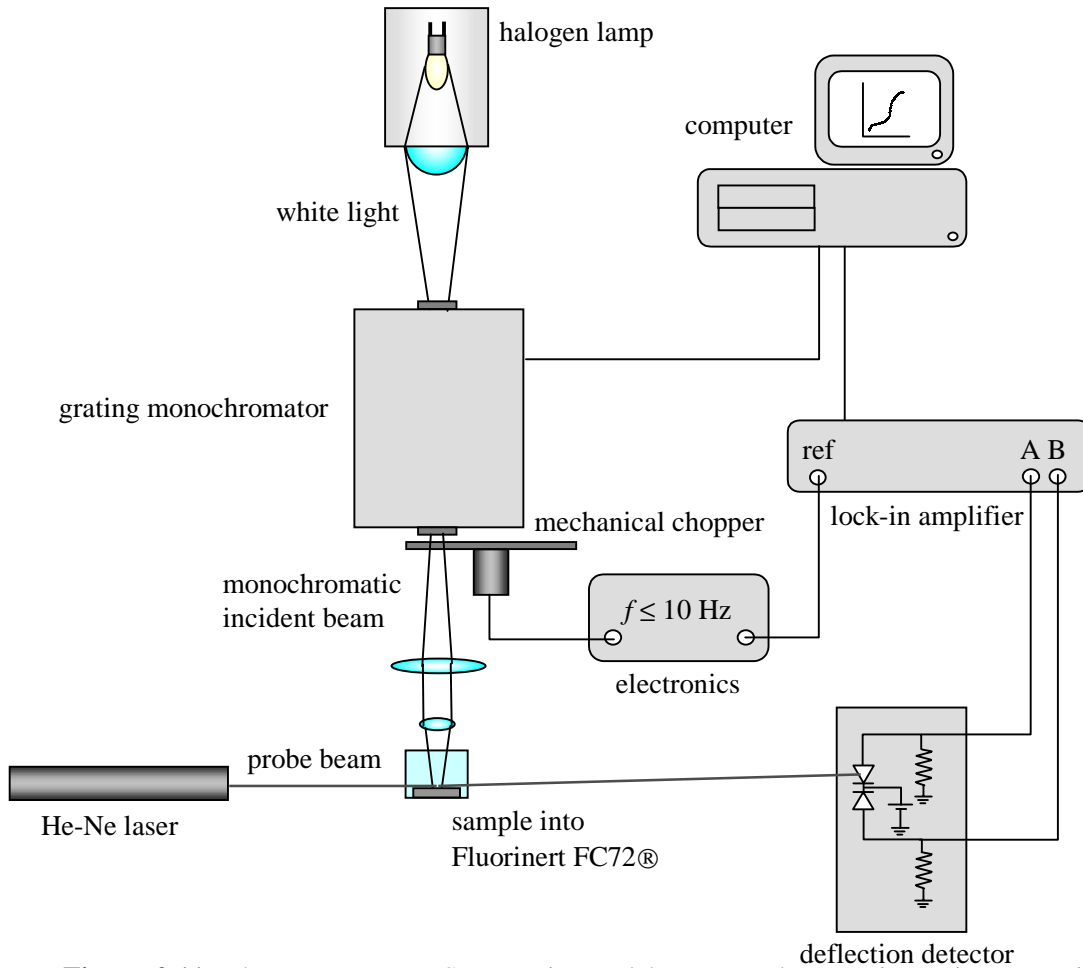


**Figure 2.11:** The transverse PDS set-up in our laboratory. The experiment is automatized with a personal computer. The deflection detector consists of two adjacent reverse biased photodetectors.

**Table 2.1:** Thermal and optical properties of different materials at 25°C.  $k$  is the thermal conductivity,  $\rho$  the density and  $C$  the specific heat.  $L$  is the thermal diffusion length calculated at the typical modulation frequency of 10 Hz. Though carbon tetrachloride ( $\text{CCl}_4$ ) even presents better specific properties than Fluorinert FC72™ for the PDS experiment, we discarded the use because of its health hazards by inhalation.

|                | $k$ (W/cmK)          | $\rho$ (g/cm <sup>3</sup> ) | $C$ (J/gK) | $L$ ( $\mu\text{m}$ ) | $1/n \partial n/\partial T$ |
|----------------|----------------------|-----------------------------|------------|-----------------------|-----------------------------|
| air            | $2.5 \cdot 10^{-4}$  | $1.29 \cdot 10^{-3}$        | 1          | 785                   | -                           |
| water          | $5.92 \cdot 10^{-3}$ | 1                           | 4.18       | 67                    | $0.78 \cdot 10^{-4}$        |
| $\text{CCl}_4$ | $1.05 \cdot 10^{-3}$ | 1.59                        | 0.87       | 49                    | $3.9 \cdot 10^{-4}$         |
| FC72™          | $5.7 \cdot 10^{-4}$  | 1.68                        | 1.03       | 32                    | $3.12 \cdot 10^{-4}$        |
| Corning        | 0.1                  | 2.76                        | 0.7        | 405                   | -                           |
| c-Si           | 0.84                 | 2.33                        | 0.69       | 1286                  | -                           |

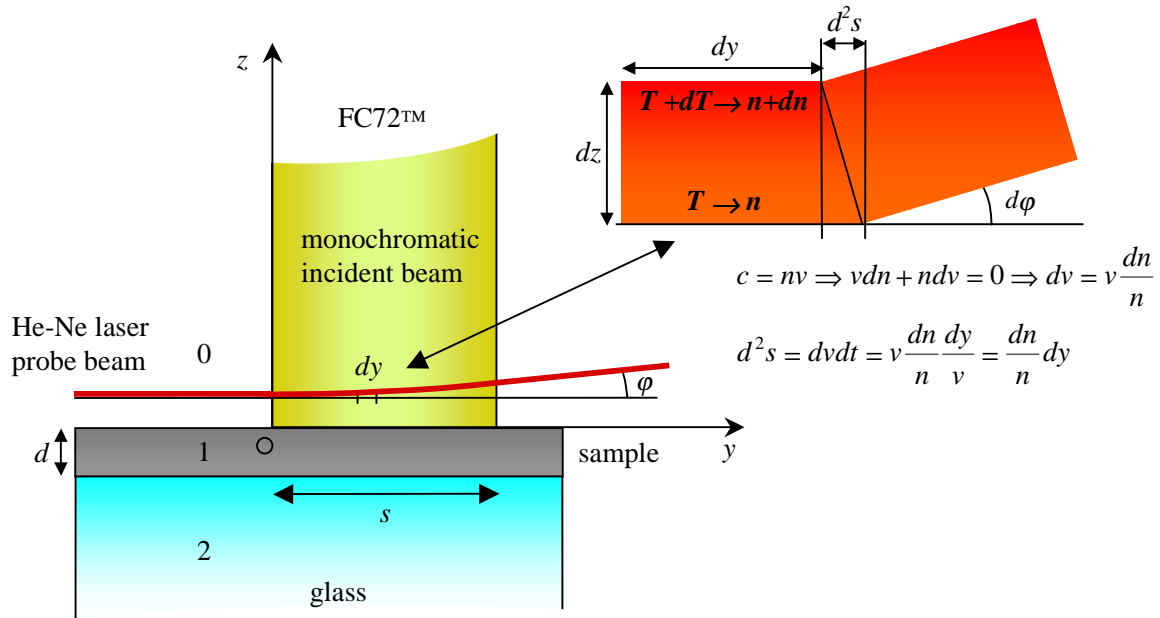


**Figure 2.12:** Deflection of the probe beam by the mirage effect. The thickness of the He-Ne laser probe beam is considered infinitesimal ( $dz$ ).

According to figure 2.12 the infinitesimal deflection  $d\phi$  in the length element  $dy$  is given by

$$d\phi = \frac{d^2s}{dz} = \frac{1}{n} \frac{dn}{dz} dy = \frac{1}{n} \frac{\partial n}{\partial T} \frac{\partial T}{\partial z} dy \quad (2.9)$$

Hence, in the whole length  $s$  the angle of deflection  $\varphi$  will be

$$\varphi = \int_s \frac{1}{n} \frac{\partial n}{\partial T} \frac{\partial T}{\partial z} dy \approx \frac{1}{n} \frac{\partial n}{\partial T} \frac{\partial T}{\partial z} s \quad (2.10)$$

where in the integral the refractive index and thermal gradients are considered constants on account of the very slight deviation. By solving the heat transport equations in a typical system FC72<sup>TM</sup>/silicon/glass we obtain that the thermal gradient  $\partial T/\partial z$  is given by

$$\frac{\partial T}{\partial z} = - \frac{1}{k_2 \frac{L_o}{L_2} + k_o} A I \exp\left(-\frac{z}{L_o} (1+i)\right) \exp(i\omega t) \quad (2.11)$$

with  $\omega=2\pi f$  and  $f$  the modulation frequency,  $I$  the incident power density (irradiance),  $A$  the optical absorptance,  $k$  the thermal conductivity and  $L$  the thermal diffusion length in the corresponding medium given by

$$L = \sqrt{2 \frac{k}{\omega \rho C}} \quad (2.12)$$

where  $\rho$  is the density and  $C$  the specific heat. Therefore, if  $\xi$  is the sensitivity of the deflection detector, the complex amplitude of the signal which arrives to the lock-in amplifier will be

$$\hat{V} = -\xi s \frac{1}{n} \frac{\partial n}{\partial T} \frac{1}{k_2 \frac{L_o}{L_2} + k_o} A I \exp\left(-\frac{z}{L_o} (1+i)\right) = |\hat{V}| \exp(i\varphi) \quad (2.13)$$

whose modulus results directly proportional to the irradiance fraction absorbed within the sample

$$|\hat{V}| = \xi s \frac{1}{n} \frac{\partial n}{\partial T} \frac{1}{k_2 \frac{L_o}{L_2} + k_o} \exp\left(-\frac{z}{L_o}\right) A I = K A I \quad (2.14)$$

The constant  $K$  depends on the properties of the substrate and the FC72™, the modulation frequency, the deflection detector and the geometry. By comparing the modulus of the PDS signal of the sample and that of a thick graphite layer which virtually absorbs all the irradiance over all the spectrum, the absolute absorptance spectrum of the studied sample can be obtained. Then, the coefficient  $\alpha$  can be calculated from the absorptance spectrum by modelling the optical absorption of the thin film. This procedure will be extensively described in the next chapter[Section 3.1.1].

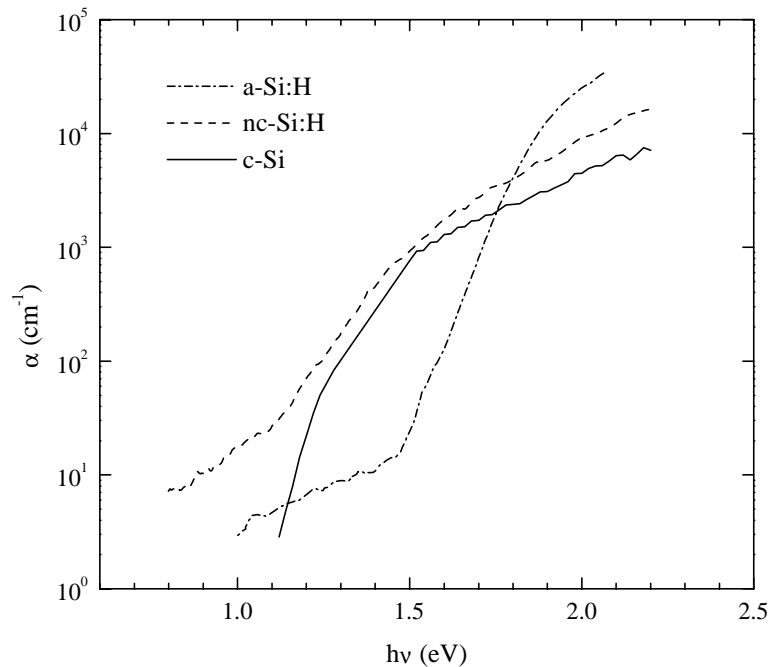


**Figure 2.13:** Optical absorption coefficient of typical hydrogenated amorphous and nanocrystalline silicon thin films measured with the PDS system in our laboratory. They are compared to the tabulated optical absorption of crystalline silicon[Möller, 1993].

## 2.3. Characterisation of devices

### 2.3.1. Current density - voltage characteristics

The prime measurement to characterise a solar cell is the dependence of its current density on the voltage applied, the so-called JV curve. As it is well-known, the current density is defined as the ratio of the total current to the active area of the device. Figure 2.14 shows the set-up for measuring the JV curves of our solar cells. Since a photovoltaic device can behave either as a power source or as a dissipative element depending on the applied voltage, a four quadrant voltage source must be used to scan the whole JV curve under illumination.

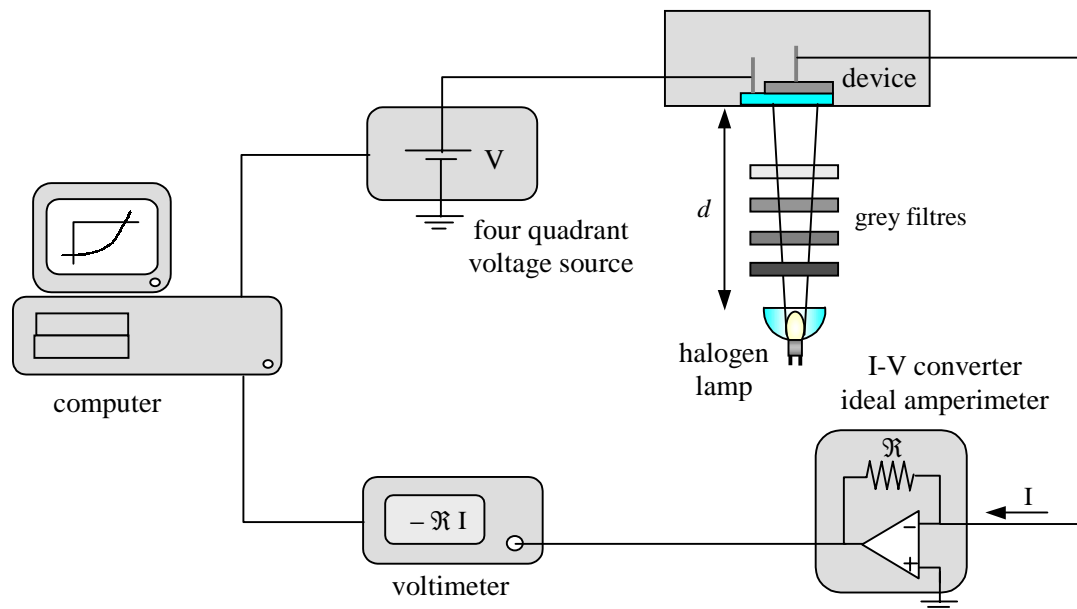


**Figure 2.14:** Experimental set-up for measuring the JV curve of solar cells in the dark or under varied irradiances. Note the four quadrant voltage source and current-voltage converter to ensure enough sensitivity without the loading effects with high shunt resistances.

Irradiances ranging over several orders of magnitude can be obtained with neutral grey filters and by varying the distance between the lamp and the device. In order to have enough current sensitivity even with very low irradiances, a current-voltage (I-V) converter

acting as an ideal amperimeter was used. In this way, loading effects related to shunt resistances are avoided.

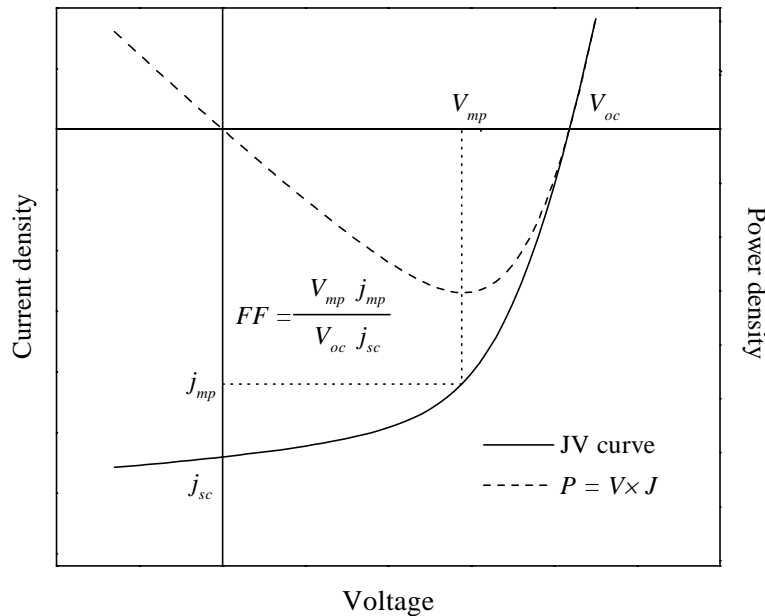


**Figure 2.15:** Typical JV curve under illumination of a p-i-n solar cell. It generates electrical power in the 4<sup>th</sup> quadrant (power dissipated  $P = V \times J < 0$ ). The fill factor  $FF$  corresponds to the ratio of the area delimited by  $j_{mp}$  and  $V_{mp}$  in the maximum power point with respect to the area determined by  $j_{sc}$  and  $V_{oc}$ .

A typical JV curve under illumination is shown in figure 2.15 with its most important features:

- the short circuit current density  $j_{sc}$  generated by the solar cell when it is connected to a low impedance such that the voltage across the device is zero
- the open circuit voltage  $V_{oc}$  which builds up across the cell as long as its terminals are kept on a high impedance forcing the current to be zero
- the fill factor  $FF$  which is the ratio of the maximum power generated by the solar cell when it is connected to a suitable charge to the product  $V_{oc} j_{sc}$ . This parameter is related to the curvature of the JV curve

The ratio of the electrical power density at the maximum power point to the incident power density due to illumination is the conversion efficiency of the solar cell  $\eta$

$$\eta = \frac{P_{max}}{P_{light}} = \frac{V_{mp} j_{mp}}{P_{light}} = \frac{FF V_{oc} j_{sc}}{P_{light}} \quad (2.15)$$

From equation 2.15 it is obvious that in order to get the highest conversion efficiency from a solar cell the three basic parameters of its JV curve have all to be maximised.

### 2.3.2. Spectral response and quantum efficiencies

The spectral response of a solar cell  $SR(V, \lambda)$  is given by the ratio of the photogenerated current  $j_{ph}(V, \lambda)$  to the incident power  $P(\lambda)$  spectral densities (magnitudes per unit area and unit wavelength)[Eq. 2.16]. It indicates, for an external voltage applied  $V$ , how much current in amperes is collected from the device per incident watt of light with wavelength  $\lambda$

$$SR(V, \lambda) = \frac{j_{ph}(V, \lambda)}{P(\lambda)} \quad (2.16)$$

With a more physical meaning it is often used the external quantum efficiency  $QE_{ext}(V, \lambda)$ , which is the fraction of incident photons of a given wavelength  $\phi_o(\lambda)$  which results in an electron-hole pair collected at the contacts of the cell. The external quantum efficiency is influenced not only by the collection efficiency but also by the optical optimisation of the device. The spectral response is related to the external quantum efficiency by equation 2.17, where if  $SR$  is in  $A/W$  and  $\lambda$  in  $nm$  we obtain  $QE_{ext}$  in  $e/ph$

$$QE_{ext}(V, \lambda) = \frac{j_{ph}(V, \lambda)}{e\phi_o(\lambda)} = SR(V, \lambda) \frac{1241}{\lambda} \quad (2.17)$$

Figure 2.16 shows the experimental set-up used for the measurements. For accurate absolute spectral measurements it was necessary to determine the spectral power density  $P(\lambda)$  incident to the solar cell under test. This was done by placing in the sample holder a

calibrated reference detector provided by the Physikalisch-Technische Bundesanstalt Braunschweig (PTB), the German bureau of standards. Lateral collection through the heavily doped layers may readily become important in p-i-n nc-Si:H solar cells, specially for small area devices. We avoided this problem by using a mask which limited an illuminated area smaller than the cell contact.

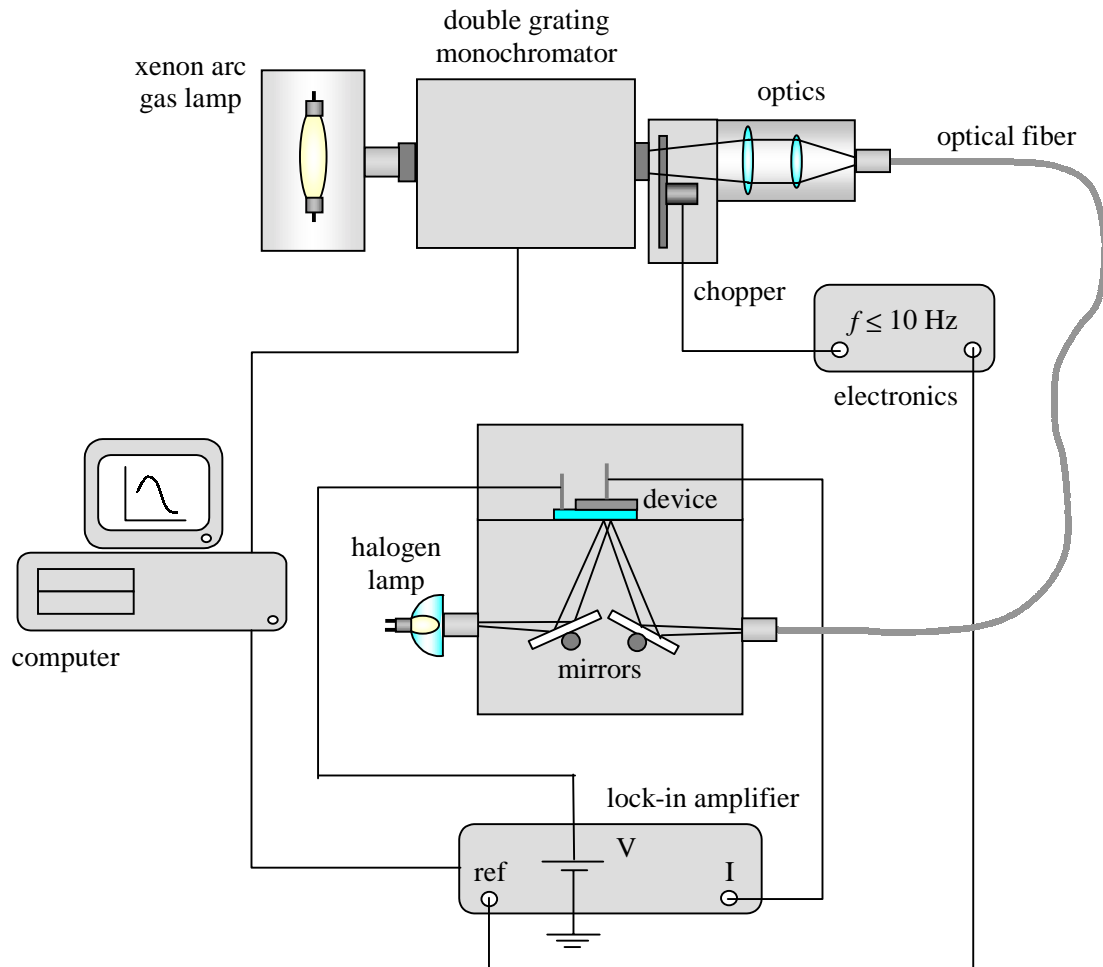


**Figure 2.16:** The spectral response measurement set-up. Bias light from the halogen lamp can be superimposed to the monochromatic probe beam arriving through the optic fiber. The experiment is automatized with a personal computer.

In figure 2.17 we compare the external quantum efficiency of a 2.1  $\mu\text{m}$  thick p-i-n nc-Si:H solar cell obtained by HWCVD [Table 2.2] with the optical absorbance of the device. The reduced optical absorption in the long wavelength range evidences the optical limitations in such thin film devices without light trapping strategies. We have also

estimated the optical absorption only in the active layer  $A_i(\lambda)$  by considering a p-layer thickness around 500 Å. It is observed a significant useless optical absorption in the p-doped layer which does not certainly result in photovoltaic conversion. The external quantum efficiency is still lower than optical absorption in the active layer because of recombination losses, i.e., not all the absorbed photons within the active layer lead to an electron-hole pair collected at the contacts of the device.

**Table 2.2:** Deposition conditions, thicknesses of the different layers and photovoltaic performance for the 990323c HWCVD solar cell in figure 2.17. The short circuit current density value has been verified by convolution of the external quantum efficiency with the irradiance spectrum.

| Cell name                | Filament temperature (°C)        | Substrate temperature (°C)     | SiH <sub>4</sub> /H <sub>2</sub> flows (sccm) | Process pressure (mbar) | Thicknesses p/i/n (μm) | $r_d$ (Å/s) |
|--------------------------|----------------------------------|--------------------------------|---|-------------------------|------------------------|-------------|
| 990323c                  | 1640                             | 125                            | 4 / 76  | $3.5 \cdot 10^{-2}$     | 0.05/2/0.05            | 2.5         |
| Photovoltaic performance | Irradiance (mW/cm <sup>2</sup> ) | $j_{sc}$ (mA/cm <sup>2</sup> ) |   | $V_{oc}$ (V)            | $FF$ (%)               |             |
|                          | 100                              | 9.5                            |   | 0.25                    | 36                     |             |

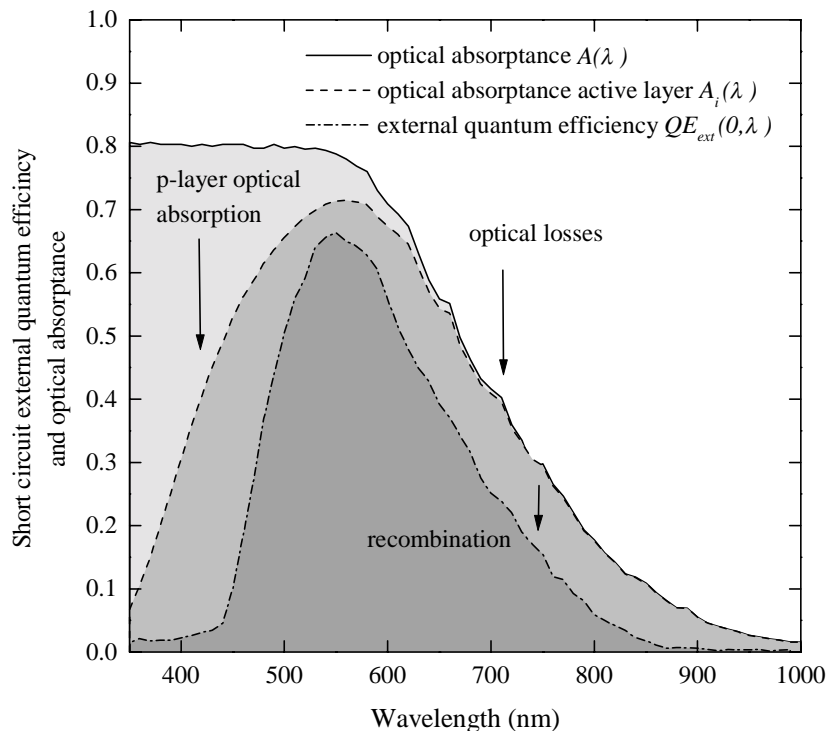


**Figure 2.17:** Optical absorbance in the whole device and only in the active layer compared to the short circuit external quantum efficiency of a 2.1 μm thick p-i-n nc-Si:H solar cell obtained by HWCVD[Table 2.2].

By normalising the external quantum efficiency with the optical absorptance in the active layer of the device

$$QE_{\text{int}}(V, \lambda) = \frac{QE_{\text{ext}}(V, \lambda)}{A_i(\lambda)} \quad (2.18)$$

we obtain the internal quantum efficiency [Figure 2.18]. Since optical losses do not influence in the internal quantum efficiency, it can be identified with the true collection efficiency of the device. The poor internal quantum efficiency for shorter wavelengths could be due to an important interface recombination due to back diffusion of minority carriers photogenerated near the p-i interface [Asensi, 1994]. Thus, although photons of high energy are quickly absorbed within the first tenths of micron in the active layer, they do not certainly result in photovoltaic conversion. On the other hand, the reduction in the long wavelength range is due to bulk recombination in the active layer of the device. Poor transport properties or a weak internal electric field (short drift length) are responsible for this reduced collection efficiency.

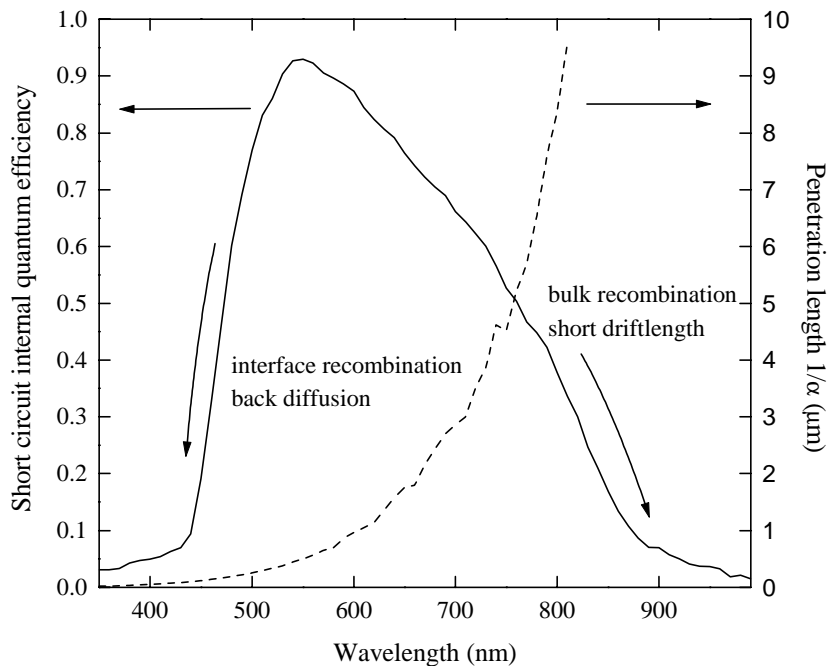


**Figure 2.18:** Short circuit internal quantum efficiency (collection efficiency) of the same solar cell in figure 2.17. It is also plotted the penetration length as a function of the wavelength.

### 2.3.3. Depletion capacitance of rectifying contacts

The space charge density in the intrinsic layer of a p-i-n structure screens the internal electric field of the device thus degrading the drift-assisted collection. Considering the simplest case of an uniform density of charged centres  $N_C$ , the Poisson's equation allows to calculate the screening length  $L_{screen}$  of the electric field at the interface  $E_o$  arriving at

$$L_{screen} = \frac{\epsilon_s}{eN_C} E_o \quad (2.19)$$

where  $e$  is the elementary charge and  $\epsilon_s$  the dielectric permittivity of silicon. Then, a reduction in the density of charged centres would lead to a proportionally longer screening length and an enhanced drift-assisted collection.

The reverse voltage dependence of the depletion capacitance of Schottky contacts has been traditionally used to study impurity profiles in crystalline silicon [Rhoderick, 1978]. We have extended the method to rectifying contacts [Fig. 2.19] with undoped nc-Si:H obtained by HWCVD in order to estimate effective values of  $N_C$  for these samples. For that purpose, a commercial impedance analyser HP4192A operating at low frequencies (<1 KHz) was used. A small AC probe voltage of 20 mV is superimposed to a variable DC voltage. Thereby the voltage dependence of the depletion capacitance of the studied pseudo-Schottky contacts is obtained.

Within the one-sided abrupt junction approximation, the space charge density within the depletion region is given by

$$\rho = eN_C \quad (2.20)$$

In the case of a uniform profile of charged centres ( $N_C \approx \text{constant}$ ), the width of the depletion region can be easily calculated by solving the Poisson's equation

$$w = \sqrt{\frac{2\epsilon_s}{eN_C} (V_d - V_{ext})} \quad (2.21)$$

with  $V_d$  the Schottky barrier and  $V_{ext}$  the external voltage applied.

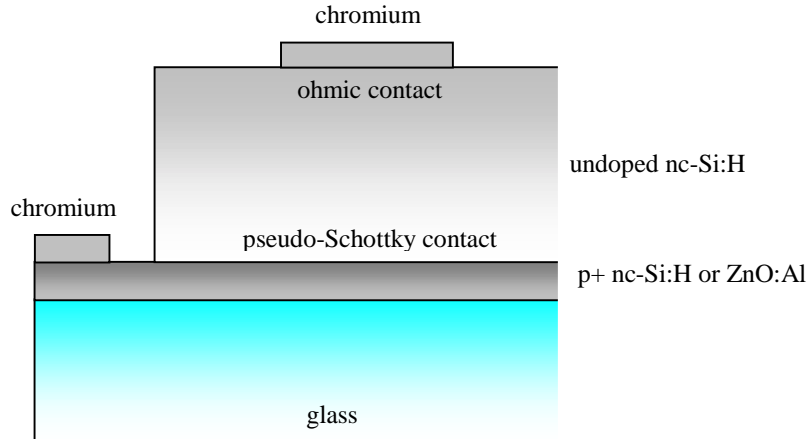


**Figure 2.19:** Structures used for the standard depletion capacitance-reverse voltage measurement. Either heavily p-doped nc-Si:H or ZnO:Al allow to obtain rectifying contacts with undoped-nc-Si:H. The evaporated chromium back contact turned out to be quasi ohmic as evidenced in Cr/undoped nc-Si:H/Cr sandwich structures which did not show any rectifying behaviour.

Hence, the total space charge within the depletion region can be calculated

$$Q = eN_c wS \quad (2.22)$$

where  $S$  is the area of the Schottky contact. Hence, the depletion capacitance is given by

$$C = \left| \frac{dQ}{dV} \right| = eN_c S \left| \frac{dw}{dV_{ext}} \right| = S \sqrt{\frac{eN_c \epsilon_s}{2} \frac{1}{V_d - V_{ext}}} \quad (2.23)$$

which leads to the well-known equation

$$\frac{1}{C^2} = \frac{2/S^2}{eN_c \epsilon_s} (V_d - V_{ext}) \quad (2.24)$$

which allows to obtain the values of  $N_c$  and  $V_d$  from a linear fit in the  $1/C^2$ - $V_{ext}$  plot. In practice, this experiment is limited to reverse bias conditions. For forward biases a large current can flow across the junction corresponding to a large number of carriers present within the depletion region. Hence, in that case the assumption that the space charge density in the depletion region is mainly due to localised states could not be true.

On the other hand, by combining equations 2.22-2.24 we arrive at

$$C = \epsilon_s \frac{S}{w} \quad (2.25)$$

as in a parallel-plate capacitor. This last equation is also valid for an arbitrary impurity profile[Sze, 1985] thereby providing a method to test whether the conditions for the simplified model hold. Once  $N_C$  and  $V_d$  are known, the width of the depletion region without any external voltage applied  $w_o$  can be easily calculated from equation 2.21 with  $V_{ext}=0$ . This value should agree with that obtained from equation 2.25, i.e.,  $w_o = \epsilon_s S / C_o$  with  $C_o$  the depletion capacitance for  $V_{ext}=0$ , where neither the values of  $N_C$  nor  $V_d$  are used[Fig. 2.20].

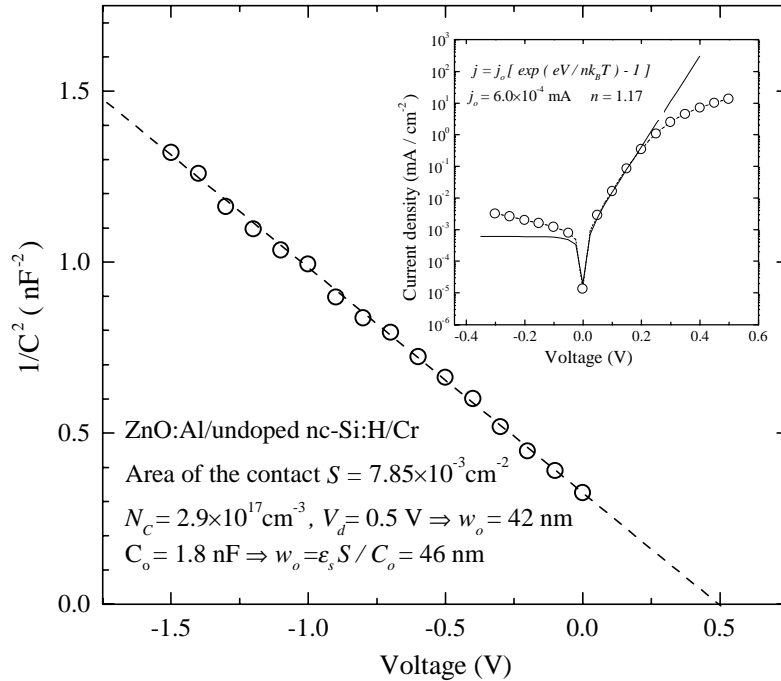


**Figure 2.20:** Voltage dependence of the depletion capacitance of a ZnO:Al/undoped nc-Si:H pseudo Schottky contact. The nice linear behaviour, together with the slight differences (<10%) between the depletion region widths obtained either from equation 2.21 or 2.25, indicate that the assumptions of the simplified model are fulfilled. The inset current density-voltage characteristic shows a satisfactory rectifying behaviour.

Figure 2.21 compares simulation results to the analytical model within the one-sided abrupt junction approximation. The relatively rough abrupt-junction approximation satisfactorily reproduces the internal electric field and voltage profiles within the depletion

region ( $x \leq w$ ). For the simulation we considered a density of donors  $N_D = 2 \times 10^{17} \text{ cm}^{-3}$  at the energy level  $E_D$  much higher than the density of deep levels (dangling bonds) which was  $N_{db} = 10^{16} \text{ cm}^{-3}$  at  $E_{db}$ . Hence, the effective density of charged centres  $N_C$  could be approximated by  $N_D$ . This could be the case for either doped or undoped but unintentionally contaminated nc-Si:H samples. Actually, a pronounced n-type character is often observed in as grown undoped nc-Si:H samples [Lucovsky et al., 1993]. For samples grown under optimised deposition conditions with a low incorporation of contaminants,  $N_D$  could be comparable to  $N_{db}$  which in addition is expected to change its state of charge within the depletion region [Fig. 2.21]. In spite of that, the density of charged centres deduced from the  $I/C^2 - V_{ext}$  plot is still representative for an average space charge density which correlates with the conversion efficiency of solar cells incorporating these active layers [Voz et al., 2000c].

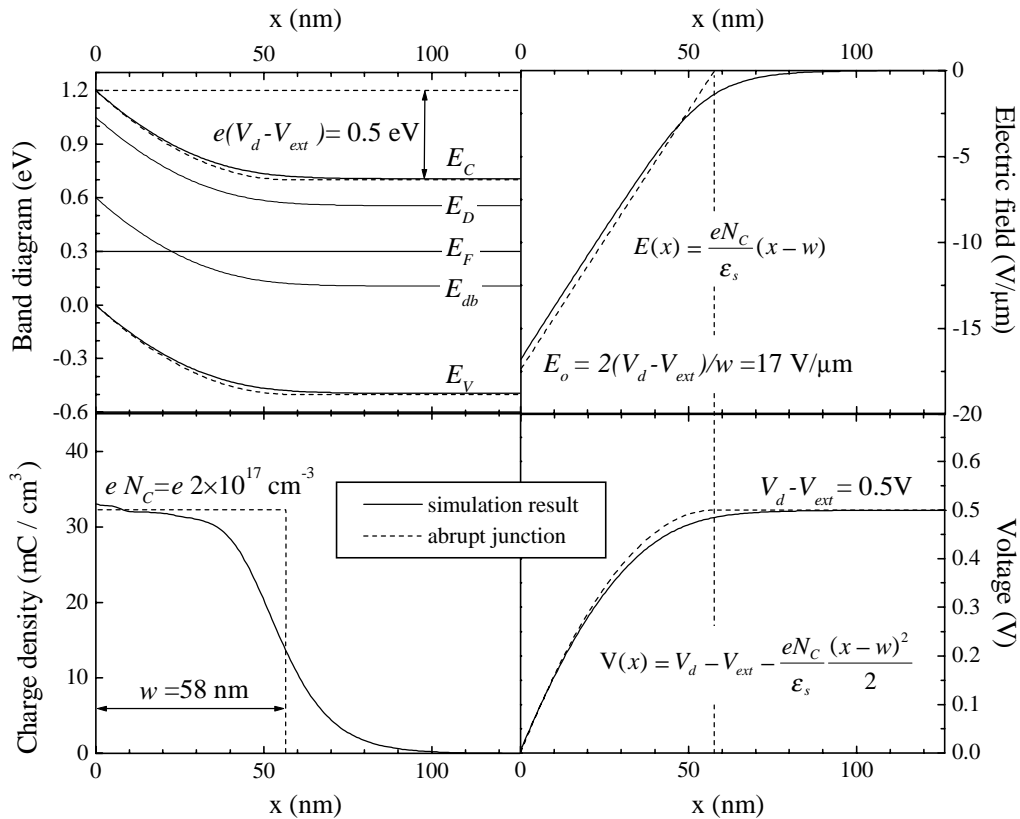


**Figure 2.21:** Simulation results compared to the analytical model within the one-sided abrupt junction approximation for an uniform density of charged centres  $N_C$  of  $2 \times 10^{17} \text{ cm}^{-3}$ . The relatively rough abrupt-junction approximation satisfactorily reproduces the electric field and voltage profiles for  $x \leq w$ .



## Chapter 3

# Nanocrystalline silicon by HWCVD: optical and electrical properties

In this chapter we will study the optical and electrical properties of nanocrystalline silicon obtained by HWCVD. Special attention will be paid to those properties which clearly influence the photovoltaic performance of devices. The influence of the deposition conditions on the photovoltaic suitability of the material is also discussed.

### 3.1. Optical properties

#### 3.1.1. Optical absorption coefficient

A semiconductor suitable for photovoltaic applications should absorb most of the incident power due to illumination. Not only the optical absorption coefficient  $\alpha$  and optical gap  $E_g$  matter, but also the refractive index  $n$ , which determines reflection losses. Figure 3.1 shows an absorbing thin film on its substrate. From the incident power density  $I$  (irradiance), a fraction  $R$  (reflectance) is reflected whereas  $T$  (transmittance) is transmitted. Hence, the irradiance fraction  $A$  absorbed within the film (absorptance) is

$$A = 1 - T - R \quad (3.1)$$

Reflection and transmission can be easily measured with a standard spectrophotometer. However, confident values of the optical absorption coefficient can only be obtained for high optical absorption ( $\alpha l \gg 1$ ) from the transmittance and reflectance spectra only. For medium or low optical absorption it is necessary to directly measure the optical absorption within the film which is not so easy. The Photothermal Deflection Spectroscopy (PDS) [Section 2.2.3][Jackson et al., 1981] or the Constant Photocurrent Method (CPM)[Vanecek et al., 1983] are well-known techniques with high sensitivity for this purpose.

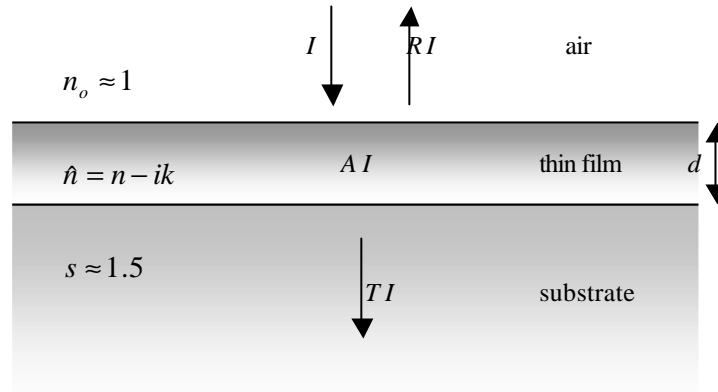


**Figure 3.1:** System formed by an absorbing smooth thin film on an infinite substrate. The extinction coefficient  $k$  in the complex refractive index  $\hat{n}$  of the film relates to the optical absorption coefficient by  $\mathbf{a} = 4\pi k / \lambda$ . A fraction  $R$  of the incident power density  $I$  is reflected whereas  $T$  is transmitted. Hence,  $A = I - T - R$  is the fraction absorbed within the film.

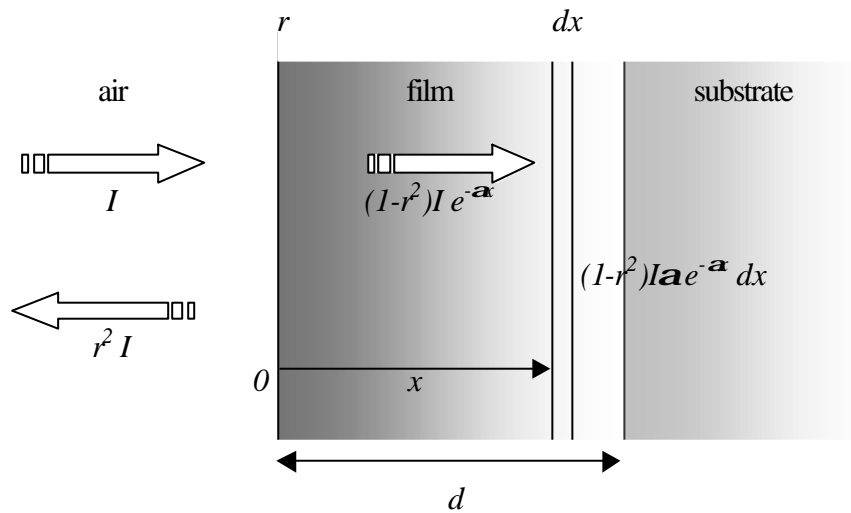


**Figure 3.2:** Simplified model to evaluate the optical absorptance  $A$  within the film. The reflection at the film-substrate interface of the attenuated irradiance is not considered while  $r$  is the Fresnel reflection coefficient at the air-film interface.

If the absorptance spectrum  $A$  is known, the optical absorption coefficient can be estimated by considering that the light only crosses once the film, i.e., overlooking interferential effects. According to the Lambert-Beer's absorption formula, the power density absorbed in an infinitesimal slice at a distance  $x$  from the air-film interface is given by  $(1-r^2)I a e^{-ax} dx$  [Fig. 3.2]. Therefore, the total power density absorbed within the film can be approximated by

$$A \approx \frac{\int_0^d (1-r^2) I \mathbf{a} e^{-ax} dx}{I} = (1-r^2)(1-e^{-ad}) = \frac{4n_o n}{(n_o+n)^2} (1-e^{-ad}) \quad (3.2)$$

where  $r=(n_o-n)/(n_o+n)$  is the Fresnel reflection coefficient at the air-film interface. Although it is possible to deduce the optical absorption coefficient from the sole absorptance measurement with equation 3.2, the deduced values present interference fringes which annoy in fitting procedures. This problem can be solved by combining the transmittance and absorptance spectra in the calculation. For a smooth absorbing thin film on an infinite transparent substrate[Fig. 3.1] the reflectance and transmittance are given by[Abelès, 1967]

$$R = \frac{(n_o - n)^2(n + s)^2 + (n - s)^2(n_o + n)^2 e^{-2ad} + (n_o^2 - n^2)(n^2 - s^2) e^{-ad} 2 \cos(2\mathbf{b}l)}{(n_o + n)^2(n + s)^2 + (n_o - n)^2(n - s)^2 e^{-2ad} + (n_o^2 - n^2)(n^2 - s^2) e^{-ad} 2 \cos(2\mathbf{b}l)} \quad (3.3)$$

$$T = \frac{16n_o n^2 s e^{-ad}}{(n_o + n)^2(n + s)^2 + (n_o - n)^2(n - s)^2 e^{-2ad} + (n_o^2 - n^2)(n^2 - s^2) e^{-ad} 2 \cos(2\mathbf{b}l)} \quad (3.4)$$

where  $n_o$ ,  $n$  and  $s$  are the refractive indexes of the air, film and substrate,  $\mathbf{a}$  is the optical absorption coefficient, and  $\mathbf{b}$  is the wave number given by  $2\pi n/l$  with  $l$  the wavelength (in the air) of the incident light. The fact that the substrate is actually finite only introduces slight corrections in these magnitudes[Swanepoel, 1983]. Note that from equations 3.3-3.4, considering that  $R+T+A=I$ , we can deduce a more accurate expression for the absorptance which takes into account interferencial effects[Ritter et al., 1986]

$$A = 4n_o n \frac{(n + s)^2 - (n - s)^2 e^{-2ad} - 4ns e^{-ad}}{(n_o + n)^2(n + s)^2 + (n_o - n)^2(n - s)^2 e^{-2ad} + (n_o^2 - n^2)(n^2 - s^2) e^{-ad} 2 \cos(2\mathbf{b}l)} \quad (3.5)$$

which combined with equation 3.4 leads to

$$e^{ad} = \frac{4ns \left(1 + \frac{A}{T}\right) + \sqrt{\left[4ns \left(1 + \frac{A}{T}\right)\right]^2 + 4(n^2 - s^2)^2}}{2(n + s)^2} \quad (3.6)$$

which turns out to be a very useful equation to analytically calculate the optical absorption coefficient from the measured absorptance and transmittance data by considering interference effects. In figure 3.3 we compare the optical absorption coefficient of a nanocrystalline silicon sample calculated with only the optical absorptance [Eq. 3.2] and with the combined absorptance-transmittance measurement [Eq. 3.6]. The film thickness was around 2  $\mu\text{m}$ . Note how interference fringes disappear with the improved calculation. Since the reflection at the film-substrate interface is not considered within the simpler treatment, the optical absorption coefficient results slightly overestimated.

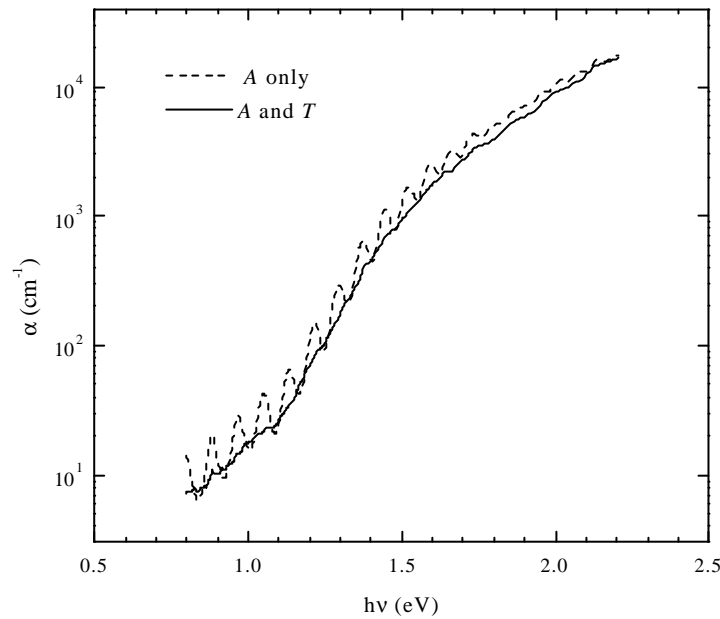


**Figure 3.3:** Optical absorption coefficient calculated from the sole absorptance spectrum and improved calculation considering also the transmittance spectrum for a HWCVD nanocrystalline silicon layer 2  $\mu\text{m}$  thick.

### 3.1.2. Enhanced optical absorption

The calculated optical absorption coefficient of nc-Si:H layers with a high crystalline fraction is generally higher than that of single crystal silicon. The most obvious attempt to explain this enhanced optical absorption consists in considering an effective media model to take into account the amorphous phase present in the samples [Ward, 1994]. In this way, the effective optical absorption coefficient  $\alpha_{\text{eff}}$  of a nc-Si:H sample with a  $X_C$  crystalline fraction is expected to be

$$\mathbf{a}_{eff} = X_C \mathbf{a}_{c-Si} + (1 - X_C) \mathbf{a}_{a-Si:H} \quad (3.7)$$

where  $\mathbf{a}_{c-Si}$  and  $\mathbf{a}_{a-Si:H}$  are the optical absorption coefficients of single crystal silicon and hydrogenated amorphous silicon respectively. In figure 3.4 we plot together  $\mathbf{a}_{c-Si}$ ,  $\mathbf{a}_{a-Si:H}$  and the calculated  $\mathbf{a}_{eff}$  for a 90% crystalline fraction. While  $\mathbf{a}_{c-Si}$  is well determined and unique,  $\mathbf{a}_{a-Si:H}$  depends on the properties of the amorphous fraction in the sample. For this plot we considered an amorphous phase of poor quality with an Urbach front of 90 meV and a dangling bond density of  $10^{18} \text{ cm}^{-3}$ . The optical gap of this amorphous phase was chosen 1.8 eV.

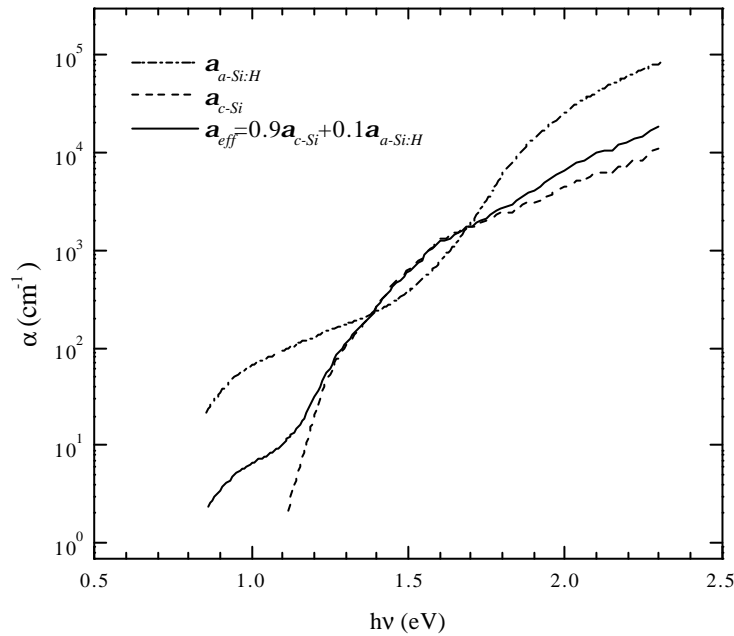


**Figure 3.4:** Effective optical absorption coefficient, according to the effective media model, for a nc-Si:H sample with a 90% of crystalline fraction. The amorphous phase, with an optical gap of 1.8 eV, was considered of poor quality: defect density of  $10^{18} \text{ cm}^{-3}$  and Urbach front of 90 meV.

In practice, this straightforward model does not allow to precisely fit the optical absorption coefficient of most nc-Si:H samples overall the spectrum. Furthermore, the optical absorption spectra usually present clear differences between samples with very similar crystalline fractions but obtained under different deposition conditions.

**Table 3.1:** HWCVD nc-Si:H samples obtained at different process pressures. Both were obtained with a substrate temperature of 150°C and a 95% hydrogen dilution (4 sccm of SiH<sub>4</sub> mixed with 76 sccm of H<sub>2</sub>). The wire was heated to 1700°C.

| Sample | Process pressure (mbar) | Thickness (μm) | $r_d$ (Å/s) | $E_g$ (eV) | $\alpha(1.5 \text{ eV})$ (cm <sup>-1</sup> ) |
|--------|-------------------------|----------------|-------------|------------|--|
| LP     | $7 \cdot 10^{-3}$       | 1.8            | 2.4         | 1.16       | 611  |
| HP     | $3.5 \cdot 10^{-2}$     | 2.1            | 8.7         | 1.12       | 1066   |

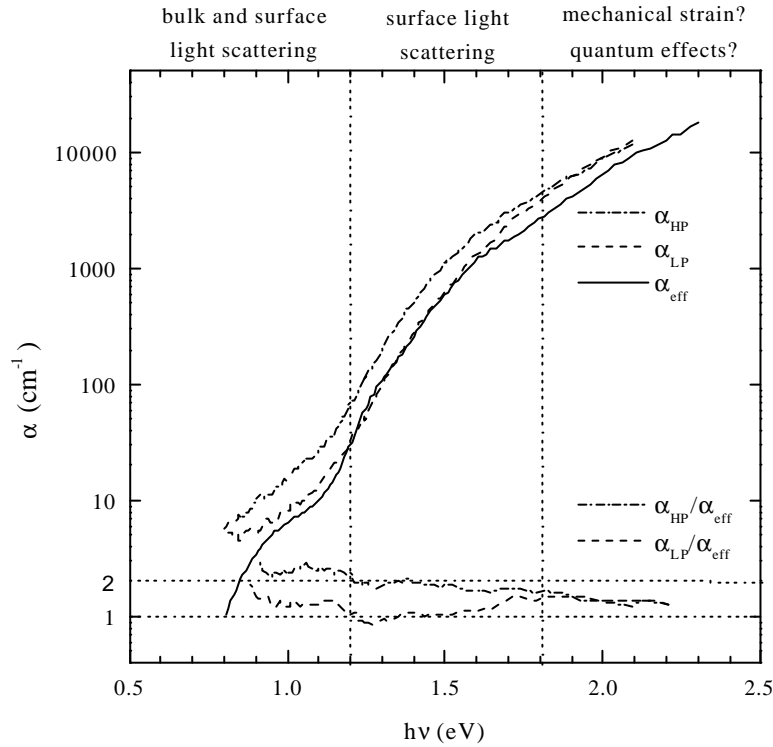


**Figure 3.5:** Optical absorption coefficients measured by PDS for the HWCVD nc-Si:H samples in table 3.1. It is also shown the effective optical absorption coefficient expected for a 90% crystalline fraction. The corresponding ratios are also plotted as a measure of the optical absorption enhancement.

In figure 3.5 we show the optical absorption coefficient spectra of two HWCVD nc-Si:H samples. They were obtained at clearly different process pressures while the rest of deposition conditions remained unchanged [Table 3.1]. Both samples presented very similar crystalline fractions around 90% deduced from their Raman spectra [Peiró, 1999]. Hence, an effective optical absorption  $\alpha_{eff}$  was calculated with  $X_C=0.9$  in equation 3.7 and plotted together with the optical absorption coefficients  $\alpha_{LP}$  and  $\alpha_{HP}$  of the studied samples for

comparison. The ratios  $\mathbf{a}_{LP}/\mathbf{a}_{eff}$  and  $\mathbf{a}_{HP}/\mathbf{a}_{eff}$  ( $\geq 1$ ) are a direct measurement of the enhanced optical absorption. Three different regions can be easily distinguished:

*a)  $h\nu < 1.2$  eV ( $\mathbf{l} > 1000$  nm):* It is generally accepted that the subgap optical absorption is due to deep states in the gap. Hence, the density of dangling bonds could be determined by deconvoluting this part of the absorption coefficient spectrum [Jackson et al., 1982]. Though this is true in the case of smooth and homogeneous a-Si:H layers, for nc-Si:H layers the absorption coefficient is greatly influenced by light scattering either at the surface or in the bulk of the layer [Beck et al., 1998]. Therefore, though this part could be certainly fitted by properly choosing the defect density in the amorphous phase, the obtained densities of deep states in the gap could result highly overestimated.

*b)  $1.2$  eV  $< h\nu < 1.8$  eV ( $1000$  nm  $< \mathbf{l} < 700$  nm):* In this region the optical absorption coefficient of the HP sample is clearly higher than that of the LP sample. It is observed that  $\mathbf{a}_{LP} \gg \mathbf{a}_{eff}$  whereas  $\mathbf{a}_{HP} \gg 1.75 \mathbf{a}_{eff}$ . A careful optical study with VHF-PECVD nc-Si:H samples [Poruba et al., 1998] shows that enhanced optical absorption in this part of the spectrum is undoubtedly due to light scattering at the surface of the films. It was observed that after chemomechanically polishing the samples up to a mirror-like surface, the enhanced optical absorption disappeared in this region. We deduce that the HP sample presented a much rougher surface than the LP sample, which was optically smooth for this wavelength interval.

*c)  $h\nu > 1.8$  eV ( $\mathbf{l} < 700$  nm):* In the visible region the optical absorption coefficients of both samples coincide in a value higher than expected according to their measured crystalline fractions ( $\mathbf{a}_{HP} \gg \mathbf{a}_{LP} \gg 1.5 \mathbf{a}_{eff}$ ). The amorphous phase, which was taken into account with the effective media approximation [Eq. 3.7], does not allow to explain the enhanced optical absorption in the visible region. Neither light scattering can explain this enhanced optical absorption because rough and smooth samples behave here in the same way. It has been proposed that either strong mechanical strain causing a relaxation in the  $\vec{k}$  selection rule [Schroop et al., 1998] or quantum effects related to the grain

size[Kalkan et al.,1997] could be responsible for the enhanced optical absorption in this part of the spectrum. Furthermore, correlations with the hydrogen content have been also detected by stepwise annealing the samples[Beck et al., 1996].

### 3.1.3. Benefits from enhanced optical absorption

While optical absorption in the subgap region is not interesting for photovoltaic applications, absorbed photons of energy over the band gap certainly photogenerate useful electron-hole pairs. Then, however it is caused, enhanced optical absorption for photon energies higher than the band gap is advantageous for photovoltaic applications. In figure 3.6 we compare the optical absorptances  $A_{HP}$  and  $A_{LP}$  expected for 2  $\mu\text{m}$  thick films with the optical absorption coefficient spectra  $\mathbf{a}_{HP}$  and  $\mathbf{a}_{LP}$  in figure 3.5, respectively. A thickness of 2  $\mu\text{m}$  was chosen for the calculation because it is in the order of the thickness of the active layer in a p-i-n nc-Si:H solar cell. We observe that 2  $\mu\text{m}$  thick films are already optically dense in the visible part of the spectrum. Therefore, though there is some optical absorption enhancement there, it would not suppose a great improvement in the solar cell performance. By contrast, enhanced absorption in the near infrared certainly results in an advantageous gain of photogeneration. Under AM1.5 irradiance conditions, the maximum current density generated in such layers can be calculated as

$$j_{max} = \int_{\mathbf{I} < \mathbf{I}_o} J_{AM1.5}(\mathbf{I}) A(\mathbf{I}) d\mathbf{I} \quad (3.8)$$

where  $A(\mathbf{I})$  is the absorptance spectrum related to the optical absorption coefficient spectrum  $\mathbf{a}(\mathbf{I})$  by equation 3.2. The integral extends over the wavelength interval  $\mathbf{I} < \mathbf{I}_o$  where  $\mathbf{I}_o = hc/E_g$ , i.e., for photon energies higher than the band gap. For simplicity, in equation 3.8 the AM1.5 spectrum  $J_{AM1.5}(\mathbf{I})$  is in current density units ( $\text{mA cm}^{-2} \text{nm}^{-1}$ ) assuming one electron-hole pair generated per absorbed photon. That is

$$J_{AM1.5}(\mathbf{I}) = \frac{\mathbf{I}}{1241} P_{AM1.5}(\mathbf{I}) \quad (3.9)$$

where the wavelength  $\lambda$  is in  $nm$  and  $P_{AM1.5}(\lambda)$  is the AM1.5 spectral power density in the more commonly used power units ( $mW\ cm^{-2}\ nm^{-1}$ ). By using equation 3.8, the optical absorptance of the HP sample would lead to a maximum current density of  $17.2\ mA/cm^2$ , while the LP sample would result in only  $16.1\ mA/cm^2$ . Though it could seem a small improvement, this gain results much greater in actual p-i-n structures due to the metallic back contact acting as a diffusive back reflector[Poruba et al., 1998]. For that reason, back contact technologies have been developed in order to increase the internal reflection at the back contact[Carlson et al., 1984]. The group at University of Neuchâtel successfully incorporates back contacts consisting of highly textured zinc oxide and silver in their solar cells[Torres et al., 1996].

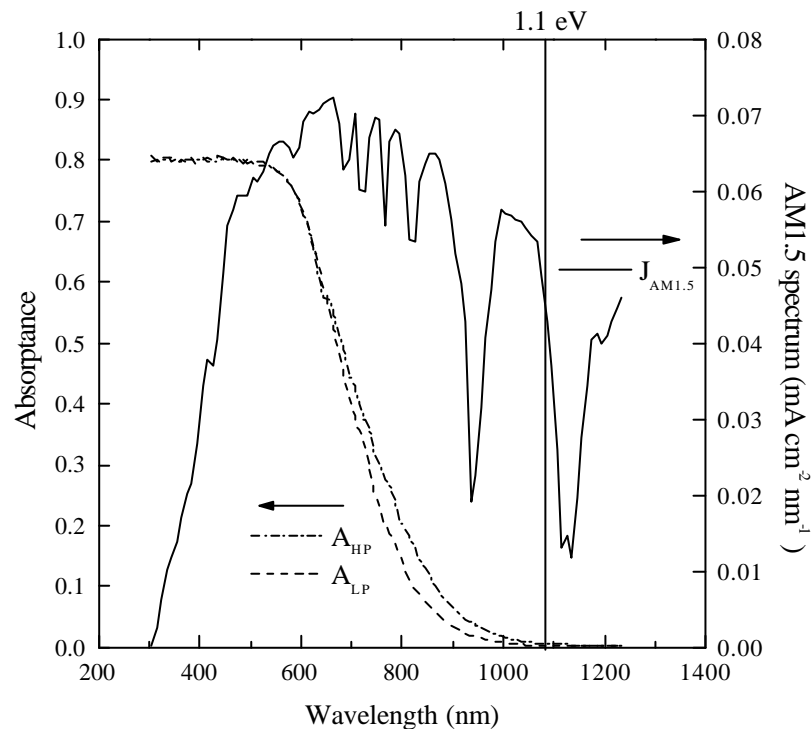


**Figure 3.6:** Optical absorptances expected for  $2\ \mu m$  thick films with the optical absorption coefficient spectra in figure 3.5. Note the higher absorptance in the near infrared obtained when  $a_{HP}$  was used for the calculation.

The structural characterisation of our samples showed that higher process pressures enhance the columnar growth along the  $[220]$  crystalline direction, as observed by X-ray diffraction (XRD) and Scanning Electron Microscopy (SEM) investigations[Peiró, 2000]. It has been observed that such preferential crystalline growth also results in enhanced optical

absorption coefficients for VHF-PECVD nc-Si:H samples[Torres, 1998] in the same range ( $1.2 \text{ eV} < h\nu < 1.8 \text{ eV}$ ). Hence, we deduce that the [220] crystalline preferential growth is linked to a higher surface roughness and consequently an enhanced optical absorption due to light scattering at the surface of the films. Therefore, the process pressure turns out to be a proper deposition parameter to control the surface texture of HWCVD nc-Si:H samples in order to obtain an advantageous enhanced optical absorption.

Figure 3.7 compares the optical absorbance expected for a HWCVD nc-Si:H sample (HP in table 3.1) to that of a device quality PECVD a-Si:H sample[Asensi, 1994]. The thicknesses chosen for the calculation were  $2 \text{ }\mu\text{m}$  and  $0.4\mu\text{m}$  respectively, typical values for the active layers of nc-Si:H and aSi:H p-i-n solar cells. Note what a great part of the solar AM1.5 power density is not absorbed in the case of the a-Si:H layer due to its relatively high band gap. By using equation 3.8, the optical absorbance of the nc-Si:H sample would lead to a maximum current density of  $17.2 \text{ mA/cm}^2$ , while the a-Si:H sample would result in just  $11.4 \text{ mA/cm}^2$ .

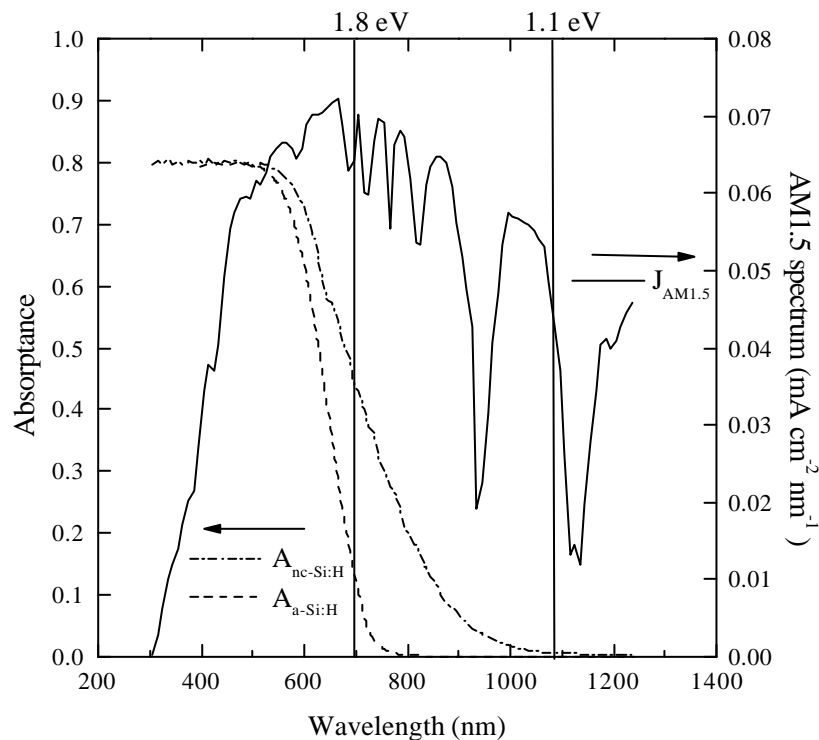


**Figure 3.7:** Optical absorbance of a  $2 \text{ }\mu\text{m}$  thick HWCVD nc-Si:H sample (HP in table 3.1) compared with that of a  $0.4 \text{ }\mu\text{m}$  thick PECVD a-Si:H sample. The relatively high a-Si:H band gap causes important optical losses when the solar AM1.5 spectrum is considered.

In regard to p-i-n structures, the optical absorbance within the active layer could be considered the optical limit of the external quantum efficiency[Fig. 3.8]. Therefore, the maximum short-circuit current density can be calculated from equation 3.8 with the optical absorbance in the active layer weighting the AM1.5 solar irradiance. These results are shown in table 3.2 for different p-i-n structures. Very thin doped layers of 100 Å with a 3.5 μm thick active layer and back-reflector (A) is the structure proposed by the Institut de Microtechnique[Meier et al., 1998]. Note how thicker doped layers (C and D) or a thinner active one without light confinement strategies (B and D) result in lower current densities.

**Table 3.2:** Optical limits in the maximum short circuit current density under AM1.5 for different p-i-n structures. Equation 3.8 is used for the calculation considering only the absorbance in the active layer. As usual, it is assumed that all the carriers photogenerated within the doped layers recombine (dead layers).

| name | doped layers thickness<br>(Å) | active layer thickness<br>(μm) | back-reflector | $j_{max}$<br>(mA/cm <sup>2</sup> ) |
|------|-------------------------------|--------------------------------|----------------|------------------------------------|
| A    | 100                           | 3.5                            | yes            | 22.7                               |
| B    | 100                           | 2                              | no             | 16.9                               |
| C    | 500                           | 3.5                            | yes            | 20.5                               |
| D    | 500                           | 2                              | no             | 14.8                               |

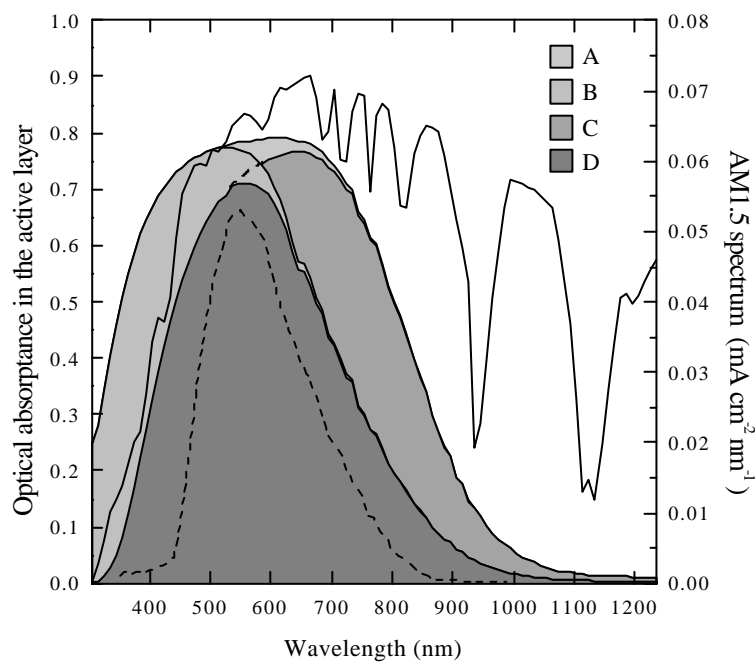


**Figure 3.8:** Calculated optical absorbances in the active layer for the device structures in table 3.2. The measured external quantum efficiency of the 990323c solar cell[Section 2.3.2] is also shown for comparison (dashed line). Note the additional losses due to either interface or bulk recombination depending on the wavelength range.

### 3.1.4. Light scattering

Since it has been shown that light scattering is determining the enhanced optical absorption of nc-Si:H layers in the useful wavelength interval from 700 to 1000 nm, we are specially interested in studying this effect. Different optical characterisations evidence elastic light scattering in nc-Si:H silicon films. An extremely simple experiment which allows to observe this effect consists in comparing the transmittance spectra measured with the detector placed just behind the sample (integrated transmittance)[Fig. 3.9a] or away from it (specular transmittance)[Fig. 3.9b]. All the transmitted irradiance contributes to the integrated transmittance  $T_i$  while only the irradiance transmitted in a direction near to that of the incident beam contributes to the specular transmittance  $T_s$ . The difference between both spectra is the diffuse transmittance  $T_d$ . The Haze ratio[Eq. 3.10], defined as the ratio of the diffuse transmittance to the integrated or total transmittance is a measure of the degree of elastic light scattering.

$$H = \frac{T_d}{T_i} = \frac{T_i - T_s}{T_i} = 1 - \frac{T_s}{T_i} \quad (3.10)$$

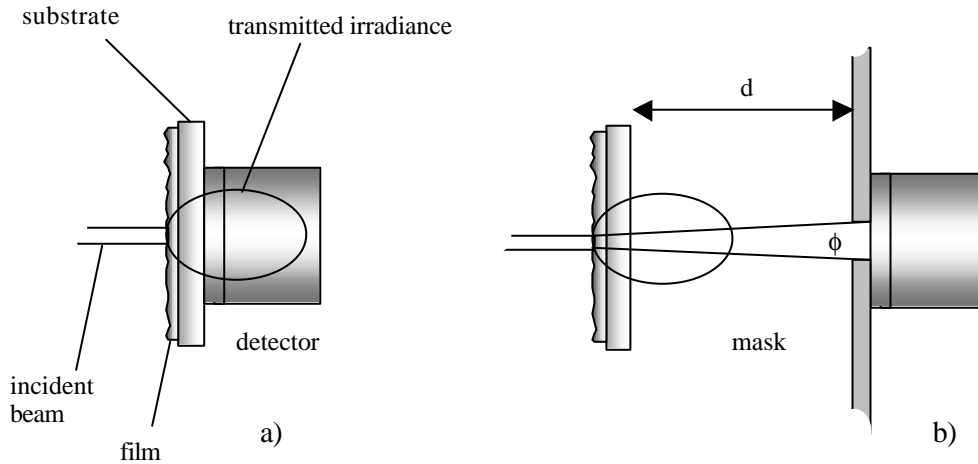


**Figure 3.9:** Experiment to easily detect elastic light scattering. a) When the detector is placed just behind the substrate, all the transmitted irradiance contributes to the measured spectrum (integrated transmittance). b) If it is placed away from the substrate and its aperture  $\phi$  is reduced with a mask, only the transmitted irradiance in a direction near to that of the incident beam will reach the detector (specular transmittance).

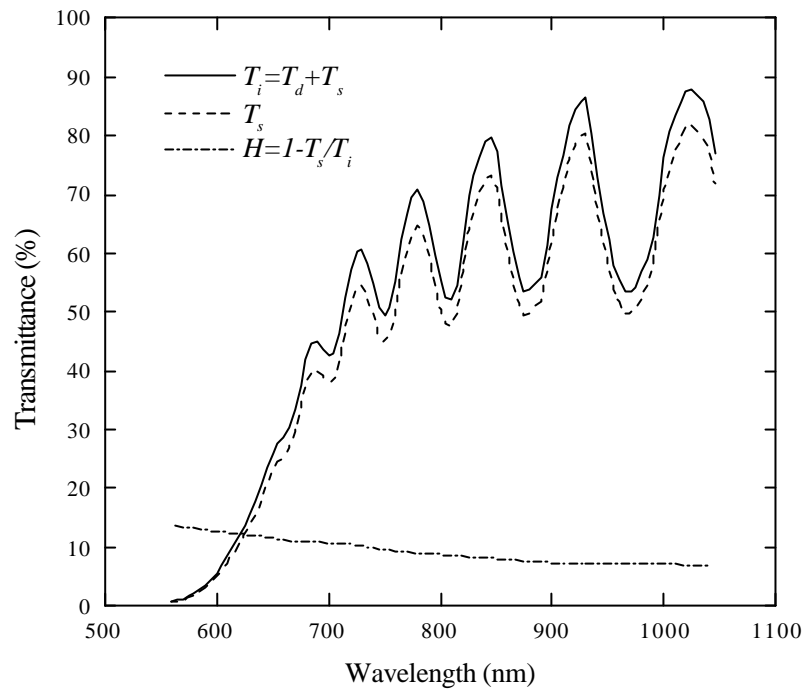


**Figure 3.10:** Integrated and specular transmittances for a 1.5  $\mu\text{m}$  thick HWCVD nc-Si:H silicon sample. The specular transmittance was measured by placing the detector 2 cm away from the sample and reducing its aperture to 1 cm (deviation of  $14^\circ$  from the incident direction). With this geometry, the measured Haze ratio was around 10% over the whole spectrum.

We performed the experiment described in figure 3.9 with a nc-Si:H sample obtained by HWCVD. Though the pronounced interference pattern indicates that no strong light scattering takes place, a Haze ratio around 10% was obtained over the whole spectrum [Fig. 3.10]. These values are of the same order than those reported for similar samples [Diehl et al., 1998]. However direct comparison would require the same experimental set up or, at least, similar geometries.

### 3.1.5. Surface roughness

The as grown textured surface of nc-Si:H thin films is responsible for surface scattering while its heterogeneity and columnar structure cause bulk scattering. Since bulk scattering seems to be important only in the subgap spectral region [Poruba et al., 1998], it does not significantly contribute to enhance photovoltaic generation. By contrast, surface light

scattering certainly enhances the band to band photogeneration of electron-hole pairs. Hence, we are specially interested in getting some more insight in light scattering at the surface of the films. The as grown textured surface of nc-Si:H samples can be regarded as a flat interface with a small stochastic disturbance, which is characterised by an *rms* roughness  $S_r$ . According to the scalar theory, which is applied to such surfaces, the ratio of the specular reflectance  $R_s$  to the total or integrated reflectance  $R_i$  is related to the *rms* roughness and the angle of incidence  $q$  by [Bennett et al., 1961]

$$\frac{R_s}{R_i} = \frac{R_s}{R_s + R_d} = \exp \left[ - \left( \frac{4 p S_r n_o \cos q}{I} \right)^2 \right] \quad (3.11)$$

where  $n_o$  is the refractive index of the medium of incidence and  $R_d$  the diffuse reflectance.

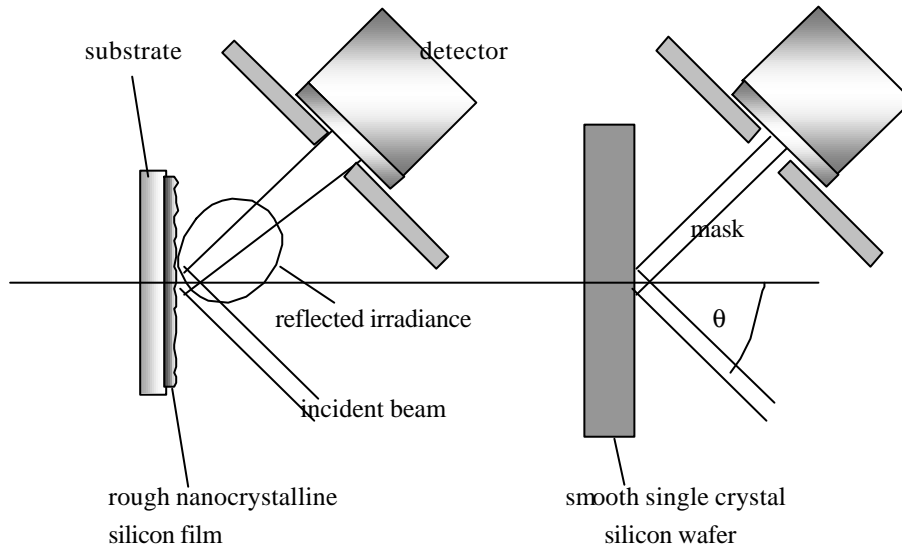


**Figure 3.11:** Experiment to evaluate the *rms* roughness of a nc-Si:H film according to equation 3.11. The smooth wafer does not present diffuse reflection. Hence, specular reflectance equals total reflectance in that case.

In practice, this experiment can be performed by comparing the specular reflectance spectra of a rough nc-Si:H film and a polished single crystal silicon wafer. Since no diffuse reflection is expected at the smooth surface of the wafer, its specular reflectance can be used as the total reflectance in equation 3.11 [Chiang et al., 1979]. We have estimated the *rms* roughness of two nc-Si:H samples obtained by HWCVD. Both samples were obtained with the following common deposition conditions: filament temperature of 1700°C,

substrate temperature of 200 °C, process pressure of 0.18 mbar and a gas mixture of 2 sccm of silane with 18 sccm of hydrogen. The deposition rate was around 20 Å/s and the different thicknesses were obtained by varying the deposition time. As deduced from the XRD spectra, these films presented a clear [220] preferential orientation [Peiró, 1999]. The SEM images also showed a pronounced columnar microstructure [Fig. 3.12]. The obtained values of  $\sigma_r$  are around 2% of the film thickness [Fig. 3.13]. Similar values were previously reported for nc-Si:H samples obtained by VHF-PECVD [Poruba et al., 1998].

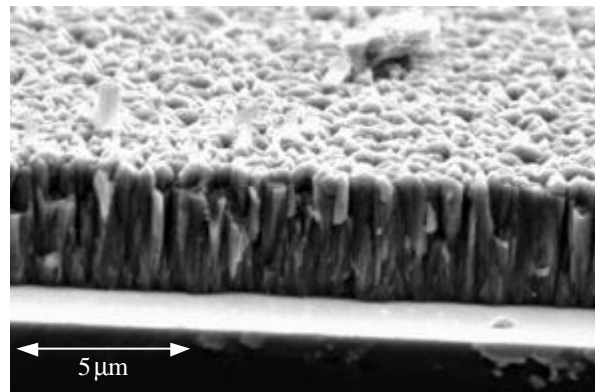


**Figure 3.12:** Scanning Electron Microscopy view of a nc-Si:H sample. Note the columnar structure of the film (bulk scattering) and its as grown textured surface (surface scattering).

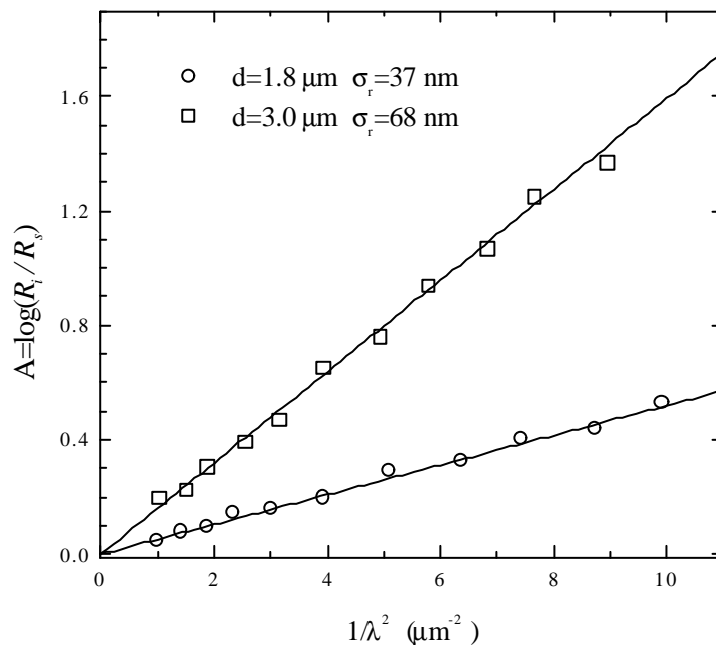


**Figure 3.13:** Determination of the rms roughness of the HWCVD nc-Si:H samples from reflectance measurements. The angle of incidence was 45°.

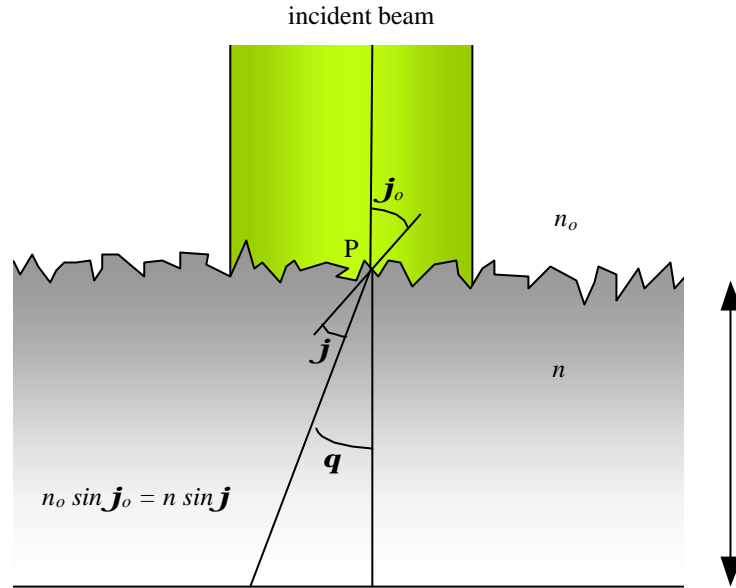


**Figure 3.14:** Trajectory of a ray from the incident beam of light scattered at the rough surface of the film. Its effective optical path through the sample becomes  $d/\cos q$ .

To accurately predict how light scattering is going to enhance the optical absorption, complex optical models and large computational calculations are required [Sopori et al., 1998]. However, it is clear that the optical absorption is enhanced because scattered light has a longer effective path through the film. As shown in figure 3.14, the ray arriving at the point P is scattered under an angle  $q$  with respect to the normal direction of the incident beam. Hence, its effective optical path through the film is  $d/\cos q$  which is greater than just the film thickness. A complete calculation considering all the possible scattered rays from the incident beam would require a large amount of computational work and an unattainable exact three-dimensional mapping of the textured surface. Anyway, the expected optical absorption enhancement can be estimated assuming a Lambertian distribution for the scattered light ( $F = F_0 \cos q$ ). This is the case for a film with a random surface roughness. For the calculation we consider that, after reflection losses, an irradiance  $I$  enters the film scattered according to a cosine distribution. Then, considering polar coordinates, the irradiance fraction scattered within an angle  $q$  is given by

$$\frac{dI(\mathbf{q})}{I} = 2 \sin \mathbf{q} \cos \mathbf{q} d\mathbf{q} \quad (3.12)$$

and the expected enhanced absorptance can be calculated as

$$A_{enh} = \int_0^{\frac{p}{2}} (1 - e^{-\mathbf{a} d / \cos \mathbf{q}}) 2 \sin \mathbf{q} \cos \mathbf{q} d\mathbf{q} \quad (3.13)$$

For weakly absorbed light, which is certainly the case in the near infrared for typical film thicknesses, the above integral can be solved arriving at

$$A_{enh} \approx \int_0^{\frac{p}{2}} \frac{\mathbf{a}d}{\cos \mathbf{q}} 2 \sin \mathbf{q} \cos \mathbf{q} d\mathbf{q} = 2\mathbf{a}d \approx 1 - e^{-2\mathbf{a}d} = 1 - e^{-\mathbf{a}_{enh}d} \quad (3.14)$$

Therefore, within this model, a factor 2 in the enhanced optical absorption coefficient would be expected with respect to the true optical absorption coefficient of the material. If additional scattering in the bulk of the sample takes place, it results in still longer effective paths and enhanced optical absorption coefficients with factors greater than 2. But bulk scattering seems to be only important in the subgap spectral region of some samples [Poruba et al., 1998]. We have obtained factors near 2 for our HWCVD nc-Si:H samples which presented enhanced optical absorption. In section 3.1.2 we calculated a factor 1.75 for the rough film grown at a high process pressure. In fact, values lower than 2 point to a not complete diffuse scattering. Such effect can be introduced by modifying the cosine angular distribution with an exponent  $n$  ( $\mathbf{F} = \mathbf{F}_0 \cos^n \mathbf{q}$ ). Then the enhanced optical absorptance is

$$A_{enh} = \int_0^{\frac{p}{2}} C (1 - e^{-\mathbf{a} d / \cos \mathbf{q}}) n \sin \mathbf{q} \cos^n \mathbf{q} d\mathbf{q} \quad (3.15)$$

where  $n$  and  $C$  is a normalising factor given by

$$C = \frac{1}{\int_0^{\frac{p}{2}} n \sin \mathbf{q} \cos^n \mathbf{q} d\mathbf{q}} \quad (3.16)$$

We have calculated that the measured optical absorption enhancement  $\mathbf{a}_{enh}/\mathbf{a}=1.75$  would correspond to an exponent  $n=1.4$  [Fig. 3.15]. Very similar angle resolved

distributions of scattered light have been experimentally measured and reported for nc-Si:H samples obtained by VHF-PECVD [Poruba et al., 1998].

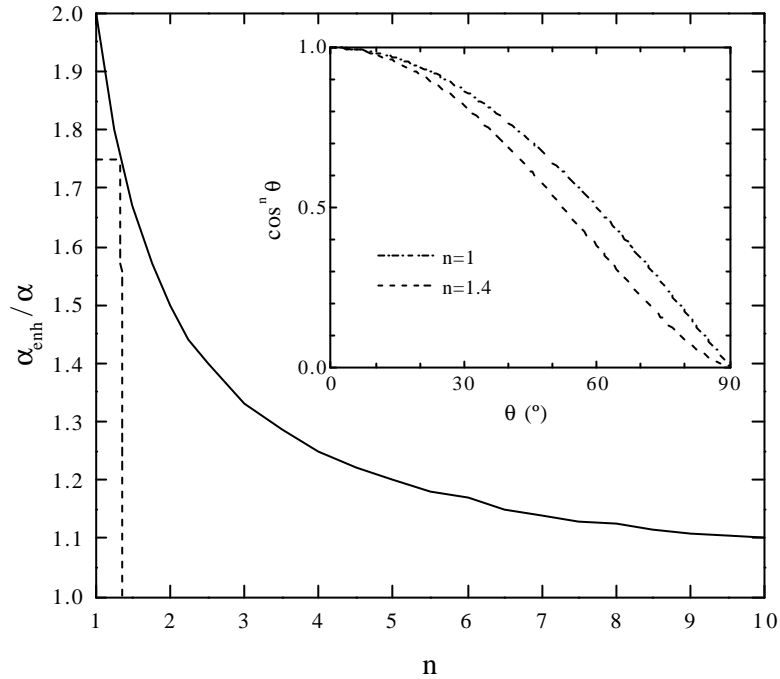


**Figure 3.15:** Expected optical absorption coefficient enhancement as a function of the scattered light distribution ( $F=F_0 \cos^n \theta$ ). For  $n=1.4$  we obtain the factor 1.75 experimentally observed in our rough samples.

## 3.2. Electrical properties

### 3.2.1. Dark conductivity of undoped nanocrystalline silicon

Though dark conductivity is possibly the most simple electrical characterisation of a semiconductor, it allows to extract valuable information if the obtained data are accurately analysed. The dark conductivity  $\mathbf{s}$  of any semiconductor can be calculated as

$$\mathbf{s} = e(\mathbf{m}_n n + \mathbf{m}_p p) \quad (3.17)$$

where  $e$  is the elementary charge,  $n$  and  $p$  the electron and hole densities and  $\mathbf{m}_n$  and  $\mathbf{m}_p$  their mobilities in the conduction and valence bands respectively. To take into account the effect of the temperature we must consider that

$$n = N_C \exp\left(-\frac{E_C - E_F}{k_B T}\right) \quad p = N_V \exp\left(-\frac{E_F - E_V}{k_B T}\right) \quad (3.18)$$

with  $E_C$  and  $E_V$  the energy levels of the conduction and valence band edges,  $E_F$  the Fermi-level,  $N_C$  and  $N_V$  the conduction and valence band effective densities of states respectively and  $k_B$  the Boltzmann's constant. In an ideally intrinsic semiconductor, electrons in the conduction band can be only those thermally activated from previously occupied states in the valence band, i.e.,  $n=p=n_i$  where  $n_i$  is the intrinsic carrier density given by

$$n_i = \sqrt{np} = \sqrt{N_C N_V} \exp\left(-\frac{E_g / 2}{k_B T}\right) \quad (3.19)$$

Hence, the dark conductivity of an intrinsic semiconductor is

$$\mathbf{s} = e(\mathbf{m}_n + \mathbf{m}_p) \sqrt{N_C N_V} \exp\left(-\frac{E_g / 2}{k_B T}\right) = \mathbf{s}_o \exp\left(-\frac{E_a}{k_B T}\right) \quad (3.20)$$

where we have introduced the thermal activation energy  $E_a$  and prefactor  $\mathbf{s}_o$  of the dark conductivity. In the same way, for n- and p-type semiconductors we obtain a similar behaviour but with different expressions for  $E_a$  and  $\mathbf{s}_o$

$$\text{n - type } \mathbf{s} \approx e\mathbf{m}_n n = e\mathbf{m}_n N_C \exp\left(-\frac{E_C - E_F}{k_B T}\right) = \mathbf{s}_o \exp\left(-\frac{E_a}{k_B T}\right) \quad (3.21a)$$

$$\text{p - type } \mathbf{s} \approx e\mathbf{m}_p p = e\mathbf{m}_p N_V \exp\left(-\frac{E_F - E_V}{k_B T}\right) = \mathbf{s}_o \exp\left(-\frac{E_a}{k_B T}\right) \quad (3.21b)$$

Actually, the effective band densities of states, mobilities and the band gap are also slow varying functions of the temperature. However, a thermal activated behaviour is experimentally observed within a wide temperature range.

### a) The simplest case: ideally intrinsic single crystal silicon

Though electronic transport must be definitely different in nc-Si:H, it is interesting to previously analyse the simplest case of ideally intrinsic single crystal silicon. The required parameters to calculate the dark conductivity are shown in table 3.3[Sze, 1985].

**Table 3.3:** Main electrical parameters for ideally intrinsic single crystal silicon as a function of the absolute temperature. Without impurities, only lattice scattering determines the temperature dependence of the carrier mobilities ( $\sim 1/T^{3/2}$ ).

| $N_C$ (cm <sup>-3</sup> )         | $N_V$ (cm <sup>-3</sup> )          | $\mu_n$ (cm <sup>2</sup> V <sup>-1</sup> s <sup>-1</sup> ) | $\mu_p$ (cm <sup>2</sup> V <sup>-1</sup> s <sup>-1</sup> ) | $E_g$ (eV)                     |
|-----------------------------------|------------------------------------|--|--|--------------------------------|
| $2.8 \cdot 10^{19} (T/300)^{3/2}$ | $1.04 \cdot 10^{19} (T/300)^{3/2}$ | $1900 (300/T)^{3/2}$                                       | $495 (300/T)^{3/2}$  | $1.12-3 \cdot 10^{-4} (T-300)$ |

In figure 3.16 we compare the dark conductivity considering all the thermal dependencies in table 3.3 to the approximated calculation taken the values at 300 K as constants within the studied temperature range. Though the other parameters also vary with the temperature, the significant differences are mainly due to the thermal shrinking of the band gap. Hence, considering only this effect, it is expected a proportional reduction in the activation energy when the temperature is increased

$$\begin{aligned} E_a(T) &= \frac{E_g(T)}{E_g(T_o)} E_a(T_o) = \frac{E_g(T_o) - \mathbf{g}(T - T_o)}{E_g(T_o)} E_a(T_o) = \\ &= E_a(T_o) - \frac{E_a(T_o)}{E_g(T_o)} \mathbf{g}(T - T_o) \end{aligned} \quad (3.22)$$

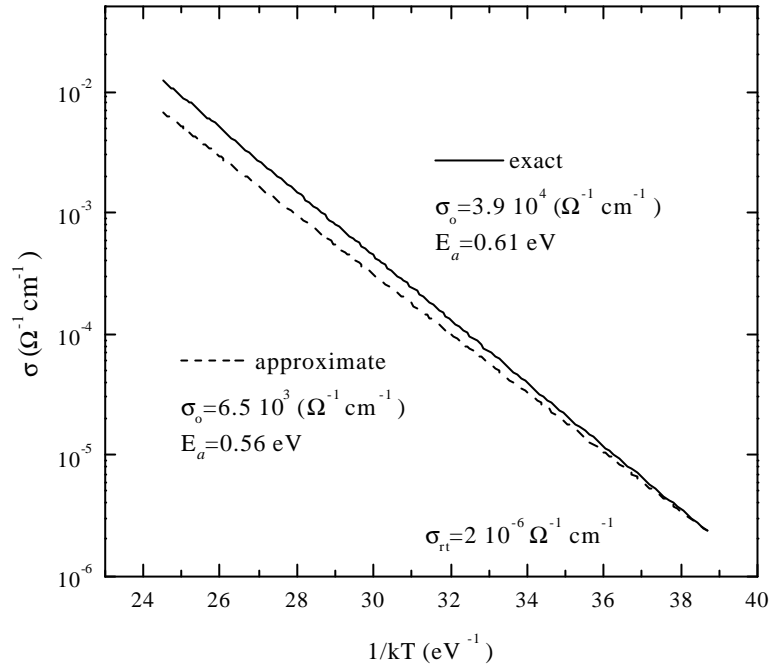


**Figure 3.16:** Approximate and exact calculation of the dark conductivity of ideally intrinsic single crystal silicon as a function of the temperature.

which leads to the following corrections in the activation energy and dark conductivity prefactor

$$\begin{aligned} \mathbf{s} &= \mathbf{s}_o \exp\left(-\frac{E_a(T)}{k_B T}\right) = \mathbf{s}_o \exp\left(\frac{E_a(T_o) \mathbf{g}}{E_g(T_o) k_B}\right) \exp\left(-\frac{E_a(T_o) + \frac{E_a(T_o)}{E_g(T_o)} T_o}{k_B T}\right) = \\ &= \mathbf{s}_o' \exp\left(-\frac{E_a'}{k_B T}\right) \end{aligned} \quad (3.23)$$

where we have identified

$$\mathbf{s}_o' = \mathbf{s}_o \exp\left(\frac{E_a(T_o) \mathbf{g}}{E_g(T_o) k_B}\right) \quad E_a' = E_a(T_o) + \frac{E_a(T_o)}{E_g(T_o)} T_o \quad (3.24)$$

and for  $E_a(T_o) = E_g(T_o)/2$  with  $T_o = 300$  K and  $\mathbf{g} = 3 \times 10^{-4}$  eV/K [Table 3.3] we obtain

$$\mathbf{s}_o' = 5.7 \mathbf{s}_o(T_o) \quad E_a' = \frac{E_g(T_o)}{2} + 0.045 \text{ eV} \quad (3.25)$$

which virtually corrects the miscalculation.

### b) The complex case: hydrogenated nanocrystalline silicon

Actually, our subject of study is the certainly different case of nc-Si:H samples. However, the thermal shrinking of the band gap is so intimately related to the local atomic bonding that it is also expected to happen in nc-Si:H. Therefore, though it is generally accepted that fully intrinsic samples are those which satisfy the midgap condition, this asseveration could result uncertain. Furthermore, the mechanism of charge transport in nc-Si:H has not been clarified yet and the carrier mobilities could also present relatively strong activated thermal dependences[Ruff et al., 1998]. On the other hand, as observed in many disordered or inhomogeneous semiconductors[Jackson, 1988], a correlation is found between the activation energy and the prefactor of the dark conductivity[Fig. 3.17]. The observed exponential behaviour is known as the Meyer-Neldel rule[Meyer et al., 1937]

$$s_o = s_{oo} \exp\left(\frac{E_a}{E_{MN}}\right) \quad (3.26)$$

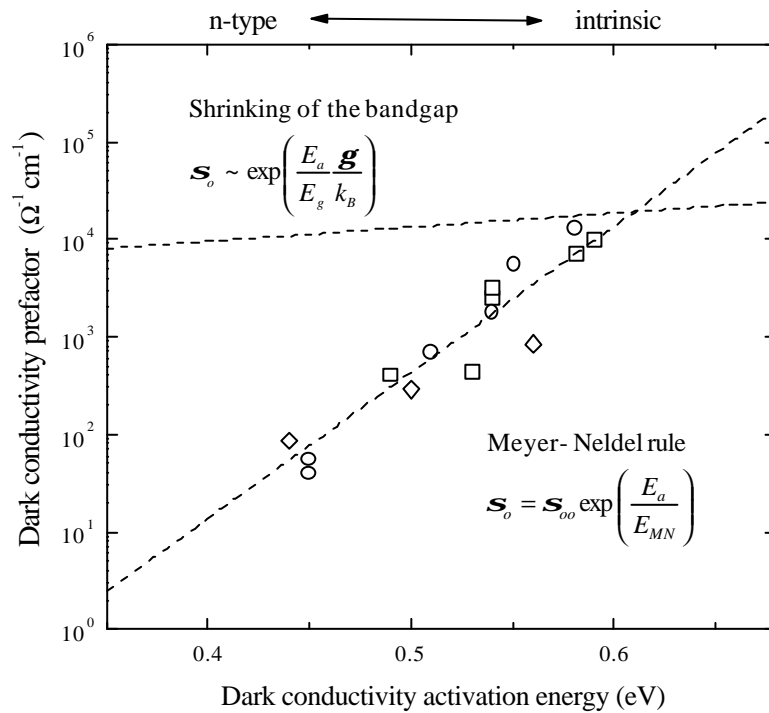


**Figure 3.17:** Conventional Meyer-Neldel rule observed in different series of undoped nc-Si:H samples obtained by HWCVD[Table 3.4]. The thermal shrinking of the band gap does not fully explain the strong exponential behaviour.

**Table 3.4:** Deposition conditions and main electrical properties of the series of undoped nc-Si:H samples in figure 3.17. The first six samples( $\square$ ) were grown with a filament of 1 mm of diameter whereas the following six( $\circ$ ) and the last three ones( $\diamond$ ) were obtained with a thinner filament of 0.5 mm. A wider technological description and the structural properties of these samples can be found elsewhere[Peiró, 1999].

| Filament temp. ( $^{\circ}\text{C}$ ) | $\text{SiH}_4 / \text{H}_2$ flows (sccm) | Pressure (mbar)     | Substrate temp. ( $^{\circ}\text{C}$ ) | Deposition rate ( $\text{\AA}/\text{s}$ ) | Activation energy (eV) | Prefactor ( $\Omega^{-1}\text{cm}^{-1}$ ) | SSPC $\mu\tau$ ( $\text{cm}^2/\text{V}$ ) |
|---------------------------------------|--|---------------------|--|---|------------------------|---|---|
| 1650                                  | 2 / 18                                   | $7 \cdot 10^{-3}$   | 200                                    | 2.9                                       | 0.49                   | 405                                       | $1.3 \cdot 10^{-9}$                       |
| 1650                                  | 2 / 18                                   | $7 \cdot 10^{-3}$   | 200                                    | 3.2                                       | 0.53                   | 443                                       | $5.4 \cdot 10^{-7}$                       |
| 1600                                  | 2 / 18                                   | $10^{-2}$           | 225                                    | 3.4                                       | 0.54                   | 3223                                      | $1.1 \cdot 10^{-7}$                       |
| 1600                                  | 2 / 18                                   | $10^{-2}$           | 250                                    | 4.6                                       | 0.59                   | 9674                                      | $7.6 \cdot 10^{-6}$                       |
| 1700                                  | 2 / 0                                    | $1.5 \cdot 10^{-2}$ | 200                                    | 4.8                                       | 0.54                   | 2564                                      | $6.4 \cdot 10^{-8}$                       |
| 1600                                  | 2 / 18                                   | $10^{-2}$           | 200                                    | 7.5                                       | 0.58                   | 7014                                      | $9.2 \cdot 10^{-6}$                       |
| 1750                                  | 2 / 18                                   | $7 \cdot 10^{-3}$   | 200                                    | 2.0                                       | 0.45                   | 39.4                                      | $9.2 \cdot 10^{-7}$                       |
| 1750                                  | 2 / 18                                   | $7 \cdot 10^{-3}$   | 250                                    | 2.3                                       | 0.45                   | 54.7                                      | $2.4 \cdot 10^{-6}$                       |
| 1750                                  | 2 / 2                                    | $10^{-2}$           | 200                                    | 2.3                                       | 0.51                   | 681                                       | $2.1 \cdot 10^{-7}$                       |
| 1750                                  | 2 / 0                                    | $10^{-2}$           | 200                                    | 2.9                                       | 0.54                   | 1753                                      | $2.7 \cdot 10^{-7}$                       |
| 1750                                  | 2 / 18                                   | $1.5 \cdot 10^{-2}$ | 200                                    | 5.7                                       | 0.55                   | 5448                                      | $10^{-7}$                                 |
| 1750                                  | 2 / 6                                    | $10^{-2}$           | 200                                    | 6.2                                       | 0.58                   | 12843                                     | $4.8 \cdot 10^{-6}$                       |
| 1750                                  | 1 / 19                                   | $7 \cdot 10^{-3}$   | 200                                    | 1.2                                       | 0.44                   | 85.7                                      | $2.1 \cdot 10^{-6}$                       |
| 1750                                  | 4 / 76                                   | $10^{-2}$           | 200                                    | 2.8                                       | 0.50                   | 286                                       | $1.0 \cdot 10^{-6}$                       |
| 1750                                  | 4 / 76                                   | $3.5 \cdot 10^{-2}$ | 200                                    | 8.8                                       | 0.56                   | 839                                       | $2.3 \cdot 10^{-7}$                       |

We have obtained  $E_{MN}=0.029$  eV and  $\sigma_{o0}=1.4 \cdot 10^{-5} \Omega^{-1} \text{cm}^{-1}$  for several series of nc-Si:H HWCVD samples obtained under varied deposition conditions[Table 3.4]. This result agrees with reported values for similar samples[Meiling et al., 1999]. Though the correction that the thermal dependence of the band gap introduces in the prefactor predicts this kind of behaviour[Eq. 3.24], a much weaker dependence would be expected. Hence, there must be additional contributions affecting the conductivity prefactor. The thermal dependence of transport mechanisms involving localised states or the statistical shift of the Fermi-level have been proposed to explain the Meyer-Neldel rule[Wang et al., 1988]. Previous results indicate that it makes no sense to calculate carrier mobilities or effective densities of states from the dark conductivity prefactor by using equation 3.20. Besides, the measured activation energy should not be necessarily the exact distance between the Fermi-level and the band which mainly contributes to the electronic transport. Nevertheless, as long as samples of similar crystallinity and microstructure are compared, higher activation energies should, in principle, point to a more intrinsic character.

### 3.2.2. Evidences of contaminants incorporation

A problem often encountered with as grown undoped nc-Si:H is its generally pronounced n-type character. It has been suggested that either a large content of oxygen impurities or native defects within the layers could be responsible for this unwanted Fermi-level shift [Lucovsky et al., 1993]. The group at University of Neuchâtel showed that the n-type behaviour of their VHF-PECVD layers was mainly linked to oxygen impurities acting as unwanted donor levels in the gap [Torres et al., 1996]. Depending on the deposition conditions, our undoped nc-Si:H samples obtained by HWCVD also present activation energies far from the midgap condition [Voz et al., 2000]. Besides, the thermopower of these samples evidences a certain as grown n-type character. In addition, several shallow donor levels ( $E_C - E_D \leq 0.14 \text{ eV}$ ) which could be attributed to oxygen were resolved by Deep Level Transient Spectroscopy (DLTS) in our samples [Stöger et al., 1999]. Low p-type doping levels (solid phase B/Si ratio  $\sim 10^{-4}$ ) lead to higher activation energies as well as lower room temperature dark conductivities [Fig. 3.18]. This result could be explained by the compensation of donor levels related to the incorporation of contaminants [Voz et al., 2000]. Similar results have been reported for similar boron concentrations in HWCVD samples [Wanka et al., 1995]. By contrast, in the case of nc-Si:H obtained by VHF-PECVD, compensation was achieved at much lower concentrations (B/Si  $\sim 10^{-6}$ ) [Flückiger, 1995]. Actually, several studies point to a higher incorporation of contaminants in HWCVD nc-Si:H samples when they are compared to VHF-PECVD material [Schubert et al., 1998]. Though the eventual incorporation of metallic components from the wire could explain this result, a higher incorporation of residual gas phase contaminants (oxygen, carbon...) was also detected. This difference was found even with the same ultra-high vacuum specifications and feedgas purity. There are some differences between HWCVD and PECVD related processes which could explain this result. Much more atomic hydrogen is generated at the hot wire than in a glow discharge. Thus, chemical reduction of the highly oxidised silicon on the walls of the chamber could increase the outgassing rate. This would lead to a higher incorporation of contaminants. Actually, we have certainly observed a clearly increased outgassing rate from the walls of the chamber after any HWCVD process. Furthermore, we have observed that nc-Si:H samples by HWCVD oxidise much faster

under illumination than in the dark. Hence, this photooxidation enhancement could also take place in situ during growth due to the very intense radiation from the wire.

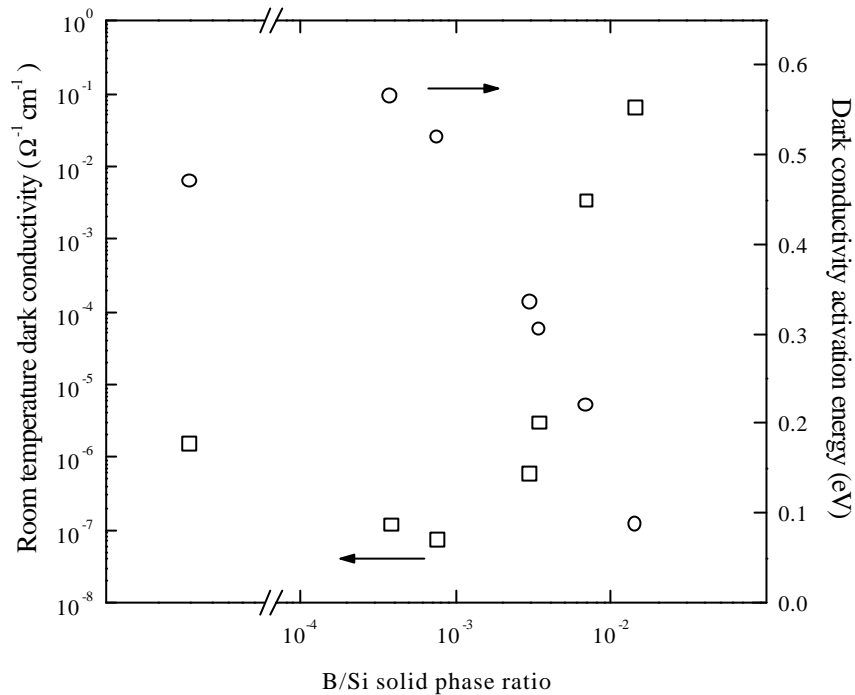


**Figure 3.18:** Room temperature dark conductivity and corresponding activation energies for a p-doping series of samples [Table 3.5]. An increase in the activation energy as well as a lower room temperature dark conductivity is observed for low p-doping levels.

**Table 3.5:** Technological parameters, room temperature dark conductivity and thermal activation energy for the p-doping series in figure 3.18. The B/Si solid phase ratio was calculated by comparing the SIMS profiles of these samples with those of patterns (implanted wafers). All the samples were obtained with a process pressure of  $7 \cdot 10^{-3}$  mbar whereas the substrate temperature was around 200 °C and the filament was heated above 1700 °C.

| SiH <sub>4</sub> / H <sub>2</sub><br>flows (sccm) | B / Si<br>(gas phase) | B / Si<br>(solid phase) | Dark conductivity<br>(Ω <sup>-1</sup> cm <sup>-1</sup> ) | Activation energy<br>(eV) |
|---|-----------------------|-------------------------|--|---------------------------|
| 2 / 18  | -                     | -                       | $1.6 \cdot 10^{-6}$                                      | 0.47                      |
| 2 / 18  | $4 \cdot 10^{-5}$     | $3.8 \cdot 10^{-4}$     | $7.5 \cdot 10^{-8}$                                      | 0.52                      |
| 2 / 18  | $1.6 \cdot 10^{-4}$   | $7.6 \cdot 10^{-4}$     | $1.2 \cdot 10^{-7}$                                      | 0.57                      |
| 2 / 18  | $4 \cdot 10^{-4}$     | $3.0 \cdot 10^{-3}$     | $3.1 \cdot 10^{-6}$                                      | 0.31                      |
| 2 / 18  | $1.6 \cdot 10^{-3}$   | $3.5 \cdot 10^{-3}$     | $5.9 \cdot 10^{-7}$                                      | 0.34                      |
| 2 / 18  | $4 \cdot 10^{-3}$     | $6.9 \cdot 10^{-3}$     | $3.4 \cdot 10^{-3}$                                      | 0.22                      |
| 2 / 18  | $1.6 \cdot 10^{-2}$   | $1.4 \cdot 10^{-2}$     | $6.3 \cdot 10^{-2}$                                      | 0.09                      |

### 3.2.3. Dependence on the deposition rate

Either coming from the wire or degassed from the walls of the chamber, we can assume that there is a determined flow of contaminants per second and unit area arriving to the surface where the film grows. In this case, the concentration of contaminants incorporated into the film is expected to be proportional to  $1/r_d$ [Kroll et al., 1995], where  $r_d$  is the deposition rate. Hence, a faster deposition rate results in a lower incorporation of contaminants. This reasoning strengthens when the activation energies of undoped samples obtained at increasing deposition rates[Table 3.4] are compared in figure 3.19. Faster deposition rates lead to higher dark conductivity activation energies for samples of similar crystalline fractions ( $\geq 90\%$ ) and optical band gaps ( $E_g \approx 1.2$  eV). Though the midgap condition can not be fully asserted, an enhanced intrinsic character for the samples obtained at high deposition rates is expected.

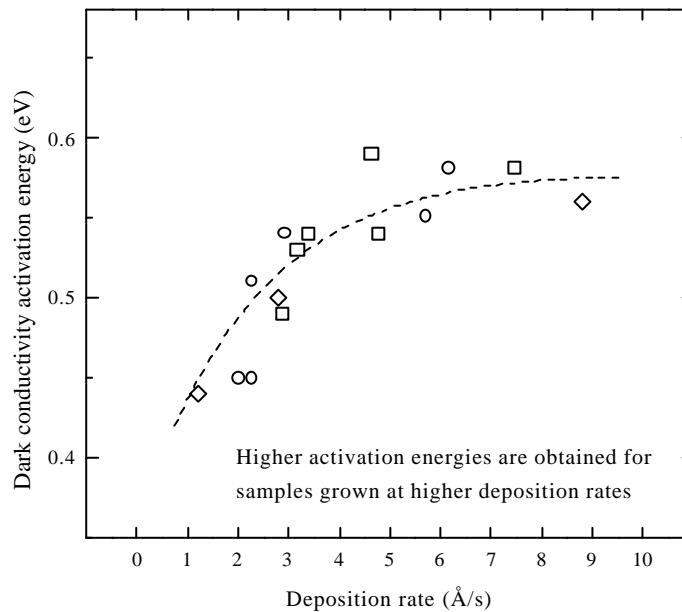


**Figure 3.19:** Effect of the deposition rate on the intrinsic character of undoped nc-Si:H samples[Table 3.4]. The dark conductivity activation energy increases with the deposition rate.

### 3.2.4. Effective density of localised states

A high internal electric field is essential for the drift-assisted collection in p-i-n structures of low mobility semiconductors. This is definitely the case in nc-Si:H p-i-n solar cells. The screening length of the internal electric field is determined by the charge density in the active layer. This charge is mainly trapped at localised states in the band gap with densities very much larger than the free carrier densities. These localised states can be attributed to dangling bonds at the grain boundaries and other levels in the band gap related to contaminants. Its reduction in the active layer of the solar cell would certainly enhance the drift collection of photogenerated carries. In order to quantify somehow this effective charged trap density, we studied the voltage dependence of the depletion capacitance of several rectifying contacts. In the case of undoped but unintentionally contaminated nc-Si:H with a relatively pronounced n-type character ( $E_a < 0.5$  eV), ZnO:Al provides good pseudo-Schottky contacts. For cleaner undoped nc-Si:H samples ( $E_a \geq 0.5$  eV), it was necessary a heavily p-doped nc-Si:H layer to obtain acceptable rectifying characteristics [Fig. 3.20]. Nevertheless, the deduced Schottky barrier was quite similar in any case.

**Table 3.6:** Undoped nc-Si:H layers deposited by HWCVD on p+ nc-Si:H (A,B) and ZnO:Al (C) in order to perform the depletion capacitance-reverse voltage experiment. Higher deposition rates  $r_d$  were obtained by increasing the process pressure and gas flows. The effect of the filament temperature  $T_f$  is also studied by comparing the A and B contacts each other. The density of charged centres  $N_C$  and the width of the depletion region without any external voltage applied  $w_o$  are indicated for each contact.

| Name                   | Process pressure<br>(mbar) | SiH <sub>4</sub> /H <sub>2</sub> flows<br>(sccm) | $T_f$<br>(°C) | $r_d$<br>(Å/s) | $N_C$<br>(cm <sup>-3</sup> ) | $w_o$<br>(nm) |
|------------------------|----------------------------|--|---------------|----------------|------------------------------|---------------|
| A (↑ $r_d$ , ↓ $T_f$ ) | 10 <sup>1</sup>            | 4/76   | 1600          | 11.3           | 2.2×10 <sup>16</sup>         | 160           |
| B (↑ $r_d$ , ↑ $T_f$ ) | 10 <sup>1</sup>            | 4/76   | 1800          | 11.8           | 6.0×10 <sup>16</sup>         | 108           |
| C (↓ $r_d$ , ↓ $T_f$ ) | 7×10 <sup>-3</sup>         | 1/19   | 1600          | 2.2            | 2.9×10 <sup>17</sup>         | 42            |

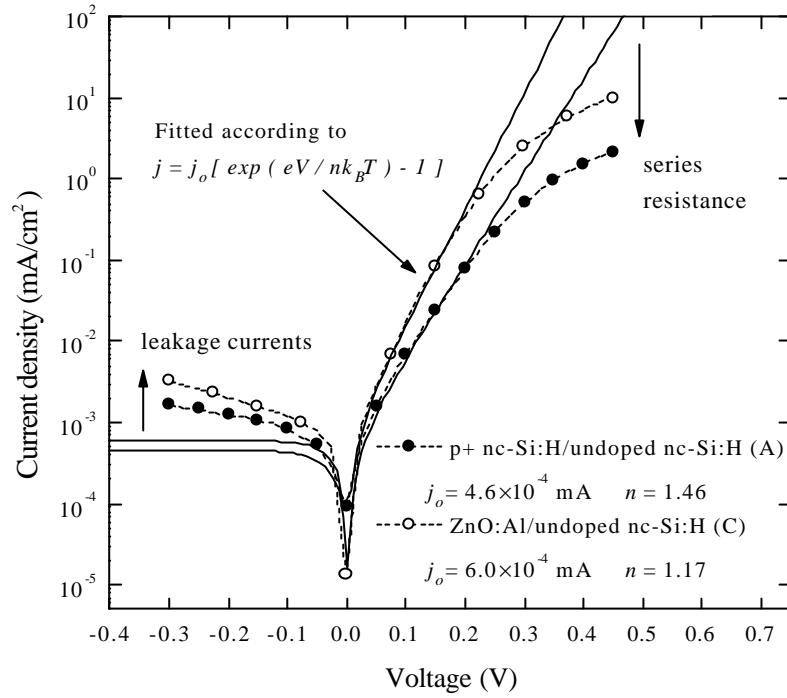


**Figure 3.20:** Current density-voltage characteristics for both types of studied pseudo-Schottky contacts. Slight differences in the rectifying behaviours were observed which however do not influence the depletion capacitance-voltage experiment.

Table 3.6 shows three selected rectifying structures representative for the overall trend. Actually, we study the effect of the deposition rate and the filament temperature on the density of charged centres in undoped nc-Si:H samples. The motivation was the clearly enhanced photovoltaic performance that we observed in p-i-n structures whose active layers were grown faster or with lower filament temperatures[Voz et al., 2000c]. The values of  $N_C$  and  $V_d$  were obtained from a linear fit in the  $I/C^2$ - $V$  plot[Figure 3.21] according to equation 2.24. These results are valid within the one-sided abrupt junction approximation for uniform space charge profiles[Section 2.3.3]. The widths of the depletion region without any external voltage applied  $w_0$  can also be calculated from equation 2.21 with  $V_{ext} = 0$ . These values show an excellent agreement with those in table 3.6 obtained directly from equation 2.25, i.e.,  $w_0 = e_s S / C_0$  with  $C_0$  the depletion capacitance for  $V_{ext} = 0$  where neither the values of  $N_C$  nor  $V_d$  are used. This result, together with the nice linear behaviour in figure 3.21, indicates that the assumptions for the experiment to obtain confident results are fulfilled. Actually, the highly doped ZnO:Al or p+ nc-Si:H layers allow the one-sided abrupt junction approximation whereas in the case of a background incorporation of

contaminants a uniform impurity profile is certainly expected. The sample A deposited at a fast deposition rate of  $11.3 \text{ \AA/s}$  showed a density of charged centres of  $2.2 \times 10^{16} \text{ cm}^{-3}$ . For a lower deposition rate of only  $2.2 \text{ \AA/s}$  we obtained a density of charged centres as high as  $2.9 \times 10^{17} \text{ cm}^{-3}$ , more than one order of magnitude higher. Therefore, as previously pointed in section 3.2.3, an increase in the deposition rate leads to a lower incorporation of contaminants. On the other hand, by comparing the A to the B contact, both grown at fast deposition rates, we observe that a higher filament temperature also results in a higher density of charged centres. This last result points to the eventual incorporation of metallic impurities evaporated from the filament or its holder. The subgap optical absorption of these samples, measured by PDS, did not correlate with the calculated values of  $N_C$ . Furthermore, according to reported calibrations with electron-spin resonance measurements [Jackson et al., 1983], the density of dangling bonds was lower than  $10^{16} \text{ cm}^{-3}$  for all the layers. Therefore, calculated densities of charged centres significantly higher than  $10^{16} \text{ cm}^{-3}$  must be due to states not resolvable by subgap optical absorption due to its shallow position in the band gap. We can attribute the origin of these levels to the undesired incorporation of contaminants.

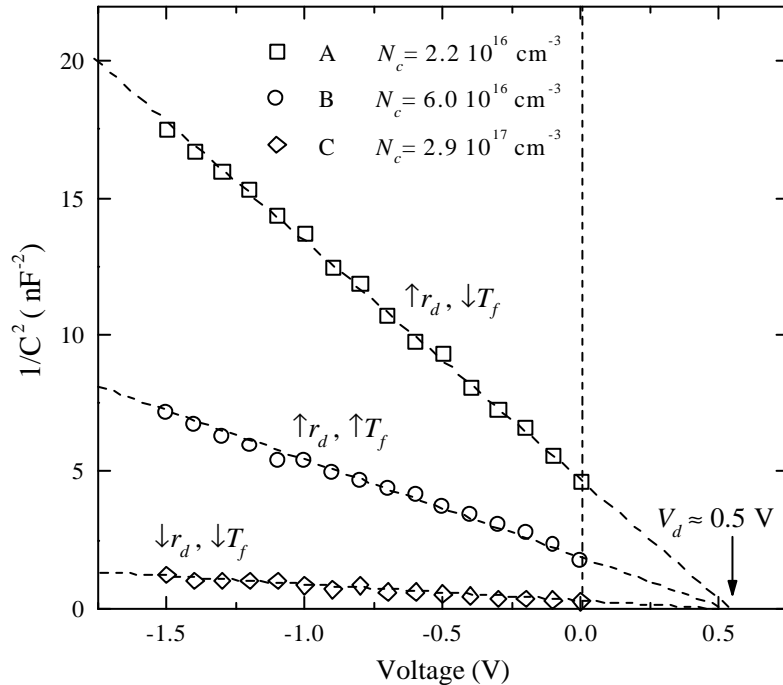


**Figure 3.21:** Determination of the concentration of charged centres from the voltage dependence of the depletion capacitance for the pseudo-Schottky contacts in table 3.6.

### 3.2.5. Anticorrelation between photoconductivity and layer quality

At one time, a misleading increase in the SSPC  $\mu\tau$ -product is observed for the less intrinsic samples [Fig. 3.22]. This effect is not due to better transport properties but to a change in the thermal occupation of recombination centres which results in a longer lifetime for the majority carriers [Brüggemann et al., 1998]. The lifetime of minority carriers, which in fact is what it matters for collection in photovoltaic devices, results undoubtedly degrade in the less intrinsic samples. Actually, samples with higher SSPC  $\mu\tau$ -products yield poorer conversion efficiencies when they are incorporated as the active layer in p-i-n structures [Voz et al., 2000c]. This effect, which was already observed in amorphous silicon solar cells [Isomura et al., 1994], turns out to be more detrimental in nanocrystalline silicon devices.

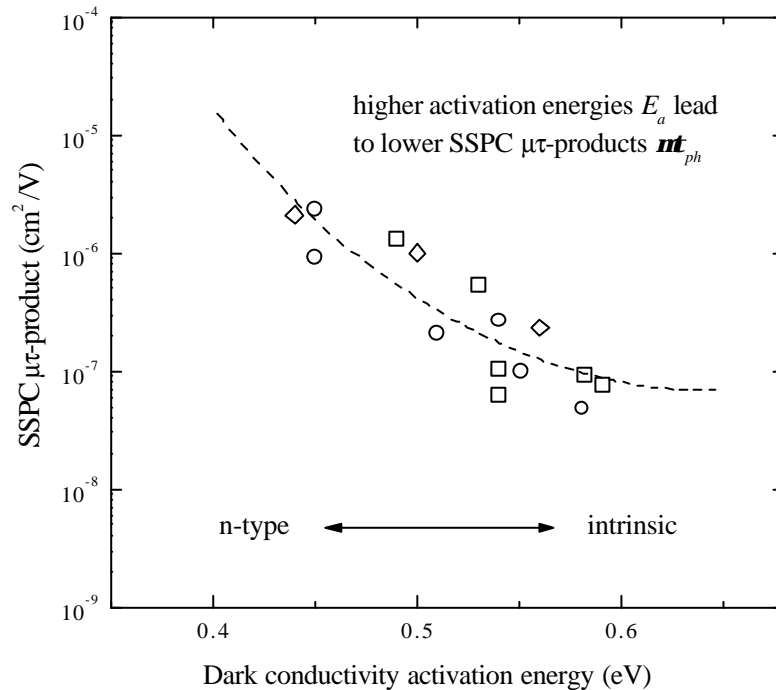


**Figure 3.22:** Steady state photoconductivity  $\mu\tau$ -product as a function of the dark conductivity activation energy for several series of undoped nc-Si:H samples [Table 3.4]. The values of  $\mu\tau_{ph}$  are those obtained for a mean generation rate of  $10^{19} \text{ cm}^{-3} \text{ s}^{-1}$  [Section 2.2.2]. A misleading increase in  $\mu\tau_{ph}$  is observed for the less intrinsic samples.

If we consider that the mechanism which mainly determines the recombination of photogenerated carriers is the simultaneous capture of electrons and holes by the amphoteric distribution of dangling bonds[Goerlitzer et al., 2000], then the recombination rate  $R$  is given by

$$R = v_{th} (n\mathbf{s}_n^o + p\mathbf{s}_p^o) \frac{N_{db}}{1 + \frac{p\mathbf{s}_p^o}{n\mathbf{s}_n^+} + \frac{n\mathbf{s}_n^o}{p\mathbf{s}_p^-}} \quad (3.27)$$

with  $v_{th}$  the carrier thermal velocity ( $\approx 10^7$  cm/s),  $N_{db}$  the density of dangling bonds and the capture cross-sections of electrons and holes by dangling bonds in their three possible states of charge (+/o/-) defined in table 3.7[Beck, 1996b]. The band tails or other shallow levels in the band gap due to contaminants, lying outside the quasi Fermi-levels, will act as carrier traps but not as recombination centres[Rose, 1963]. The recombination rate [Eq. 3.27] takes into account the occupation state of the dangling bond[Fig. 3.23] depending on the electron and hole densities[Eq. 3.28]

$$F^+ = \frac{\frac{p\mathbf{s}_p^o}{n\mathbf{s}_n^+}}{1 + \frac{p\mathbf{s}_p^o}{n\mathbf{s}_n^+} + \frac{n\mathbf{s}_n^o}{p\mathbf{s}_p^-}} \quad F^o = \frac{1}{1 + \frac{p\mathbf{s}_p^o}{n\mathbf{s}_n^+} + \frac{n\mathbf{s}_n^o}{p\mathbf{s}_p^-}} \quad F^- = \frac{\frac{n\mathbf{s}_n^o}{p\mathbf{s}_p^-}}{1 + \frac{p\mathbf{s}_p^o}{n\mathbf{s}_n^+} + \frac{n\mathbf{s}_n^o}{p\mathbf{s}_p^-}} \quad (3.28)$$

**Table 3.7:** Capture cross-sections of electrons and holes by dangling bonds in their three possible states of charge. Corresponding capture times as a function of the dangling bond density  $N_{db}$ .

|  |                                   |
|--|-----------------------------------|
| Capture cross-section of electrons by neutral dangling bonds $\mathbf{s}_n^o$  | $10^{-15} \text{ cm}^2$           |
| Capture cross-section of holes by neutral dangling bonds $\mathbf{s}_p^o$      | $\mathbf{s}_n^o / 3$              |
| Capture cross-section of electrons by positive dangling bonds $\mathbf{s}_n^+$ | $\mathbf{s}_n^o \times 50$        |
| Capture cross-section of holes by negative dangling bonds $\mathbf{s}_p^-$     | $\mathbf{s}_p^o \times 50$        |
| Capture time of electrons by neutral dangling bonds $\mathbf{t}_n^o$           | $1/(v_{th}\mathbf{s}_n^o N_{db})$ |
| Capture time of holes by neutral dangling bonds $\mathbf{t}_p^o$               | $1/(v_{th}\mathbf{s}_p^o N_{db})$ |
| Capture time of electrons by positive dangling bonds $\mathbf{t}_n^+$          | $1/(v_{th}\mathbf{s}_n^+ N_{db})$ |
| Capture time of holes by negative dangling bonds $\mathbf{t}_p^-$              | $1/(v_{th}\mathbf{s}_p^- N_{db})$ |

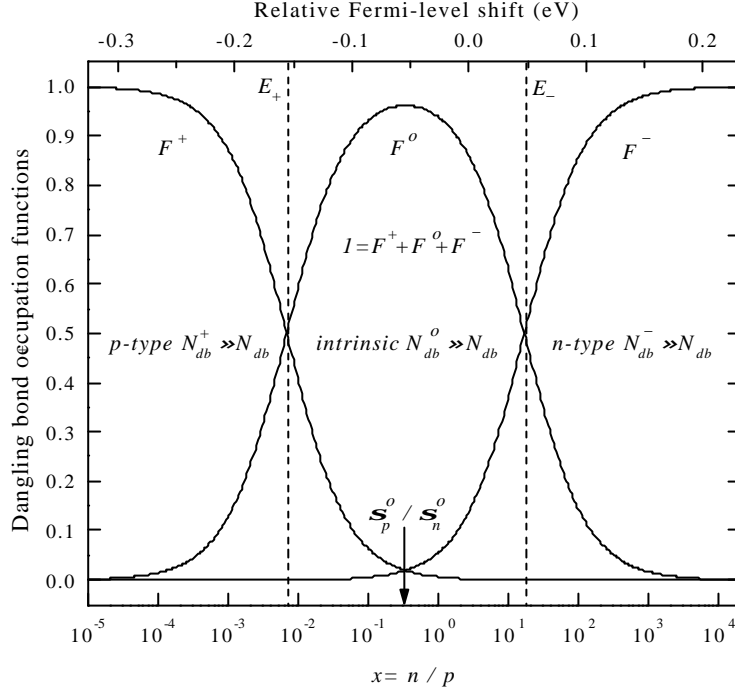


**Figure 3.23:** Calculated occupation functions of the dangling bond[Eq. 3.28] depending on the electron to hole densities ratio (bottom axis) or the relative Fermi-level shift from midgap(top axis). The slight dissymmetry is due to the factor 3 between the capture cross-sections of electrons and holes by neutral dangling bonds[Table 3.7].

In equations 3.27-3.28 and in the following ones, we consider that sample is under an illumination level high enough to overlook the electron and hole densities in equilibrium and the thermal reemission rates, i.e.,  $Dn \gg n$  and  $Dp \gg p$ . The irradiances used for the SSPC experiment fulfil this condition in the case of undoped samples. Since  $\tau_p^o = 3\tau_n^o$ , for practical purposes we define an effective lifetime  $\tau_{eff}$  given by

$$\tau_{eff} = 3\tau_n^o/2 = \tau_p^o/2 \quad (3.29)$$

which introduced in equation 3.27 leads to

$$R = \left( \frac{3}{2} \frac{n}{\tau_{eff}} + \frac{1}{2} \frac{p}{\tau_{eff}} \right) \frac{1}{1 + \frac{1}{50} \left( \frac{1}{3} \frac{p}{n} + 3 \frac{n}{p} \right)} \quad (3.30)$$

Since recombination equals the generation rate in steady state conditions, the lifetimes of electrons and holes can be calculated from  $R = G = n/\tau_n = p/\tau_p$  arriving at

$$\tau_n = \tau_{eff} \frac{2x}{3x+1} \left[ 1 + \frac{1}{50} \left( \frac{1}{3x} + 3x \right) \right] \quad (3.31a)$$

$$\tau_p = \tau_{eff} \frac{2}{3x+1} \left[ 1 + \frac{1}{50} \left( \frac{1}{3x} + 3x \right) \right] \quad (3.31b)$$

where  $x=n/p$  is the ratio of the electron to hole densities. Depending on the character of the samples, equation 3.31 can be further simplified.

a) n-type samples,  $x \gg 1$

$$\tau_n \approx x \frac{2\tau_{eff}}{50} = x \frac{\tau_p^o}{50} = x\tau_p^- \quad \tau_p \approx \frac{2\tau_{eff}}{50} = \frac{\tau_p^o}{50} = \tau_p^- \quad (3.32a)$$

$$R \approx \frac{p}{\tau_p^-} \quad (3.32b)$$

b) p-type samples,  $x \ll 1$

$$\tau_n \approx \frac{2\tau_{eff}/3}{50} = \frac{\tau_n^o}{50} = \tau_n^+ \quad \tau_p \approx \frac{2\tau_{eff}/3}{50x} = \frac{\tau_n^o}{50x} = \frac{\tau_n^+}{x} \quad (3.33a)$$

$$R \approx \frac{n}{\tau_n^+} \quad (3.33b)$$

c) midgap samples,  $x \gg 1$

$$\tau_n \approx \tau_p \approx \frac{\tau_{eff}}{2} \quad (3.34a)$$

$$R \approx \frac{n}{\tau_n^o} + \frac{p}{\tau_p^o} \quad (3.34b)$$

As expected, in n-type and p-type samples the recombination rate is determined by the very much shorter capture time of the minority carrier by the charged dangling bonds. In the case of midgap samples, the recombination rate is simultaneously given by the capture

times of both carriers by neutral dangling bonds. In fact, by SSPC we have only access to  $\mathbf{nt}_{ph} = \mathbf{m}_n \mathbf{t}_n + \mathbf{m}_p \mathbf{t}_p$  which depending on the character of the samples can be approximated by

$$n\text{-type} \Rightarrow x \gg 1 \Rightarrow \mathbf{t}_n \gg \mathbf{t}_p \Rightarrow \mathbf{nt}_{ph} \approx \mathbf{m}_n \mathbf{t}_n \approx x \mathbf{m}_p \mathbf{t}_p^- \quad (3.35a)$$

$$p\text{-type} \Rightarrow x \ll 1 \Rightarrow \mathbf{t}_n \ll \mathbf{t}_p \Rightarrow \mathbf{nt}_{ph} \approx \mathbf{m}_p \mathbf{t}_p \approx \frac{\mathbf{m}_n \mathbf{t}_n^+}{x} \quad (3.35b)$$

$$\text{midgap} \Rightarrow x \approx 1 \Rightarrow \mathbf{t}_n \approx \mathbf{t}_p \approx \mathbf{t}_{eff} / 2 \Rightarrow \mathbf{nt}_{ph} \approx \frac{\mathbf{m}_n + \mathbf{m}_p}{2} \mathbf{t}_{eff} \quad (3.35c)$$

Whereas either in n- or p-type samples the SSPC  $\mu\tau$ -product strongly depends on position of the Fermi-level, only in midgap samples it directly correlates with the electronic transport quality of the material. The carrier mobilities in nc-Si:H measured by Hall effect [Ruff et al., 1998] are in the order of a few  $\text{cm}^2/\text{Vs}$ . However, these values are uncertain, since they could strongly depend on the microstructure of the samples. For the calculation in figure 3.24, we have chosen  $\mathbf{m}_n = 10 \text{ cm}^2/\text{Vs}$ ,  $\mathbf{m}_p = 3 \text{ cm}^2/\text{Vs}$  and  $N_{db} = 10^{16} \text{ cm}^{-3}$  which leads to  $\mathbf{nt}_{ph} = 10^{-7} \text{ cm}^2/\text{V}$  for midgap samples. We observe that a Fermi-level shift from midgap results in a longer lifetime for the carrier which becomes majority whereas the lifetime of the minority carrier results clearly reduced. Since the different carrier mobilities introduce dissymmetries with respect to positive (n-type) or negative (p-type) Fermi-level shifts, the parameter  $b = \mathbf{m}_n n / \mathbf{m}_p p$  [Shah et al., 1997] is also used for the plot. Note that, on account of  $\mathbf{m}_n > \mathbf{m}_p$ , electrons and holes equally contribute to the electronic transport ( $b=1$ ) for slight negative Fermi-level shifts. Though many parameters used for this calculation are not well-established, the overall trend in  $\mathbf{nt}_{ph}$  shows not only qualitative but even quantitative agreement with the experimental values shown in figure 3.22. A Fermi-level shift of around 0.15 eV towards the conduction band results in  $\mathbf{nt}_{ph}$  values an order of magnitude higher.

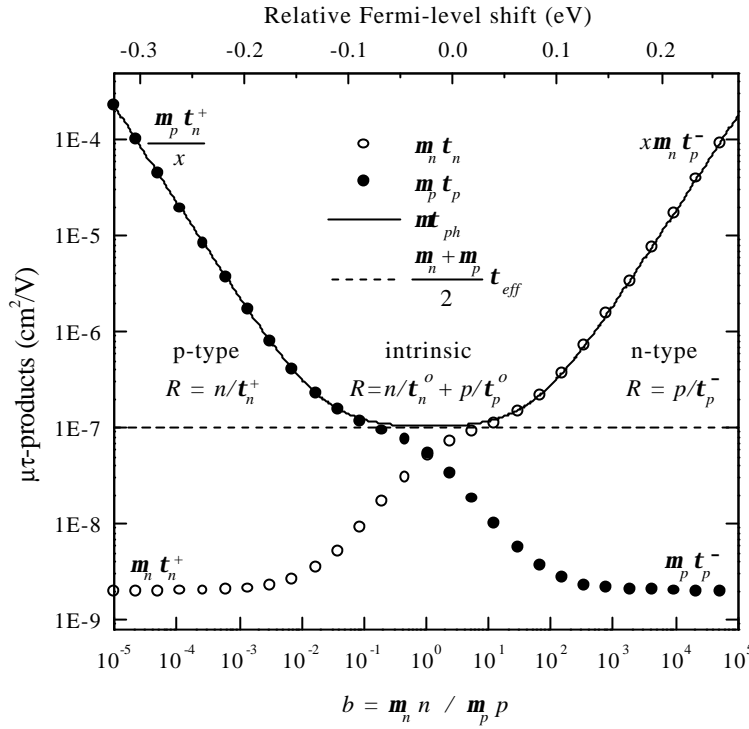


**Figure 3.24:** Different  $\mu\tau$ -products as a function of the parameter  $b$  (bottom axis) or the relative shift of the Fermi-level from midgap (top axis). For the calculation we have used  $m_n=10 \text{ cm}^2/\text{Vs}$ ,  $m_p=3 \text{ cm}^2/\text{Vs}$  and  $N_{db}=10^{16} \text{ cm}^{-3}$  which leads to  $m_n t_n^o = 10^7 \text{ cm}^2/\text{V}$  for midgap samples.

The previous discussion shows that the SSPC  $\mu\tau$ -product alone does not allow to discern the suitability of the material to be incorporated as the active layer in p-i-n structures. Furthermore, materials with higher  $m_n t_n^o$  usually result in poorer photovoltaic performances [Voz et al., 2000c] due to the degraded minority carrier  $\mu\tau$ -product. The group at the Institute de Microtechnique successfully combines the SSPC  $\mu\tau$ -product with the ambipolar diffusion length  $L_{amb}$  [Sauvain, 1992] to discern the intrinsic electronic transport quality of their samples, the so-called true  $\mu\tau$ -product  $m_n t_n^o$ . Moreover, this last parameter correlates with the conversion efficiency of their amorphous [Beck et al., 1996b] and nanocrystalline p-i-n solar cells [Goerlitzer et al., 2000]. Actually,  $m_n t_n^o$  is the SSPC  $\mu\tau$ -product that we would measure in midgap samples [Eq. 3.35c] which is not usually the real case.

$$m_n t_n^o = \frac{m_n + m_p}{2} t_{eff} \quad (3.36)$$

### 3.2.6. Chemical stability

We have not observed any degradation effect under light soaking attributable to an increase in the defect density of nc-Si:H samples obtained by HWCVD. For instance, the subgap optical absorption does not evidence any significant increase after light soaking. By contrast, the steady state photoconductivity steadily grows in samples kept under high irradiances for a long time[Fig. 3.25].

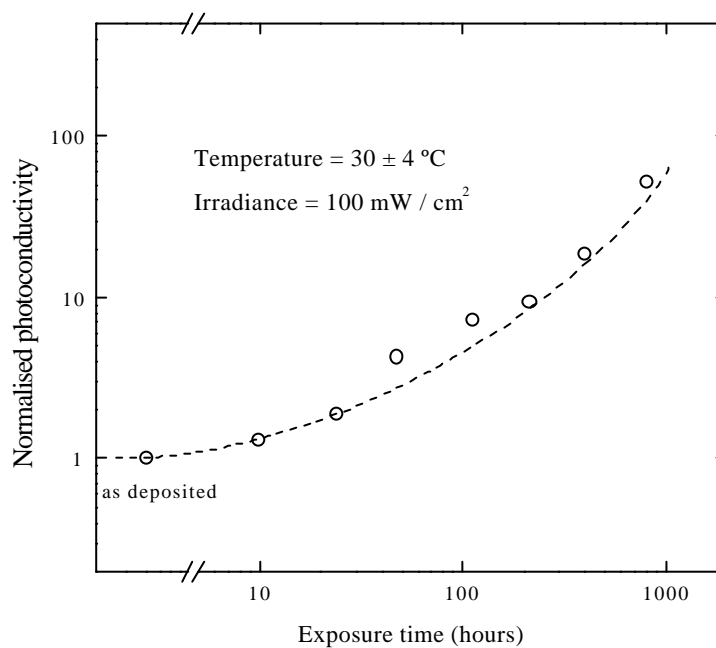


**Figure 3.25:** An steady increase is observed in the photoconductivity of samples kept under high irradiances for a long time. The light soaking experiment was performed with  $100\text{mW}/\text{cm}^2$  of white light. Hence, the Staebler-Wronski effect does not play an important role in the stability of nc-Si:H.

These results indicate that fortunately the Staebler-Wronski effect does not play an important role in the stability of nc-Si:H. However, a significant post-oxidation leading to an increased n-type character seems to be the reason of such misleading photoconductivity enhancement. Actually, oxidation through the surface of nc-Si:H samples starts as soon as films are exposed to air[Veprek et al., 1983]. This effect leads to an increasing dark conductivity[Fig. 3.26] as the undoped sample becomes n-type on account of the donor character of oxygen levels in silicon. Besides, this post-oxidation is somehow accelerated

under high irradiances when photons are able to break weak bonds thus favouring oxidation[Fig. 3.27]. This relative chemical instability is a general feature of most (if not all) nc-Si:H samples independently of the deposition technique[Goerlitzer et al., 1998].

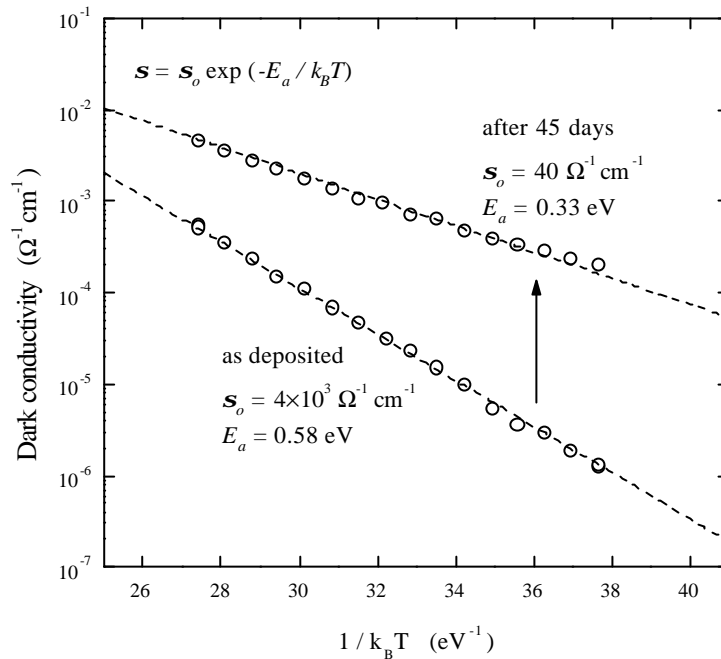


**Figure 3.26:** Change in the dark conductivity and activation energy of a nc-Si:H sample obtained by HWCVD due to post-oxidation in air. A pronounced n-type character is observed after 45 days.

We will show in the next chapter that the intrinsic character of the undoped active layer in p-i-n structures is fundamental for successful photovoltaic conversion. Hence, the fearful question which arises after evidencing this chemical instability is whether it bears the risk of complete deterioration of nc-Si:H solar cells. Actually, this post-oxidation effect which causes a serious problem for the characterisation of layers, could not be so dramatic in devices where the active layer is sealed off by the doped and contact layers. Long-term stable nc-Si:H p-i-n solar cells have been reported by VHF-PECVD[Meier et al., 1998b]. These devices incorporated a TCO/Ag back contact that could act as a capping layer apart from enhancing light trapping.

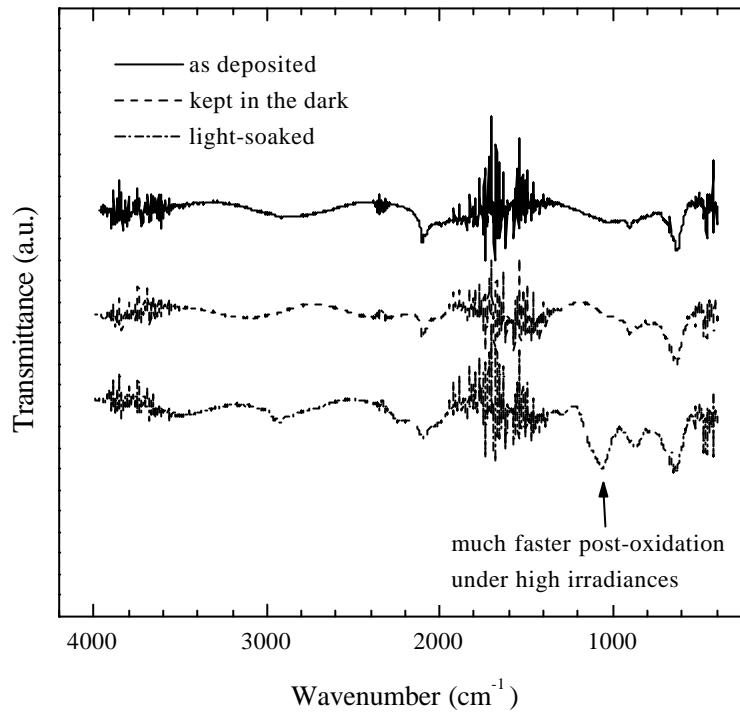


**Figure 3.27:** Infrared transmittance spectra for two pieces of the same sample 24 hours after deposition either kept in the dark or light-soaked under  $100\text{mW}/\text{cm}^2$  of white light. The as deposited transmittance is also shown for comparison. The pronounced overlapped bands at  $1050$  and  $1140\text{cm}^{-1}$  corresponding to Si-O-Si stretching modes indicate a faster post-oxidation in the light soaked piece.

# Chapter 4

## Physical aspects in thin film p-i-n solar cells

The fundamental understanding of the device performance will be discussed in this chapter. An extended equivalent circuit and analytical model used in the literature to study thin film p-i-n structures is briefly described. An improved model which treats analytically the more general case including a non constant electric field is presented.

### 4.1. Motivation of p-i-n structures

Although nc-Si:H silicon presents slightly better transport properties than a-Si:H, it must be considered a low mobility semiconductor. The best values of diffusion length reported up to now by leading groups in the research of nc-Si:H do not exceed 400 nm [Goerlitzer et al., 1998]. Therefore, diffusion alone is definitely not enough as transport mechanism for satisfactory collection efficiencies. In order that the major part of generated free carriers do not recombine within the device, it is imperative to have drift assisted transport based on an internal electric field extending the active layer of the device [Shah et al., 1995]. This is the reason why p-i-n structures are preferred in contrast to the classical p-n diode used in virtually all crystalline solar cells so far. The diffusion length can quite generally be written as

$$L_{diff} = \sqrt{D\tau} = \sqrt{\frac{k_B T}{e} \mu \tau} \quad (4.1)$$

whereas the drift length is also quite generally given by

$$L_{drift} = \mu \tau E \approx \mu \tau \frac{V_{bi}}{d} \quad (4.2)$$

and from these last equations it is easy to arrive at

$$\frac{L_{drift}}{L_{diff}} = \left( \frac{V_{bi}}{k_B T / e} \right) \frac{L_{diff}}{d} \approx 40 \frac{L_{diff}}{d} \quad (4.3)$$

This expression means that, for example, if the diffusion length is only a half of the active layer thickness, the drift length would be ten times greater than it. Thus, a material whose properties hardly allow collection by diffusion can perfectly be suitable for drift assisted devices. Actually, the internal electric field is partially screened by trapped charge in the active layer. Hence, in order to enhance the photovoltaic conversion, it is essential to minimise the density of dangling bonds and the incorporation of contaminants in the active layer.

## 4.2. Equivalent circuit for low mobility thin film solar cells

### 4.2.1. The recombination term

Equivalent circuits are often used to describe the electrical behaviour of electronic devices [Sze, 1985]. A simplistic view of a solar cell would be a diode plus a current source connected in parallel which represents the photogenerated current. A parasitic parallel resistance should also be included to correctly describe the device, especially in thin film structures where shunting paths are easily formed. An additional series resistance takes into account the voltage drop in the electrodes and the contact resistance. In most thin film solar cells the series resistance is mainly determined by the sheet resistance of the TCO. Generally speaking, recombination is relatively intense within low mobility a-Si:H and nc-Si:H p-i-n solar cells because of the relatively high density of recombination centres (dangling bonds) in the active layer. It is therefore intuitively reasonable to describe low mobility i-n silicon solar cells by introducing an additional recombination loss term  $j_{rec}$  into the equivalent circuit [Merten, 1996], a term which is symbolised by the current density sink (dashed lines) in figure 4.1.

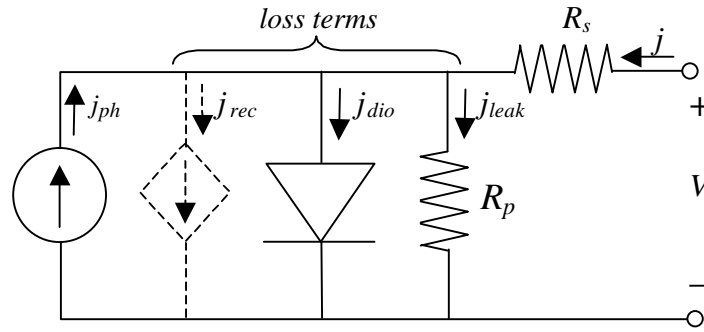


**Figure 4.1:** Equivalent circuit of a photovoltaic device. For low mobility p-i-n structures a recombination term must be added to the typical single exponential model. In order to allow the more reasonable work with current densities,  $R_s$  and  $R_p$  are actually effective series and parallel resistances calculated as the product of the corresponding absolute values  $\mathcal{R}_s$  and  $\mathcal{R}_p$  and the active area of the device  $S$ , i.e.,  $R_s = S\mathcal{R}_s$  and  $R_p = S\mathcal{R}_p$ .

#### 4.2.2. Analytical model

The equivalent circuit shown in figure 4.1 combined with a proper analytical model provides a useful insight in the device, allowing to discern eventual technological problems from more fundamental limiting factors related to the material.

$$j = -j_{ph} + j_{rec} + j_{dio} + j_{leak} \quad (4.4)$$

Note that the voltage applied to the loss components in figure 4.1 (diode, recombination current sink and leakage through the parallel resistance  $R_p$ ) is not just the external voltage applied  $V$  but  $V - R_s j$  which we will call  $V'$ . Hence, the diode current density is given by

$$j_{dio} = j_o \left( e^{\frac{V - R_s j}{nV_T}} - 1 \right) = j_o \left( e^{\frac{V'}{nV_T}} - 1 \right) \quad (4.5)$$

with  $j_o$  the reverse saturation current density of the diode and  $n$  its ideality factor. In the same way, the leakage current density is

$$j_{leak} = \frac{V - R_s j}{R_p} = \frac{V'}{R_p} \quad (4.6)$$

The less known term in equation 4.4 is the recombination current density. However, in a first approximation, recombination losses within the i-layer are proportional to the carrier generation, and thus to the photogenerated current  $j_{ph}$ .

$$j_{rec} = (1 - \chi)j_{ph} \quad (4.7)$$

where  $\chi$  is the collected fraction of the photogenerated current, as previously introduced by several authors [Hubin et al., 1995]. In p-i-n devices with drift assisted collection, the collection efficiency  $\chi$  is expected to depend mainly on the voltage  $V'$

$$\chi = \chi(V') = \chi(V - R_s j) \quad (4.8)$$

apart from the thickness, optical and electrical properties of the active layer. Introducing equation 4.7 in 4.4 we obtain

$$j = -\chi j_{ph} + j_{dio} + j_{leak} \quad (4.9)$$

The derivatives of the loss terms are

$$\frac{dj_{dio}}{dV} = \frac{dj_{dio}}{dV'} \frac{dV'}{dV} = \frac{j_o e^{\frac{V'}{nV_T}}}{nV_T} \frac{dV'}{dV} \quad (4.10a)$$

$$\frac{dj_{leak}}{dV} = \frac{dj_{leak}}{dV'} \frac{dV'}{dV} = \frac{1}{R_p} \frac{dV'}{dV} \quad (4.10b)$$

$$\frac{d\chi}{dV} = \frac{d\chi}{dV'} \frac{dV'}{dV} \quad (4.10c)$$

where

$$V' = V - R_s j \Rightarrow \frac{dV'}{dV} = 1 - R_s \frac{dj}{dV} \quad (4.11)$$

Therefore, by differentiating equation 4.9 and using equation 4.10, we obtain an expression for the dynamic resistance of the device

$$\frac{dV}{dj} = \frac{1}{\frac{dj}{dV}} = R_s + \frac{1}{-\frac{d\chi}{dV'} j_{ph} + \frac{j_o e^{\frac{V'}{nV_T}}}{nV_T} + \frac{1}{R_p}} \quad (4.12)$$

### 4.2.3. The VIM method

Since the terms in equation 4.4 have different weights depending on the irradiance level, the Variable Illumination Measurement (VIM method) has been proposed [Merten et al., 1998] in order to analytically discern the relevant parameters of the equivalent circuit

shown in figure 4.1. The VIM method consists in measuring the current density-voltage characteristics (JV curves) of the device under illumination levels which vary several orders of magnitude. For each one of these JV curves we determine these five parameters:

- the short circuit current  $j_{sc}$
- the open circuit voltage  $V_{oc}$
- the fill factor  $FF$
- the reciprocal slope at the short circuit point  $R_{sc}$
- the reciprocal slope at the open circuit point  $R_{oc}$

which are indicated in figure 4.2.

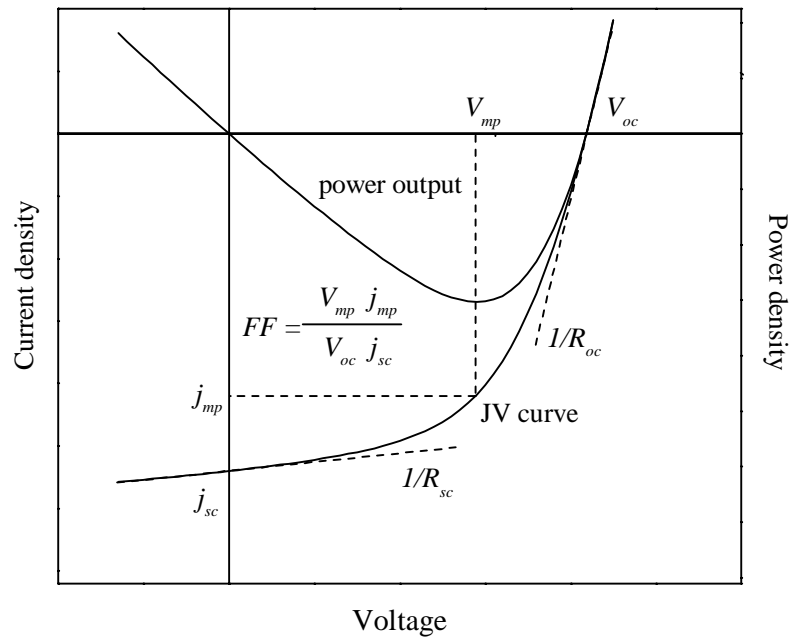


**Figure 4.2:** Parameters to determine for each JV curve which are used for the VIM analysis.

Balancing the photogeneration and the loss terms in equation 4.4 at the short circuit point we obtain that for a wide range of irradiance levels

$$-j_{sc} = -\chi_{sc} j_{ph} + j_o \left( e^{\frac{R_s j_{sc}}{nV_T}} - 1 \right) + \frac{R_s j_{sc}}{R_p} \approx -\chi_{sc} j_{ph} \quad (4.13)$$

$$j_{sc} = \chi_{sc} j_{ph}$$

whereas at the open circuit poin

$$0 = -\chi_{oc} j_{ph} + j_o \left( e^{\frac{V_{oc}}{nV_T}} - 1 \right) + \frac{V_{oc}}{R_p} \approx -\chi_{oc} j_{ph} + j_o e^{\frac{V_{oc}}{nV_T}} \quad (4.14)$$

$$\chi_{oc} j_{ph} = j_o e^{\frac{V_{oc}}{nV_T}} \Rightarrow V_{oc} = nV_T \ln \left( \chi_{oc} \frac{j_{ph}}{j_o} \right) = nV_T \ln \left( \frac{\chi_{oc} j_{sc}}{\chi_{sc} j_o} \right)$$

which is basically the well known logarithmic dependence of the open circuit voltage as a function of the short circuit current density[Möller,1993], but corrected with the ratio of the collection efficiencies at the open and short circuit points. Within the model, according to equation 4.12, the short circuit dynamic resistance is given by

$$V' = V - R_s j \Rightarrow \text{in short circuit } V' = 0 - R_s j_{sc} = -R_s j_{sc}$$

$$R_{sc} = \left. \frac{dV}{dj} \right|_{sc} = R_s + \frac{1}{\left. -\frac{d\chi}{dV'} \right|_{sc} j_{ph} + \frac{j_o e^{\frac{-R_s j_{sc}}{nV_T}}}{nV_T} + \frac{1}{R_p}} \quad (4.15)$$

This expression can be simplified depending on the irradiance:

a) for darkness and low illumination levels (  $j_{ph} \approx 0$  and  $j_{sc} \approx 0$  )

$$R_{sc} \approx \frac{1}{\frac{j_o}{nV_T} + \frac{1}{R_p}} = \frac{nV_T}{j_o} \parallel R_p \quad (4.16)$$

b) whereas for medium and high illumination levels

$$R_{sc} \approx \frac{1}{\left. -\frac{d\chi}{dV'} \right|_{sc} j_{ph}} = \frac{1}{\left. -\frac{d\chi}{dV'} \right|_{sc} \frac{j_{sc}}{\chi_{sc}}} = \frac{V_C}{j_{sc}} \quad (4.17)$$

$$V_C = R_{sc} j_{sc} = \frac{\chi_{sc}}{\left. -\frac{d\chi}{dV'} \right|_{sc}}$$

where we have defined the collection voltage  $V_C$  as previously introduced by other authors[Hof, 1999], a parameter intimately related to the collection mechanisms in the active layer of the device.

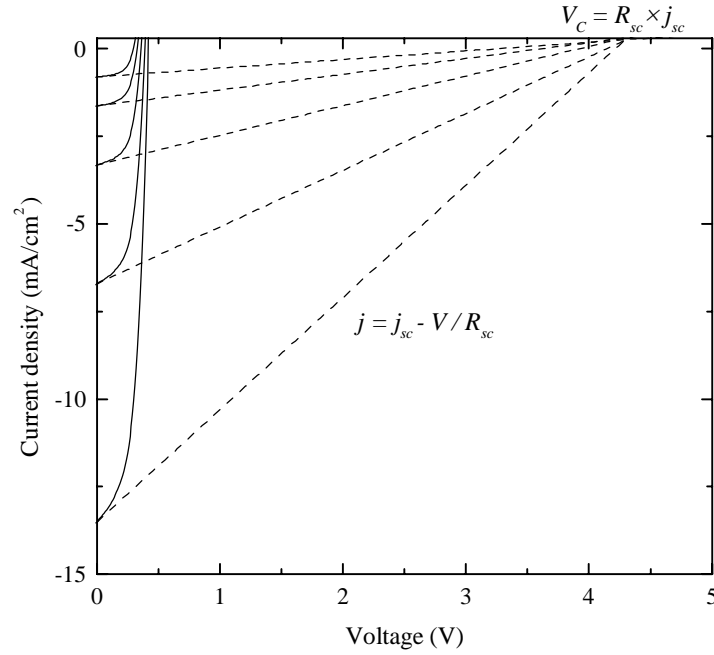


**Figure 4.3:** Determination of the voltage collection from linear fits to the JV curves around the short circuit point.

- c) and finally, for very high illumination it is only the series resistance which determines the short circuit slope of the JV curve, i.e.,  $R_{sc} \approx R_s$

On the other hand, the open circuit dynamic resistance is

$$V' = V - R_s j \Rightarrow \text{in open circuit } V' = V_{oc}$$

$$R_{oc} = \left. \frac{dV}{dj} \right|_{oc} = R_s + \frac{1}{-\left. \frac{d\chi}{dV'} \right|_{oc} j_{ph} + \frac{j_o e^{\frac{V_{oc}}{nV_T}}}{nV_T} + \frac{1}{R_p}} \quad (4.18)$$

which again takes simplified forms depending on the irradiance:

- a) for darkness and very low illumination levels ( $j_{ph} \approx 0$  and  $V_{oc} \approx 0$ )

$$R_{oc} \approx \frac{1}{\frac{j_o}{nV_T} + \frac{1}{R_p}} = \frac{nV_T}{j_o} \parallel R_p \quad (4.19)$$

b) whereas for medium and high illumination

$$R_{oc} \approx \frac{1}{\frac{j_o e^{\frac{V_{oc}}{nV_T}}}{nV_T}} = \frac{1}{\frac{\chi_{oc}}{nV_T} j_{ph}} = \frac{1}{\frac{\chi_{oc}}{nV_T} \frac{j_{sc}}{\chi_{sc}}} = \frac{\chi_{sc} nV_T}{j_{sc}} = \frac{n'V_T}{j_{sc}} \quad (4.20)$$

$$n' = \frac{\chi_{sc}}{\chi_{oc}} n \geq n$$

c) and finally, for very high illumination it is again the series resistance which determines the dynamic resistance and  $R_{oc} \approx R_s$

#### 4.2.4. The VIM method applied to nc-Si:H p-i-n structures

According to equations 4.16 and 4.19, for very low illumination levels both  $R_{sc}$  and  $R_{oc}$  tend to  $R_p \parallel nV_T / j_o \approx R_p$ . This allows to evidence in figure 4.4 the increase in  $R_p$  achieved by etching the n-doped layer of the device [Section 5.1.2] to avoid lateral leakage currents. Apart from these technological aspects, the VIM method also gets a higher insight in the collection mechanism of the device. An special attention must be paid to the short circuit resistance at medium -high illumination levels where it is mainly determined by recombination losses.

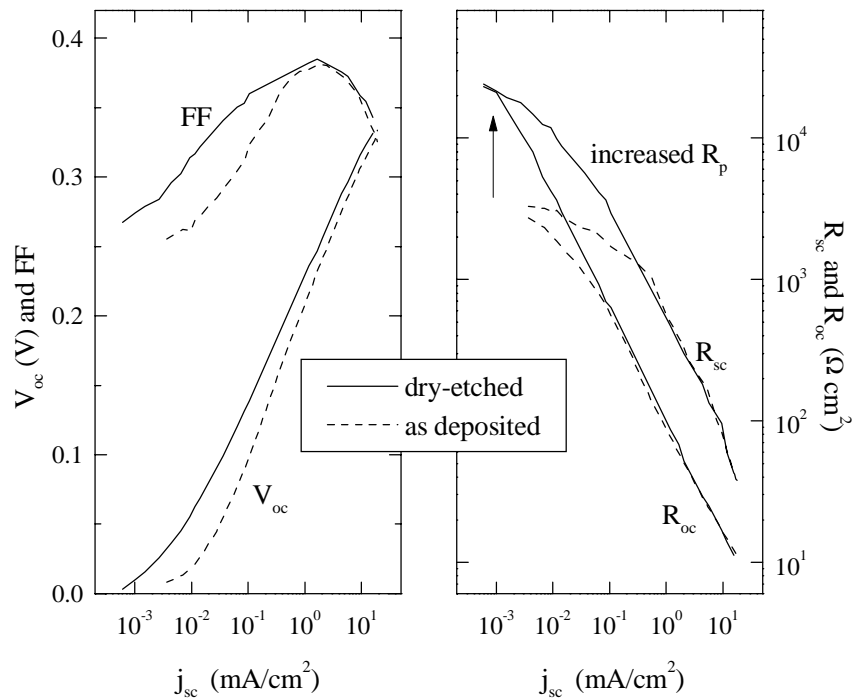


**Figure 4.4:** Results from the VIM characterisation method for the same device before and after dry-etching the surrounding layers.

Results of the VIM method applied to one of our nanocrystalline silicon solar cells obtained by HWCVD are shown in figure 4.5. The experimental data could be perfectly fitted within the model over irradiance levels varying more than four orders of magnitude.

**Table 4.1:** Deposition conditions, photovoltaic performance and equivalent circuit parameters deduced from the VIM data for the 990409c HWCVD solar cell.

| Cell name                     | Filament Temperature (°C)        | Substrate Temperature (°C)     | SiH <sub>4</sub> /H <sub>2</sub> flows (sccm) | Process Pressur (mbar)    | Thickness (μm) | $r_d$ (Å/s) |
|-------------------------------|----------------------------------|--------------------------------|---|---------------------------|----------------|-------------|
| 990409c                       | 1640                             | 125                            | 4 / 76  | $3.5 \cdot 10^{-2}$       | 2.2            | 8.5         |
| Photovoltaic performance      | Irradiance (mW/cm <sup>2</sup> ) | $j_{sc}$ (mA/cm <sup>2</sup> ) | $V_{oc}$ (V)                                  | $FF$ (%)                  |                |             |
|                               | 100                              | 9.12                           | 0.39  | 56                        |                |             |
| Equivalent circuit parameters | $j_o$ (mA/cm <sup>2</sup> )      | $n$                            | $R_s$ (Ωcm <sup>2</sup> )                     | $R_p$ (Ωcm <sup>2</sup> ) | $V_C$ (V)      |             |
|                               | $7 \cdot 10^{-4}$                | 1.67                           | 3.7   | $10^5$                    | 7.04           |             |

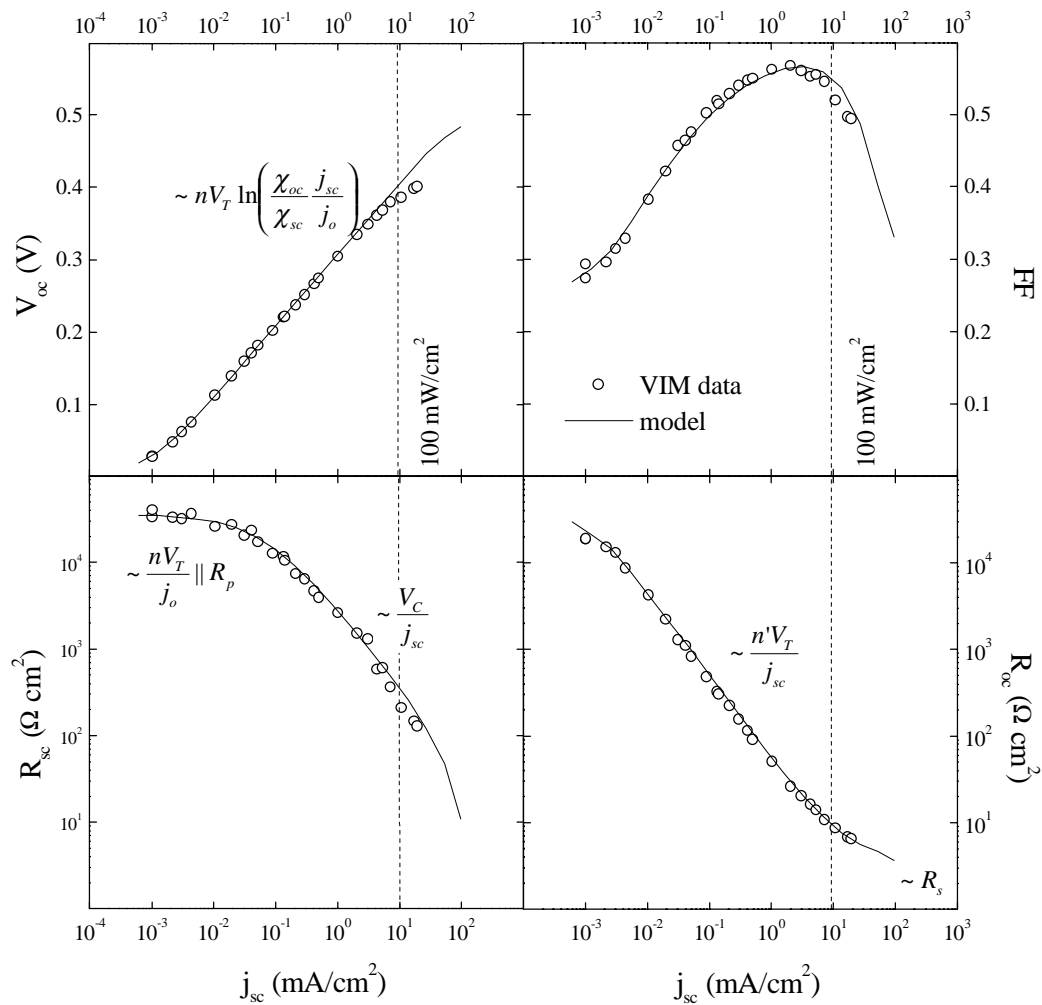


**Figure 4.5:** VIM data for the 990409c HWCVD solar cell [Table 4.1]. The measured values can be perfectly fitted over irradiances varying more than four orders of magnitude.

According to equation 4.17, the short circuit resistance is inversely proportional to the short circuit current density for high enough illumination levels. In that case, the recombination current density is the dominant loss term at the short circuit point whereas the diode and leakage currents densities can be overlooked. In this situation, the short circuit resistance arises as a parameter of capital interest in order to evaluate the electronic quality of the active layer. Besides, in short circuit the electric field profile within the active layer is not altered by any external voltage. At this stage we can only say that the better the collection mechanism throughout the active layer is, the greater the collection voltage  $V_c$  will be in equation 4.17. In order to analytically relate the collection voltage with the electronic properties of the device, it is necessary to obtain, at least near the short circuit point, a proper expression for the collection efficiency  $\chi$ . But this is not an easy subject at all.

### 4.3. Collection in p-i-n solar cells

#### 4.3.1. The complexity of the problem

The collection mechanism in low mobility p-i-n solar cells has been studied by means of numerical [Hack et al., 1985] and analytical models [Crandall, 1983]. Either numerically or analytically, the whole set of equations which describe the photovoltaic behaviour of the device are:

- the Poisson's equation

$$\frac{dE}{dx} = \frac{e}{\epsilon_s} [(p - n) + Q(p, n)] \quad (4.21)$$

where  $Q(p, n)$  is the density of charged localised states,

- the electron and hole current density equations considering drift and diffusion transport mechanisms

$$j_p(x) = e\mu_p p(x)E(x) - k_B T \mu_p \frac{dp(x)}{dx} \quad (4.22a)$$

$$j_n(x) = e\mu_n n(x)E(x) + k_B T \mu_n \frac{dn(x)}{dx} \quad (4.22b)$$

- and two additional continuity equations

$$\frac{dj_p(x)}{dx} = e[G - R(p, n)] \quad (4.23a)$$

$$\frac{dj_n(x)}{dx} = -e[G - R(p, n)] \quad (4.23b)$$

where  $G$  and  $R(p, n)$  are the generation and recombination rates respectively.

On account of the undoubtful complexity of the problem, there have been very few attempts to obtain analytical descriptions. Most of these models assume an uniform electric field throughout the active layer[Hubin et al., 1995]. The uniform field hypothesis could be a reasonably good approximation to thin a-Si:H solar cells but it is definitely not for the relatively thick nc-Si:H silicon solar cells. Some authors have introduced an electric field distortion which lead to reduced effective driftlengths to correct somehow the deviation from the uniform field approximation[Hof, 1994]. Furthermore, the lifetimes of electrons and holes are strongly varying within the active layer depending on the  $p/n$  ratio[Fig. 3.24]. Therefore, models based on constant driftlengths could also lead to important miscalculations. Therefore, even if an uniform electric field profile can be considered, a regional approach is required to correctly calculate recombination losses throughout the whole active layer[Asens et al., 1999].

### 4.3.2. Non uniform internal electric field

In this section we will consider a clean active layer without any other level in the band gap that an standard deep distribution of dangling bonds. This situation would describe our p-i-n structures obtained under optimised deposition conditions where the incorporation of contaminants was minimised. In this situation, three different regions within the active layer can be distinguished[Fig. 4.6] depending on the position of the Fermi -level with respect to the dangling bond transition energy levels  $E_+$  and  $E_-$  pointed in figure 3.23.

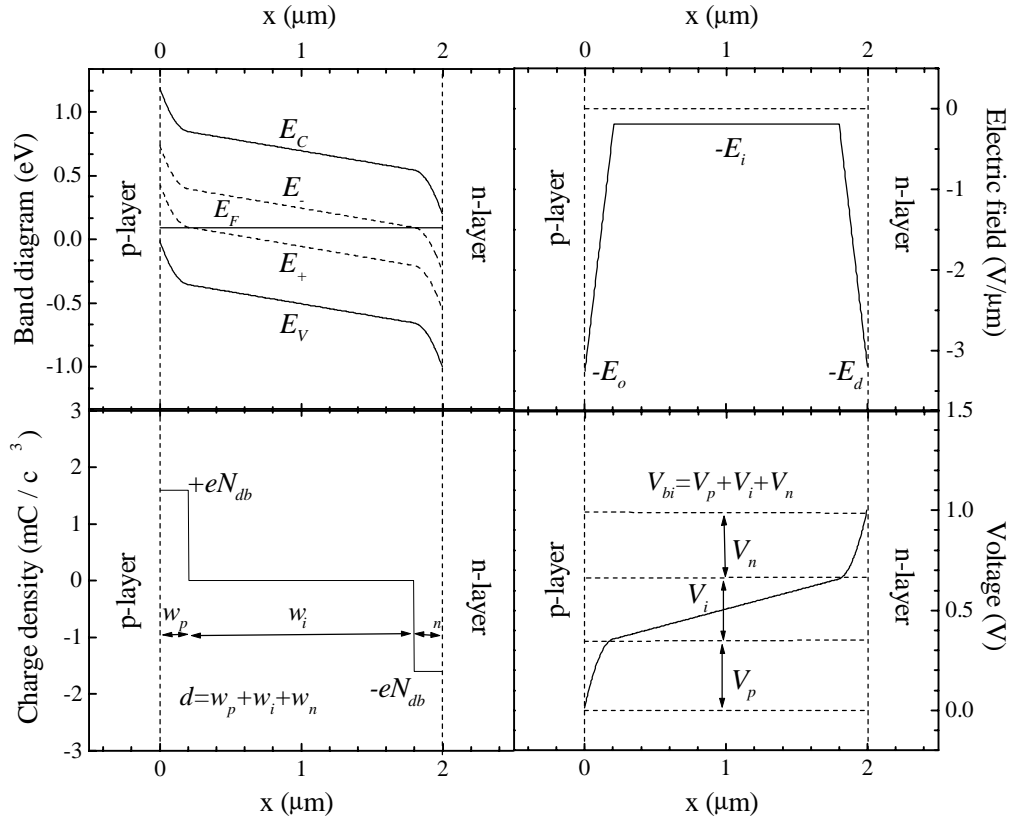


**Figure 4.6:** Results from the analytical description for an active layer thickness  $d$  of  $2 \mu\text{m}$  and a dangling bond density  $N_{db}$  of  $10^{16} \text{ cm}^{-3}$ . The built-in potential  $V_{bi}$  is 1 V which considering a band gap of 1.2 eV corresponds to doped layers with the typically obtained dark conductivity activation energies around 0.1 eV. We have considered a dangling bond correlation energy  $U_{eff} = V_i$  of 0.3 eV and  $V_p = V_n = 0.35 \text{ V}$ . Note that  $V_{bi} = V_p + V_i + V_n$ .

- a) PI region ( $0 \leq x < w_p$ ): The voltage drop  $V_p$  across this region is determined by the difference between the  $E_+$  level of the dangling bond and the Fermi level position in the p-doped layer. Since throughout this region,  $E_F < E_+$ , the dangling bonds are positively charged. Hence, the internal electric field strength reduces due to the screening of the space charge density  $+eN_{db}$  as

$$E(x) = -E_o + \frac{eN_{db}}{\epsilon_s} x \quad (4.24)$$

- b) I region ( $w_p \leq x \leq d - w_n$ ): The voltage drop across this region is given by the difference between the dangling bond transition energy levels, i.e.,  $V_i = (E_+ - E_-)/e$ . In equilibrium, without any external voltage applied and in the dark, it must equal the correlation energy  $U_{eff}$  of the dangling bond distribution [Street, 1991]. Since here the dangling bonds are neutral, the electric field strength remains constant at  $E_i$ .

c) IN region ( $d-w_n < x \leq d$ ): Similarly to the PI region, the voltage drop  $V_n$  is determined by the difference between the Fermi-level position in the n-doped layer and the  $E_c$  level of the dangling bond. The space charge density is  $-eN_{db}$  because  $E_F > E_c$  and the internal electric field strength increases as

$$E(x) = -E_d + \frac{eN_{db}}{\epsilon_s}(d-x) \quad (4.25)$$

Thus, the electric field profile can be expressed in terms of five parameters:  $E_o$ ,  $E_i$ ,  $E_d$ ,  $w_p$  and  $w_n$ . These parameters can be obtained as a function of the active layer thickness, the density of dangling bonds and the potentials  $V_p$ ,  $V_n$  and  $V_i$  by solving the following set of coupled equations

$$(E_o + E_i)w_p = 2V_p \quad (4.26a)$$

$$(E_d + E_i)w_n = 2V_n \quad (4.26b)$$

$$E_i(d - w_p - w_n) = V_i \quad (4.26c)$$

$$E_o - E_i = \frac{eN_{db}}{\epsilon_s} w_p \quad (4.26d)$$

$$E_d - E_i = \frac{eN_{db}}{\epsilon_s} w_n \quad (4.26e)$$

which are obtained by integrating the electric field profile across the different regions and imposing its continuity. Note that the potentials  $V_p$ ,  $V_n$  and  $V_i$  depend only on the position of the Fermi-level in the doped layers and the transition energy levels of the dangling bond distribution in the intrinsic layer. The sum of these potentials equals the built-in potential  $V_{bi}$  of the device. As shown in figure 4.7, a significant deviation from the uniform field approximation is expected for typical values describing the active layer of nc-Si:H p-i-n structures. The usual dangling bond densities ( $\geq 10^{16} \text{ cm}^{-3}$ ) and active layer thicknesses ( $\geq 2 \mu\text{m}$ ) result in field strengths in the neutral I region more than one order of magnitude weaker than those at the interfaces ( $E_i \ll E_o, E_d$ ).

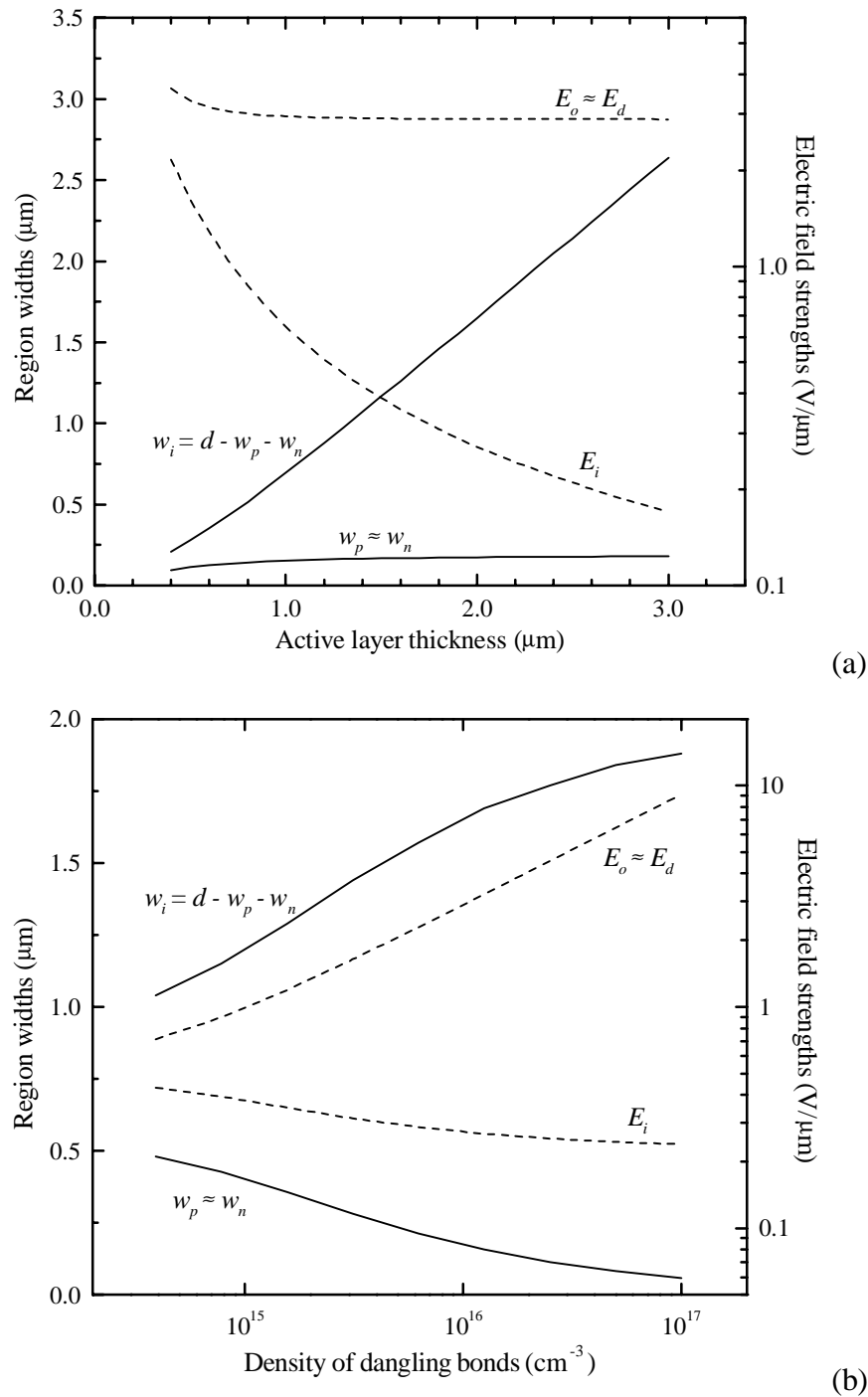


**Figure 4.7:** (a) Set of parameters determining the electric field profile as a function of the active layer thickness considering a dangling bond density of  $10^{16} \text{ cm}^{-3}$ . (b) As a function of the dangling bond density considering an active layer thickness of  $2 \mu\text{m}$ .

### 4.3.3. Short circuit recombination losses

Under illumination, an increase in the free electron and hole densities will appear in the respective bands. Nevertheless, it can be considered that, even for medium-high illumination levels, the space charge density is still determined by the very much higher

densities of localised states. Hence, the electric field profile will not be greatly perturbed and, in any case, we could consider that under illumination it is quite similar to that in equilibrium with slight corrections in the set of parameters  $E_o$ ,  $E_i$ ,  $E_d$ ,  $w_p$  and  $w_n$ . Now, as a first approximation, we neglect recombination and we assume that field assisted drift is the dominant transport mechanism in the neutral region. Then, considering a uniform generation rate due to illumination with weakly absorbed light

$$j_p \approx e\mu_p p(x)(-E_i) \quad \Rightarrow \quad p(x) \approx \frac{G(d-x)}{\mu_p E_i} \quad w_p \leq x \leq d-w_n \quad (4.27a)$$

$$\frac{dj_p}{dx} \approx eG$$

$$j_n \approx e\mu_n n(x)(-E_i) \quad \Rightarrow \quad n(x) \approx \frac{Gx}{\mu_n E_i} \quad w_p \leq x \leq d-w_n \quad (4.27b)$$

$$\frac{dj_n}{dx} = -eG$$

where the boundary conditions  $p(d) \approx 0$  and  $n(0) \approx 0$  have been used. The exact profiles obtained by numerical calculation have shown that this crude approximation is also valid for minority carriers in the interface regions [Asensi et al., 1999]

$$p(x) \approx \frac{G(d-x)}{\mu_p \left( E_d - \frac{eN_{db}}{\epsilon_s} (d-x) \right)} \quad d-w_n < x \leq d \quad (4.28a)$$

$$n(x) \approx \frac{Gx}{\mu_n \left( E_o - \frac{eN_{db}}{\epsilon_s} x \right)} \quad 0 \leq x < w_p \quad (4.28b)$$

At this point, recombination losses can be calculated. In the PI region, where dangling bonds are positively charged and electrons are minority carriers, the recombination rate is obtained according to equations 3.33b and 4.28b

$$R_{PI} = \frac{n(x)}{\tau_n^+} = \frac{Gx}{\mu_n \tau_n^+ \left( E_o - \frac{eN_{db}}{\epsilon_s} x \right)} \quad 0 \leq x < w_p \quad (4.29)$$

and its contribution to the recombination current density can be calculated as

$$\begin{aligned}
j_{rec}^{PI} &= \int_0^{w_p} eR_{PI}(x)dx = \int_0^{w_p} \frac{eGx}{\mu_n \tau_n^+ \left( E_o - \frac{eN_{db}x}{\epsilon_s} \right)} dx = \\
&= \frac{eG}{\mu_n \tau_n^+} \left( \frac{\epsilon_s}{eN_{db}} \right)^2 \left[ E_o \ln E_o - \frac{eN_{db}}{\epsilon_s} w_p - E_o \ln \left( E_o - \frac{eN_{db}}{\epsilon_s} w_p \right) \right]
\end{aligned}$$

which considering equation 4.26 reduces to

$$j_{rec}^{PI} = \frac{eG}{\mu_n \tau_n^+} \frac{w_p^2}{(E_o - E_i)^2} \left[ E_o \ln \frac{E_o}{E_i} - (E_o - E_i) \right]$$

Usually  $E_o \gg E_i$  and this expression can be further simplified arriving finally at

$$j_{rec}^{PI} \approx \frac{eG}{\mu_n \tau_n^+} \frac{w_p^2}{E_o} \left( \ln \frac{E_o}{E_i} - 1 \right) = eG \frac{w_p^2}{L_{PI}} \left( \ln \frac{E_o}{E_i} - 1 \right) \quad (4.30)$$

where we have introduced the effective driftlength for the PI region  $L_{PI} = \mu_n \tau_n^+ E_o$ .

Proceeding in the same way, in the IN region where dangling bonds are negatively charged and holes are minority we obtain

$$j_{rec}^{IN} = \frac{eG}{\mu_p \tau_p^-} \frac{w_n^2}{E_d} \left( \ln \frac{E_d}{E_i} - 1 \right) = eG \frac{w_n^2}{L_{IN}} \left( \ln \frac{E_d}{E_i} - 1 \right) \quad (4.31)$$

with  $L_{IN}$  the effective driftlength for the IN region  $L_{IN} = \mu_p \tau_p^- E_d$ .

Finally, in the neutral I region, equations 3.34b and 4.28 lead to

$$R_I = \frac{p(x)}{\tau_p^o} + \frac{n(x)}{\tau_n^o} = \frac{G(d-x)}{\mu_p \tau_p^o E_i} + \frac{Gx}{\mu_n \tau_n^o E_i} \quad (4.32)$$

Here, we will consider that  $\mu_p \tau_p^o \approx \mu_n \tau_n^o \approx \mu \tau^o$ . This result has been extensively justified for a-Si:H [Beck et al., 1996b] and seems to be also consistent in nc-Si:H [Goerlitzer et al., 2000]. Anyway, there should not be great differences between these  $\mu\tau$ -products, and this assumption allows a closer expression for the recombination current without losing generality

$$R_I = \frac{Gd}{\mu\tau^o E_i} = \frac{Gd}{L_I} \quad (4.33)$$

where the effective driftlength in the neutral I region is given b

$$L_I = \mu\tau^o E_i \quad (4.34)$$

This constant recombination rate allows to easily calculate more precise carrier profiles in the I region by solving again equation 4.27 neglecting again transport by diffusion but taking into account the first approximation recombination rate[Eq. 4.33]

$$\begin{aligned} j_p &\approx e\mu_p p(x)(-E_i) \\ \frac{dj_p}{dx} &\approx eG \left(1 - \frac{d}{L_I}\right) \Rightarrow p(x) \approx \frac{G(d-x)}{\mu_p E_i} \left(1 - \frac{d}{L_I}\right) \quad w_p \leq x \leq d - w_n \end{aligned} \quad (4.35a)$$

$$\begin{aligned} j_n &\approx e\mu_n n(x)(-E_i) \\ \frac{dj_n}{dx} &\approx -eG \left(1 - \frac{d}{L_I}\right) \Rightarrow n(x) \approx \frac{Gx}{\mu_n E_i} \left(1 - \frac{d}{L_I}\right) \quad w_p \leq x \leq d - w_n \end{aligned} \quad (4.35b)$$

with the boundary conditions  $p(d) \approx 0$  and  $n(0) \approx 0$ . This profiles introduced in equation 4.32 lead to a corrected recombination rate

$$R_I = G \frac{d}{L_I} \left(1 - \frac{d}{L_I}\right) \quad (4.36)$$

This correction can be easily iterated arriving finally a

$$R_I = G \frac{d}{L_I} \left(1 - \frac{d}{L_I} + \left(\frac{d}{L_I}\right)^2 - \left(\frac{d}{L_I}\right)^3 + \dots\right) = G \frac{d}{d + L_I} \quad (4.37)$$

which turns out to be the exact analytical solution. As it could be expected,  $d \gg L_I$  leads to  $R_I \approx G$  whereas if  $L_I \gg d$  then  $R_I \ll G$ . Therefore, the recombination current density in the I region is obtained as

$$j_{rec}^I = \int_{w_p}^{d-w_n} eR_I dx = \int_{w_p}^{d-w_n} eG \frac{d}{d + L_I} dx = eG \frac{d}{d + L_I} (d - w_p - w_n) \quad (4.38)$$

Finally, the short circuit collection efficiency is given by

$$\begin{aligned}
 \chi_{sc} &= 1 - \frac{j_{rec}^{PI} + j_{rec}^I + j_{rec}^{IN}}{j_{ph}} = 1 - \frac{j_{rec}^{PI} + j_{rec}^I + j_{rec}^{IN}}{eGd} = \\
 &= 1 - \underbrace{\frac{1}{d} \left[ \frac{w_p^2}{L_{PI}} \left( \ln \frac{E_o}{E_i} - 1 \right) + \frac{w_n^2}{L_{IN}} \left( \ln \frac{E_d}{E_i} - 1 \right) \right]}_{\text{recombination in the PI+IN regions}} - \underbrace{\frac{d - w_p - w_n}{d + L_I}}_{\text{recombination in the I region}} \quad (4.39)
 \end{aligned}$$

#### 4.3.4. Predictions of the model

Within this simplified model, the short circuit collection efficiency can be calculated from equation 4.39 by solving the coupled set of equations 4.26 by simple iterative methods. This can be done for different dangling bond densities and active layer thicknesses leading to the results shown in figure 4.7. For the calculation of the collection efficiency, we have considered the  $\mu\tau$ -products already introduced in figure 3.24, i.e.,  $\mu_n \tau_n^+ \approx \mu_p \tau_p^- \approx 2 \times 10^{-9} \text{ cm}^2/\text{V}$  and  $\mu\tau^o \approx 10^{-7} \text{ cm}^2/\text{V}$  (for  $N_{db} = 10^{16} \text{ cm}^{-3}$ ). Figure 4.8a shows the results obtained as a function of the active layer thickness for a fixed dangling bond density of  $10^{16} \text{ cm}^{-3}$ . While recombination in the PI+IN regions remains almost constant, that in the I region grows with the active layer thickness due to the increase in  $w_i = d - w_p - w_n$  together with the reduction in  $E_i$ . Though the net collection efficiency steadily lowers with the active layer thickness, what it actually matters is the collected short circuit current density. For an uniform generation rate  $G$ , it can be calculated as

$$j_{sc}(d) = \chi_{sc}(d) j_{ph}(d) = \chi_{sc}(d) eGd \quad (4.40)$$

which increases with the active layer thickness within the typical value range ( $1 \mu\text{m} \leq d \leq 3 \mu\text{m}$ ). However, for non uniform generation rates, as in the case of solar irradiance, more efficient devices could be obtained by enhancing the electric field in the I region with thinner active layers.

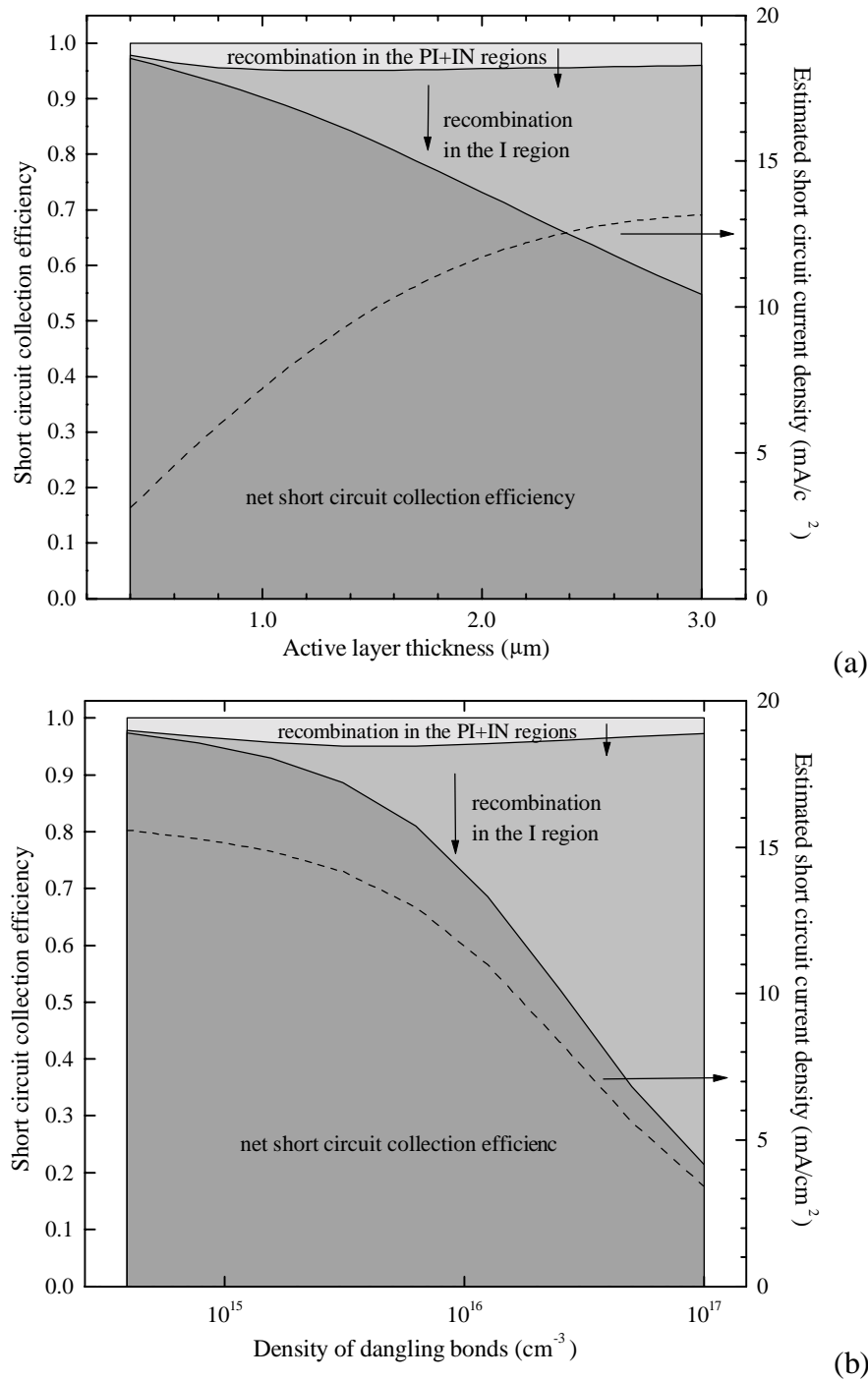


**Figure 4.8:** (a) Short circuit collection efficiency as a function of the active layer thickness for a fixed dangling bond density of  $10^{16} \text{ cm}^{-3}$ . (b) Short circuit collection efficiency as a function of the dangling bond density for a fixed active layer thickness of  $2 \mu\text{m}$ . In this last calculation it is essential to include the dependence of the different lifetimes on the dangling bond density ( $\tau \sim 1/N_{ab}$ ). The dashed line (left axis) indicates the estimated short circuit current density which would be obtained for an irradiance of  $100 \text{ mW/cm}^2$  of weakly absorbed light  $\alpha(h\nu=1.5\text{eV}) \approx 10^3 \text{ cm}^{-1}$  (mean generation rate of  $5 \times 10^{20} \text{ cm}^{-3}\text{s}^{-1}$ ).

The dependence on the dangling bond density for a fixed thickness of 2  $\mu\text{m}$  is shown in figure 4.8b. Here, it is important to include in the calculation the dependence of the lifetimes on the dangling bond density ( $\tau \sim 1/N_{db}$ ). As it could be expected, the collection efficiency steadily improves when lowering the dangling bond density. Recombination in the neutral I region becomes the most significant loss for dangling bond densities in the order of  $10^{16} \text{ cm}^{-3}$ .

As a conclusion, for typical active layer thicknesses  $d \geq 2 \mu\text{m}$  and dangling bond densities  $N_{db} \geq 10^{16} \text{ cm}^{-3}$ , it is recombination in the I region which basically limits the collection efficiency, which thus can be approximated by

$$\chi_{sc} \approx 1 - \frac{d - w_p - w_n}{d + L_I} = \frac{L_I - w_p - w_n}{d + L_I} \approx \frac{L_I}{d + L_I} \quad (4.41)$$

When an external voltage is applied to the device, equation 4.41 could still be valid by including in  $L_I$  (actually in  $E_i$ ) its dependence on the applied voltage

$$\chi(V) = \frac{L_I(V)}{d + L_I(V)} = \frac{\mu\tau^o E_i(V)}{d + \mu\tau^o E_i(V)} \quad (4.42)$$

### 4.3.5. The link with the voltage collection

If we were able to differentiate equation 4.42 with respect to the applied voltage, we could obtain the link between the collection voltage defined in equation 4.17 and the mechanism determining recombination losses in the device. For small voltages applied, we can neglect the variations in the widths of the different regions. Besides, it is expected that the main voltage drop takes place in the more resistive part of the device depleted from free carriers. Then, we could consider that it is basically the field strength  $E_i$  in the neutral I region what depends on the applied voltage. Within these assumptions, confirmed by numerical calculation, near the short circuit point we have

$$V_{bi} - V = E_o \frac{w_p}{2} + E_i(V)(d - w_p - w_n) + E_d \frac{w_n}{2} \quad (4.43)$$

which differentiated with respect to the applied voltage leads to

$$\frac{dE_i}{dV} = -\frac{1}{d - w_p - w_n} \quad (4.44)$$

From this last equation and differentiating equation 4.42 we arrive a

$$\left. \frac{d\chi}{dV} \right)_{sc} = -\chi_{sc}^2 \frac{d}{L_l} \frac{1}{V_i} \quad (4.45)$$

Therefore, the collection voltage can be obtained from equations 4.41 and 4.45 arriving a

$$V_C = -\frac{\chi_{sc}}{\left. \frac{d\chi}{dV} \right)_{sc}} = \frac{1}{\chi_{sc} \frac{d}{L_l} \frac{1}{V_i}} = V_i \left( 1 + \frac{L_l}{d} \right) \quad (4.46)$$

Therefore, a higher voltage collection indicates a longer effective drift length  $L_l$  compared to the width  $d$  of the active layer. According to the definition of  $L_l$ , its increase is due either to better transport properties in the neutral I region or to an enhanced electric field therein.

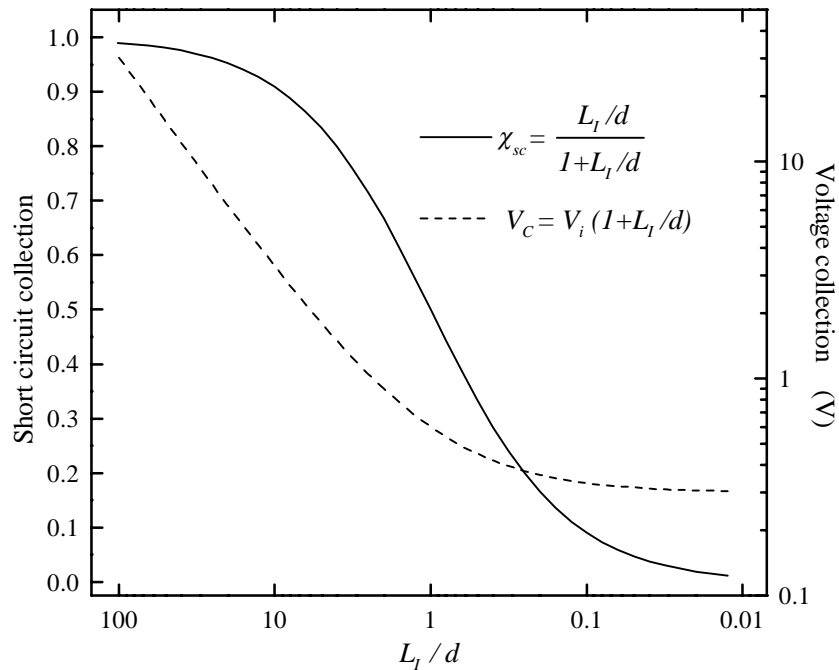


**Figure 4.9:** Short circuit collection efficiency and corresponding voltage collection as a function of the  $L_l/d$  ratio. It has been considered  $V_i = 0.3$  V. Voltage collections of a few volts indicate a drift length around one order of magnitude longer than the active layer thickness.

### 4.3.6. Contaminated devices

In the case of contaminated devices, we should take into account the non fully intrinsic character of the active layer. Anyway, the Fermi-level has to move across the band gap throughout the active layer from the p- to the n-type doping levels. Hence, dangling bonds will also change their state of charge depending on the position of the Fermi-level with respect to the transition energy levels  $E_+$  and  $E_-$ . However, a comparable or higher density of contaminants greatly perturbs the space charge density and thus the electric field profile. The band diagram in the most usual case of n-type contaminants incorporated to the active layer is shown in figure 4.10. For the calculation it was considered a deep distribution of  $10^{16} \text{ cm}^{-3}$  dangling bonds and a shallow distribution of  $8 \times 10^{15} \text{ cm}^{-3}$  donors related to contaminants 0.2 eV below the conduction band. This situation leads to  $E_C - E_F \approx 0.4 \text{ eV}$  in equilibrium which is similar to the dark conductivity activation energy measured in non optimised undoped samples showing a pronounced n-type character. As in section 4.3.2, three different regions can be distinguished depending on the sign of the space charge density therein. However, now the space charge density is not due to just dangling bonds which makes an analytical description much more complex.

- a) PI region: The voltage drop  $V_p$  across this region is determined by the difference between the equilibrium Fermi-level positions in the p-doped and the undoped but contaminated active layer. Throughout this region the space charge density is positive and screens the internal electric field strength until it completely vanishes. The distribution of dangling bonds is positively charged only in the first tenth of micron while in the rest of this region the space charge density is given by the concentration of positively charged donors.
- b) I region: Between the PI and IN regions extends a quasineutral region where the positively charged donors are compensated by the fraction  $F^-$  of negative dangling bonds. By contrast to the case of an ideally intrinsic active layer, here the flat bands indicate there is no voltage drop across this quasineutral region and thus the field strength is null.

- c) IN region: Similarly to the PI region, the voltage drop  $V_n$  across this region is determined by the difference between the equilibrium Fermi-level positions in the n-doped and the contaminated active layer. The space charge density throughout this region is negative due to the difference between the densities of negative dangling bonds and positive donors. The density of free electrons in the conduction band can not be neglected near the interface with the n-layer.

In this situation, the built-in voltage is given by the sum of the voltage drops in the charged PI and IN regions whereas the voltage drop in the quasineutral I region can be neglected. Besides, the main contribution is due to the PI region since  $V_p$  is significantly higher than  $V_n$ . Actually, simulation shows that these devices behave as p-n junctions (in fact  $p^+-n-n^+$ ) instead of p-i-n structures.

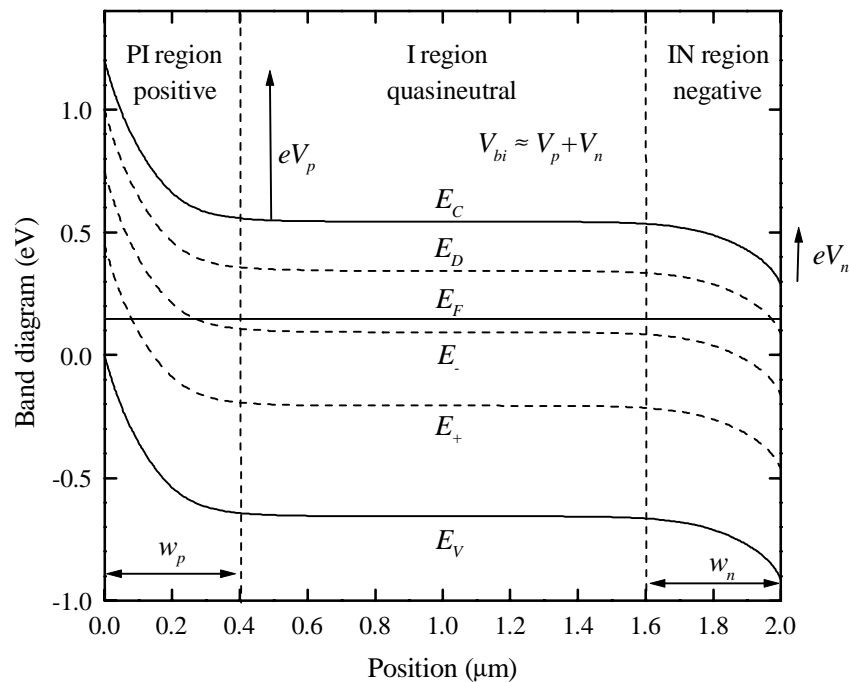


**Figure 4.10:** Calculated band diagram within the active layer of a contaminated (n-type) active layer. There is not a significant voltage drop across the quasineutral region (flat bands) where the field strength is null. The voltage drop in the PI region is significantly higher than that in the IN region. The device actually behaves as a  $p^+-n-n^+$  structure.

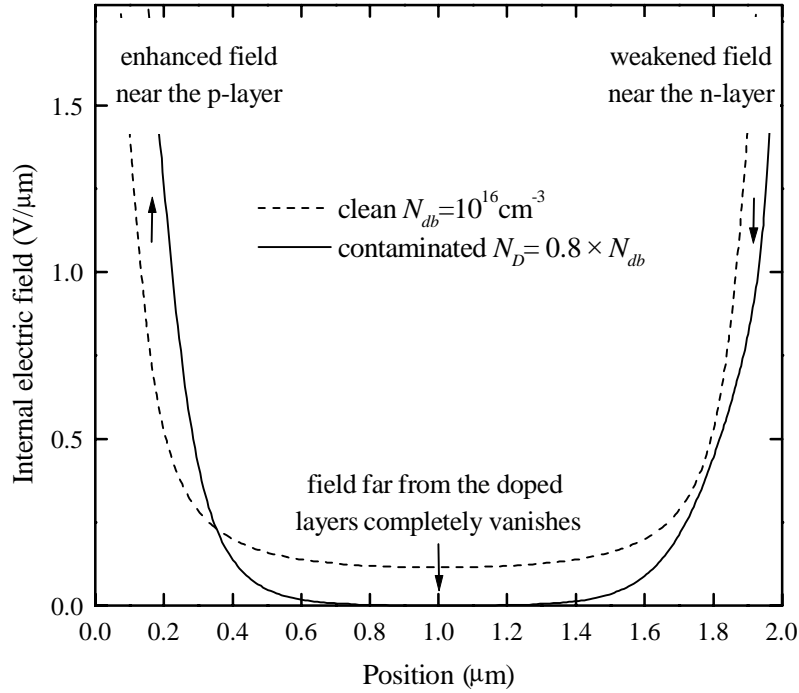


**Figure 4.11:** Calculated magnitude of the internal electric field within clean (ideally intrinsic) and contaminated (n-type) active layers. Note that the electric field is enhanced in the PI region at expense of the weakened field in the IN region. It completely vanishes in the quasineutral I region.

In this situation, there is not too error in considering that collection is only possible for carriers generated near the p-doped layer, within the PI region where the field strength is enhanced. Either in the I region where the field vanishes or in the IN region where it is much weaker than in clean devices, high recombination losses avoid collection. A more precise analytical description would be further complicated. Therefore, for thick enough devices ( $d > w_p + w_n$ ) it is expected a collection efficiency inversely proportional to the active layer thickness

$$\chi_{sc} \approx 1 - \frac{eG(d - w_p)}{eGd} = \frac{w_p}{d} \quad (4.47)$$

Therefore, in the case of uniform generation rates, the short circuit current density should not significantly vary when devices incorporating active layers of different thicknesses are compared [Eq. 4.48]. This behaviour was certainly observed in our preliminary non optimised p-i-n structures which always showed very similar short circuit current values

$$j_{sc} = \chi_{sc} j_{ph} = \frac{w_p}{d} eGd = eGw_p = \text{constant} \quad (4.48)$$

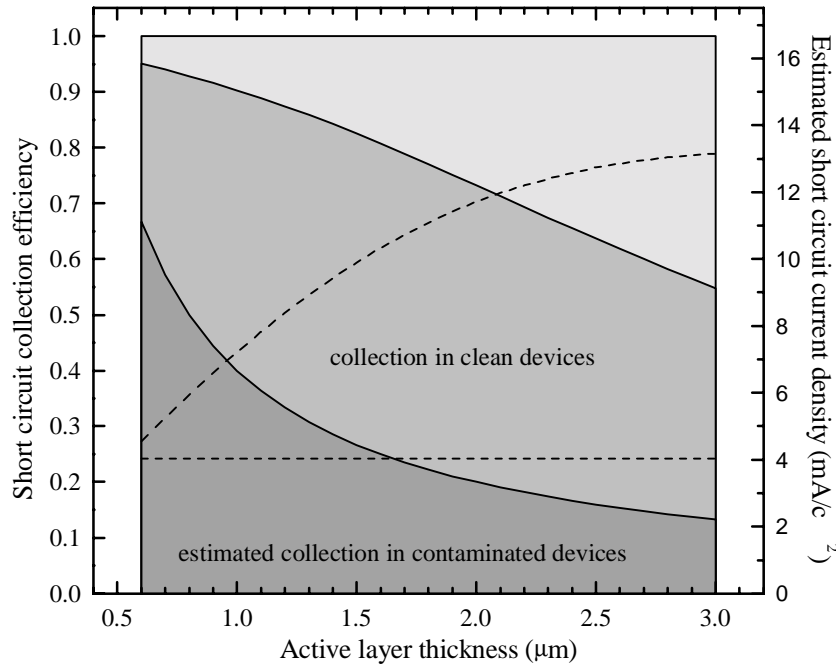


**Figure 4.12:** Calculated short circuit collection efficiency for a clean active layer (as in figure 4.8a) compared to the case of a contaminated active layer [Eq. 4.47]. The dashed line (left axis) indicates the estimated short circuit current density which would be obtained for a mean generation rate of  $5 \times 10^{20} \text{ cm}^{-3} \text{ s}^{-1}$ .

The expected voltage collection in these devices can be estimated by introducing in equation 4.47 the voltage dependence in  $w_p$ . The most resistive part in a device incorporating a contaminated active layer with a pronounced n-type character is actually the PI region where the conduction band is depleted from free electrons in the conduction band. Hence, it is expected that the external voltage applied mainly drops in this region. Then, though a precise dependence is complex because both donors and dangling bonds contribute to the space charge, we can estimate that

$$w_p \approx \sqrt{\frac{2\epsilon_s}{eN_{PI}}(V_p - V)} \quad (4.49)$$

where  $N_{PI}$  is an effective density of positively charged centres representative for the average space charge density within the PI region. Therefore

$$\frac{d\chi}{dV} = \frac{1}{d} \frac{dw_p}{dV} \approx -\frac{1}{d} \frac{\epsilon_s}{eN_{PI} w_p} \quad (4.50)$$

$$V_C = - \left. \frac{\chi_{sc}}{dV} \right)_{sc} = \frac{eN_{PI} w_p^2}{\epsilon_s} \Big)_{sc} = 2V_p \quad (4.51)$$

Typical voltage drops around 0.5 V are expected in the PI region of devices incorporating contaminated active layers[Fig. 4.10]. This would lead to voltage collections slightly higher than 1 V in full agreement with our VIM measurements for solar cells grown under non optimised deposition conditions.

# Chapter 5

## Nanocrystalline silicon solar cells by HWCVD. Technological aspects

In this chapter we will consider some subjects which must be taken into account to fabricate thin film solar cells. Technological aspects such as the selection of a suitable front electrode or a method to reduce lateral leakage currents are considered. Besides, a comprehensive study of the p-i-n devices obtained by HWCVD during the period of research within the project *Crystalline Silicon Solar Cells on Low Temperature Substrates CRYSTAL* (JOR3-CT97-0126) is presented.

### 5.1. Previous technological aspects

#### 5.1.1. Selection of the TCO

In most thin film solar cells, the carrier on which the various thin film materials are deposited, usually glass, also serves as a window to the cell. The front electrode usually consists in a transparent conductive oxide (TCO) layer directly deposited onto the carrier [Fig. 5.1]. The most common ones are aluminium-doped zinc oxide or AZO ( $\text{ZnO:Al}$ ), tin-doped indium oxide or ITO ( $\text{In}_2\text{O}_3:\text{Sn}$ ) and fluorine-doped tin oxide or FTO ( $\text{SnO}_2:\text{F}$ ). The requirements for the electrode material are [Schropp et al., 1998]:

- a) high transmission (preferably  $>85\%$ ) in the entire wavelength region where the photovoltaic absorber layers are active
- b) low sheet resistance (preferably  $<10\Omega/\square$ ) to minimise series resistance losses
- c) low contact resistance with the p-type layer of the p-i-n structure
- d) rough surface to increase the optical path of the light by scattering, while the morphology should be such that shunting paths or pinholes are avoided
- e) chemical resistance against the strongly reducing hydrogen ambient during chemical vapour deposition
- f) high thermal stability to avoid diffusion of elements into the growing layer

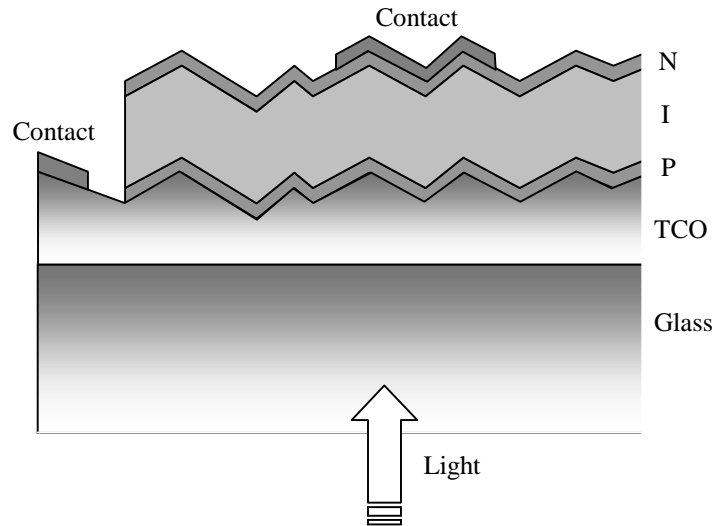


**Figure 5.1:** Thin film p-i-n solar cell structure. Glass is used as a carrier for the front electrode (TCO) and the active device, in this case a p-i-n structure. Contacts are usually thin metallic films thermally evaporated in high vacuum.

Though ITO presents the best electrical properties and the highest optical transmission, its chemical stability is very low. Therefore, protective transparent coatings are required to avoid severe reduction or diffusion of indium. FTO is usually made by Atmospheric Pressure CVD (APCVD)[Gordon et al., 1989] which produces natively textured coatings excellent for light trapping. Besides, its sheet resistance is low ( $6-15 \Omega/\square$ ) and forms ohmic contacts with p-type silicon layers. AZO also presents a low enough sheet resistance ( $6-15 \Omega/\square$ ), but it forms a barrier with amorphous silicon p-layers. However, the contact resistance clearly improves with nanocrystalline silicon p-layers. The optical transmission is high and smooth films can be textured by etching in dilute HCl to produce a rough scattering surface for light confinement purposes[Kluth et al., 1997].

Once ITO is discarded because of its low stability under CVD processes, we subjected FTO and AZO layers to a durability test in order to choose a proper TCO for our superstrate devices. The FTO was Asahi-U™ whereas AZO was obtained by magnetron sputtering from a ceramic target ( $\text{ZnO}:\text{Al}_2\text{O}_3$  98:2 wt%, 99.99% purity) in the load-lock chamber[Section 2.1]. These layers were exposed to a flow of hydrogen decomposed by the tungsten filament heated to  $1700^\circ\text{C}$  for fifteen minutes. The transmittance of AZO slightly improved in the visible range while the electrical properties remained unchanged. By contrast, FTO drastically darkened under the strongly reducing ambient. Such darkening could be due to a tin enrichment at the layer surface. Small variations were

observed in the electrical properties, probably because the reduction mainly affected the surface but not the whole layer. X-ray photoelectron spectroscopy measurements (XPS) also revealed a change in the local bonding of tin atoms in the FTO layer whereas zinc remained basically unchanged in the AZO one. Previous studies also concluded that AZO presents an excellent chemical stability against atomic hydrogen[Wanka et al., 1994]. On the contrary, though FTO shows good chemical stability in a reactive PECVD hydrogen plasma, it does not withstand the strongly reducing ambient during HWCVD processes[Wallinga, 1998]. Actually, much higher atomic hydrogen concentrations are involved in HWCVD than in PECVD processes[Starobinski et al., 1995].

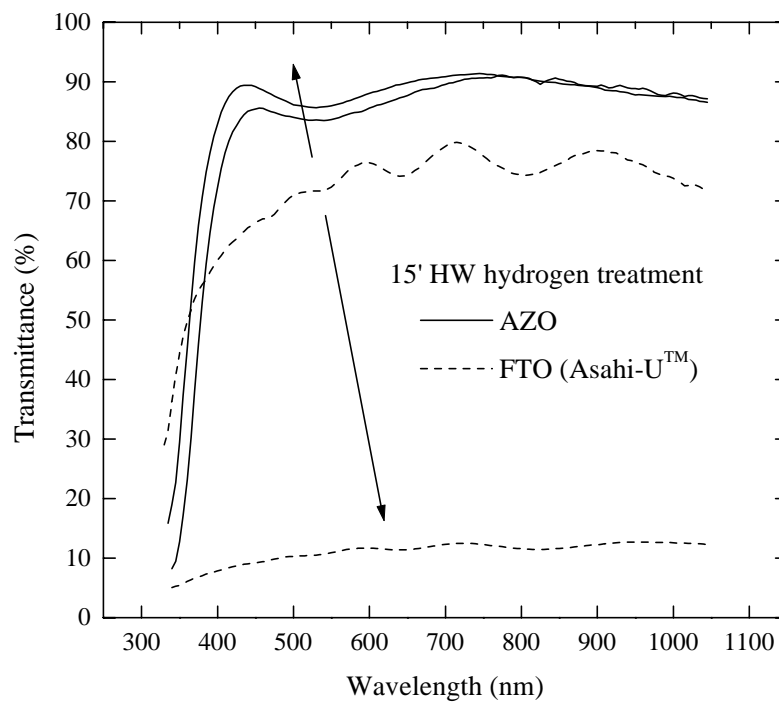


**Figure 5.2:** Effect of a 15 minutes HW hydrogen treatment on AZO and FTO (Asahi-U™). While the transmittance of AZO slightly improves in the visible range, FTO is drastically darkened by the strongly reducing ambient.

Therefore, AZO was the TCO which we chose for obtaining our superstrate p-i-n solar cells by HWCVD. Front electrodes are expected to present a high transmission in the visible range  $T_{vis}$  and a low sheet resistance  $R_{sheet}$ . A figure of merit  $F_{JK}$  [Jain et al., 1981] can be formulated which joins both desired properties

$$F_{JK} = -R_{sheet} \ln T_{vis} \quad (5.1)$$

Our optimised coatings which have been used for devices presented the optical and electrical properties summarised in table 5.1. These values are similar to the best reported in the literature[Jäger et al., 1998]. The transmittance is higher than 85% for the whole wavelength range where the solar irradiance is important[Fig. 5.3]. The optical gap was approximately 3.5 eV whereas for undoped ZnO it is expected a lower value around 3.3 eV. This blue shift has been attributed to the degeneration of the semiconductor[Burstein E., 1982]. An apparent band gap widening is observed when the Fermi-level enters the conduction band. However, this effect results beneficial because it increases the useful solar irradiance.

**Table 5.1:** Average electrical properties of the optimised ZnO:Al coatings selected for devices.

| $\rho$ ( $\Omega$ cm) | $n$ ( $\text{cm}^{-3}$ ) | $\mu$ ( $\text{cm}^2/\text{Vs}$ ) | $R_{sheet}$ ( $\Omega/\square$ ) | $T_{vis}$ (%) | $E_g$ (eV) | $F_{JK} = -R_{sheet} \ln T$ ( $\Omega/\square$ ) |
|-----------------------|--------------------------|-----------------------------------|----------------------------------|---------------|------------|--|
| $8 \times 10^{-4}$    | $6 \times 10^{20}$       | 13                                | 11.4                             | >85           | 3.5        | <1.85  |

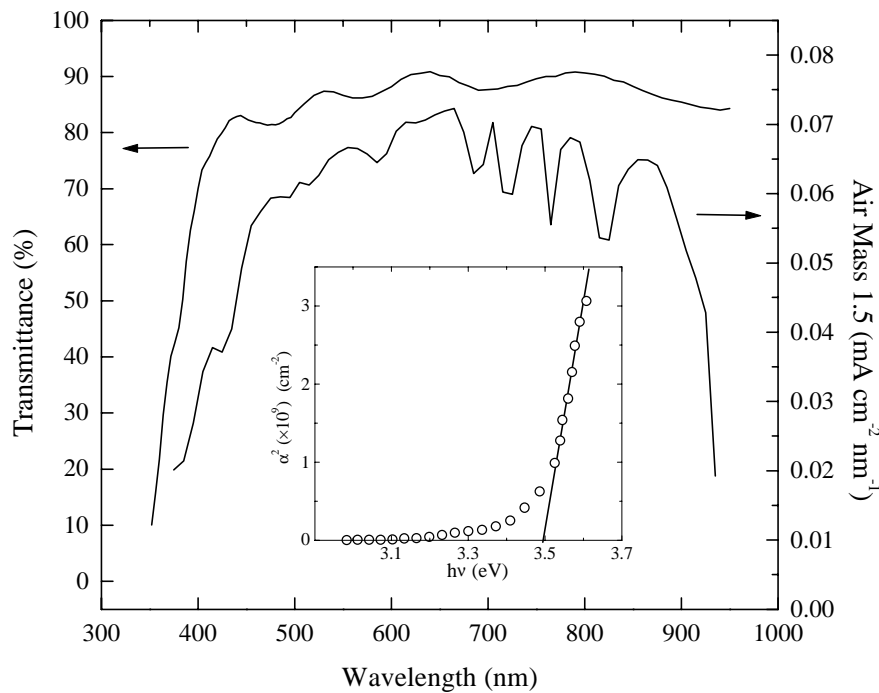


**Figure 5.3:** Optical transmittance of an optimised AZO coating compared with the Air Mass 1.5 solar spectrum[Wenham et al., 1994]. In the wavelength range of interest, the optical transmittance remains over 85%. The inset plot shows the dependence of the square optical absorption coefficient on the photon energy, which allows to deduce a direct optical gap of 3.5 eV.

Apart from the proved chemical resistance to strongly reducing ambients[Fig. 5.2], it is also required for the TCO a high thermal stability to avoid diffusion of contaminants into the growing layer. Tails of zinc and aluminium measured by SIMS certainly rise in

samples deposited at higher substrate temperatures[Fig. 5.4]. The profiles of sodium and calcium are also higher when the substrate temperature is increased. However, these elements diffuse not only from the substrate but also from the top of the cell. A careful cleaning procedure of the substrates is mandatory to avoid diffusion of contaminants to the device which ruin the photovoltaic performance[Merten, 1996].

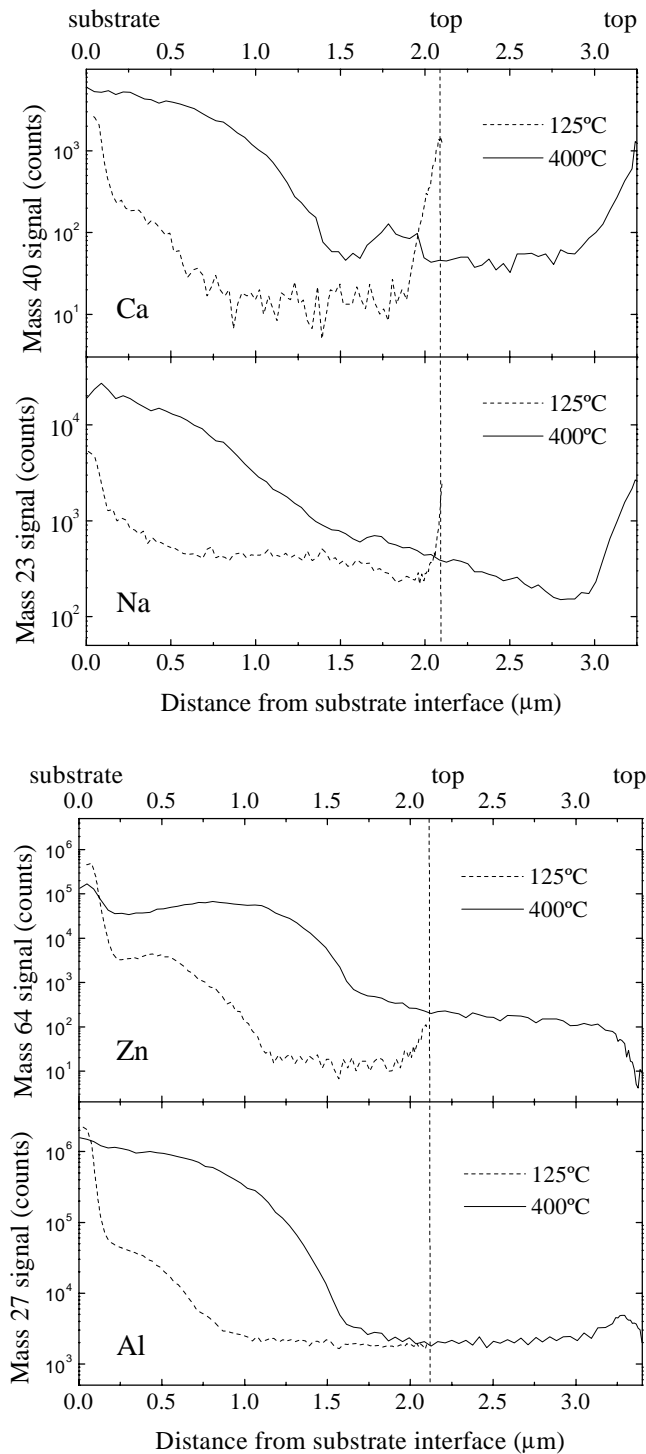


**Figure 5.4:** SIMS profiles of zinc and aluminium in samples grown onto AZO at different substrate temperatures. Profiles of sodium and calcium for the same samples.

### 5.1.2. Leakage currents

Thin film rectifying devices result often affected by leakage currents [Puigdollers, 1995b]. As shown in figure 5.5, when a reverse voltage is applied to a p-i-n device, the current which circulates is the reverse diode saturation current  $I_o$  plus leakage currents. We distinguish two kinds depending on the path which they follow:

- a lateral leakage current  $I_l$  mainly through the n-doped layer. It is well-known that in CVD processes, edges result not well defined [Tsai, 1987]. Therefore, the i- and n-layers grown on the p-layer could laterally contact the TCO. Furthermore, in multichamber systems the substrate must be transferred between each process, which usually cause important misalignments.
- a transverse leakage current  $I_t$  through the device due to the eventual formation of shunting paths or pinholes. These shunts usually originate from dust in the substrates, either prior to the deposition or formed during the CVD process from gas phase nucleation.

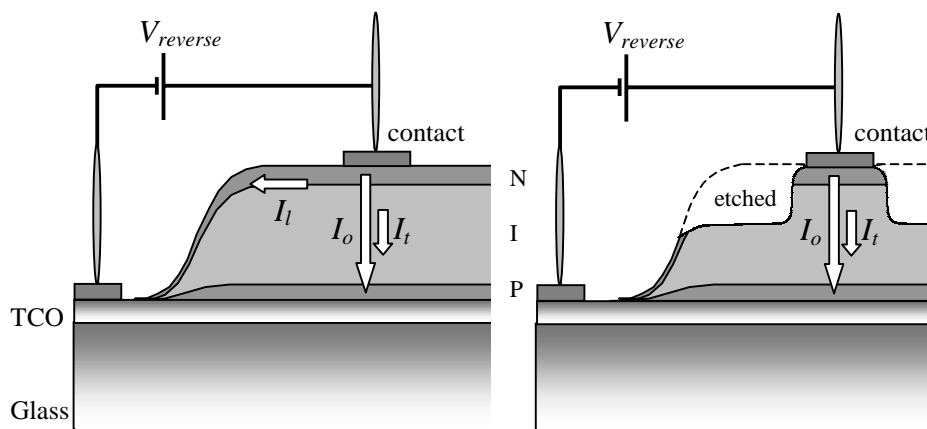


**Figure 5.5:** The lateral leakage current in thin film rectifying devices can be avoided by etching the material surrounding the device.

Either lateral or transverse leakage currents usually present an ohmic behaviour which allows them to be modelled by a parallel resistance  $\mathcal{R}_p$  shunting the device. As it was shown in figure 4.4 [Section 4.2.4], low values of  $\mathcal{R}_p$  could significantly degrade the open circuit voltage and fill factor at low-medium irradiances. The dominant kind of leakage current can be identified from the slope of the dark JV curve in reverse as a function of the contact size.

For transverse leakage currents,  $\mathfrak{R}_p \sim 1/S$  with  $S$  the area of the circular contact of radius  $r$ , i.e.  $S = \pi r^2$

$$\left. \frac{dj}{dV} \right)_{reverse} = \left. \frac{1}{S} \frac{dI}{dV} \right)_{reverse} = \frac{1}{S} \frac{1}{\mathfrak{R}_p} \sim const. \frac{1}{r^2} \frac{1}{1/r^2} \sim const. \quad (5.2)$$

whereas in the case of lateral leakage currents,  $\mathfrak{R}_p \sim \ln(a/r)$  with  $a$  the average distance between the contact and the lateral electrode (typically  $a \gg r$ )

$$\left. \frac{dj}{dV} \right)_{reverse} = \left. \frac{1}{S} \frac{dI}{dV} \right)_{reverse} = \frac{1}{S} \frac{1}{\mathfrak{R}_p} \sim const. \frac{1}{r^2} \frac{1}{\ln(a/r)} \sim const. \frac{1}{r^2} \quad (5.3)$$

which is the dependence that we actually observe in most of our p-i-n structures [Fig. 5.6].

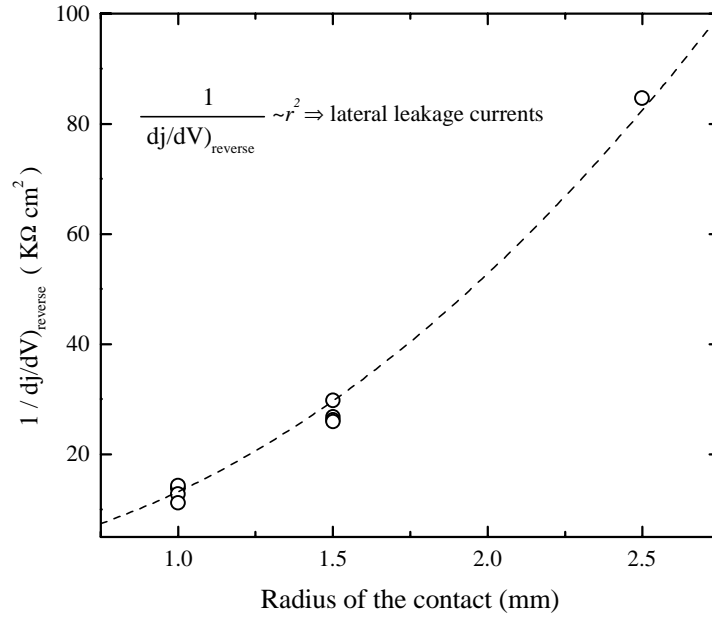


**Figure 5.6:** Reciprocal slope of the dark JV curve in reverse as a function of the contact size. The quadratic dependence indicates dominant lateral leakage currents.

Once the device has been obtained, transverse leakage currents can not be solved. By contrast, laser scribing reduces lateral leakage currents by cutting the n-doped layer around the contact. For that purpose Q-switched Nd:YAG lasers operating in doubled mode ( $\lambda = 0.53 \mu\text{m}$ ) are generally used in the case of a-Si:H technology [Schropp et al., 1998]. The group at University of Neuchâtel has also succeeded in laser scribing their laboratory nc-Si:H solar cells [Meier et al., 1998]. However, the implementation and upkeep costs of an operative laser scribing set-up is high. Besides, the limited linear speed of the laser scribing process imposes a throughput limitation in production lines. Alternatively, lateral leakage

currents can also be avoided by etching the material surrounding the device itself or, at least, the upper highly conductive n-doped layer. Etching could result faster than laser scribing and it is definitely cheaper. After trying wet-chemical and dry-plasma etching, we have found the second one cleaner and much more easy to control in the case of thin film devices. In collaboration with the Universitat Politècnica de Catalunya (UPC), we have satisfactorily dry-etched our nc-Si:H solar cells with a plasma of  $\text{CF}_4$  diluted into oxygen (20%) at a process pressure of 0.4 mbar. The resulting etch rate was around  $15 \text{ \AA/s}$  for an RF power of  $15 \text{ mW/cm}^2$ . Hence, less than half minute is necessary to completely etch the top n-doped layer of the cell with a typical thickness of  $300 \text{ \AA}$ .

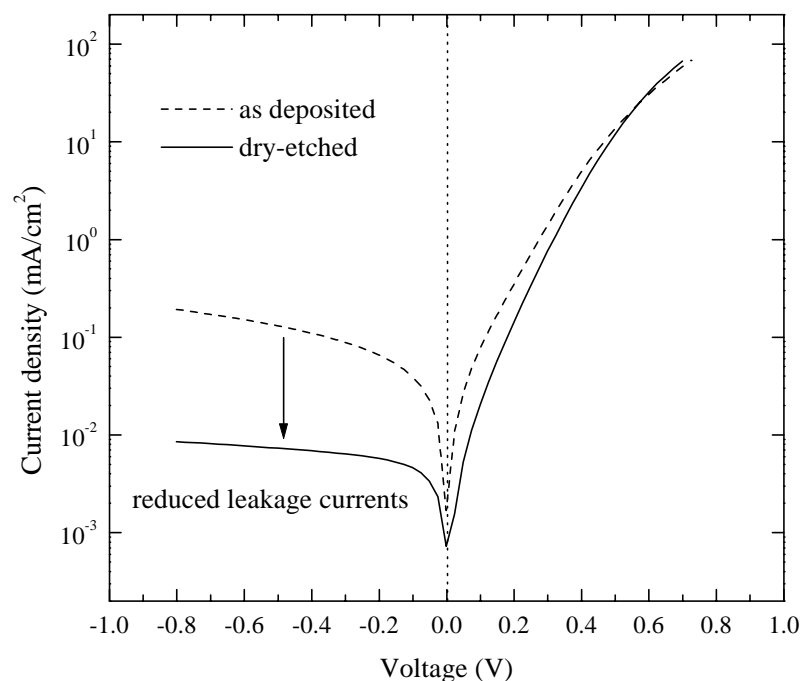


**Figure 5.7:** Dark current-voltage characteristics before and after dry-etching the device. Lateral leakage currents were clearly reduced.

### 5.1.3. Doped layers

On account of the preliminary character of our research, an special attention was paid to the undoped active layer in the p-i-n structure. Nevertheless, several series of p- and n-type nc-Si:H samples were deposited in order to select doped layers suitable for be incorporated in devices. These results are extensively reported in previous works[Peiró, 1999; Voz, 2000] but the most significant conclusions will be briefly pointed in this section. Doped layers were obtained by adding controlled amounts of diborane and phosphine to the silane-hydrogen gas mixture during the deposition[Section 2.1].

N-type layers suitable for device applications were obtained with phosphorous to silicon gas phase ratios in the order of 2%. The corresponding phosphorous to silicon solid phase ratios estimated by SIMS were around 0.1% which results in a gas to solid phase phosphorous incorporation efficiency of 5%. These layers presented room temperature dark conductivities ranging from 1 to 10  $\Omega^{-1}\text{cm}^{-1}$  and activation energies well below 0.1eV. Any significant dependence was not observed within the typical substrate temperature range (150-300°C) or when the hydrogen dilution was increased from 90 to 95%. The process pressure was around  $10^{-2}$  mbar.

On the other hand, in the case of p-doped layers, boron to silicon solid phase ratios as high as 1% were required to obtain room temperature dark conductivities ranging from 0.5 to 5  $\Omega^{-1}\text{cm}^{-1}$  and activation energies below 0.1eV. These heavily p-doped layers could be achieved for gas phase boron to silicon ratios in the order of 1%. Hence, the gas to solid phase boron incorporation efficiency approached 100%. This result could be explained by the well-known thermal dissociation of diborane [Tarui et al., 1989]. Whereas silane, hydrogen or phosphine are only dissociated by the hot filament, diborane is additionally dissociated at the hot surfaces inside the deposition chamber. Amorphisation at such high p-type doping levels could be prevented by lowering the substrate temperature to 150°C and increasing the hydrogen dilution to 95%. The crystallinity enhancement for decreasing substrate temperatures could seem surprising, since higher crystallinity is usually expected when increasing the substrate temperature. However, this effect could be explained by structural changes when less hydrogen is incorporated due to a higher substrate temperature. Actually, it is well established that atomic hydrogen favours the crystalline growth either by etching stressed bonds [Tsai et al., 1988] or increasing the diffusion length of the growth precursors [Matsuda, 1983]. The process pressure remained unchanged around  $10^{-2}$  mbar.

The optimised doped layers could be scaled to thicknesses proper for devices maintaining good structural and electrical properties. Our preliminar p-i-n structures incorporate doped layers with typical thicknesses around 500 Å. This relatively high value ensures good rectifying characteristics and prevents from shunting paths. However, significant optical losses due to the absorption within the p-layer limit the maximum expected efficiency of such devices [Section 3.1.3].

## 5.2. The role of the active layer in the device performance

### 5.2.1. The microdoping approach

The incorporation of contaminants during the growth of the intrinsic layer of the p-i-n structure not only increases the concentration of recombination centres, but also results in the screening of the internal electric field. Both effects directly worsen the drift length [Eq. 4.2] and consequently the collection of photogenerated carriers. Therefore, the reduction of contaminant sources is a major problem to be solved, specially in low pressure deposition techniques such as PECVD or HWCVD. Many aspects can cause an undesired contamination:

- a) the cleanness of the chamber and the gas lines. The outgassing rate has to be minimised as much as possible. Accessories inside the chamber must be specific for high vacuum applications and a special care of the heater design must be taken
- b) the cleanness of the substrates and its stability. Substrates must be degreased and carefully cleaned. They must resist the deposition conditions without diffusing species into the growing layer and they should not suffer chemical reactions which alter their properties
- c) the purity of the gas bottles. Often it is necessary to use additional gas purifiers or selective gas getters to enhance the purity of the mixture which enters the deposition chamber
- d) the pumping system. A good base pressure is certainly necessary for electronic applications and backstreaming has to be avoided

But sometimes contamination is intimately related to the deposition process. For instance, the filament used in HWCVD is a potential source of tungsten contamination. In such cases the only possibility is to try to minimise or, if possible, compensate its effects. Conceptually, p-type microdoping could counterbalance the as grown n-type character of nc-Si:H usually associated to oxygen contamination [Torres et al., 1996]. Actually, several shallow donor levels ( $E_C - E_D \leq 0.14$  eV) which could be attributed to oxygen were resolved by DLTS in our samples [Stöger et al., 1999]. We have certainly found that low p-type doping levels ( $\sim 10^{19}$  cm<sup>-3</sup>) yield activation energies near midgap and lower room temperature dark conductivities [Voz et al., 2000]. When this compensated samples are

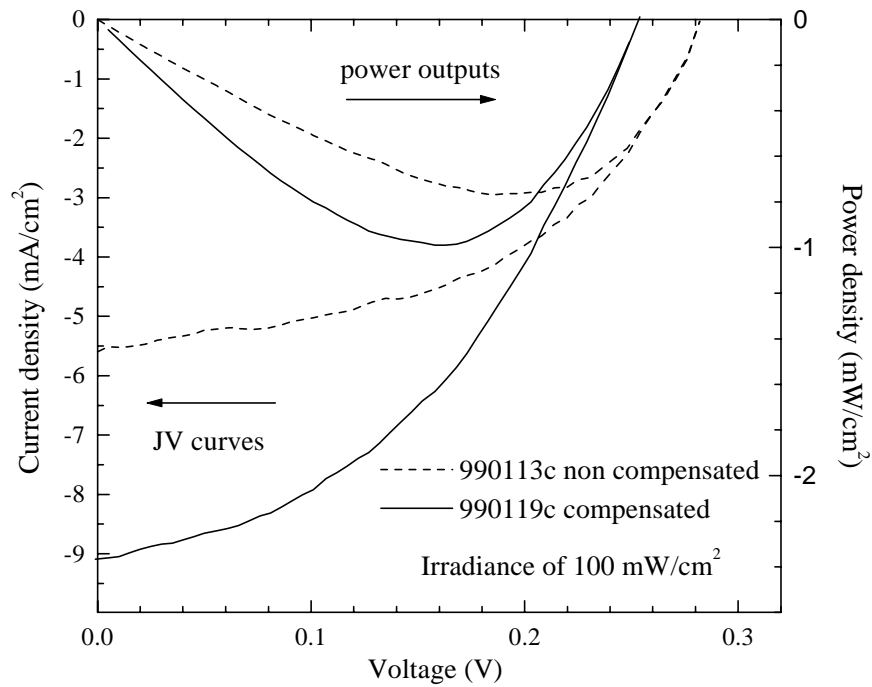
incorporated as active layers in p-i-n structures, the negatively charged acceptors due to the boron incorporation compensate the positively charged donors due to contaminants. As a result, there is a reduction in the charged trap density and consequently, the internal electric field within the active layer is enhanced. This approach was first successfully implemented in a nanocrystalline photovoltaic devices by the group at University of Newchâtel[Meier et al., 1994]. We have also tried to obtain compensated p-i-n solar cells by depositing the intrinsic layer with controlled low flows of diborane[Table 5.2].

Figure 5.8 compares the JV curves of a compensated and non compensated cell under an irradiance of  $100 \text{ mW/cm}^2$ . The short circuit current density is clearly raised in the compensated cell whereas both fill factor and open circuit voltage are slightly better for the non compensated device. Since diffusion is expected to play a more important role in the non compensated device, it can be halfway between a p-i-n and a p-n (actually  $p^+ - n - n^+$ ) structure, which would explain the improved open circuit voltage and fill factor.

**Table 5.2:** Compensated p-i-n structures compared with non compensated ones for different silane flows. The short circuit current and open circuit voltage were measured under an irradiance of  $100 \text{ mW/cm}^2$ . They are grouped in low flow-non compensated, low flow-compensated, high flow-non compensated, high flow-overcompensated and high flow-compensated.

| Cell name | SiH <sub>4</sub> /H <sub>2</sub> flows<br>(sccm) | B/Si ratio<br>(gas phase) | Thickness<br>( $\mu\text{m}$ ) | $j_{sc}$<br>(mA/cm <sup>2</sup> ) | $V_{oc}$<br>(V) | $r_d$<br>( $\text{\AA}/\text{s}$ ) |
|-----------|--|---------------------------|--------------------------------|-----------------------------------|-----------------|------------------------------------|
| 981127c   | 1 / 19   | 0                         | 2.4                            | 5.5                               | 0.26            | 1.6                                |
| 990113c   | 1 / 19   | 0                         | 1.4                            | 5.6                               | 0.28            | 1.7                                |
| 990119c   | 1 / 19   | $10^{-4}$                 | 0.96                           | 9.1                               | 0.25            | 0.8                                |
| 990115c   | 1 / 19   | $10^{-4}$                 | 1.06                           | 7.8                               | 0.23            | 0.9                                |
| 990319c   | 4 / 76   | 0                         | 2.15                           | 6.42                              | 0.27            | 3.6                                |
| 990311c   | 4 / 76   | $10^{-4}$                 | 2.5                            | 1.51                              | 0.16            | 2.4                                |
| 990323c   | 4 / 76   | $10^{-5}$                 | 2.1                            | 9.5                               | 0.25            | 2.5                                |

In figure 5.9 we compare the spectral responses of compensated and non compensated structures obtained with low gas flows. The compensated cell was not too far from the optical limit for long wavelengths while the non compensated one showed a much poorer collection. Losses in the short wavelength range are mainly due to the optical absorption of the p-doped layer and to interface recombination.



**Figure 5.8:** JV curves and power outputs for the compensated 990119c and non compensated 990113c p-i-n structures.

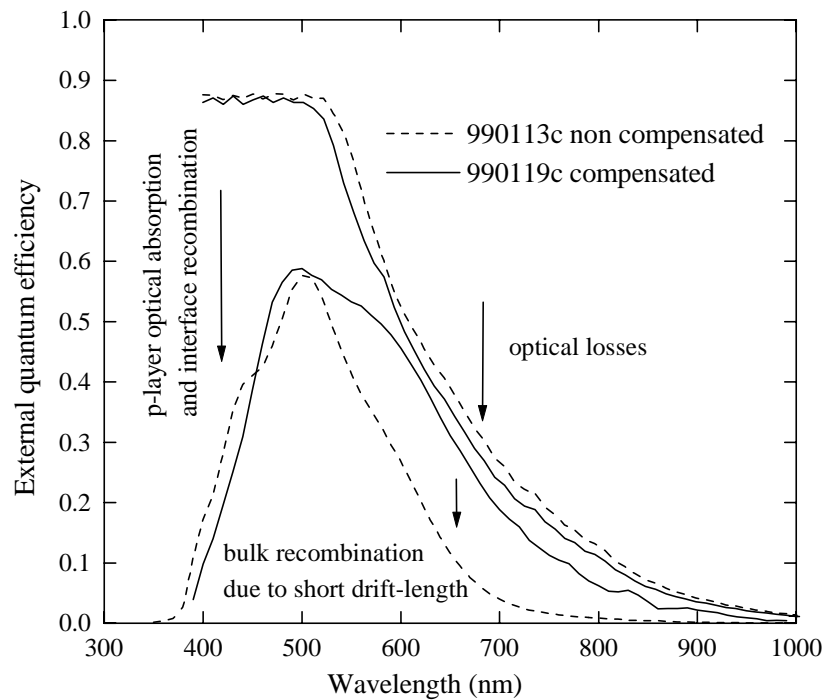


**Figure 5.9:** External quantum efficiency for the compensated 990119c and non compensated 990113c p-i-n structures. The estimated optical absorptances of these devices are also plotted.

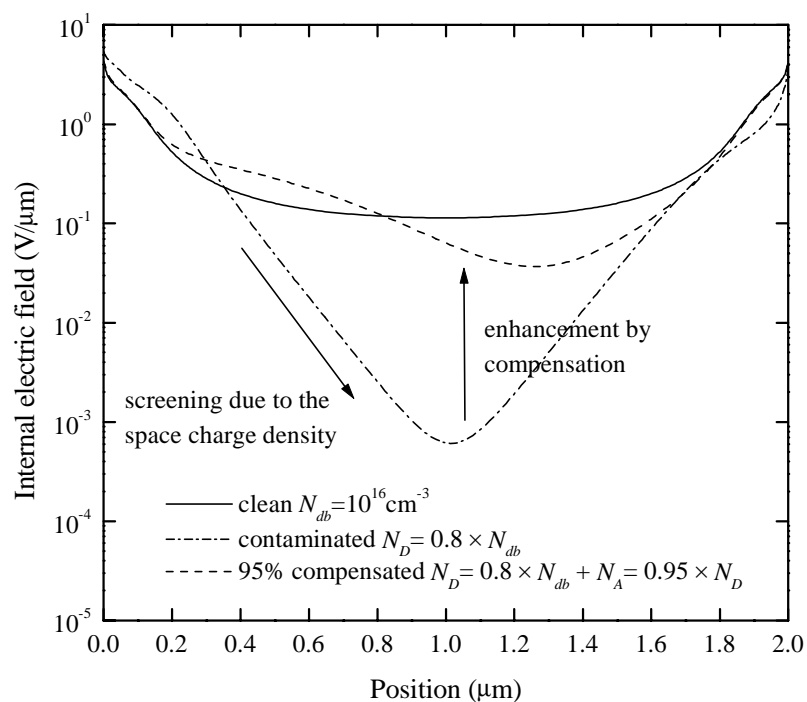


**Figure 5.10:** Simulated internal field profile in equilibrium for a clean (not contaminated), contaminated ( $8 \times 10^{15} \text{ cm}^{-3}$  donors) and 95% compensated ( $7.6 \times 10^{15} \text{ cm}^{-3}$  acceptors) p-i-n structures.

Some calculations were done to get a further understanding of the results. Figure 5.10 shows the internal field profile in equilibrium obtained by numerical simulation for an ideally clean, contaminated and compensated p-i-n structures. The density of dangling bonds, estimated from PDS, was fixed to  $10^{16} \text{ cm}^{-3}$  in any case whereas the concentration of donors in the contaminated cell was chosen  $8 \times 10^{15} \text{ cm}^{-3}$ . The 95% compensated device was simulated by adding an acceptor density of  $7.6 \times 10^{15} \text{ cm}^{-3}$ . Note the drastically screened field of the non compensated cell. Though the field is more intense near the p-i (actually  $p^+ \text{-} n$ ) interface, in the middle of the active layer it is almost four orders of magnitude weaker than in either the clean or the compensated cell. Therefore, electron-hole pairs generated far from the interfaces are hardly separated by drift and only diffusion can help to collect them. The low mobility of nanocrystalline silicon does not allow diffusion alone to be enough to efficiently collect the photogenerated carriers [Section 4.1]. This fact explains the low response for long wavelengths of non compensated p-i-n structures which mainly collect those pairs generated near the p-i interface.

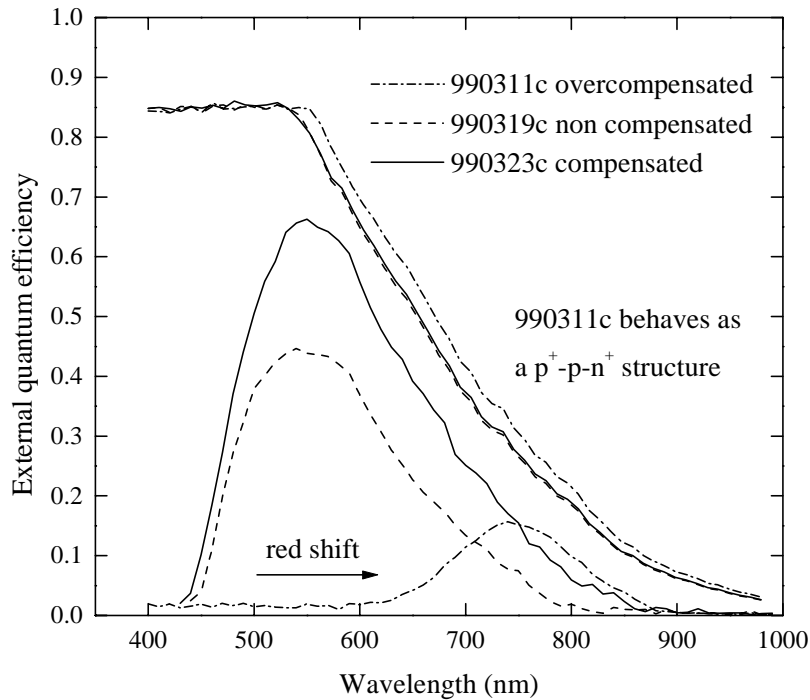


**Figure 5.11:** External quantum efficiencies of the structures deposited with high gas flows compared to their optical absorptances. The 990319c was non compensated while the compensated cell 990323c showed a clearly enhanced collection. The low and shifted response of the 990311c structure points to overcompensation.

We note that the gas phase B/Si ratio that efficiently compensates with a silane flow of 1 sccm is not proper for 4 sccm, when the deposition rate is greater. Instead, the 990311c solar cell showed disastrous results due to overcompensation. The spectral response is clearly shifted to longer wavelengths [Fig. 5.11], which indicates that the electric field at the p-i interface is lowered at the expense of the i-n interface. We actually have a  $p^+ - p - n^+$  structure illuminated from the  $p^+$  side. If the B/Si ratio is reduced an order of magnitude, as in the 990323c cell, an improved short circuit current is recovered and the spectral response points again to a better collection for long wavelengths. The high flow compensated structures grew three times faster than those obtained with low flows, which leads to a lower incorporation of contaminants [Kroll et al., 1995]. This fact, joined to a possible blower effect of the gas inlet near the substrate, could explain a much cleaner active layer when it is obtained with high gas flows [Section 5.2.3]. In fact, the non compensated reference cell obtained with high gas flows (990319c) already showed a significantly better short circuit current than the low flow non compensated cell with a similar thickness (981127c). Therefore, in order to compensate, the microdoping level must be also accordingly lowered.

### 5.2.2. Influence of the filament temperature

One of the main unsolved questions related to the HWCVD technique is the possibility of tungsten incorporation into the growing layer. If it is present, tungsten contamination should depend on the filament temperature. Concentrations of tungsten with clear detrimental electronic effects are hardly detectable by compositional analysis, even for most SIMS systems [Delgado et al., 1990]. By contrast, as it was pointed in section 3.2.4, a higher density of charged centres is deduced from the depletion capacitance of pseudo-Schottky contacts grown with higher filament temperatures. Besides, two donor levels were resolved by DLTS which could be attributed to contamination with tungsten ( $E_C - E_D = 0.336\text{eV}$ ) and interstitial copper ( $E_C - E_D = 0.185\text{eV}$ ) [Stöger et al., 1999]. This last element could come from impurities in the filament or more probably, from copper parts of the filament holder. Moreover, copper could be also detected by SIMS in samples grown at high filament temperatures. Therefore, several cells were obtained with exactly the same technological parameters except for the temperature of the filament when the active layer was grown [Table 5.3].

These cells were obtained paying special attention to the cleanness of the substrates and the outgassing rate of the chamber in order to avoid any additional difference than the filament temperature. Moreover, they were obtained consecutively, without any process between them, in order to discard any evolution of the wire. Though devices obtained at higher filament temperatures resulted slightly thicker due to a higher dissociation of the gases, this very small difference should not be representative when comparing the characteristics of the cells. By contrast, clear differences were observed in the photovoltaic performance, which worsens when the filament temperature is increased. We observe a more drastic effect at higher process pressures [Table 5.3], probably because these conditions are more aggressive for the filament. We must consider that the tungsten incorporation into the growing layer could be not only due to just evaporation from the filament but also to chemical reactions with the growing precursors. X-ray diffraction of filaments used in deposition processes evidenced the eventual formation of tungsten silicides which certainly have a higher vapour pressure than clean tungsten.

**Table 5.3:** Effect of the filament temperature on the device photovoltaic response. The short circuit current, open circuit voltage and fill factor were measured under an irradiance of 100 mW/cm<sup>2</sup>. The solar cells are grouped in low and high process pressure.

| Cell name | Filament Temperature (°C) | Process Pressure (mbar) | Thickness (μm) | $V_{oc}$ (V) | $j_{sc}$ (mA/cm <sup>2</sup> ) | $FF$ (%) |
|-----------|---------------------------|-------------------------|----------------|--------------|--------------------------------|----------|
| 990319c   | 1750                      | $7 \cdot 10^{-3}$       | 2.1            | 0.275        | 6.42                           | 47       |
| 990322c   | 1600                      | $7 \cdot 10^{-3}$       | 1.8            | 0.34         | 8.3                            | 48       |
| 990414c   | 1750                      | $3.5 \cdot 10^{-2}$     | 2.2            | 0.27         | 4.1                            | 49       |
| 990409c   | 1600                      | $3.5 \cdot 10^{-2}$     | 2.0            | 0.39         | 9.12                           | 56       |

Since the tungsten level detected is relatively deep in the band gap, it could affect in the device not only as a carrier trap but also as recombination centre. Numerical simulations indicated that the open circuit voltage is clearly dependent on the concentration of recombination centres within the active layer. This correlation was clearly observed in the VIM data of these cells[Fig. 5.12]. Moreover, the respective collection voltages deduced from the  $R_{sc}$ - $j_{sc}$  dependence at medium-high illumination levels also pointed to a better collection for the low filament temperature device. While the solar cell 990409c presented a collection voltage  $V_c$  of 3.4 V, for 990414c it was only 1.0 V which indicates much higher recombination losses within its active layer.

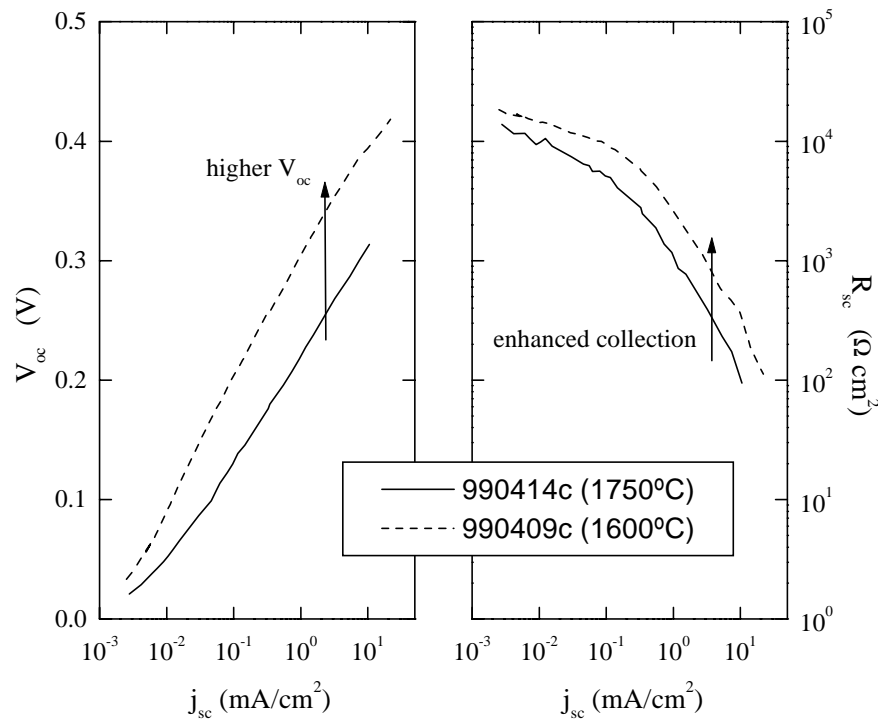


**Figure 5.12:** VIM results for high (990414c) and low filament temperature (990409c) solar cells.

As shown in figure 5.13, the much lower spectral response of the high filament temperature device indicates a clearly worsened collection, specially for longer wavelengths, when carriers are photogenerated far from the interfaces.

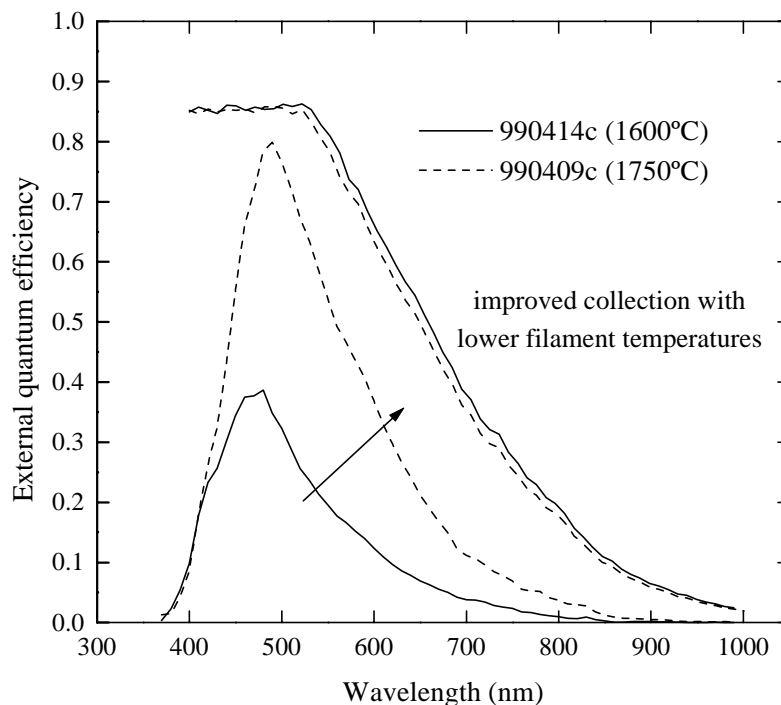


**Figure 5.13:** External quantum efficiency of the high (990414c) and low filament temperature (990409c) solar cells compared with the optical absorptances of these devices.

### 5.2.3. Cleaner deposition conditions

The process pressure at which the intrinsic layer of the p-i-n structure is obtained has arisen as a key parameter in order to improve the device performance. One of the main effects of increasing the process pressure is to rise the deposition rate. Higher gas flows also help to increase the deposition rate. In fact, at medium-high process pressures ( $>10^{-2}$  mbar) we have observed a linear increase of the deposition rate with the silane flow. Actually, it is the silane partial pressure which mainly determines the deposition rate[Peiró, 1999] and it depends not only on the silane flow but also on the pumping cross section, which we vary to fix the total process pressure by means of a butterfly valve[Section 2.1]. Since evidences of the incorporation of contaminants in the material were found by different techniques, a faster growth would reduce the concentration of contaminants in the active layer[Section 3.2.3]. If we assume that there is a determined flow of contaminants per second and unit area arriving to the surface where the film grows, then the

concentration of contaminants is expected to be proportional to  $1/r_d$ [Kroll et al., 1995], where  $r_d$  is the deposition rate. Furthermore, at higher pressures the gas phase transport is more laminar and this effect could help the gas inlet to blow away contaminants which are supposed to come mainly from the walls of the reactor. This idea has been refined and used at the LPICM of the École Polytechnique in Paris by means of a confinement box[Guillet, 1998]. In their set-up the gas inlet, filament and substrates are located inside a clean semiclosed stainless steel box. The pressure in this region results slightly increased which partially avoids contaminants outgassed from the reactor walls to reach the filament, be dissociated and arrive to the substrate.

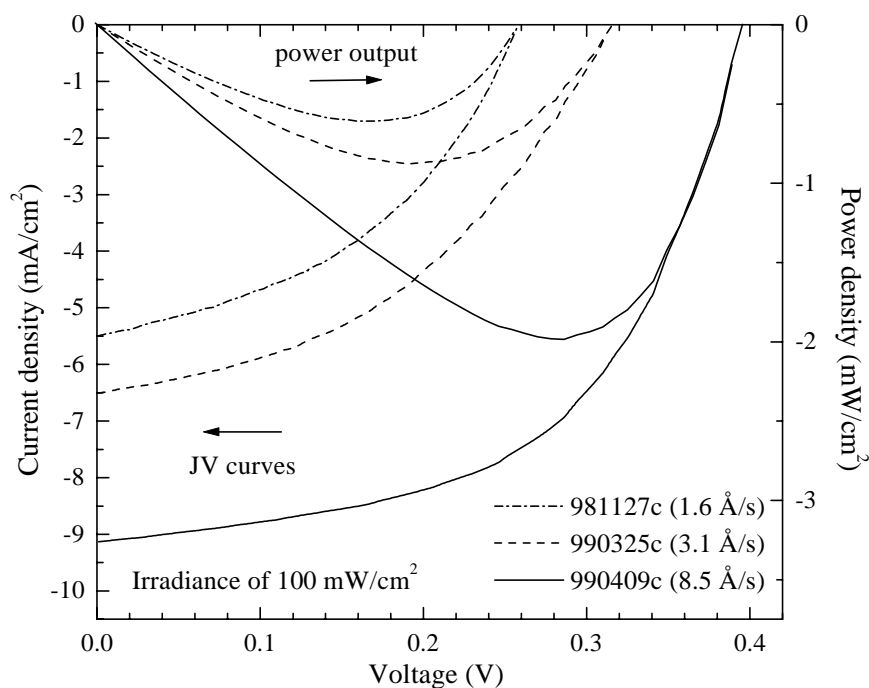
Table 5.4 compares p-i-n structures obtained with the same nominal hydrogen dilution but different flows and process pressures. Note the clear correlation between the short circuit current and the deposition rate. The later can be enhanced either by increasing the process pressure or the silane flow at a fixed process pressure. Both options lead to an increase in the silane partial pressure which actually determines the deposition rate.

**Table 5.4:** Solar cells obtained with different process pressures and gas flows. The short circuit current density, open circuit voltage and fill factor were measured under an irradiance of  $100 \text{ mW/cm}^2$ . They are grouped in low flow-low pressure, high flow-low pressure and high flow-high pressure, i.e., they are grouped by the deposition rate.

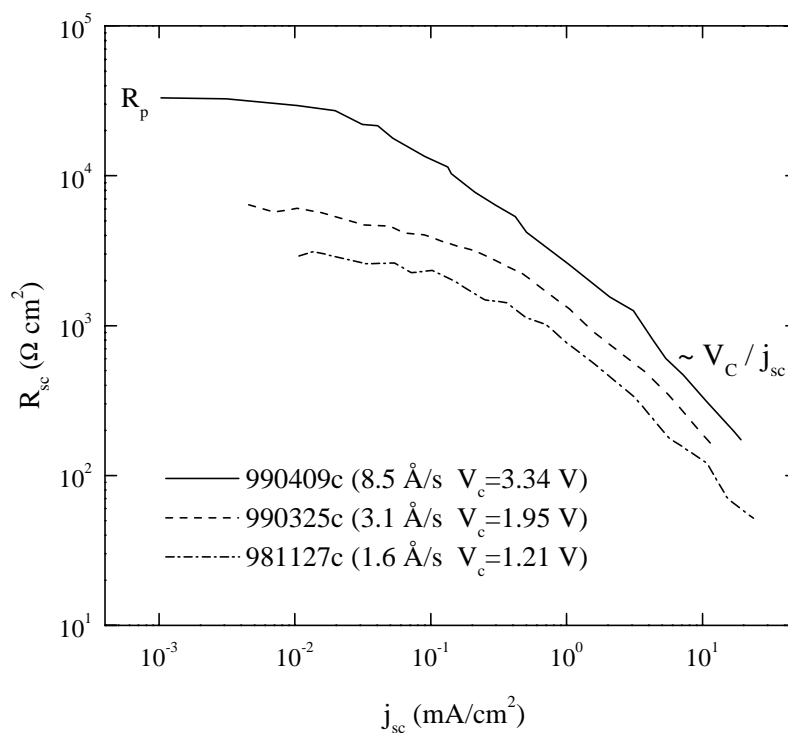
| Cell name | SiH <sub>4</sub> /H <sub>2</sub><br>Flows (sccm) | Process pressure<br>(mbar) | Thickness<br>( $\mu\text{m}$ ) | $j_{sc}$<br>(mA/cm <sup>2</sup> ) | $V_{oc}$<br>(V) | FF<br>(%) | $r_d$<br>( $\text{\AA}/\text{s}$ ) |
|-----------|--|----------------------------|--------------------------------|-----------------------------------|-----------------|-----------|------------------------------------|
| 981127c   | 1 / 19   | $7 \cdot 10^{-3}$          | 2.4                            | 5.5                               | 0.26            | 43        | 1.6                                |
| 990113c   | 1 / 19   | $7 \cdot 10^{-3}$          | 1.4                            | 5.6                               | 0.285           | 48        | 1.7                                |
| 990325c   | 4 / 76   | $7 \cdot 10^{-3}$          | 2                              | 6.1                               | 0.305           | 47        | 3.1                                |
| 990319c   | 4 / 76   | $7 \cdot 10^{-3}$          | 2.15                           | 6.42                              | 0.275           | 48        | 3.5                                |
| 990326c   | 4 / 76   | $3.5 \cdot 10^{-2}$        | 1.5                            | 9.54                              | 0.375           | 53        | 7.2                                |
| 990409c   | 4 / 76   | $3.5 \cdot 10^{-2}$        | 2.2                            | 9.12                              | 0.39            | 56        | 8.5                                |

Figure 5.14 compares the JV curves for three cells in table 5.4 measured under an irradiance of  $100 \text{ mW/cm}^2$ . The photovoltaic performance is clearly enhanced when the deposition rate is higher, which confirms that the main limiting factor in the initial efficiency of our cells is probably the undesired contamination incorporated within the active layer during its growth. Accordingly, in the  $R_{sc}$ - $j_{sc}$  plot from VIM data[Fig. 5.15] we observe that the collection voltage  $V_c$  rises with the deposition rate. We obtain collection voltages of 3.34, 1.95 and 1.21 V for the solar cells 990409c, 990325c and 981127c respectively. As a comparison, a typical laboratory amorphous silicon cell with 10.7% initial efficiency presented a collection voltage of 31.1 V which lowered to 5.09 V in its

degraded state[Merten et al., 1998]. The external quantum efficiency of these cells is also shown in figure 5.16.



**Figure 5.14:** JV curves and power outputs under an irradiance of  $100 \text{ mW/cm}^2$  for three solar cells obtained at different deposition rates. The efficiency is clearly correlated with the deposition rate.



**Figure 5.15:**  $R_{sc}$  as a function of  $j_{sc}$  from VIM data for the same solar cells in figure 5.14. The collection voltage clearly increases with the deposition rate.

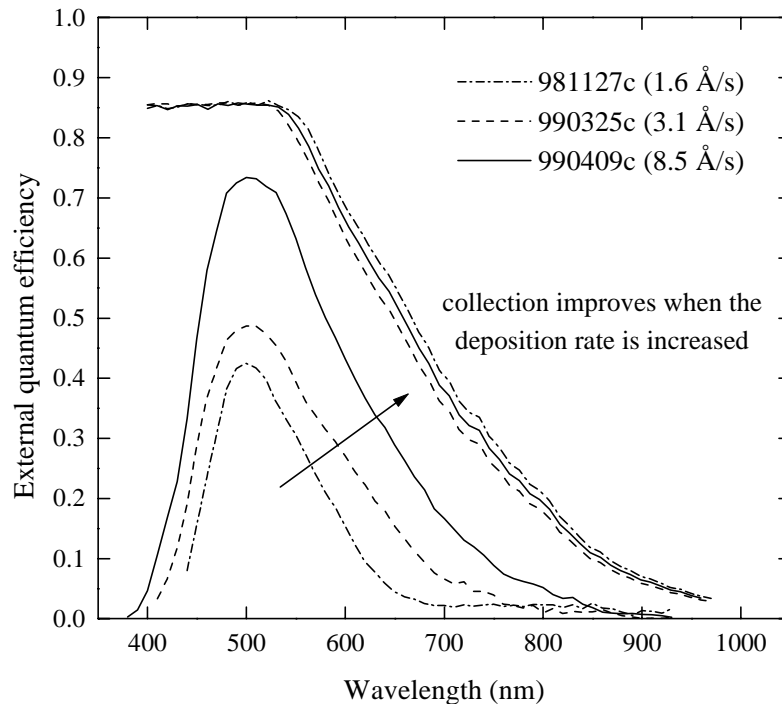


**Figure 5.16:** External quantum efficiencies of the same cells plotted in figures 5.14 and 5.15 compared to their optical absorptances. The quantum efficiency is enhanced when the deposition rate is increased.

#### 5.2.4. Influence of the substrate temperature

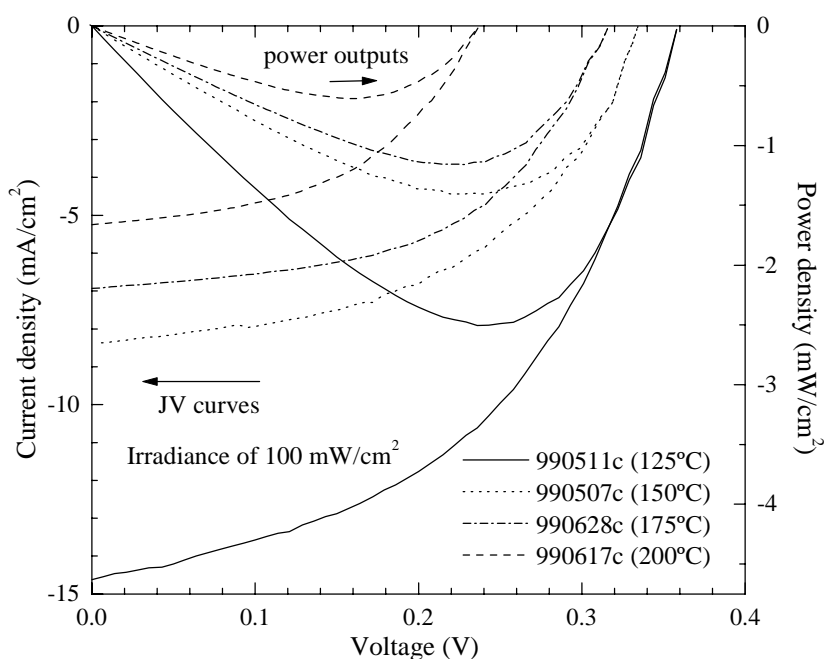
It is widely known that the substrate temperature during growth clearly influences the hydrogen content in amorphous silicon thin films [Knights et al., 1980]. Since hydrogen passivates dangling bonds in defective silicon networks [Street, 1991], it plays a fundamental role to reduce the density of deep states in the band gap, which is the main recombination path in this kind of semiconductors. Electron spin resonance studies also identify as dangling bonds the deep distribution of states in the band gap of nanocrystalline silicon [Veprek et al., 1983] which cause the subgap optical absorption [Jackson W.B., 1983]. In this case, dangling bonds are expected to be concentrated at the grain boundaries and in the amorphous phase present in the samples. It has been demonstrated the passivation role of hydrogen by thermal annealing which leads to higher subgap optical absorption [Beck et al., 1996] and spin densities [Lips et al., 1998] when hydrogen is effused from the film.

The Si-H wagging absorption band of infrared transmittance spectra also indicate that the hydrogen concentration in the films decreases when they are grown at higher substrate temperatures[Peiró, 1999]. This result is correlated with a higher subgap optical absorption measured by PDS which indicates an increase in the density of dangling bonds.

**Table 5.5:** Effect of the substrate temperature on the device photovoltaic response. The short circuit current density, open circuit voltage and fill factor were measured under an irradiance of  $100 \text{ mW/cm}^2$ .

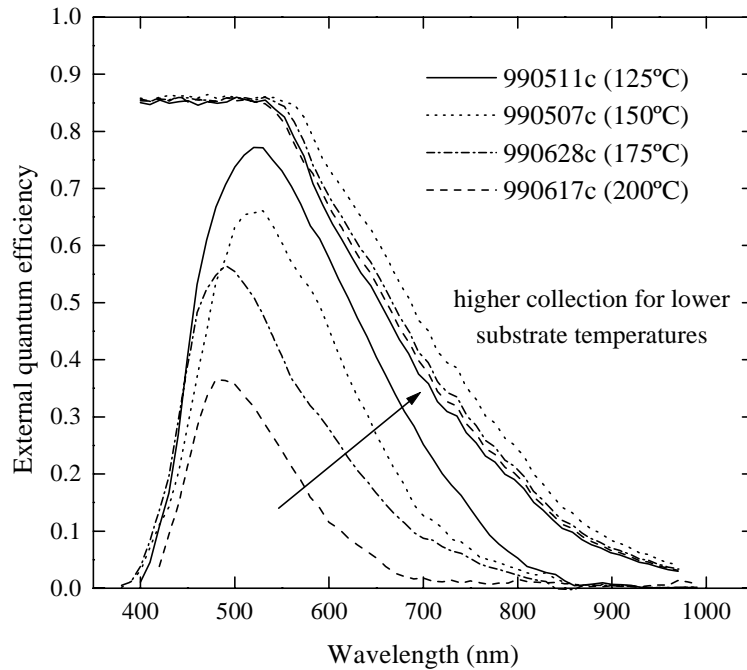
| Cell name | Substrate Temperature ( $^{\circ}\text{C}$ ) | Thickness ( $\mu\text{m}$ ) | $V_{oc}$ (V) | $j_{sc}$ ( $\text{mA/cm}^2$ ) | FF (%) |
|-----------|--|-----------------------------|--------------|-------------------------------|--------|
| 990511c   | 125  | 2.1                         | 0.36         | 14.6                          | 48     |
| 990507c   | 150  | 2.9                         | 0.325        | 8.35                          | 45     |
| 990628c   | 175  | 2.4                         | 0.315        | 6.93                          | 53     |
| 990617c   | 200  | 2.25                        | 0.24         | 5.25                          | 48     |

Table 5.5 shows a series of cells where the intrinsic layer was obtained with increasing substrate temperatures. We observe that the photovoltaic performance of these devices clearly improves when the active layer is grown at lower substrate temperatures[Fig. 5.17], i.e., when it is more hydrogen passivated and the density of dangling bonds is lower. A reduced defect density means both an enhanced internal electric field and lower recombination losses. Figure 5.18 shows how the external quantum efficiency of these solar cells clearly worsen when the substrate temperature is increased.



**Figure 5.17:** JV curves and power outputs for the solar cells in table 5.5. The efficiency clearly worsens when the substrate temperature is increased.

On the other hand, a higher diffusion of contaminants from the substrate at higher temperatures should not be discarded [Fig. 5.4]. This detrimental effect would additionally contribute to ruin the performance of devices grown at higher substrate temperatures. Moreover, a higher outgassing rate inside the deposition chamber is expected for higher temperatures thus causing a higher incorporation of contaminants.



**Figure 5.18:** External quantum efficiencies and estimated optical absorptances of the cells in the substrate temperature series [Table 5.5].

### 5.3. Stability of devices

As it was previously discussed in section 3.2.6, the feared Staebler-Wronski effect is fortunately not important in nc-Si:H samples. By contrast, the chemical instability of this material could compromise its suitability for reliable photovoltaic devices. Independently of the deposition technique, undoped nc-Si:H layers become clearly n-type due to post-oxidation as evidenced by electrical and compositional characterisations [Section 3.2.6]. Moreover, this effect turned out to be enhanced by intense illumination [Kondo et al., 1998] which thus could accelerate the degradation of the device under operation. In spite of that, entirely nc-Si:H solar cells by VHF-PECVD have been reported without any significant degradation after several operating months [Meier et al., 1998b]. It seems that the back doped layer and contact electrode capping the undoped active layer should be thank for this fortunate result. We have also observed an undoubtful enhancement in the stability of nc-

Si:H p-i-n solar cells by HWCVD by increasing the thickness of the n-doped layer [Fig. 5.19]. However, to date we can not ensure reliable long-term stabilities without encapsulating the device. Besides, too thick doped layers could lead to a high parasitic series resistance. Nevertheless, this problem could be not so dramatic as it seemed at first sight. Several studies point to indeed thin (~10 nm) a-Si:H layers by PECVD as efficient capping layers to prevent post-oxidation [Kondo et al., 1998]. However, a-Si:H by HWCVD seems to be less efficient as a barrier to oxygen diffusion [Brühne et al., 2000]. Actually, the much lower ion bombardment in HWCVD processes compared to PECVD ones, could lead to lower density materials which are thus more permeable to contaminants. Probably this is one of the reasons why the group at the Debye Institute grows both doped layers in their nc-Si:H p-i-n solar cells by PECVD instead of HWCVD [Schropp et al., 1999]. Anyway, the deposition of a thin n-doped a-Si:H layer by PECVD to encapsulate the entirely nc-Si:H solar cell obtained by HWCVD would not be a dramatic drawback.

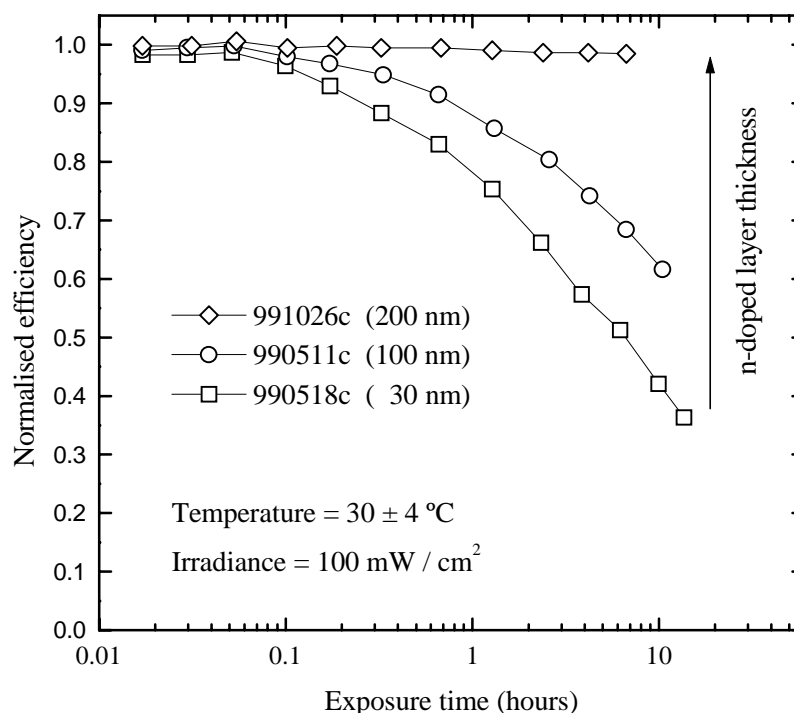


**Figure 5.19:** Normalised efficiency of devices under light soaking. Steadily increasing stabilities are achieved by increasing the thickness of the n-doped layer which seems to cap the undoped active layer.



# Conclusions

1. Thin film crystalline silicon solar cells have recently arisen as a very promising alternative to the worn out amorphous silicon or the save but costly wafer technologies. As the ratio of the drift length to the active layer thickness becomes the factor determining the collection efficiency in thin film p-i-n structures, materials of lower quality could be used. Therefore, microcrystalline and nanocrystalline silicon emerge as exciting new materials with potentially higher improvement perspectives than other traditional photovoltaic materials. In addition, this kind of small-grain silicon films can be grown at moderate temperatures allowing the use of low cost foreign substrates such as glass or even transparent polymer foils.
2. Among the different deposition techniques to obtain thin film hydrogenated nanocrystalline silicon, the Hot-Wire Chemical Vapour Deposition has allowed the highest deposition rates ever reported to date. Deposition rates in the range of several tens of Å/s could be easily achieved maintaining reasonably good microstructural properties over large areas. Furthermore, a HWCVD set-up is much easier to handle and the implementation and upkeep costs are much lower than in a PECVD one. However, multichamber set-ups are required in order to grow the undoped active layer of p-i-n structures in a separate chamber to avoid cross-contamination.
3. The optimised hydrogenated nanocrystalline silicon layers by Hot-Wire CVD with high crystalline fractions (>90%) showed an optical absorption coefficient significantly higher than that of single crystal silicon. This enhanced optical absorption could not be fully explained by the amorphous phase in the samples but elastic light scattering mechanisms should be considered. Higher process pressures (>10<sup>-2</sup> mbar) enhance the columnar growth along the [220] crystalline direction, as observed by X-ray diffraction and Scanning Electron Microscopy. This microstructure leads to highly textured film surfaces with root mean square roughness in the range of a few per cent (~2%) of the

film thickness. The optical absorption enhancement in the near infrared could be quantified in around a factor 2 for typical samples, which certainly causes an advantageous increase in photogeneration.

4. Several electrical characterisations evidence an undesired as grown n-type character in undoped nanocrystalline silicon samples obtained at low deposition rates ( $\sim 2 \text{ \AA/s}$ ). The dark conductivity activation energy is far from midgap and the sign of the thermopower indicates that the electronic transport is certainly due to free electrons in the conduction band. In addition, very low p-type doping levels (solid phase B/Si ratio  $\sim 10^{-4}$ ) lead to higher activation energies as well as lower room temperature dark conductivities. A misleading increase in the Steady State Photoconductivity  $\mu\tau$ -product is observed for the less intrinsic samples. This effect is definitely not due to better transport properties but to a change in the thermal occupation of recombination centres which results in a longer lifetime for the majority carriers. The lifetime of minority carriers, which actually limits the collection efficiency in photovoltaic devices, results undoubtedly degrade in the less intrinsic samples.
  
5. By increasing the deposition rate over  $5 \text{ \AA/s}$ , dark conductivity activation energies around midgap were obtained. At one time, the density of charged centres in the gap could be lowered from  $10^{17}$  to  $10^{16} \text{ cm}^{-3}$ , as determined from the voltage dependence of the depletion capacitance of Schottky structures. These results could be explained by the undesired incorporation of contaminants which could be attributed either to gas phase impurities or to metallic components evaporated from the wire. Actually, several shallow donor levels which could be attributed to oxygen ( $E_C - E_D \leq 0.14 \text{ eV}$ ) and copper ( $E_C - E_D \leq 0.185 \text{ eV}$ ) were resolved by Deep Level Transient Spectroscopy in our samples. In any case, the concentration of contaminants incorporated into the film would be inversely proportional to the deposition rate.

6. Fortunately, the Staebler-Wronski effect does not play an important role in the stability of nanocrystalline silicon by Hot-Wire CVD. However, a relative chemical instability leading to an increased n-type character is observed for samples exposed to air for a long time. A significant post-oxidation through the surface of the nanocrystalline silicon films seems to be the reason of such instability. Besides, this post-oxidation is somehow accelerated under high irradiances when photons are able to break weak bonds thus favouring oxidation.
7. The front electrode selected for our superstrate solar cells was aluminium-doped zinc oxide (AZO) on account of its excellent chemical stability against atomic hydrogen. On the contrary, fluorine-doped tin oxide or tin-doped indium oxide do not withstand the strongly reducing ambient during Hot-Wire processes. The AZO coatings were obtained by magnetron sputtering from a ceramic target in the load-lock chamber. The optimised front electrodes presented sheet resistances around  $10 \Omega/\square$  and optical transmittances over 85% in the wavelength range of interest. These values are similar to the best reported in the literature. However, the relatively high substrate temperatures required to obtain these optimised films ( $>300^\circ\text{C}$ ) prevent them from being incorporated as top TCO on low temperature nc-Si:H solar cells.
8. Our preliminary solar cells with p-i-n structure point to the screening of the internal electric field within the active layer as the main limiting factor in the photovoltaic conversion. Lower filament temperatures and faster deposition rates allowed a very significant improvement in the performance of the solar cells. This result fully agrees with the enhanced intrinsic character of the samples obtained under these cleaner deposition conditions. To date, our best solar cell showed a 2.5% photovoltaic conversion efficiency. It was entirely obtained by Hot-Wire CVD on AZO-coated glass at an indeed low substrate temperature of  $150^\circ\text{C}$ . The undoped active layer  $2.4 \mu\text{m}$  thick was grown at a high deposition rate of  $15 \text{ \AA}/\text{s}$ , thus the process time was less than 30 minutes. On account of the preliminary character of the work, neither textured front electrodes nor back reflectors were incorporated in the solar cell design. Besides, since

the p-layer was certainly too thick ( $\sim 500 \text{ \AA}$ ), just optical losses severely limited the maximum expected efficiency.

9. From optical calculations, we estimate that our current devices would present short circuit currents around  $20 \text{ mA/cm}^2$  if they incorporated light confinement strategies. Considering the open circuit voltage and fill factor already obtained, this would result in conversion efficiencies over 4%. In the future, the optimisation of a low temperature top TCO, most probably ITO, will allow to incorporate back reflectors in our structures. Besides, inverted n-i-p solar cells illuminated from the top side will be also tested. These structures would benefit from the enhanced quality of the material at the top interface with respect to the initial stages of growth.

# References

- Abelès F., Advanced optical techniques, A.C.S. van Heel, Amsterdam, 145 (1967).
- Asensi J.M., Ph.D.Thesis, University of Barcelona (1994).
- Asensi J.M., Merten J., Voz C., Andreu J., Journal of Applied Physics, 85, 5, 2939-2951 (1999).
- Bai Y., Ford D.H., Rand J.A., Proc. 14<sup>th</sup> European Photovoltaic Solar Energy Conference, 999 (1997).
- Beck N., Meier J., Fric J., Remes Z., Poruba A. Flückiger R., Pohl J., Shah A., Vanecek M., Journal of Non-Crystalline Solids, 198-200, 903-906 (1996).
- Beck N., Wyrsh N., Hof C., Shah A., J. Appl. Phys., 79, 9361-9367 (1996b).
- Beneking C., Rech B., Wieder S., Kluth O., Wagner H., Frammelsberger W., Geyer R., Lechner P., Rübél H., Schade H., Thin Solid Films, 351, 241-246 (1999).
- Bennet H.E., Porteus J.O., J. Opt. Soc. Am. A, 51, 1234 (1961).
- Bergmann, R.B., Applied Physics A, 69, 187-194 (1999).
- Brüggemann R., Main C., Physical Review B, Volume 57, Number 24, R15 080-083 (1998).
- Brühne K., Klein S., Schubert M.B., 16<sup>th</sup> European Photovoltaic Solar Energy Conference, Glasgow, in press (2000).
- Burstein E., Physical Review B, 25, 7826 (1982).
- Carlson D.E., Williams B.F., U.S. Patent No. 4442310, April 10, 1984.
- Chiang K.L., Dell'Oca C.J., Schwettmann, J. Electrochem. Soc., 126, 2267-2269 (1979).
- Cifre J., Bertomeu J., Puigdollers J., Polo M.C., Andreu J., Applied Physics A, 59, 645 (1994).
- Crandall R.S., J. Appl. Phys., 54, 7176 (1983).
- Curry R., Photovoltaic Insiders' Report, 17, 1 (1998).
- Curtins H., Favre M., Amorphous Silicon and Related Materials, World Scientific Publishing Company, 329-363 (1988).

- Delgado J.C., Andreu J., Sardin G., Morenza J.L., *Thin Solid Films*, 191, 283-295 (1990).
- Diehl F., Schröder B., Oechsner H., *Journal of Applied Physics*, 84, 6, 3416-3418 (1998).
- Dusane R.O., Dusane S.R., Bhide V.G., Kshirsagar S.T., *Appl. Phys. Lett.*, 63, 2201-2203 (1993).
- Flückiger R.S., Ph.D.Thesis, University of Neuchâtel (1995).
- Goerlitzer M., Beck N., Torres P., Meier J., Wyrsh N., Shah A., *J. Appl. Phys.* 80 (9), 5111-5115 (1996).
- Goerlitzer M., Torres P., Beck N., Wyrsh N., Keppner H., Pohl J., Shah A., *Journal of Non-Crystalline Solids*, 227-230, 996-1000 (1998).
- Goerlitzer M., Torres P., Droz C., Shah A., *Solar Energy Materials and Solar Cells*, 60, 195-200 (2000).
- Goetz M., Vaucher S., Tscherner R., Shah A., *Proc. 12<sup>th</sup> EC Photovoltaic Science Engineering Conf.*, Amsterdam, 1229-1232 (1994).
- Gordon R., Proscia J., Ellis F.B., Delahoy A.E., *Solar Energy Mater.*, 18, 263-281 (1989).
- Green M.A., *Prog. Photovolt. Res. Appl.*, 2, 87-94 (1994).
- Guillet J., Ph.D.Thesis, INPG Grenoble (1998).
- Hack M., Shur M., *J. Appl. Phys.* 58, 997 (1985).
- Hagedorn G., *Kumulierter Energieaufwand von Photovoltaik- und Windkraftanlagen*, IFE Schriftenreihe Heft 25, Ed. Lehrstuhl f. Energiewirtschaft und Kraftwerkstechnik, TU München (1992).
- Hof C., Ph.D. Thesis, Institut de Microtechnique, Université de Neuchâtel (1999).
- Hubin J., Shah A.V., *Philos. Mag. B*, 72(6), 589-599 (1995).
- Isomura M., Kinoshita T., Hishikawa Y., Tsuda S., *Appl. Phys. Lett.*, 65(18), 2329-2331 (1994).
- Jackson W.B., Amer N.M., Boccara A.C., Fournier D., *Appl. Optics*, 20, 1333 (1981).
- Jackson W.B., Amer N.M., *Phys. Rev. B*, 25, 5559 (1982).
- Jackson W.B., Johnson N.M., Biegelsen D.K., *Appl. Phys. Lett.*, 43(2), 195-197 (1983).
- Jackson W.B., *Phys. Rev. B*, 38, 3595 (1988).

- Jäger S., Szyszka B., Szczyrbowski J., Bräuer G., *Surface and Coatings Technology*, 98, 1304-1314 (1998).
- Jain V.K., Kulshreshtha A.P., *Solar Energy Mater.*, 4, 151 (1981).
- Kalkan K., Fonash S.J., *Materials Research Society Symp. Proc.*, 467, 319-324 (1997).
- Kamins T., *Polycrystalline silicon for integrated circuit applications*, Kluwer Academic Publishers, Norwell (1988).
- Keppner H., Meier J., Torres P., Fischer D. Shah A., *Appl. Phys. A*, 69, 169-177 (1999).
- Kim K.H., Park K.C., Ma D. Y., *J. Appl. Phys.*, 81(12), 7764-7772 (1997).
- Kluth O., Löffl A., Wieder S., Beneking C., Appenzeller W., Houben L., Rech B., Wagner H., Hoffmann S., Waser R., Anna Selvan J.A., Keppner H., *Proc. of the 26<sup>th</sup> IEEE Photovoltaics Specialists Conference, Anaheim CA (USA)*, 715-718 (1997).
- Knights J.C., Lucovsky G., *CRC Critical Reviews in Solid State Materials Sciences*, 21, 211 (1980).
- Kondo M., Nishimiya T., Saito K., Matsuda A., *Journal of Non-Crystalline Solids*, 227-230, 1031-1035 (1998).
- Kroll U., Meir J., Keppner H., Shah A., Littlewood S.D., Kelly I.E., Giannoulès P., *J. Vac. Sci. Technol. A*, 13, 2742-2746 (1995).
- Kroll U., Shah A., Keppner H., Meier J., Torres P., Fischer D., *Solar Energy Materials and Solar Cells*, 48, 343-350 (1997).
- Lips K., Kanschä P., Will D., Lerner C., Fuhs W., *Journal of Non-Crystalline Solids*, 227-230, 1021-1025 (1998).
- Lucovsky G., Wang C., Williams M.J., Chen Y.L., Maher D.M., *Mater. Res. Soc. Symp., Proc.* 283, 443 (1993).
- Mahan H., Reedy R.C., Iwaniczko E., Wang Q., Nelson B.P., Xu Y., Gallagher A.C., Branz H.M., Crandall R.S., Yang J., Guha S., *Materials Research Society Symp. Proc.*, 507 (1998).
- Masuda A., *J. Non-Cryst. Solids*, 59-60, 767 (1983).
- Matsumura H., *Jpn. J. Appl. Phys.*, 25, L949 (1986).
- Matsumura H., *Materials Research Society Symp. Proc.*, 118, 43-48 (1988).
- Matsumura H., *Jpn. J. Appl. Phys.*, 30, L1522 (1991).

- Matsuyama T., Baba T., Takahama T., Tsuda S., Nishiwaki H., 13<sup>th</sup> European Photovoltaic Solar Energy Conference and Exhibition, Nice (1995).
- Matsuyama T., Terada N., Baba T., Sawada T., Tsuge S., Wakisaka K., Tsuda T., *J. Non-Cryst. Solids*, 198-200, 940 (1996).
- Meier J., Flückiger R., Keppner H., Shah A., *Appl. Phys. Lett.*, Volume 65, 860 (1994).
- Meier J., Dubail S., Platz R., Torres P., Kroll U., Anna Selvan J.A., Vaucher N.P., Hof C., Fischer D., Keppner H., Flückiger R., Shah A., Shklover V., Ufert K.D., *Solar Energy Materials and Solar Cells* 49, 35-44 (1997).
- Meier J., Keppner H., Dubail S., Ziegler Y., Feitknecht L., Torres P., Hof Ch., Kroll U., Fischer D., Cuperus J., Anna Selvan J.A., Shah A., 2<sup>nd</sup> World Conf. on Photovoltaic Solar Energy Conversion, Vienna, Volume I, 375-379 (1998).
- Meier J., Dubail S., Cuperus J., Kroll U., Platz R., Torres P., Anna Selvan J.A., Pernet P., Beck N., Pellaton Vaucher N., Hof Ch., Fischer D., Keppner H., Shah A., *Journal of Non-Crystalline Solids*, 227-230, 1250-1256 (1998b).
- Meiling H., Schropp R.E.I., *Appl. Phys. Lett.*, 70, 2681-2683 (1997).
- Meiling H., Schropp R.E.I., *Appl. Phys. Lett.*, Vol. 74, No. 7, 1012-1014 (1999).
- Merten J., Ph.D.Thesis, University of Barcelona (1996).
- Merten J., Asensi J.M., Voz C., Shah A.V., Platz R., Andreu J., *IEEE Transactions on Electron Devices*, Vol. 45, No. 2, 423-429 (1998).
- Meyer W., Neldel H., *Z. Tech. Phys. (Leipzig)* 18, 588 (1937).
- Milford E., *Renewable Energy World*, Vol. 2, N° 1, 80 (1999).
- Möller H.J., *Semiconductors for Solar Cells*, Artech House, Norwood (1993).
- Nelson B.P., Iwaniczko E., Schropp R.E.I., Mahan H., Molenbroek E., Salamon S., Crandall R.S., 12<sup>th</sup> International EC Photovoltaic Solar Energy Conference, 679-682 (1994).
- Niikura C., Brenot R., Vanderhaghen R., Poisant Y., Roca P., Bourée J.E., Kleider J.P., Longeaud C., 16<sup>th</sup> European Photovoltaic Solar Energy Conference and Exhibition, Glasgow, in press (2000).
- Palz W., *Renewable Energy World*, Vol. 3, N° 2, 24-37 (2000).
- Pauli M., Doscher M., Salentiny G., Homberg F., Muller J., 11<sup>th</sup> EC Photovoltaic Solar Energy Conference, Montreux, 525 (1992).

Papadopoulos P., Scholz S., Bauer S., Schröder B., Öchsner H., *J. Non-Cryst. Solids*, 164-166, 87-90 (1993).

Peiró D., Bertomeu J., Voz C., Asensi J.M., Puigdollers J., Andreu J., 14<sup>th</sup> European Photovoltaic Solar Energy Conference, Barcelona, 1428 (1997).

Peiró D., Ph.D.Thesis, University of Barcelona (1999).

Peiró D., Bertomeu J., Voz C., Fonrodona M., Soler D., Andreu J., *Materials Science and Engineering B*, 60-70, 536-541 (2000).

Pernet P., Goetz M., Niquille X., Fischer D., Shah A., Althaus H., Haller A., 2<sup>nd</sup> World Conf. on Photovoltaic Solar Energy Conversion, Vienna, Volume I, 976-979 (1998).

Poruba A., Remes Z., Springer J., Vanecek M., Fejfar A., Kocka J., Meier J., Torres P., Shah P., 2<sup>nd</sup> World Conf. on Photovoltaic Solar Energy Conversion, Vienna, Volume I, 781-785 (1998).

Puigdollers J., Cifre J., Polo M.C., Asensi J.M., Bertomeu J., Andreu J., Lloret A., *Appl. Surf. Sci.*, 86, 600 (1995).

Puigdollers J., Ph.D.Thesis, University of Barcelona (1995b).

Puigdollers J., Dosev D., Orpella A., Voz C., Peiró D., Bertomeu J., Marsal L.F., Pallarés J., Andreu J., Alcubilla R., *Materials Science and Engineering B*, 69-70, 526-529 (2000).

Rath J.K., Galetto M., Van der Werf C.H.M., Feenstra K., Meiling H., Van Cleef M.W.M., Schropp R.E.I., *Technical Digest of the 9<sup>th</sup> International Photovoltaic Science and Engineering Conference*, Miyazaki, 227 (1996)

Rath J.K., Meiling H., Schropp R.E.I., *Jpn. J. Appl. Phys.*, 36, 5436 (1997).

Rath J.K., Meiling H., Schropp R.E.I., *Solar Energy Materials and Solar Cells*, 48, 269-277 (1998).

Rath J.K., Schropp R.E.I., *Materials Research Society Symp. Proc.*, 557, in press (1999).

Rhoderick E.H., *Metal-Semiconductor Contacts*, Clarendon Oxford (1978).

Ritter D., Weiser K., *Optics Communications*, Volume 57, 336-338 (1986).

Rose A., *Concepts in photoconductivity and allied problems*, John Wiley & Sons, New York (1963).

Ruff D., Mell H., Tóth L., Sieber I., Fuhs W., *Journal of Non-Crystalline Solids*, 227-230, 1011-1015 (1998).

- Saito K., Sano M., Matuda K., Kondo T., Nishimoto T., Ogawa K., Kajita I., 2<sup>nd</sup> World Conf. on Photovoltaic Solar Energy Conversion, Vienna, Volume I, 351-354 (1998).
- Sauvain E., Ph.D. Thesis, Institut de Microtechnique, Université de Neuchâtel (1992).
- Shah A.V., Platz R., Keppner H., Solar Energy Materials and Solar Cells, 38, 501-520 (1995).
- Shah A., Sauvain E., Hubin J., Pipoz P., Hof C., Philosophical Magazine B, 75(6), 925-936 (1997).
- Shi Z., Green M.A., Prog. Photovolt. Res. Appl., 6, 247-257 (1998).
- Schropp R.E.I., Zeman M., Amorphous and microcrystalline silicon solar cells, Kluwer Academic Publishers, Dordrecht (1998).
- Schropp R.E.I., Rath J.K., IEEE Transactions on Electron Devices, Vol. 46, No. 10, 2069-2071 (1999).
- Schubert M.B., Brüggemann R., Bilger G., Hierzenberger A., 2<sup>nd</sup> World Conf. On Photovoltaic Solar Energy Conversion, Vienna, Volume I, 834-837 (1998).
- Sopori B.L., Madjdpour J., Chen W., 2<sup>nd</sup> World Conf. on Photovoltaic Solar Energy Conversion, Vienna, Volume I, 156-159 (1998).
- Staebler D.L., Wronski C.R., Appl. Phys. Lett., Volume 31, 292 (1977).
- Starobinski L., Dus R., Vacuum, 46, 433 (1995).
- Stöger M., Breymesser A., Schlosser V., Ramadori M., Plunger V., Peiró D., Voz C., Bertomeu J., Nelhiebel M., Schattschneider P., Andreu J., Physica B, 273-274, 540-543 (1999).
- Street R.A., Hydrogenated Amorphous Silicon, Cambridge University Press, Cambridge (1991).
- Strese D., Die Ludwig-Bölkow-Studie: Solarstrom wird retabel in: Bild der Wissenschaft 7, 49-56 (1998).
- Swanepoel R., J. Phys. E:Sci. Instrum., Volume 16, 1214-1222 (1983).
- Sze S.M., Physics of semiconductor devices, Wiley & Sons, New York (1985).
- Tarui H., Matsuyama T., Okamoto S., Dohjoh H., Hishikawa Y., Nakamura N., Tsuda S., Nakano S., Ohnishi M., Kuwano Y., Jpn. J. Appl. Phys., 28, 2436 (1989).

Tsai C.C., Thompson R., Doland C., Ponce F.A., Anderson G.B., Wacker B., Materials Research Society Symp. Proc. 118, 49-54 (1988).

Torres P., Meier J., Flückiger, Kroll U., Anna Selvan J.A., Keppner H., Shah A., Appl. Phys. Lett., 69, 1373-1375 (1996).

Torres P., Ph.D. Thesis, Institut de Microtechnique, Université de Neuchâtel (1998).

Tsai C.C., Proc. of the Int. Workshop on Amorphous Semiconductors, World Scientific Publishing Co., 113 (1987).

Twidell J., Renewable Energy World, Vol. 2, N° 1, 45-49 (1999).

Vanecek M., Kocka J., Stuchlik J., Kozisek Z., Stika O., Triska A., Solar Energy Materials, 8, 411 (1983).

Varadi P., Renewable Energy World, Vol. 1, N° 3, 12-19 (1998).

Veprek S., Iqbal Z., Kühne R.O., Capezzuto P., Sarott F.A., Gimzewski J.K., J. Phys. C Solid State Phys., 16, 6241 (1983).

Vetterl O., Hapke P., Kluth O., Lambertz A., Wieder S., Rech B., Finger F., Wagner H., Solid State Phenom., 67-68, 101 (1999).

Voz C., Peiró D., Bertomeu J., Soler D., Fonrodona M., Andreu J., Materials Science and Engineering B, 69-70, 278-283 (2000).

Voz C., Peiró D., Fonrodona M., Soler D., Bertomeu J., Andreu J., Solar Energy Materials & Solar Cells, 63, 237-246 (2000b).

Voz C., Fonrodona M., Soler D., Peiró D., Asensi J.M., Bertomeu J., Andreu J., 16<sup>th</sup> European Photovoltaic Solar Energy Conference, Glasgow, in press (2000c).

Wallinga J., Arnoldbik W.M., Vredenberg A.M., Schropp R.E.I., van der Weg W.F., J. Phys. Chem. B, 102, 6219-6224 (1998).

Wang X., Bar-Yam Y., Adler D., Joannopoulos J.D., Phys. Rev. B, 38, 1601 (1988).

Wanka H.N., Lotter E., Schubert M.B., Materials Research Society. Symp. Proc., 336, 657-662 (1994).

Wanka H.N., Zedlitz R., Heintze M., Schubert M.B., 13<sup>th</sup> European Photovoltaic Solar Energy Conference, Nice, Volume II, 1753-1756 (1995).

Ward L., The optical constants of bulk materials and films, IOP Publishers 2<sup>nd</sup> Edition, Bristol, 246 (1994).

Wenham S.R., Green M.A., Watt M.E., Applied Photovoltaics, Bridge Printery, Sydney (1994).

Wiesmann H., Ghosh A.K., McMahon T., Strongin M., J. Appl. Phys., 50, 3752 (1979).

Wiesmann H., Method of producing hydrogenated amorphous silicon film, U.S. Patent 4237150, (1980).

Yamamoto K., Yoshimi M., Suzuki T., Tawada Y., Okamoto T., Nakajima A., 2<sup>nd</sup> World Conf. on Photovoltaic Solar Energy Conversion, Vienna, Volume II, 1284-1289 (1998).

# Acronym list

- $A$  absorptance  
 $\alpha$  optical absorption coefficient  
AM1.5 Air Mass 1.5  
a-Si:H hydrogenated amorphous silicon  
AZO aluminium-doped zinc oxide  
 $\chi$  collection efficiency  
 $C$  depletion capacitance  
Cat-CVD Catalytic CVD  
c-Si monocrystalline silicon  
CVD Chemical Vapour Deposition  
 $d$  layer thickness  
 $E$  electric field strength, energy level  
 $e$  elementary charge  
 $E_a$  dark conductivity activation energy  
 $E_g$  optical band gap  
 $E_{MN}$  Meyer-Neldel rule activation energy  
 $\epsilon_s$  dielectric permittivity of silicon  
 $FF$  fill factor  
FTO fluorine-doped tin oxide  
 $G$  generation rate  
 $\gamma$  SSPC gamma exponent,  
linear coefficient of the band gap thermal dependence  
 $\eta$  conversion efficiency  
 $H$  Haze ratio  
HWCVD Hot-Wire CVD  
 $I$  irradiance  
ITO tin-doped indium oxide  
 $j$  current density  
 $k_B$  Boltzmann's constant  
 $\lambda$  wavelength  
 $L_{diff}$  diffusion length  
 $L_{drift}$  drift length  
 $L_{screen}$  screening length  
 $\mu$ c-Si:H hydrogenated microcrystalline silicon  
MFC mass flow controller  
 $\mu_n$  electron mobility  
 $\mu_p$  hole mobility  
 $\mu\tau_{ph}$  steady state photoconductivity  $\mu\tau$ -product  
 $n$  density of electrons,  
refractive index,  
diode ideality factor  
 $N_C$  effective density of charged centres,  
conduction band effective density of states

---

nc-Si:H hydrogenated nanocrystalline silicon  
 $N_D$  density of donor states  
 $N_{db}$  density of dangling bonds  
 $N_V$  valence band effective density of states  
 $p$  density of holes  
 $P$  power density,  
pressure  
PDS Photothermal Deflection Spectroscopy  
PECVD Plasma-Enhanced CVD  
PID proportional-integral-derivative temperature control  
p-Si polycrystalline silicon  
PV photovoltaic  
 $QE$  quantum efficiency  
 $R$  reflectance,  
resistance,  
recombination rate  
 $\rho$  space charge density,  
resistivity  
 $r_d$  deposition rate  
RF radio frequency  
 $\sigma$  dark conductivity,  
capture cross-section  
SEM Scanning Electron Microscopy  
SIMS Secondary Ion Mass Spectroscopy  
 $\sigma_o$  dark conductivity prefactor  
 $\sigma_{oo}$  Meyer-Neldel rule prefactor  
 $\sigma_{ph}$  steady state photoconductivity  
 $\sigma_r$  root mean square surface roughness  
scm standard cubic centimetre  
 $SR$  spectral response  
SSPC Steady State Photoconductivity  
 $T$  transmittance,  
absolute temperature  
TCO transparent conductive oxide  
TFT thin film transistor  
UHV ultra-high vacuum  
 $V_{bi}$  built-in voltage  
 $V_C$  voltage collection  
 $V_d$  Schottky barrier  
VHF-PECVD Very High Frequency PECVD  
 $w$  width of the depletion region  
 $X_C$  crystalline fraction  
XPS X-ray photoelectron spectroscopy  
XRD X-ray diffraction

# Figure list

**Figure 1.1:** Expected global warming due to the Greenhouse effect during the next century computed at the Max Planck Institute for Meteorology a) for an unabated increase in carbon dioxide emissions and b) with accelerated policies promoting renewable energy sources in order to reduce carbon dioxide emissions[www.dkrz.de].

**Figure 1.2:** Prediction of averaged component costs in PV systems and price reduction over time[acre.murdoch.edu.au]. Thin film technologies must allow to reduce significantly the costs of module manufacturing.

**Figure 1.3:** Worldwide PV shipments production[Curry, 1998]. The major manufacturers of solar panels are Solarex and USSC in the USA, Sanyo, Canon and Kyocera in Japan and BP Solar and Siemens Solar in Europe. There are many other smaller manufacturers.

**Figure 1.4:** Percentage of costs for the production of crystalline-Si photovoltaic modules based on wafer technology (450  $\mu\text{m}$ ).

**Figure 1.5:** Typical thin film solar cell structure. Glass is used as a carrier for the front electrode and the active device, in this case a p-i-n structure. Contacts are usually thin metallic films thermally evaporated in high vacuum.

**Figure 1.6:** Relative thicknesses of conventional bulk silicon and thin film crystalline silicon solar cells compared to the thickness of a human hair.

**Figure 1.7:** Processing temperatures and thicknesses of absorber materials for several photovoltaic technologies[Beneking et al., 1999].

**Figure 1.8:** Deposition time as a function of the deposition rate. The filled region represents the field of interest for photovoltaic applications[Keppner et al., 1999].

**Figure 2.1:** Picture of the multichamber HWCVD set-up at University of Barcelona. The three inline UHV chambers were fabricated at the Vacuum Unit of the Scientific-Technical Service of University of Barcelona.

**Figure 2.2:** Boron profile by SIMS in the active layer of a p-i-n structure obtained in a sole chamber compared to the case of a p-i-n solar cell where the intrinsic layer was grown in a different chamber.

**Figure 2.3:** Schematic of one of the HWCVD chambers showing the inner arrangement of its accessories.

**Figure 2.4:** Detailed schematics of the multichamber HWCVD set-up and the pumping system [Peiró, 1999].

**Figure 2.5:** Diagram of the gas panels[Peiró, 1999]. Microflows of diborane and phosphine are added to the base silane-hydrogen gas mixture in the feedgas to p- and n-type dope respectively. Nitrogen is the purging gas.

**Figure 2.6:** Experimental set-up used to perform the high-impedance dark conductivity measurements in vacuum.

**Figure 2.7:** Geometry of the coplanar electrodes on the samples. They are obtained by thermal evaporation of aluminium in high vacuum. The distance  $l$  between them is 1mm while their width  $w$  is 10mm. Since  $l \sim 10^3 d$  for typical film thickness', we neglect edge effects in the current lines to calculate the conductivity.

**Figure 2.8:** Thermal dependence of the dark conductivity for an undoped nc-Si:H sample obtained by HWCVD. Its high activation energy indicates the intrinsic character of the sample.

**Figure 2.9:** Experimental set-up for the steady state photoconductivity measurement. The monochromatic incident photon flux  $\Phi$  is determined with a calibrated photodetector. The absorption of these photons with energies higher than the band gap mainly result in the generation of electron-hole pairs.

**Figure 2.10:** Mean steady state photoconductivity and SSPC  $\mu\tau$ -product as a function of the mean generation rate for a typical undoped nc-Si:H sample obtained by HWCVD. A sublinear behaviour  $\langle\sigma_{ph}\rangle\sim\langle G\rangle^\gamma$  with  $\gamma=0.85$  is observed because  $\mu\tau_{ph}$  significantly depends on the generation rate.

**Figure 2.11:** The transverse PDS set-up in our laboratory. The experiment is automatised with a personal computer. The deflection detector consists of two adjacent reverse biased photodetectors.

**Figure 2.12:** Deflection of the probe beam by the mirage effect. The thickness of the He-Ne laser probe beam is considered infinitesimal ( $dz$ ).

**Figure 2.13:** Optical absorption coefficient of typical hydrogenated amorphous and nanocrystalline silicon thin films measured with the PDS system in our laboratory. They are compared to the tabulated optical absorption of crystalline silicon[Möller, 1993].

**Figure 2.14:** Experimental set-up for measuring the JV curve of solar cells in the dark or under varied irradiances. Note the four quadrant voltage source and current-voltage converter to ensure enough sensitivity without the loading effects with high shunt resistances.

**Figure 2.15:** Typical JV curve under illumination of a p-i-n solar cell. It generates electrical power in the 4<sup>th</sup> quadrant (power dissipated  $P=V\times J<0$ ). The fill factor  $FF$  corresponds to the ratio of the area delimited by  $j_{mp}$  and  $V_{mp}$  in the maximum power point with respect to the area determined by  $j_{sc}$  and  $V_{oc}$ .

**Figure 2.16:** The spectral response measurement set-up. Bias light from the halogen lamp can be superimposed to the monochromatic probe beam arriving through the optic fiber. The experiment is automatised with a personal computer.

**Figure 2.17:** Optical absorbance in the whole device and only in the active layer compared to the short circuit external quantum efficiency of a 2.1 $\mu\text{m}$  thick p-i-n nc-Si:H solar cell obtained by HWCVD[Table 2.2].

**Figure 2.18:** Short circuit internal quantum efficiency (collection efficiency) of the same solar cell in figure 2.17. It is also plotted the penetration length as a function of the wavelength.

**Figure 2.19:** Structures used for the standard depletion capacitance-reverse voltage measurement. Either heavily p-doped nc-Si:H or ZnO:Al allow to obtain rectifying contacts with undoped-nc-Si:H. The evaporated chromium back contact turned out to be quasi ohmic as evidenced in Cr/undoped nc-Si:H/Cr sandwich structures which did not show any rectifying behaviour.

**Figure 2.20:** Voltage dependence of the depletion capacitance of a ZnO:Al/undoped nc-Si:H pseudo Schottky contact. The nice linear behaviour, together with the slight differences (<10%) between the depletion region widths obtained either from equation 2.21 or 2.25, indicate that the assumptions of the simplified model are fulfilled. The inset current density-voltage characteristic shows a satisfactory rectifying behaviour.

**Figure 2.21:** Simulation results compared to the analytical model within the one-sided abrupt junction approximation for an uniform density of charged centres  $N_C$  of  $2\times 10^{17}\text{cm}^{-3}$ . The relatively rough abrupt-junction approximation satisfactorily reproduces the electric field and voltage profiles for  $x\leq w$ .

**Figure 3.1:** System formed by an absorbing smooth thin film on an infinite substrate. The extinction coefficient  $k$  in the complex refractive index  $\hat{n}$  of the film relates to the optical absorption coefficient by  $\alpha = 4\pi k/\lambda$ . A fraction  $R$  of the incident power density  $I$  is reflected whereas  $T$  is transmitted. Hence,  $A=I-T-R$  is the fraction absorbed within the film.

**Figure 3.2:** Simplified model to evaluate the optical absorptance  $A$  within the film. The reflection at the film-substrate interface of the attenuated irradiance is not considered while  $r$  is the Fresnel reflection coefficient at the air-film interface.

**Figure 3.3:** Optical absorption coefficient calculated from the sole absorptance spectrum and improved calculation considering also the transmittance spectrum for a HWCVD nanocrystalline silicon layer 2  $\mu\text{m}$  thick.

**Figure 3.4:** Effective optical absorption coefficient, according to the effective media model, for a nc-Si:H sample with a 90% of crystalline fraction. The amorphous phase, with an optical gap of 1.8 eV, was considered of poor quality: defect density of  $10^{18} \text{ cm}^{-3}$  and Urbach front of 90 meV.

**Figure 3.5:** Optical absorption coefficients measured by PDS for the HWCVD nc-Si:H samples in table 3.1. It is also shown the effective optical absorption coefficient expected for a 90% crystalline fraction. The corresponding ratios are also plotted as a measure of the optical absorption enhancement.

**Figure 3.6:** Optical absorptances expected for 2  $\mu\text{m}$  thick films with the optical absorption coefficient spectra in figure 3.5. Note the higher absorptance in the near infrared obtained when  $\alpha_{HP}$  was used for the calculation.

**Figure 3.7:** Optical absorptance of a 2  $\mu\text{m}$  thick HWCVD nc-Si:H sample (HP in table 3.1) compared with that of a 0.4  $\mu\text{m}$  thick PECVD a-Si:H sample. The relatively high a-Si:H band gap causes important optical losses when the solar AM1.5 spectrum is considered.

**Figure 3.8:** Calculated optical absorptances in the active layer for the device structures in table 3.2. The measured external quantum efficiency of the 990323c solar cell [Section 2.3.2] is also shown for comparison (dashed line). Note the additional losses due to either interface or bulk recombination depending on the wavelength range.

**Figure 3.9:** Experiment to easily detect elastic light scattering. a) When the detector is placed just behind the substrate, all the transmitted irradiance contributes to the measured spectrum (integrated transmittance). b) If it is placed away from the substrate and its aperture  $\phi$  is reduced with a mask, only the transmitted irradiance in a direction near to that of the incident beam will reach the detector (specular transmittance).

**Figure 3.10:** Integrated and specular transmittances for a 1.5  $\mu\text{m}$  thick HWCVD nc-Si:H silicon sample. The specular transmittance was measured by placing the detector 2 cm away from the sample and reducing its aperture to 1 cm (deviation of  $14^\circ$  from the incident direction). With this geometry, the measured Haze ratio was around 10% over the whole spectrum.

**Figure 3.11:** Experiment to evaluate the *rms* roughness of a nc-Si:H film according to equation 3.11. The smooth wafer does not present diffuse reflection. Hence, specular reflectance equals total reflectance in that case.

**Figure 3.12:** Scanning Electron Microscopy view of a nc-Si:H sample. Note the columnar structure of the film (bulk scattering) and its as grown textured surface (surface scattering).

**Figure 3.13:** Determination of the *rms* roughness of the HWCVD nc-Si:H samples from reflectance measurements. The angle of incidence was  $45^\circ$ .

**Figure 3.14:** Trajectory of a ray from the incident beam of light scattered at the rough surface of the film. Its effective optical path through the sample becomes  $d/\cos\theta$ .

**Figure 3.15:** Expected optical absorption coefficient enhancement as a function of the scattered light distribution ( $\Phi = \Phi_0 \cos^n \theta$ ). For  $n=1.4$  we obtain the factor 1.75 experimentally observed in our rough samples.

**Figure 3.16:** Approximate and exact calculation of the dark conductivity of ideally intrinsic single crystal silicon as a function of the temperature.

**Figure 3.17:** Conventional Meyer-Neldel rule observed in different series of undoped nc-Si:H samples obtained by HWCVD [Table 3.4]. The thermal shrinking of the band gap does not fully explain the strong exponential behaviour.

**Figure 3.18:** Room temperature dark conductivity and corresponding activation energies for a p-doping series of samples [Table 3.5]. An increase in the activation energy as well as a lower room temperature dark conductivity is observed for low p-doping levels.

**Figure 3.19:** Effect of the deposition rate on the intrinsic character of undoped nc-Si:H samples [Table 3.4]. The dark conductivity activation energy increases with the deposition rate.

**Figure 3.20:** Current density-voltage characteristics for both types of studied pseudo-Schottky contacts. Slight differences in the rectifying behaviours were observed which however do not influence the depletion capacitance-voltage experiment.

**Figure 3.21:** Determination of the concentration of charged centres from the voltage dependence of the depletion capacitance for the pseudo-Schottky contacts in table 3.6.

**Figure 3.22:** Steady state photoconductivity  $\mu\tau$ -product as a function of the dark conductivity activation energy for several series of undoped nc-Si:H samples[Table 3.4]. The values of  $\mu\tau_{ph}$  are those obtained for a mean generation rate of  $10^{19} \text{ cm}^{-3} \text{ s}^{-1}$ [Section 2.2.2]. A misleading increase in  $\mu\tau_{ph}$  is observed for the less intrinsic samples.

**Figure 3.23:** Calculated occupation functions of the dangling bond[Eq. 3.28] depending on the electron to hole densities ratio (bottom axis) or the relative Fermi-level shift from midgap(top axis). The slight dissymmetry is due to the factor 3 between the capture cross-sections of electrons and holes by neutral dangling bonds[Table 3.7].

**Figure 3.24:** Different  $\mu\tau$ -products as a function of the parameter  $b$  (bottom axis) or the relative shift of the Fermi-level from midgap (top axis). For the calculation we have used  $\mu_n=10 \text{ cm}^2/\text{Vs}$ ,  $\mu_p=3 \text{ cm}^2/\text{Vs}$  and  $N_{db}=10^{16} \text{ cm}^{-3}$  which leads to  $\mu\tau_{ph}=10^{-7} \text{ cm}^2/\text{V}$  for midgap samples.

**Figure 3.25:** An steady increase is observed in the photoconductivity of samples kept under high irradiances for a long time. The light soaking experiment was performed with  $100\text{mW}/\text{cm}^2$  of white light. Hence, the Staebler-Wronski effect does not play an important role in the stability of nc-Si:H.

**Figure 3.26:** Change in the dark conductivity and activation energy of a nc-Si:H sample obtained by HWCVD due to post-oxidation in air. A pronounced n-type character is observed after 45 days.

**Figure 3.27:** Infrared transmittance spectra for two pieces of the same sample 24 hours after deposition either kept in the dark or light-soaked under  $100\text{mW}/\text{cm}^2$  of white light. The as deposited transmittance is also shown for comparison. The pronounced overlapped bands at  $1050$  and  $1140\text{cm}^{-1}$  corresponding to Si-O-Si stretching modes indicate a faster post-oxidation in the light soaked piece.

**Figure 4.1:** Equivalent circuit of a photovoltaic device. For low mobility p-i-n structures a recombination term must be added to the typical single exponential model. In order to allow the more reasonable work with current densities,  $R_s$  and  $R_p$  are actually effective series and parallel resistances calculated as the product of the corresponding absolute values  $\mathcal{R}_s$  and  $\mathcal{R}_p$  and the active area of the device  $S$ , i.e.,  $R_s=S\mathcal{R}_s$  and  $R_p=S\mathcal{R}_p$ .

**Figure 4.2:** Parameters to determine for each JV curve which are used for the VIM analysis.

**Figure 4.3:** Determination of the voltage collection from linear fits to the JV curves around the short circuit point.

**Figure 4.4:** Results from the VIM characterisation method for the same device before and after dry-etching the surrounding layers.

**Figure 4.5:** VIM data for the 990409c HWCVD solar cell[Table 4.1]. The measured values can be perfectly fitted over irradiances varying more than four orders of magnitude.

**Figure 4.6:** Results from the analytical description for an active layer thickness  $d$  of  $2\mu\text{m}$  and a dangling bond density  $N_{db}$  of  $10^{16}\text{cm}^{-3}$ . The built-in potential  $V_{bi}$  is  $1\text{V}$  which considering a band gap of  $1.2\text{eV}$  corresponds to doped layers with the typically obtained dark conductivity activation energies around  $0.1\text{eV}$ . We have considered a dangling bond correlation energy  $U_{eff}=V_i$  of  $0.3\text{eV}$  and  $V_p=V_n=0.35\text{V}$ . Note that  $V_{bi}=V_p+V_i+V_n$ .

**Figure 4.7:** (a) Set of parameters determining the electric field profile as a function of the active layer thickness considering a dangling bond density of  $10^{16}\text{cm}^{-3}$ . (b) As a function of the dangling bond density considering an active layer thickness of  $2\mu\text{m}$ .

**Figure 4.8:** (a) Short circuit collection efficiency as a function of the active layer thickness for a fixed dangling bond density of  $10^{16} \text{ cm}^{-3}$ . (b) Short circuit collection efficiency as a function of the dangling bond density for a fixed active layer thickness of  $2 \mu\text{m}$ . In this last calculation it is essential to include the dependence of the different lifetimes on the dangling bond density ( $\tau \sim 1/N_{db}$ ). The dashed line (left axis) indicates the estimated short circuit current density which would be obtained for an irradiance of  $100 \text{ mW/cm}^2$  of weakly absorbed light  $\alpha(h\nu=1.5 \text{ eV}) \approx 10^3 \text{ cm}^{-1}$  (mean generation rate of  $5 \times 10^{20} \text{ cm}^{-3} \text{ s}^{-1}$ ).

**Figure 4.9:** Short-circuit collection efficiency and corresponding voltage collection as a function of the  $L_I/d$  ratio. It has been considered  $V_i=0.3 \text{ V}$ . Voltage collections of a few volts indicate a drift length around one order of magnitude longer than the active layer thickness.

**Figure 4.10:** Calculated band diagram within the active layer of a contaminated (n-type) active layer. There is not significant voltage drop across the quasineutral region (flat bands) where the field strength is null. The voltage drop in the PI region is significantly higher than that in the IN region. The device actually behaves as a  $p^+-n-n^+$  structure.

**Figure 4.11:** Calculated magnitude of the internal electric field within clean (ideally intrinsic) and contaminated (n-type) active layers. Note that the electric field is enhanced in the PI region at expense of the weakened field in the IN region. It completely vanishes in the quasineutral I region.

**Figure 4.12:** Calculated short circuit collection efficiency for a clean active layer (as in figure 4.8a) compared to the case of a contaminated active layer [Eq. 4.47]. The dashed line (left axis) indicates the estimated short circuit current density which would be obtained for a mean generation rate of  $5 \times 10^{20} \text{ cm}^{-3} \text{ s}^{-1}$ .

**Figure 5.1:** Thin film p-i-n solar cell structure. Glass is used as a carrier for the front electrode (TCO) and the active device, in this case a p-i-n structure. Contacts are usually thin metallic films thermally evaporated in high vacuum.

**Figure 5.2:** Effect of a 15 minutes HWCVD hydrogen treatment on AZO and FTO (Asahi-U<sup>TM</sup>). While the transmittance of AZO slightly improves in the visible range, FTO is drastically darkened by the strongly reducing ambient.

**Figure 5.3:** Optical transmittance of an optimised AZO coating compared with the Air Mass 1.5 solar spectrum [Wenham et al., 1994]. In the wavelength range of interest, the optical transmittance remains over 85%. The inset plot shows the dependence of the square optical absorption coefficient on the photon energy which allows to deduce a direct optical gap of 3.5 eV.

**Figure 5.4:** SIMS profiles of zinc and aluminium in samples grown onto AZO at different substrate temperatures. Profiles of sodium and calcium for the same samples.

**Figure 5.5:** The lateral leakage current in thin film rectifying devices can be avoided by etching the material surrounding the device.

**Figure 5.6:** Reciprocal slope of the dark JV curve in reverse as a function of the contact size. The quadratic dependence indicates dominant lateral leakage currents.

**Figure 5.7:** Dark current-voltage characteristics before and after dry-etching the device. Lateral leakage currents were clearly reduced.

**Figure 5.8:** JV curves and power outputs for the compensated 990119c and non compensated 990113c p-i-n structures.

**Figure 5.9:** External quantum efficiency for the compensated 990119c and non compensated 990113c p-i-n structures. The estimated optical absorptances of these devices are also plotted.

**Figure 5.10:** Simulated internal field profile in equilibrium for a clean (not contaminated), contaminated ( $8 \times 10^{15} \text{ cm}^{-3}$  donors) and 95% compensated ( $7.6 \times 10^{15} \text{ cm}^{-3}$  acceptors) p-i-n structures.

**Figure 5.11:** External quantum efficiencies of the structures deposited with high gas flows compared to their optical absorptances. The 990319c was non compensated while the compensated cell 990323c showed a clearly enhanced collection. The low and shifted response of the 990311c structure points to overcompensation.

**Figure 5.12:** VIM results for high (990414c) and low filament temperature (990409c) solar cells.

**Figure 5.13:** External quantum efficiency of the high (990414c) and low filament temperature (990409c) solar cells compared with the optical absorptances of these devices.

**Figure 5.14:** JV curves and power outputs under an irradiance of  $100 \text{ mW/cm}^2$  for three solar cells obtained at different deposition rates. The efficiency is clearly correlated with the deposition rate.

**Figure 5.15:**  $R_{sc}$  as a function of  $j_{sc}$  from VIM data for the same solar cells in figure 5.14. The collection voltage clearly increases with the deposition rate.

**Figure 5.16:** External quantum efficiencies of the same cells plotted in figures 5.14 and 5.15 compared to their optical absorptances. The quantum efficiency is enhanced when the deposition rate is increased.

**Figure 5.17:** JV curves and power outputs for the solar cells in table 5.5. The efficiency clearly worsens when the substrate temperature is increased.

**Figure 5.18:** External quantum efficiencies and estimated optical absorptances of the cells in the substrate temperature series[Table 5.5].

**Figure 5.19:** Normalised efficiency of devices under light soaking. Steadily increasing stabilities are achieved by increasing the thickness of the n-doped layer which seems to cap the undoped active layer.

# Table list

**Table 1.1:** Global trends in energy use by source, 1991-1997. Data provided by the Worldwatch Institute[Milford, 1999].

**Table 2.1:** Thermal and optical properties of different materials at 25°C.  $k$  is the thermal conductivity,  $\rho$  the density and  $C$  the specific heat.  $L$  is the thermal diffusion length calculated at the typical modulation frequency of 10 Hz. Though carbon tetrachloride ( $\text{CCl}_4$ ) even presents better specific properties than Fluorinert FC72™ for the PDS experiment, we discarded the use because of its health hazards by inhalation.

**Table 2.2:** Deposition conditions, thicknesses of the different layers and photovoltaic performance for the 990323c HWCVD solar cell in figure 2.17. The short circuit current density value has been verified by convolution of the external quantum efficiency with the irradiance spectrum.

**Table 3.1:** HWCVD nc-Si:H samples obtained at different process pressures. Both were obtained with a substrate temperature of 150°C and a 95% hydrogen dilution (4 sccm of  $\text{SiH}_4$  mixed with 76 sccm of  $\text{H}_2$ ). The wire was heated to 1700°C.

**Table 3.2:** Optical limits in the maximum short circuit current density under AM1.5 for different p-i-n structures. Equation 3.8 is used for the calculation considering only the absorptance in the active layer. As usual, it is assumed that all the carriers photogenerated within the doped layers recombine (dead layers).

**Table 3.3:** Main electrical parameters for ideally intrinsic single crystal silicon as a function of the absolute temperature. Without impurities, only lattice scattering determines the temperature dependence of the carrier mobilities ( $\sim 1/T^{3/2}$ ).

**Table 3.4:** Deposition conditions and main electrical properties of the series of undoped nc-Si:H samples in figure 3.17. The first six samples( $\square$ ) were grown with a filament of 1 mm of diameter whereas the following six( $\circ$ ) and the last three ones( $\diamond$ ) were obtained with a thinner filament of 0.5 mm. A wider technological description and the structural properties of these samples can be found elsewhere[Peiró, 1999].

**Table 3.5:** Technological parameters, room temperature dark conductivity and thermal activation energy for the p-doping series in figure 3.18. The B/Si solid phase ratio was calculated by comparing the SIMS profiles of these samples with those of patterns (implanted wafers). All the samples were obtained with a process pressure of  $7 \cdot 10^{-3}$  mbar whereas the substrate temperature was around 200 °C and the filament was heated above 1700 °C.

**Table 3.6:** Undoped nc-Si:H layers deposited by HWCVD on p+ nc-Si:H (A,B) and ZnO:Al (C) in order to perform the depletion capacitance-reverse voltage experiment. Higher deposition rates  $r_d$  were obtained by increasing the process pressure and gas flows. The effect of the filament temperature  $T_f$  is also studied by comparing the A and B contacts each other. The density of charged centres  $N_C$  and the width of the depletion region without any external voltage applied  $w_o$  are indicated for each contact.

**Table 3.7:** Capture cross-sections of electrons and holes by dangling bonds in their three possible states of charge. Corresponding capture times as a function of the dangling bond density  $N_{ab}$ .

**Table 4.1:** Deposition conditions, photovoltaic performance and equivalent circuit parameters deduced from the VIM data for the 990409c HWCVD solar cell.

**Table 5.1:** Average electrical properties of the optimised ZnO:Al coatings selected for devices.

**Table 5.2:** Compensated p-i-n structures compared with non compensated ones for different silane flows. The short circuit current and open circuit voltage were measured under an irradiance of 100 mW/cm<sup>2</sup>. They are grouped in low flow non compensated, low flow compensated, high flow non compensated, high flow overcompensated and high flow compensated.

**Table 5.3:** Effect of the filament temperature on the device photovoltaic response. The short circuit current, open circuit voltage and fill factor were measured under an irradiance of 100 mW/cm<sup>2</sup>. The solar cells are grouped in low and high process pressure.

**Table 5.4:** Solar cells obtained with different process pressures and gas flows. The short circuit current density, open circuit voltage and fill factor were measured under an irradiance of 100 mW/cm<sup>2</sup>. They are grouped in low flow-low pressure, high flow-low pressure and high flow-high pressure, i.e., they are grouped by the deposition rate.

**Table 5.5:** Effect of the substrate temperature on the device photovoltaic response. The short circuit current density, open circuit voltage and fill factor were measured under an irradiance of 100 mW/cm<sup>2</sup>.

## Introducción

Una vez comenzado el nuevo siglo debemos plantearnos sin más demora la necesidad de desarrollar y explotar diferentes fuentes de energía renovable. No sólo por la escasez de las fuentes tradicionales sino también por motivos ecológicos. Las energías solar y eólica son con diferencia las más importantes de estas fuentes renovables. Aunque es indudable el avance de la energía eólica, los paneles solares se pueden integrar mucho más fácilmente en las ciudades que las gigantescas turbinas actuales de conversión eólica. Actualmente ya podemos encontrar sistemas fotovoltaicos autónomos en los tejados y fachadas de nuestras ciudades que pueden conectarse directamente a la red eléctrica. La biblioteca pública Pompeu Fabra en el centro de Mataró (53 kWp) o el tejado fotovoltaico en el ayuntamiento de Barcelona (100 kWp) son ejemplos muy cercanos.

Sin embargo, el elevado coste de producción de las tradicionales células solares en oblea de silicio monocristalino ha impedido la aplicación extensiva de la energía solar. Por tanto, diferentes tecnologías en capa fina se han investigado con el objetivo de reducir costes. Las células solares en capa fina suelen ser estructuras p-i-n en que la colección de los portadores fotogenerados es asistida por el campo eléctrico interno del dispositivo. Por tanto, más que un ahorro de materia prima, se busca la posibilidad de utilizar materiales menos restrictivos en cuanto a propiedades electrónicas tales como movilidad y tiempo de vida. En este ámbito, las células solares de silicio amorfo se comercializan desde hace muchos años y son las más comunes en calculadoras o relojes solares. En cambio, la opción del silicio cristalino en capa fina no se ha considerado hasta hace poco debido a su baja absorción óptica en comparación con el silicio amorfo. A pesar de ello, estrategias de confinamiento óptico tales como electrodos texturados y reflectores posteriores permiten solventar este problema. De este modo el silicio microcristalino ( $\sim 1 \mu\text{m}$ ) y nanocristalino ( $\sim 10 \text{ nm}$ ) ganan un gran interés de cara a una inmediata aplicación en el futuro. Además, este tipo de materiales de grano pequeño pueden ser depositados a temperaturas de sustrato relativamente bajas sobre soportes económicos tales como plástico o vidrio. El depósito químico en fase vapor asistido por plasma (PECVD) y por filamento caliente (HWCVD) parecen ser las técnicas de depósito más prometedoras para la obtención de este tipo de materiales. Aunque la primera en su variedad de alta frecuencia (VHF-PECVD) ha permitido la obtención de dispositivos p-i-n de silicio nanocristalino hidrogenado (nc-Si:H)

con eficiencias del 8.5% [Meier et al., 1998], el bajo ritmo de depósito ( $2 \text{ \AA/s}$ ) requiere más de cinco horas de proceso. En cambio, la técnica HWCVD permite obtener sin dificultad ritmos de depósito por encima de los  $10 \text{ \AA/s}$  aunque la eficiencia más alta referenciada hasta hoy es del 4.4% [Schropp et al., 1999]. No obstante, la optimización óptica de esta última estructura daría mucho margen para la mejora. Por otra parte, la implementación de un sistema de depósito por HWCVD resulta significativamente más económica que en el caso de un sistema de PECVD.

Por lo que se refiere a nuestro laboratorio, nuestro mejor dispositivo de silicio nanocristalino hidrogenado obtenido enteramente mediante HWCVD presenta una eficiencia de conversión del 2.5%. Se trata de una estructura p-i-n cuya capa activa de  $2.4 \mu\text{m}$  de grosor se obtiene en menos de 30 minutos de proceso ( $15 \text{ \AA/s}$ ) a una temperatura de sustrato realmente baja de  $150^\circ\text{C}$ . Considerando la total ausencia de estrategias de confinamiento óptico así como la escasa optimización de las capas dopadas, este resultado puede considerarse muy prometedor.

## Sistema experimental

### Equipo de depósito

En 1998 se puso en marcha un sistema de depósito multicámara sellado en ultra alto vacío para la obtención de dispositivos fotovoltaicos mediante la técnica HWCVD. Este sistema, ampliamente descrito en un trabajo previo [Peiró, 1999], fue construido en la Universidad de Barcelona durante los dos primeros años de investigación dentro del proyecto CRYSTAL (JOR3-CT97-0126) en el programa JOULE de la Comunidad Europea. Este equipo consta de tres cámaras separadas mediante válvulas de guillotina. Una de las cámaras se utiliza para la carga de sustratos y para el depósito del electrodo transparente mediante pulverización catódica magnetrón. Las otras dos cámaras se utilizan para procesos HWCVD. Se utilizan cámaras diferentes para el crecimiento del material intrínseco y dopado para evitar la indeseada contaminación cruzada en la capa activa del dispositivo. Cada una de las cámaras dispone de los accesorios habituales para la medida de la presión y el control de la temperatura del sustrato. Un brazo acoplado magnéticamente permite la transferencia del sustrato de una cámara a otra sin romper en ningún momento el vacío.

El sistema de bombeo está formado por bombas turbomoleculares (360 l/s) en cada una de las cámaras seguidas de un depresor Roots y una bomba rotatoria de paletas (144 l/s). Permite una presión base del orden de  $10^{-9}$  mbar y un amplio rango de presiones de proceso que se fijan mediante válvulas de mariposa entre la cámara y la bomba turbomolecular. El panel de gases consta de las cinco líneas requeridas para los diferentes depósitos: silano, hidrógeno, diborano, fosfina y nitrógeno. La mezcla base de silano diluido en hidrógeno se regula mediante controladores de flujo másico mientras que los gases dopantes se añaden en muy bajas proporciones mediante válvulas de aguja. El nitrógeno se utiliza como gas de purga. Cabe resaltar la incorporación de un purificador SAES Getters MonoTorr® para reducir la presencia de contaminantes (oxígeno, carbono...) en la mezcla de gases que entra en la cámara por debajo de las partes por billón.

## Técnicas de caracterización

Dada la aplicación fotovoltaica que se busca estamos especialmente interesados en las propiedades ópticas y eléctricas del silicio nanocrystalino hidrogenado obtenido mediante la técnica HWCVD. Para todas las muestras se ha medido sistemáticamente la conductividad y fotoconductividad en geometría coplanar. Para ello se depositan contactos de aluminio sobre las muestras por evaporación térmica en alto vacío. La energía de activación de la conductividad en oscuridad en función de la temperatura permite, en primera aproximación, estimar la posición del nivel de Fermi en la banda prohibida del semiconductor. Por otro lado, el producto movilidad-tiempo de vida obtenido de la fotoconductividad en estado estacionario puede considerarse, aunque con ciertas reservas, indicativo de la calidad del material de cara a ser incorporado como zona activa en dispositivos fotovoltaicos. La caracterización óptica de las muestras se ha realizado a partir de medidas de transmisión, reflexión y absorción óptica. Para ello se ha utilizado un espectrofotómetro así como un sistema de espectroscopía por deflexión fototérmica en geometría transversal. El principal interés se tiene en el coeficiente de absorción óptica que determina en buena medida el aprovechamiento de la energía luminosa incidiendo sobre el dispositivo.

La caracterización de las células solares depositadas ha consistido en la medida de la característica corriente-tensión para diferentes niveles de iluminación. Los datos obtenidos se han analizado de acuerdo con un modelo analítico para el estudio de dispositivos

fotovoltaicos en capa fina[Merten et al., 1998]. También se ha medido la eficiencia cuántica externa de todos los dispositivos obtenidos en el rango de longitudes de onda de interés. Por otra parte, se ha medido la capacidad de la unión en diferentes contactos p-i a fin de determinar la densidad efectiva de estados cargados cerca de la interficie frontal de la célula solar. Esta carga atrapada determina la longitud de apantallamiento del campo eléctrico interno en la zona activa del dispositivo.

## **Silicio nanocristalino obtenido por Hot-Wire CVD**

### **Propiedades ópticas**

La absorción óptica del silicio nanocristalino hidrogenado resulta mayor de lo que cabría esperar atendiendo a las altas fracciones cristalinas obtenidas (>90%) y a un modelo simple de medio efectivo que considere la contribución de las fases amorfa y cristalina. Este efecto debe atribuirse principalmente a la rugosidad superficial de las muestras que depende de las condiciones de depósito. Presiones de proceso más altas ( $>10^{-2}$  mbar) favorecen la orientación cristalina [220] que da lugar a muestras de superficie texturada y microestructura de tipo columnar. Diferentes medidas de reflectancia en incidencia oblicua han permitido estimar el valor cuadrático medio de la rugosidad en capas crecidas a altas presiones de proceso en aproximadamente un 2% del grosor de las capas. Estos pequeños valores ya son suficientes para multiplicar en casi un factor 2 la absorción óptica en el infrarrojo cercano y consecuentemente la fotogeneración en el dispositivo. Además, este beneficioso efecto podría incrementarse sin duda alguna con la incorporación de reflectores posteriores en el diseño de la célula solar.

### **Propiedades eléctricas**

La medida de la conductividad eléctrica en función de la temperatura ha evidenciado que muestras no intencionadamente dopadas resultaron no totalmente intrínsecas. La energía de activación obtenida indica un cierto desplazamiento del nivel de Fermi hacia una de las bandas a la vez que el signo del efecto Seebeck indica un indudable carácter n. Este resultado queda corroborado al observar que niveles de microdopado tipo *p* dan lugar a muestras compensadas en que el nivel de Fermi se sitúa en la mitad del gap. Se trata de un problema frecuentemente observado y referenciado ampliamente por otros grupos que

trabajan en este tipo de material. Este dopado no intencionado puede atribuirse a la contaminación de la capa durante su crecimiento. Entre las fuentes de contaminantes a considerar están las impurezas en fase gas así como evaporadas desde el filamento. Medidas de espectroscopía de niveles profundos detectaron la presencia de niveles en la banda prohibida que podrían atribuirse oxígeno, tungsteno y cobre, entre otros menos reproducibles. En cualquier caso y como sería de esperar, la incorporación de contaminantes es inversamente proporcional al ritmo de depósito. De este modo, la energía de activación térmica de la conductividad eléctrica se aproxima a la mitad del gap para muestras depositadas a más altos ritmos de depósito ( $>5 \text{ \AA/s}$ ). Además, la densidad efectiva de estados localizados en la banda prohibida calculada a partir de capacidades de unión también disminuye al aumentar el ritmo de depósito. En cuanto a las medidas de fotoconductividad en estado estacionario, se observa una evidente anticorrelación entre el valor del producto movilidad-tiempo de vida y el carácter intrínseco de la muestra. Así, una fotoconductividad mayor no necesariamente indica un material de mayor calidad sino que puede ser debida sólo a un dopado no intencionado que alarga el tiempo de vida de los portadores mayoritarios. El tiempo de vida de los portadores minoritarios resulta indudablemente degradado en estas muestras contaminadas. Los productos movilidad-tiempo de vida en muestras con el nivel de Fermi cercano al centro del gap sí pueden considerarse indicativos de la calidad del material de cara a aplicaciones fotovoltaicas.

En cuanto a la estabilidad del silicio nanocrystalino hidrogenado obtenido por HWCVD, afortunadamente no se ha observado ninguna degradación atribuible al temido efecto Staebler-Wronski. La absorción óptica para fotones de energía menor que el gap no aumenta al exponer las muestras a fuertes iluminaciones durante largos periodos de tiempo. Por el contrario, la fotoconductividad aumenta en muestras expuestas a fuertes iluminaciones. Además, la conductividad en oscuridad aumenta espontáneamente con el tiempo a la vez que se observa una evidente disminución en la energía de activación térmica. Un evidente carácter  $n$  es observado en muestras inicialmente intrínsecas tras haber sido expuestas a la atmósfera durante unos días. Estos resultados podrían indicar una inevitable postoxidación del material que es corroborada por los espectros de transmisión en el infrarrojo. En realidad, esta inestabilidad química ha sido ampliamente referenciada para el silicio nanocrystalino hidrogenado independientemente de la técnica de depósito y dificulta en gran medida la caracterización de las muestras. Aún así, se trata de un problema resoluble tecnológicamente mediante el encapsulado final del dispositivo.

## **Colección en células solares p-i-n en capa fina**

El estudio desde un punto de vista fundamental del funcionamiento de las estructuras de célula solar ensayadas se basó en el análisis de las características corriente-tensión bajo diferentes niveles de iluminación. Para una irradiancia media-alta la pendiente de la característica alrededor de la condición de cortocircuito sólo depende de las pérdidas por recombinación en el dispositivo. Para explicar este comportamiento se ha expuesto un modelo semianalítico para describir la colección en estructuras p-i-n de silicio nanocrystalino hidrogenado. De acuerdo con este modelo, la recombinación en la región neutra de la zona activa determina la eficiencia de colección. Las regiones cargadas de la zona activa cercanas a las interfaces con las capas dopadas en general no contribuyen significativamente en la recombinación total. En cambio su efecto sí es determinante en el apantallamiento del campo eléctrico en la región neutra, influyendo así indirecta, pero muy significativamente, en la recombinación. Dado que en este tipo de estructuras la colección de los portadores fotogenerados se realiza básicamente por arrastre, la eficiencia debe mejorarse evitando el apantallamiento del campo eléctrico. Este efecto se consigue optimizando el material, es decir, disminuyendo cuanto sea posible la densidad de carga localizada en la banda prohibida, ya sea debida a contaminantes o a defectos estructurales. La posibilidad de reducir el grosor de la zona activa también permite obtener un campo eléctrico más intenso, pero sólo puede considerarse si se utilizan estrategias de confinamiento óptico en la estructura.

## **Células solares de silicio nanocrystalino obtenidas por HWCVD**

### **Aspectos tecnológicos previos**

Los ensayos de célula solar se han realizado sobre estructuras p-i-n depositadas sobre vidrio recubierto por un electrodo transparente. El dispositivo se ilumina a través del propio sustrato de vidrio mientras que los contactos posteriores se obtienen mediante la evaporación sucesiva de cromo y aluminio en alto vacío. Un punto clave en el caso de la técnica de depósito HWCVD es la elección de un electrodo frontal transparente entre las opciones habituales, i.e.: óxido de indio dopado con estaño (ITO), óxido de estaño dopado con flúor (FTO) y óxido de zinc dopado con aluminio (AZO). El último fue elegido por ser

el único capaz de soportar el fuerte ambiente reductor debido a la alta concentración de hidrógeno atómico durante procesos HWCVD. Así un blanco cerámico adecuado para la obtención de AZO se instaló en el cabezal del equipo de pulverización catódica magnetron en la cámara de carga. Los electrodos frontales optimizados presentaban transmitancias ópticas por encima del 85% en el rango de longitudes de onda de interés y resistencias de cuadro alrededor de  $10 \Omega$ . Estos valores son similares a los mejores referenciados en la literatura. No obstante, no se ha desarrollado un método para la texturación de estos electrodos frontales de manera que no contribuyen sensiblemente al confinamiento óptico de la luz incidente sobre la célula.

Otro aspecto tecnológico de relativa importancia en el caso de este tipo de dispositivos en capa fina es la indeseada pero frecuente presencia de corrientes de fuga. Afortunadamente, las de tipo lateral pueden minimizarse a posteriori eliminando de algún modo la capa dopada alrededor del área activa del dispositivo. De este modo se mejora la tensión en circuito abierto así como el factor de forma para niveles de iluminación baja-media. En nuestro caso se consiguió el efecto deseado mediante ataque con plasma RF (13.56 MHz) de  $\text{CF}_4$  diluido en oxígeno al 20% a una presión de proceso de 0.4 mbar. El ritmo de ataque resultante, alrededor de  $15 \text{ \AA/s}$ , permite eliminar totalmente la capa dopada alrededor del contacto metálico superior en poco más de medio minuto.

## Resumen de los resultados en células solares

Se han ensayado más de 50 estructuras p-i-n de silicio nanocrystalino hidrogenado enteramente obtenidas mediante HWCVD. Estos dispositivos se han obtenido sobre sustratos de vidrio recubiertos de AZO depositado por pulverización catódica magnetron en la cámara de carga. Las capas dopadas utilizadas presentaban conductividades en oscuridad a temperatura ambiente del orden de unos pocos  $\Omega^{-1}\text{cm}^{-1}$  y energías de activación térmica menores de 100 meV. Los grosores de capa dopada en la mayoría de estructuras son del orden de  $500 \text{ \AA}$  obteniéndose características rectificadoras muy satisfactorias. No obstante, la absorción óptica en la gruesa capa dopada *p* limita severamente la máxima eficiencia alcanzable.

Los estudios más sistemáticos se han centrado en la optimización de la zona activa del dispositivo, es decir, en la capa no dopada. Dado el ligero carácter *n* muy frecuentemente observado en capas no intencionadamente dopadas, se ha ensayado la técnica del

compensado mediante microdopado tipo p. Esta opción se ha mostrado relativamente efectiva aunque parece difícil sistematizarla y se corre el dramático riesgo de sobrecompensar la zona activa. Por tanto, es preferible optimizar las condiciones de depósito para evitar la incómoda técnica del microdopado. Las medidas eléctricas en muestras no dopadas evidenciaron que éstas resultaban más intrínsecas si crecían más rápido. Este resultado parece indicar que la incorporación de contaminantes durante el crecimiento del material es responsable de que éste no resulte intrínseco aun sin estar intencionadamente dopado. Un mayor ritmo de depósito puede obtenerse aumentando el flujo de silano o la presión de proceso durante el crecimiento. De esta manera, estructuras de célula comparables muestran una muy clara correlación entre eficiencia y ritmo de depósito que, además, es adecuada de cara a una posible producción industrial. Por otra parte, zonas activas depositadas a temperaturas de filamento más bajas dieron lugar a dispositivos significativamente más eficientes. Este resultado parece indicar que, además de contaminantes en fase gas, deben tenerse en cuenta la eventual evaporación de contaminantes metálicos del filamento o su soporte. En relación a la temperatura de sustrato también se observó una clara mejora en la eficiencia para zonas activas obtenidas con temperaturas de consigna más bajas. Una mayor incorporación de hidrógeno podría explicar este resultado al pasivar enlaces de silicio no saturados. Aunque tampoco deben descartarse en este punto factores negativos como el degasado del calefactor o la difusión de contaminantes desde el electrodo transparente que aumentarían con la temperatura de consigna.

En relación a la estabilidad de los dispositivos, debemos confesar que no puede asegurarse a largo plazo sin un encapsulamiento que evite la postoxidación. De acuerdo con diferentes estudios referenciados en la literatura, el menor bombardeo iónico en procesos de filamento caliente en comparación a los asistidos por plasma podría dar lugar a materiales de menor densidad más permeables al oxígeno. En cualquier caso, la estructura podría finalizarse con una capa *n* obtenida por plasma sin perder la ventaja (mayor ritmo de depósito) del proceso HWCVD en la obtención de la zona activa. En realidad, el Debye Institute que lidera el desarrollo de la técnica HWCVD a nivel mundial obtiene las capas dopadas de sus dispositivos mediante PECVD.

Hasta la finalización del período de investigación recogido en esta memoria, el mejor dispositivo de silicio nanocristalino hidrogenado obtenido en nuestro laboratorio ofreció

una eficiencia de conversión del 2.5%. Como se avanzaba en la introducción, se trata de una estructura p-i-n obtenida enteramente mediante HWCVD. La zona activa de 2.4  $\mu\text{m}$  de grosor se obtiene en menos de 30 minutos de proceso (15  $\text{\AA}/\text{s}$ ) sin requerir compensación mediante microdopado. La temperatura de sustrato es cercana a 150  $^{\circ}\text{C}$  mientras que el filamento se sitúa alrededor de los 1600  $^{\circ}\text{C}$ . La total ausencia de estrategias de confinamiento óptico así como el excesivo grosor de la capa dopada  $p$  hacen que este resultado pueda considerarse muy prometedor.

## Conclusiones

1. Las células solares de silicio cristalino en capa fina son una prometedora alternativa a la gastada tecnología del silicio amorfo o a la segura pero costosa opción del silicio monocristalino en oblea. El factor determinante en la eficiencia de colección de estructuras p-i-n en capa fina pasa a ser el cociente entre longitud de arrastre y grosor de la zona activa. Así, materiales de menor calidad podrían aún ser válidos de manera que el silicio nanocrystalino hidrogenado aparece como una seria opción a tener en cuenta. Este tipo de material de grano pequeño puede ser obtenido a bajas temperaturas pudiéndose utilizar así sustratos de bajo coste tales como vidrio o plástico.
2. Entre las diferentes técnicas que permiten la obtención de silicio nanocrystalino hidrogenado en capa fina, el depósito químico en fase vapor asistido por filamento caliente (HWCVD) permite los mayores ritmos de depósito referenciados hasta hoy. Se alcanzan sin dificultad decenas de  $\text{\AA}/\text{s}$  manteniéndose buenas propiedades microestructurales. Además, la implementación y el mantenimiento de un sistema HWCVD es más simple y económica que la de un equipo de plasma. Sin embargo, sistemas multicámara para la obtención de dispositivos p-i-n se hacen imperativos para evitar la contaminación cruzada en la zona activa.
3. Nuestras muestras de silicio nanocrystalino hidrogenado obtenidas por HWCVD alcanzan sistemáticamente fracciones cristalinas por encima del 90%. En cambio, la absorción óptica resulta mayor de lo que cabría esperar atendiendo a un modelo de medio efectivo que considere el peso de las fases amorfa y cristalina. Este efecto puede atribuirse a la dispersión elástica de la luz en la superficie de las muestras debido a su

rugosidad nativa. Presiones de proceso más altas ( $>10^{-2}$  mbar) favorecen la orientación cristalina [220] que resulta en microestructuras columnares más texturadas. Medidas de reflectancia en incidencia oblicua permiten cuantificar el valor cuadrático medio de la rugosidad superficial alrededor de un 2% del grosor de estas muestras. Estos valores son suficientes para casi duplicar la absorción óptica en el infrarrojo cercano.

4. Diferentes caracterizaciones eléctricas indican un cierto carácter  $n$  en muestras no intencionadamente dopadas, especialmente en las obtenidas a bajos ritmos de depósito ( $\sim 2$  Å/s). La energía de activación térmica de la conductividad en oscuridad indica un desplazamiento del nivel de Fermi hacia una de las bandas a la vez que el signo del efecto Seebeck revela el carácter  $n$ . Además, niveles de microdopado tipo  $p$  dan lugar a muestras de mayor energía de activación al compensar los niveles responsables del indeseado carácter  $n$ . Las muestras menos intrínsecas presentan una engañosa alta fotoconductividad debido al aumento en el tiempo de vida de los portadores mayoritarios. Para los portadores minoritarios, que en la práctica limitan la colección en el dispositivo fotovoltaico, el tiempo de vida resulta indudablemente degradado.
5. Altos ritmos de depósito ( $>5$  Å/s) permiten obtener muestras no dopadas con el nivel de Fermi más cercano al centro del gap. A la vez, la capacidad de unión en contactos  $p$ - $i$  indica una disminución de  $10^{17}$  a  $10^{16}$  cm $^{-3}$  en la densidad efectiva de carga localizada en la zona intrínseca cercana a la interficie con la capa  $p$ . Este valor determina la longitud de apantallamiento del campo eléctrico en la zona activa del dispositivo. Los anteriores resultados apuntan a la incorporación de contaminantes como responsable del indeseado carácter  $n$  de muestras no dopadas. En realidad, medidas de espectroscopía de niveles profundos detectaron la presencia de niveles en la banda prohibida que podrían atribuirse oxígeno, tungsteno y cobre, entre otros menos reproducibles. Ya sean impurezas en fase gas o metales evaporados del filamento, su incorporación a la muestra en crecimiento se prevé inversamente proporcional al ritmo de depósito.
6. Afortunadamente, no se ha observado una degradación atribuible al efecto Staebler-Wronski en el silicio nanocristalino hidrogenado obtenido por HWCVD. Sin embargo, muestras expuestas al aire durante largos periodos de tiempo adoptan un significativo carácter  $n$ . Este efecto es atribuible a la postoxidación del material tal y como han

evidenciado medidas de transmisión en el infrarrojo. También se ha observado que esta postoxidación se ve acelerada bajo altas iluminaciones, quizá porque los fotones son capaces de romper enlaces débiles entre silicios favoreciendo así la posterior oxidación. En cualquier caso, esta relativa inestabilidad química parece inevitable y se ha referenciado para este tipo de material independientemente de la técnica de depósito.

7. El electrodo frontal transparente seleccionado para nuestros ensayos de célula solar fue óxido de zinc dopado con aluminio (AZO) debido a su excelente estabilidad química frente al hidrógeno atómico. Por el contrario, opciones como el óxido de estaño dopado con flúor o el óxido de indio dopado con estaño fueron descartadas al no soportar el ambiente fuertemente reductor en procesos de filamento caliente. Los recubrimientos de AZO sobre vidrio se obtuvieron por pulverización catódica magnetrón de un blanco cerámico en la cámara de carga. Los electrodos optimizados presentaban resistencias de cuadro alrededor de  $10 \Omega$  y transmitancias ópticas superiores al 85% en el rango de longitudes de onda de interés. Estos valores son comparables a los mejores referenciados en la literatura. No obstante, la relativamente alta temperatura de sustrato requerida para obtener estas capas ( $>300 \text{ }^\circ\text{C}$ ) no permite utilizarlas como electrodos superiores sobre estructuras de silicio nanocrystalino obtenidas a baja temperatura.
8. Los estudios sobre estructuras p-i-n apuntan al nivel de apantallamiento del campo eléctrico interno en la zona activa del dispositivo como el factor que determina la eficiencia de colección. Altos ritmos de depósito y bajas temperaturas de filamento son las condiciones que permitieron obtener dispositivos más eficientes. Este resultado coincide con el carácter más intrínseco del material crecido en estas condiciones de depósito más limpias. Hasta la finalización del período de investigación recogido en esta memoria, el mejor dispositivo de silicio nanocrystalino hidrogenado obtenido en nuestro laboratorio ofreció una eficiencia de conversión del 2.5%. La zona activa de  $2.4 \mu\text{m}$  de grosor se obtiene en menos de 30 minutos de proceso ( $15 \text{ \AA/s}$ ). La temperatura de sustrato es cercana a  $150 \text{ }^\circ\text{C}$  mientras que el filamento se sitúa alrededor de los  $1600 \text{ }^\circ\text{C}$ . La total ausencia de estrategias de confinamiento óptico así como el excesivo grosor de la capa dopada *p* hacen que este resultado pueda considerarse muy prometedor.

9. Simples cálculos ópticos indican que nuestros dispositivos actuales alcanzarían corrientes de cortocircuito de  $20 \text{ mA/cm}^2$  si las estructuras de célula solar incorporasen estrategias de confinamiento óptico. Entonces, los valores de factor de forma y tensión en circuito abierto ya obtenidos permitirían eficiencias por encima del 4%. De cara al futuro, se desea optimizar un electrodo transparente, muy probablemente ITO, que pueda depositarse a baja temperatura sobre la estructura para incorporar así reflectores posteriores. También se desean probar estructuras n-i-p invertidas iluminadas por la cara superior. Estas estructuras se beneficiarían de la mayor calidad del material en la interficie superior en relación a los estados iniciales de crecimiento.

